RICE UNIVERSITY

Experimental Characterization of Plasma Detachment from Magnetic Nozzles

by

Christopher Scott Olsen

A THESIS SUBMITTED
IN PARTIAL FULFILLMENT OF THE
REQUIREMENTS FOR THE DEGREE

Doctor of Philosophy

APPROVED, THESIS COMMITTEE:

Paul A Clout
Paul A. Cloutier, Chair
Professor Emeritus and Research Professor of
Physics and Astronomy

Franklin R. Chang-Díaz, Thesis Director
Adjunct Professor of Physics and Astronomy

David Alexander,
Professor of Physics and Astronomy
Director, Rice Space Institute

Frank K. Tittel
Frank K. Tittel,
J. S. Abercrombie Professor in Electrical and
Computer Engineering
Professor of Bioengineering

HOUSTON, TEXAS

MAY, 2013

ABSTRACT

Experimental Characterization of Plasma Detachment from Magnetic Nozzles

by

Christopher Scott Olsen

Magnetic nozzles, like Laval nozzles, are observed in several natural systems and have application in areas such as electric propulsion and plasma processing. Plasma flowing through these nozzles is inherently tied to the field lines and must separate for momentum redirection or particle transport to occur. Plasma detachment and associated mechanisms from a magnetic nozzle are investigated. Experimental results are presented from the plume of the VASIMR® VX-200 device flowing along an axisymmetric magnetic nozzle and operated at two ion energies to explore momentum dependent detachment. The argon plume expanded into a 150m^3 vacuum chamber where the background pressure was low enough that charge-exchange mean-free-paths were longer than experiment scale lengths. This magnetic nozzle system is demonstrated to hydrodynamically scale up to astrophysical plasmas, particularly the solar chromosphere, implying general relevance to many systems. Plasma parameters were mapped over a large spatial range using measurements from multiple plasma diagnostics.

The data show that the plume does not follow the magnetic field lines. A mapped integration of the ion flux shows the plume may be divided into three regions where 1) the plume briefly follows the magnetic flux, 2) diverges quadratically before 3)

expanding with linear trajectories. Transitioning from region 1→2, the ion flux departs from the magnetic flux suggesting ion detachment. An instability forms in region 2 driving an oscillating electric field that causes ions to expand before enhancing electron cross-field transport through anomalous resistivity. Transitioning from region 2→3 the electric field dissipates, the trajectories linearize, and the plume effectively detaches. A delineation of sub-to-super Alfvénic flow aligns well with the inflection points of the linearization without a change in magnetic topology. The detachment process is best described as a two part process: First, ions detach by a breakdown of the magnetic moment when the quantity $|v/f_c L_B|$ becomes of order unity. Second, the turbulent electric field enhances electron transport up to a factor of 4±1 above collisional diffusion; electron cross-field velocities approximate that of the ions and depart on more centralized field lines. Electrons are believed to detach by breakdown of magnetic moment further downstream in the weaker magnetic field.

Acknowledgements

I must first acknowledge and thank my wife Carina as well as our daughters Alana, Ariana, and Amelia for their enduring patience with me during this long process. The sacrifice of time away from their husband/father is difficult but greatly appreciated. At the same time you all are my joy, motivation, and means to preserve some resemblance of sanity. Also thanks to my parents and siblings for their continual encouragement to keep pushing through the tough times and realize that this devotion will pay off in the end. Thank you to my friends and coworkers for times of whimsy and helping me to remember the simple things in life.

Thank you to Dr. Paul Cloutier, my thesis advisor, and Dr. Franklin Chang-Díaz, my advisor for not giving up on me after all these years and for the opportunity to complete my education. It is through the cooperation of both of you that I am here and have gained valuable experience. On those same lines thanks must go to Rice University and the Ad Astra Rocket Company for allowing me to pursue this thesis research in an industry setting outside of the University. Thanks to Dr. Jared Squire, Dr. Mark Carter, and Dr. Edgar Bering III for their more detailed direction and suggestions with regards to the complexity of the VASIMR® experiment. I owe a great deal to Dr. Benjamin Longmier, who has unofficially served as a mentor these past 5 – 6 years, taught me uncountable lessons, put up with all of my questions, and in the end has made me a better scientist/researcher. Thanks goes out to Maxwell Ballenger whose help with the spectrum analyzer and assistance in running the experiment sometimes late into the night

were monumental. To Ben and Max, thanks also for the brotherhood we developed on our sailboat excursions and zero gravity flights. I will never forget them. Thanks also to Matthew Giambusso for his assistance in reducing a large amount of RPA data. To Charles Powell, Robert Peden, Robert Haun, and Ivan Ravlich, the interns who worked with me over several summers at Ad Astra, I thank for the opportunity to share my experience and learn to become a better teacher. To Frans Ebersohn, Dr. Eduardo Ahedo, and Dr. Rod Boswell I thank you all for our stimulating discussions regarding magnetic nozzle detachment theory.

This work was funded and supported by the Ad Astra Rocket Company, Webster, TX.

Table of Contents

List of Figures

List of Tables

Chapter 1: Introduction

Of particular interest in the sub-fields of astrophysics and plasma physics, and a main point in NASAs roadmap for the future of heliophysics[1, 2], are issues regarding plasma confinement, collisionless cross-field particle transport, and demagnetization or particle separation from the magnetic field lines. Charged fluids, better known as plasma, when magnetized and in the absence of collisions have the tendency to remain tied to field lines. Particles experiencing forces that cause drift motion deviate from the magnetic field line only by the gyroradius as the guiding center tracks along the magnetic lines of force. Even in collisional regimes, individual particles may cross magnetic field lines on gyroradii scale lengths through elastic, random-walk collisions but are still magnetized unless the field strength becomes too weak or the particles are neutralized upon an encounter with material boundaries. Despite this tendency for plasma to remain attached to the field lines, there is observed evidence from natural phenomena that points to the contrary. Magnetized plasma has been observed to have been transported through different regions of the solar atmosphere, such as the photosphere out to the corona, as well as out into space. The solar plasma has also been observed interacting with the earth's magnetosphere forming magnetic shocks/aurorae, as well as further out into interplanetary space where interaction with comet comas and deviation of the direction of the ion tail are seen[3-6].

One proposed medium for this separation or detachment of the particles from the applied magnetic field is through a magnetic nozzle, a region of diverging magnetic field lines that forms an inverse magnetic 'funnel' as the magnetic field strength becomes weaker with increasing distance. This type of nozzle is directly analogous to a traditional de Laval nozzle often used in neutral fluid-Mach transitions without having solid material boundaries. On the surface of the sun these nozzle-like diverging magnetic fields are seen in various regions of the photosphere ranging from sunspots to adjacent solar prominences and even coronal funnels[7]. Sweet and Parker have even hinted at the formation of magnetic nozzles to channel particle current during the ‘X’ line reconnection process in the merging of two sunspots[8-12]. Although plasma/particle transport and subsequent demagnetization is observed in these regions of diverging field lines (magnetic nozzles), it is not well understood which physical mechanisms mediate this transition. Several theories, discussed later, under various conditions and circumstances, attempt to explain some or all of the physics involved in ion and electron detachment from these magnetic structures but few have been adequately tested and verified experimentally. One theoretical mechanism may dominate more than another for a given setup or a combination of processes may be more applicable. Until recently each of the proposed mechanisms for plasma detachment have not been simultaneously and rigorously tested in a laboratory setting.

With greater understanding of the detachment process of an axially directed plasma flowing in a magnetic nozzle, it is thought that signatures of these mechanisms may be observed to be naturally occurring in environments such as the sun so long as the laboratory plasma is found to be scalable to astrophysical plasmas. With increased knowledge of such transport, new insight will be gained and questions will be answered in regards plasma/thermal transport in the solar atmosphere, astrophysical jets, aurora/magnetosphere interactions, or other applicable nozzle systems.

Section 1.1 – Magnetic nozzle applications

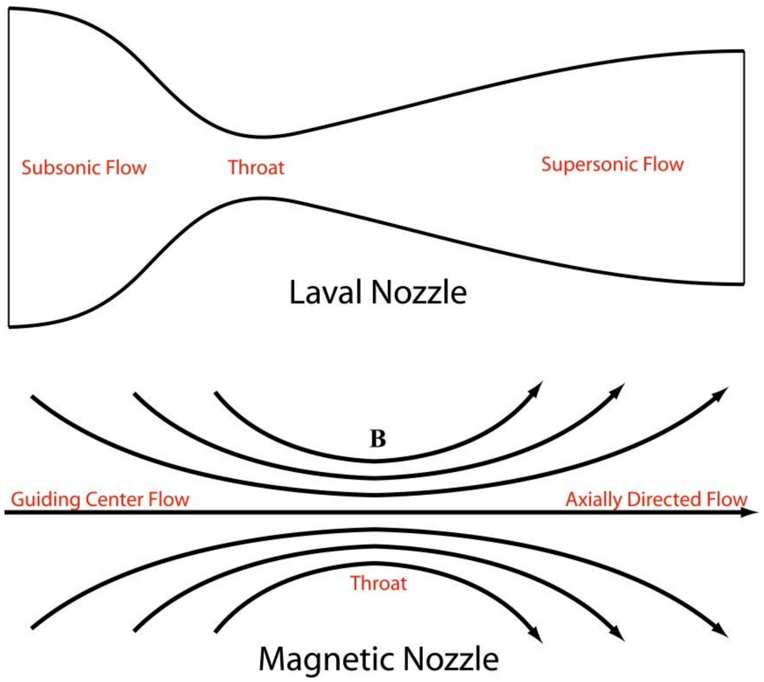

Figure 1.1: Comparison of the conventional Laval nozzle to the magnetic nozzle

Simple as they may be, magnetic nozzles consist of converging-diverging magnetic field lines and are the charged particle equivalent of the de Laval nozzle (figure 1.1). Plasma flow along these divergent magnetic nozzles can be found in a variety of natural environments. The solar atmosphere contains multiple examples including plage plasma flowing in the intense magnetic field of photosphere sunspots, spicules, plasma/reconnection jets, and near quiescent solar prominences where plasma is flowing along field lines between magnetic poles[13]. Magnetic nozzles may also be formed during the transport of hot gases from the lower atmosphere into the corona through coronal funnels[7, 13-17], during magnetic reconnection from merging sunspots[8, 9, 13], or out of the sun entirely with coronal mass ejections (CMEs)[18-20]. The largest structures with an applicable magnetic nozzle are astrophysical jets where the flow is along the magnetic axis away from stars and even galaxies[21-25]. Nozzled plasma flow has even been proposed to form in the Earth's magnetosphere during magnetic storms or during rapid magnetic reconnection being driven by whistler waves[10, 26].

In addition to natural nozzle systems there are many laboratory or otherwise direct applications of magnetic nozzles. In terms of in-space propulsion magnetic nozzles are used to contain and eject heated plasma to gain momentum[27]. The plasma processing industry, typically in the manufacture of semiconductors, uses these nozzles to direct the flow, spatial extent, and energy distribution during the etching process[28]. In the area of fusion research the flow of plasma through the diverging field lines of bundle divertors is studied and is critical to cross-field transport, confinement, and plasma material surface interactions[29-31].

Section 1.2 – Laboratory scaling to space plasmas

Considering the experimental nature of this work and the goal for a general understanding of plasma detachment mechanisms of plasma flow through a magnetic nozzle, it is desirable that the plasma source in this experiment scale up to space plasma phenomena. The issues with space plasma laboratory analogs are that size scales, time scales, densities, pressures, and velocities are not directly comparable to the objects or plasma being modeled. This laboratory plasma source is an electric magnetoplasma rocket most suited for ground-based propulsion studies; the plasma flow through its magnetic nozzle is many orders of magnitude smaller than most analogous natural plasmas.

Despite the differences in spatial scale, plasma property comparisons of the experiment with other space plasmas may be relevant so long as certain considerations are met. The first is that the flows are similar to the density and velocity structure present in natural magnetic nozzle systems. Some flows may have uniform plasma density across the flow while others may be more centrally peaked. Case by case comparisons may be required in order to be directly applicable. The plasma exhaust in this experiment is peaked in terms of density but more uniform in velocity. This profile should compare well with plasma jets/streams propagating down a magnetic field gradient. The second consideration is that fluid dynamical variables in the experiment scale up to the natural plasmas. The scaling of these fluid variables between different systems are often performed using the Euler equations for a polytropic gas[25, 32-36]:

$$\frac{\partial \rho}{\partial t} + \nabla \cdot (\rho \mathrm{v}) = 0 \qquad \text{1-1}$$

$$\rho \left(\frac{\partial \mathrm{v}}{\partial t} + \mathrm{v} \cdot \nabla \mathrm{v} \right) + \nabla P = 0 \qquad \text{1-2}$$

$$\frac{\partial P}{\partial t} + \gamma P \nabla \cdot \mathrm{v} + \mathrm{v} \cdot \nabla P = 0 \qquad \text{1-3}$$

where P is the gas pressure, v is the velocity, and ρ is the mass density. These equations have been shown to be invariant to rescaling so long as the time scale and velocity are equally modified[25, 33-36]:

$$r' = ar \qquad \text{1-4}$$

$$\rho' = b\rho \tag{1-5}$$

$$P' = cP \tag{1-6}$$

$$t' = a\sqrt{\frac{b}{c}}t \tag{1-7}$$

$$\mathrm{v}' = \sqrt{\frac{b}{c}}\mathrm{v} \tag{1-8}$$

where the primed quantity represents the scaled up fluid variable and a, b, and c are scaling constants. In other words if equations 1-7 & 1-8 are satisfied, solutions to the Euler equations will be identical in a dimensionless sense and the systems may be considered hydrodynamic equivalents[25]. With this Euler similarity, it is useful to define the Euler number as:

$$\mathrm{Eu} = \mathrm{v}\sqrt{\frac{\rho}{P}} \tag{1-9}$$

Several different systems are compared with the experiment parameters in figure 1-2. Systems with identical Euler numbers will behave equally so long as each has geometrically similar initial conditions. If the Euler numbers are different but the scaling holds, they systems may be considered hydrodynamically analogous.

The above equations assume that the fluid or plasma behave like a polytrope in that the volumetric energy density is proportional to the pressure, $\varepsilon \sim \text{const.} \times P$, which for adiabatic processes scales as $P \sim \rho^{\gamma}$ where the adiabatic index $\gamma = 1+1/\text{const.}$ When comparing to another astrophysical system, this scaling holds well when the adiabatic indices are very similar. The adiabatic index is commonly taken as 4/3 for systems

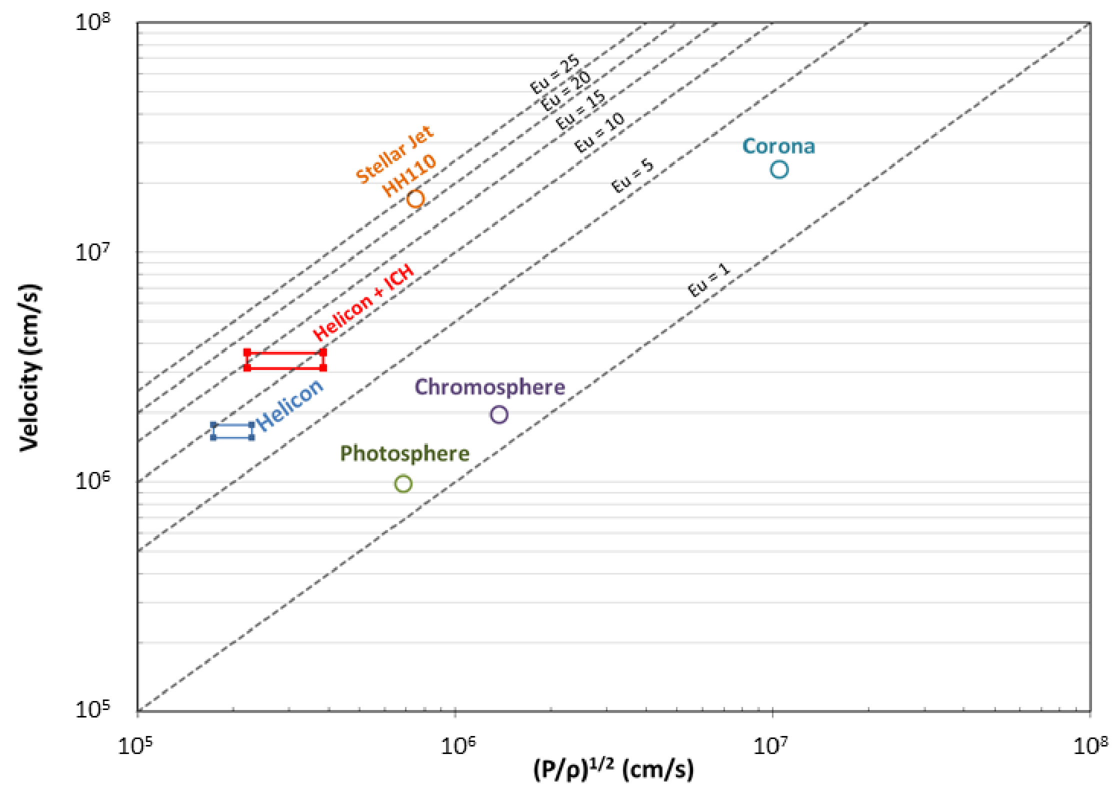

Figure 1.2: Comparison of Euler similarity for different known hydrodynamic systems. These values are also presented in Table 1.1.

dominated by radiation pressure, 5/3 for fully ionized systems with low radiation pressure, and 1 for isothermal systems. For this experiment using an argon working fluid that is near-fully ionized, $\gamma = 5/3$ is a reasonable assumption. Comparing to systems with variable or low ionization where $\gamma \sim 4/3$, such as the solar photosphere, is still permissible so long as the system is structurally stable in regards to equations of state[33]. Ryutov et. al. argues that even modest deviations from polytropic law can be tolerated so long as there are no drastic dependencies on P and ρ, such as those that occur in shocks or phase transitions[33]. With this in mind the Euler equations will apply to both experiment and specifically analogous space plasma systems.

General experiment parameters from this setup have been compared to a few specific space plasmas which exhibit magnetic nozzles and are presented in table 1.1. The laboratory values are taken along the central axis of the experiment during both the low power (~ 30 kW Helicon) and high power (~ 100 kW Helicon + ICH) operational phases. A range of values is presented when the quantity varies over the region while in other cases an average value is used. Several space plasmas that may exhibit natural magnetic nozzle properties were chosen for comparison. As mentioned above the solar atmosphere contains regions of plasma flow along divergent magnetic fields where many of the parameters are well known and are relevant for comparison. The compiled values were taken from several sources[13, 14, 37-55]. The plasma flow along the magnetic pole of the stellar jet HH110 was also a good candidate for comparison that presents drastically different scale lengths and was selected based on similar lab/jet scaling studies[21-25]. More complete tables of plasma parameters based on computations and assumptions from the NRL Plasma Formulary[37] is presented in Appendix A.

The scaling constants a, b, and c are presented for each system in table 1.1. Using Eqn. 1-7 a laboratory time window of 500 μs corresponds to 55 s for the photosphere, up to 1100 s for the chromosphere, 450 s for the corona, and 21 years for the stellar jet. The ideal laboratory time frame needed to match each system are 700 μs for the photosphere, 50 μs to 1 ms for the chromosphere, 500 μs for the corona, and 60 μs for the stellar jet. These timescales reasonably measured in the experiment and are on the same order of magnitude with the characteristic flow timescales for each layer in the solar atmosphere, and within an order of magnitude for the stellar jet (t_{flow} ~ 2 years) which is remarkably close given the scale lengths involved. The velocities transform fairly well for the

Plasma/Fluid Parameters	Laboratory Plasma		Space Plasma			
	VASIMR Magnetic Nozzle		Solar Atmosphere[13, 14, 37-55]			Stellar Jet[21-25]
	30 kW Helicon	100 kW (Helicon + ICH)	Photosphere	Chromosphere	Corona	HH110
L (cm) {Scale Size}	200	200	8x10^{7}	2x10^{8}	1x10^{10}	1x10^{15}
n_e (cm^{-3}) {Electron Density}	4x10^{11} - 1x10^{13}	5x10^{11} - 8x10^{12}	1x10^{14}	2x10^{10} - 1x10^{14}	1x10^{9}	1x10^{4}
ρ (g/cm^{3}) {Mass Density}	3x10^{-11} - 8x10^{-10}	4x10^{-11} - 6x10^{-10}	2x10^{-10}	3x10^{-14} - 1x10^{-10}	2x10^{-15}	2x10^{-20}
P (dyne/cm^{2}) {Fluid Pressure}	1 - 40	2 - 80	80	0.2 - 80	0.2	1x10^{-8}
V (cm/s) {Flow Velocity}	1.6x10^{6}	3x10^{6}	1x10^{6}	1.5x10^{6}	2x10^{7}	1.5x10^{7}
t_{flow} (s) {Flow Timescale}	1x10^{-4}	7x10^{-5}	8x10^{1}	1.5x10^{2}	5x10^{2}	7x10^{7}
Composition	Ar	Ar	H	H	H	H
Te (eV) {Electron Temperature}	1.7 - 2.1	2.1 - 6.1	0.5	0.5 - 2	1x10^{2}	0.6
Ti (eV) {Ion Temperature}	6.6 – 10.2	27.6 – 37.1	0.5	0.5 - 2	2x10^{2}	2x10^{2}
B (G) {Magnetic Field Strength}	10 - 740	10 - 740	1000	1 - 1000	10	3x10^{-3}
ν_c (s^{-1}) {Collision Frequency}	7x10^{7} - 7x10^{8}	4x10^{7} - 2x10^{7}	4x10^{10}	2x10^{6} - 4x10^{10}	4x10^{2}	9x10^{0}
χ (cm^{2}/s) {Thermal Diffusivity}	7x10^{8} - 8x10^{10}	2x10^{9} - 2x10^{11}	4x10^{7}	4x10^{7} - 2x10^{11}	8x10^{11}	5x10^{15}
ν_{mat} (cm^{2}/s) {Material Viscosity}	2x10^{7} - 9x10^{7}	2x10^{8}	3x10^{7}	3x10^{7} - 1x10^{11}	5x10^{11}	3x10^{15}
ν_{rad} (cm^{2}/s) {Radiative Viscosity}	3 - 65	800 - 2360	3x10^{-4}	3x10^{-4} - 2x10^{7}	1x10^{20}	3x10^{16}
λ_{mat} (cm) {Material mean-free-path}	0.09 - 0.7	0.8 - 1.4	8x10^{-4}	8x10^{-4} - 3x10^{1}	1x10^{6}	4x10^{6}
λ_{rad} (cm) {Radiative mean-free-path}	1x10^{11} - 3x10^{12}	2x10^{11} - 3x10^{12}	2x10^{8}	2x10^{8} - 8x10^{13}	2x10^{15}	1x10^{20}
τ_{mat} {Material optical depth}	3x10^{2} - 2x10^{3}	1x10^{2} - 3x10^{2}	1x10^{11}	6x10^{6} - 1x10^{11}	1x10^{4}	3x10^{8}
τ_{rad} {Radiative optical depth}	6x10^{-11} - 2x10^{-9}	7x10^{-11} - 1x10^{-9}	5x10^{-1}	2x10^{-6} - 1.3	7x10^{-6}	7x10^{-6}
τ_{thin} (s) {Optically thin cooling time}	3.6 - 71.8	8.3 - 76.1	0.2	0.2 - 2000	3x10^{5}	2x10^{9}
Eu {Euler Number}	5.9 - 9.8	7.0 - 15.8	1.41	1.41	1.3	22
Re {Reynolds Number}	8.4 - 63.8	6.3 - 8.4	3x10^{9}	2x10^{5} - 3x10^{9}	3x10^{2}	2x10^{8}
Rm {Magnetic Reynolds Number}	90 - 290	360 - 2360	1x10^{7}	3x10^{7} - 2x10^{8}	2x10^{13}	1x10^{15}
Pe {Peclet Number}	5.0 - 38.2	3.8 - 5.0	2x10^{9}	1x10^{5} - 2x10^{9}	2x10^{2}	1x10^{8}
β {Kinetic Plasma Beta}	0.03 - 10.7	0.09 - 54.6	0.002	0.002 - 1.6	0.02	8.8
Ω_{He} (Ω_e / ν_{ei}) {Hall Parameter}	0.4 - 2.9	0.7 - 16.0	0.08	0.08 - 1.5	7x10^{4}	9x10^{2}
a	1	1	4x10^{5}	1x10^{6}	5x10^{7}	5x10^{12}
b	1	1	3	0.001 - 5	3x10^{-5}	3x10^{-10}
c	1	1	40	0.2 - 1	9x10^{-2}	5x10^{-9}
t' (s) {for t ~ 500 μs}	1	1	~ 55	~ 35 - 1100	~ 450	~ 6x10^{8}
v' (cm/s) {for v ~ 3x10^{6} cm/s}	1	1	~ 8x10^{5}	~ 2x10^{5} - 7x10^{6}	~5x10^{4}	~ 7x10^{5}

Table 1.1: Comparison of experiment values with various space plasmas based on plasma/fluid properties and Eulerian scaling factors.

photosphere and chromosphere, but undershoot by a few orders of magnitude for the corona and stellar jet as a velocity of 30 km/s translates into 500 m/s and 7 km/s respectively. This deviation could be due to oversimplifying or overestimating the flow velocities in the corona. Another source of discrepancy may be that radiative cooling in both the corona and jet play a more dominant role resulting in a lower pressure, and hence reduced value of c, which would lead to higher scaled velocities. Despite these differences the scaling of the experiment up to these select space plasmas agrees well. The upper solar chromosphere appears to be in best agreement with the laboratory magnetic nozzle system as several if not all of the parameters, other than scale length, overlap with experimental values. This agreement is particularly interesting considering the solar atmosphere sub-to-super Alfvénic transition for flows ($\beta_k > 1$) occurs in the chromosphere and the space bound Interface Region Imaging Spectrograph (IRIS) will soon be launched to study this layer and other regions of the solar limb. This plasma source may be a useful chromosphere environment proxy should the lab conditions or results follow trends in the IRIS data.

There are a few more additional validity criteria not included in the Euler equations that must be taken into account. For all intents and purposes the laboratory system must behave as a fluid which requires the system to be localized within the scale lengths considered, either collisionally or magnetically. This localization condition may be expressed as[33]:

$$\frac{r_{Li}}{L} \approx 10^{-4} \frac{\mathrm{v}_d \left(\frac{cm}{s}\right)}{B\ (G)\ L\ (cm)} \ll 1 \qquad \text{1-10}$$

where r_{Li} is the ion Larmor radius and v_d is the drift velocity. This value ranges between 0.001 and 0.08 for low power operation and 0.003 to 0.15 during high power operation. The localization condition may therefore be considered satisfied.

Also not factored into the Euler equations are the effects due to heat conduction, viscosity, and radiative energy flux. In order for thermal conductivity and viscosity to be considered negligible, the Peclet ($Pe \sim vL/\chi$) and Reynolds ($Re \sim vL/\nu$) numbers are required to be larger than unity, where χ and ν are the thermal diffusivity and viscosity, respectively. Following expressions for χ and ν taken from Ryutov et. al.[33] involving the electron thermal velocity ($v_{te} \sim (k_B T_e/m_e)^{1/2}$) and collisional mean free path ($\lambda_{mat} \sim v_{te}/\nu_c$) it is seen that the Peclet and Reynolds numbers exceed unity for all of the considered systems (table 1.1). Ideally the Peclet and Reynolds numbers should be very large as in the case of the space plasmas, but being of order unity or larger for the laboratory plasma is sufficient to consider viscous and thermal effect unimportant in terms of the flow scalability.

Declaring radiative energy flux unimportant requires a more in depth look at the photon mean free path as well as optical depth to determine if the radiative cooling time is on the order of the characteristic flow timescale. For optically thick systems, where τ_{rad} ($\sim L/\lambda_{rad}$) > 1, the radiative cooling time should be almost entirely due to blackbody radiation and cooling times will scale $\sim \sigma T^4$. For an optically thin system, where $\tau_{rad} < 1$, the radiative cooling is due to either Bremsstrahlung or line radiation. Again referring to the formulation of Ryutov et. al. the photon mean free path, λ_{rad}, is taken as the minimum between Bremsstrahlung and Thomson scatting[33]:

$$\lambda_{brems}(cm) = 1.7\ x\ 10^{37}\,\frac{[T_e\ (eV)]^{7/2}}{Z^3[n_i\ (cm^{-3})]^2} \qquad 1\text{-}11$$

$$\lambda_{Compton}\ (cm) = \frac{1}{[n_e(cm^{-3})\sigma_T(cm^2)]} \qquad 1\text{-}12$$

where σ_T is the Thomson cross section and is taken as 6.6 x 10^{-25} cm^2. Even under the reasonable assumption of quasineutrality the minimum photon mean free path for each system considered, except the solar photosphere, use the Compton scattering formula. Applying the Compton based formula as the photon mean free path, each system is shown to be optically thin (table 1.1) and the cooling time may be estimated as[33]:

$$\tau_{thin}\ (s) = 2.4\ x\ 10^{-12}\,\frac{(Z+1)T_e(eV)}{Zn_i(cm^{-3})\Lambda_N} \qquad 1\text{-}13$$

where $\Lambda_N = 1.7 \text{ x } 10^{-25}\ Z^2\ T_e^{1/2}$ is a normalized cooling rate. Comparing these values with the characteristic flow timescale for each of the systems it is seen that the cooling time from line radiation greatly exceeds the timescales in the laboratory experiment by 4 - 6 orders of magnitude. Radiation heat flux can be now considered negligible in the application of the Euler scaling equations to the laboratory parameters. The solar photosphere, however, is no longer a good comparison candidate since the cooling is happening in a shorter amount of time than it takes the particles to traverse the system. The base of the chromosphere, at the photosphere transition, is bad due to the cooling timescales, but becomes more favorable higher up in the regions of lower plasma density and may still remain a viable comparison candidate. The solar corona and stellar jet have, similar to the laboratory plasma, negligible radiation energy flux.

The scaling relations for the Euler equations have been shown, at least on an order of magnitude basis, to be valid including the additional validity criteria regarding localization, thermal conductivity, viscosity, and radiation heat flux. The magnetic nozzle flows generated in this experiment may be scaled up to the valid space plasma analogs. The solar chromosphere remains the best comparison candidate based on the many overlapping flow parameters and questions regarding particle transport in the sun may possibly be studied using this laboratory system. As a final comparison of the systems, a density versus temperature chart is presented in figure 1.3. This lab plasma may find relevance in studying other structurally similar flows.

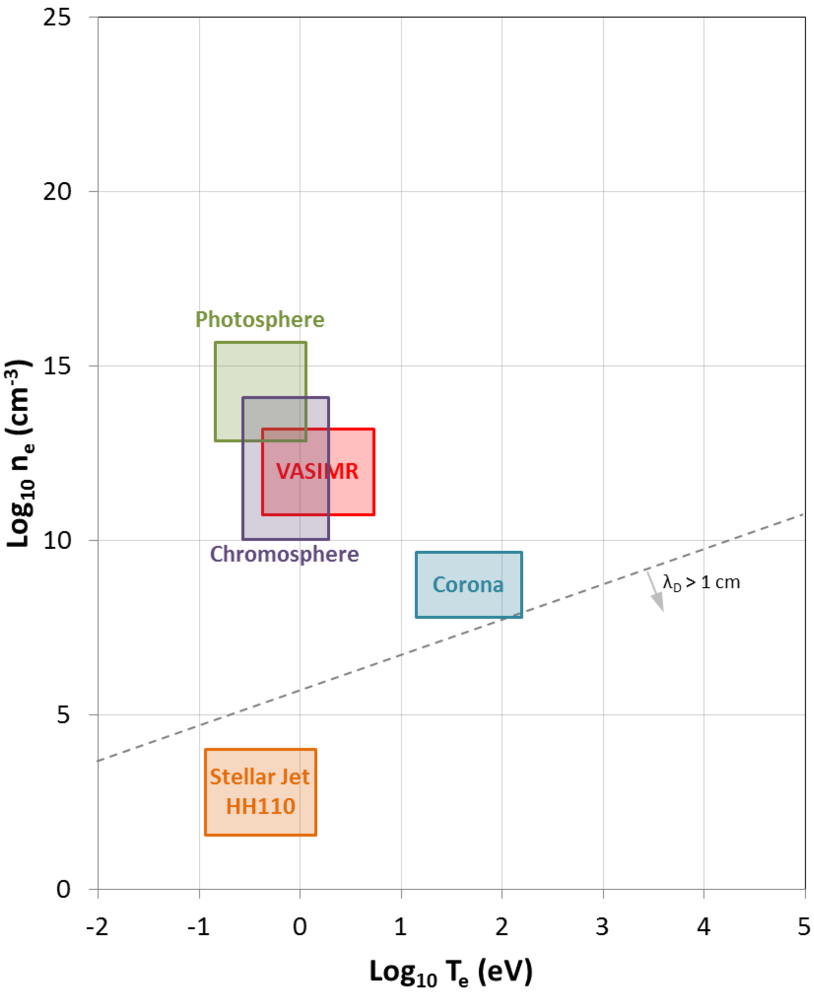

Figure 1.3: Plasma density versus electron temperature for the various hydrodynamic systems. The laboratory plasma source VASIMR is shown in red. A dashed line (gray) marks the Debye length crossover at $\lambda_D = 1$.

Section 1.3 – Organization of this thesis

This section discusses the organization and setup for the remainder of this document. Chapter 2 will feature an overview of magnetic nozzles, their background, and discuss some of the terrestrial and theoretical applications. A literature survey covering most if not all of the earlier theoretical and experimental studies of magnetic nozzles will be covered. Also in chapter 2 more detailed descriptions of the main plasma detachment theories and proposed experiment verification methods will be discussed.

Chapter 3 will focus on defining the parameters and setup important to the experiment. This includes descriptions of the VASIMR® VX-200 plasma source, the magnetic nozzle, vacuum environment & associated hardware, and the data acquisition architecture. Chapter 4 will describe the plasma diagnostics in detail covering the functional nature and theory for each probe relevant to this study including the correlation of measured values to physical parameters. Chapter 5 will present the data and any further reduction of the data in order to demonstrate plasma detachment in this magnetic nozzle system. Chapter 6 features further analysis of the data that will be compared to each of the relevant theories discussed in chapter 2 separating the valid theories apart from those which may require modification or outright rejection. Lastly Chapter 7 will serve to summarize conclusions, possibly expanding this understanding to natural plasma systems, and discuss any future outlook, direction, or application of the results of this experimental study.

Chapter 2: Magnetic Nozzle Background and Theory

Section 2.1: Introduction to magnetic nozzles

A nozzle, such as the convergent/divergent de Laval nozzle, is used to direct and accelerate the flow of a fluid. A direct analog of the de Laval nozzle is a magnetic nozzle which is used to direct and accelerate ionized fluid with a divergent magnetic field instead of material boundaries (figure 1.1). Given the similarity between neutral gas in a material nozzle and magnetized plasma in a magnetic nozzle there are other differences that add complexity to the dynamics involved. These include sources of plasma internal energy, electromagnetic forces competing with thermal pressure, plasma rotation, the generation of self-magnetic fields, and varying degrees of collisionality/ion magnetization. This high degree of complexity has resulted in a limited understanding of magnetic nozzles.

As mentioned in the previous chapter magnetic nozzles can be found in nature ranging from stellar atmospheres and astrophysics jets to the magnetosphere[10, 26]. Recently many terrestrial applications for magnetic nozzles have surfaced. In fusion research plasma is accelerated through nozzle like divertors and understanding the transport phenomena/confinement is critical for controlling thermal loads on components and reactor boundaries[29-31]. Magnetic nozzles are used in plasma processing for direct control of the plasma stream and distribution function in etching processes[28]. In the field of in space electric propulsion magnetic nozzles are used as both a thrust vectoring mechanism as well as a plasma shield[27].

In order for the nozzle to take full effect conditions require the plasma be magnetized at first to convert gyrational/thermal energy into directed flow and then subsequently separate from the magnetic field. Unlike fluid passing through material nozzles, magnetized plasma tends to remain attached to the nozzle, specifically to the magnetic field lines. One author describes this tendency as the ‘detachment problem’[56]. Clearly it is not always the case considering there is direct observation of particle/energy flow out of astrophysical bodies and detection of particle fluxes/Aurorae on Earth.

Considerable effort has been devoted to understanding the mechanisms on how plasma may separate from the nozzle magnetic field. Although most of this research has been approached theoretically and analyzed using simulation[56-96] there have been a few experiments[59, 76, 89, 90, 97-102] attempting to measure plasma detachment but have lacked the detailed measurements and/or proper environment conditions or scale length to firmly identify any specific separation mechanism. Of the more common proposed mechanisms, they can be generally categorized into collisional and collisionless detachment. Collisional detachment theories include recombination of the plasma with neutral gas and diffusion across the magnetic field by means of plasma resistivity. Collisionless detachment theories may be subdivided further into those that involve preservation of frozen-in flow and those that do not. Frozen-in flow methods include super-Alfvénic MHD flow and reconnection detachment where the plasma carries magnetic field lines outward with the flow. The remaining collisionless detachment theories include loss of magnetization/magnetic moment breakdown, varying degrees of ion magnetization and electron inertia effects, and turbulence induced anomalous resistivity.

The outline for the rest of this chapter will include the following: Section 2 will cover background information and present an extensive literature survey of the contributions to the development of magnetic nozzles, the various detachment theories, simulations, and experiments. Section 3 will present semi-detailed overviews of the collisional and collisionless based theories of plasma detachment in magnetic nozzles. Section 4 will discuss some of the experimental approaches to measure plasma detachment.

Section 2.2: Background and literature survey

Section 2.2.1: The early years

Magnetic nozzles have been studied theoretically and experimentally since the 1960s. The earliest of the studies involved ECR plasma acceleration carried out by the General Electric (GE) Corporation[103-105] and the Lewis Research Center (LeRC), now the NASA Glenn Research Center (GRC). One of the first studies was by Kilpatrick in 1963, which assumed collisional plasma in near thermal equilibrium and neglected magnetic dipole moment forces, indicated plasma will follow magnetic field lines and cannot separate unless the divergence angles are small[105]. In 1967 Kosmahl presented a theoretical particle trajectory treatment based on energy stored in the magnetic dipole moments of the electrons in collisionless plasma[62]. The simulations showed that even in collisionless flows plasma can free itself from the flux lines and trajectories are independent of ion mass/energy but dependent upon nozzle geometry.

The first mention of the term 'Magnetic Laval Nozzle' was produced by Andersen et. al.[106] in 1969 who also conducted one of the first magnetic nozzle experiments in a wind tunnel using 'plasma wind'. This experiment, conducted with cesium plasma, found the flow to be accelerated as high as Mach 3 and that the nozzle performed well regardless of precision of the nozzle shape. Another early experiment was performed by Kuriki et al. who set out to study differences between solid and magnetic nozzles attempting to come up with an analog to Bernoulli's equation for the setup[97]. Some nozzle effects such as pinching of the jet were observed and it was found that electrons were bound to the field lines.

One of the final direct studies in magnetic nozzle flow for more than a decade involved Chubb[63], who took a theoretical approach to magnetic nozzle processes using a quasi-one dimensional model that required the flow to be highly collisional. This study claimed the parameters most important for controlling the plasma flow are the nozzle geometry, thermal plasma beta, and the ratio of the throat radius to the collisional mean-free-path. Although the need to study both particle species was brought up, the detachment problem was not specifically discussed.

Section 2.2.2: Addressing the detachment problem

The study of magnetic nozzle effects and theory subsided for nearly two decades before a Los Alamos National Laboratory (LANL) study was done in the form of a NASA technical report by Gerwin[56] et al. in 1990. The study involved a 2D ideal MHD model in both meridional (longitudinal) and azimuthal magnetic nozzles across a wide range of densities (10^{13} – 10^{19} g/cm^3) and electron temperatures (1 eV – 100 eV) while keeping the plasma beta low ($\beta < 1$). The 'detachment problem' is described as the nozzle imparting a resistive drag to the particles as they try to detach from the field. The densities of this model are large enough that the plasma is highly collisional and can diffusively 'walk' across the magnetic field lines driven by pressure gradients, inertial forces, and a rapid drop in electron temperature. Despite this walk the models claim the resistive drag will be sufficient to prevent the plasma from fully detaching and instead follow the field lines. Gerwin proposes three possible solutions to enable detachment: Recombination with neutrals, sharp boundary profiles with magnetic reconnection, and anomalous transport brought on by a resistive Rayleigh-Taylor or Kelvin-Helmholtz instability from turbulence.

Similar studies of resistive detachment were later done by Moses[107] et al. in 1992 where microturbulence drives anomalous resistivity with the lower hybrid drift instability (LHDI) providing a robust turbulence mechanism. The LHDI is initiated when the 'drift parameter', a ratio of the cross field drift velocity and the ion thermal velocity (v_d/v_{ti}), exceeds unity. Moses also mentions the plausibility of field line tearing and magnetic reconnection as detachment mechanisms. This was followed by York[59] et al. who developed a 2D MHD code including all flow/dissipative effects and attempted to compare them to measurements of a dense, collisional plasma. This experiment was limited in chamber size (small measurement space) and plasma diagnostics as wall friction and interaction with neutrals were significant factors. They were able to conclude that resistivity behaves classically although electron thermal conduction does not.

Hooper[60] presented a different idea of plasma detachment determined by electron inertia. In this case the ions are un-magnetized while electrons are fully magnetized. The ions and electrons are treated as being effectively bound together (as a hybrid particle) and detachment is determined by a non-dimensional scaling parameter, G, estimated by conditions in the nozzle throat. This G parameter determines the flux surfaces where the flow is energetically able to detach. The author mentions that this mathematical model serves as a fundamental lower limit for detachment as many conditions in actual plasma flows were ignored (ionization, acceleration, dissipation, instabilities, etc.) but states that MHD effects involving super-Alfvénic flows may be a possible detachment mechanism that warrants experimentation. Carter[108] et al. proposed a collisionless particle trajectory mechanism for detachment based on breakdown of the magnetic moment of particles in an expanding magnetic field. After the ion energy stored in velocity components perpendicular to the field is mostly converted into directed energy via adiabatic expansion, they will become un-magnetized if the static B field changes on a scale length comparable to the ion gyroradius. The electrons are then thought to escape with the ions through MHD currents, cross-field diffusion, and/or other turbulent effects.

Section 2.2.3: Recent developments in detachment theory

Within the past decade more emphasis has been placed on MHD physics as a valid detachment mechanism. Ilin[67] et al. modeled plasma detachment using the VASIMR® geometry for both trajectory based particle-in-cell (PIC) and MHD simulations and found both situations to be comparable for the regions of separation. Mikellides[65, 66] et al. developed a numerical simulation based on resistive MHD showing that detached plasma has sufficient pressure to modify the magnetic field and found a reduction in flow speed due to a resistive drag force. The author also mentions magnetic reconnection to be a possible detachment mechanism.

Perhaps the largest advances in MHD based detachment theory were contributions by Arefiev[69, 70, 77, 79] et al., Breizman[78, 109-111] et al., Cassibry[72] et al., Sankaran[71, 74, 80] et al., and Winglee[89] et al. These studies involve the plasma having sufficient energy density to overcome the magnetic energy density at a transition point where the plasma becomes super-Alfvénic and drags the magnetic field with the flow effectively preserving the frozen-in condition. The theory proposed by Arefiev used ideal MHD where the conductivity at the nozzle wall boundary was infinite allowing ring currents to form and set up a rarefaction wave along the boundary. The magnetic field is then pulled straight in the plume and vanishes outside of the rarefaction wave. Breizman extends the Arefiev model, still under the premise of ideal MHD, starting with an anisotropic velocity distribution and simulates results using a Lagrangian based code. Cassibry performed a similar study assuming resistive MHD along the nozzle boundary and found that the magnetic field stretches to infinity through MACH2 simulations. Sankaran's work provided a multi-dimensional MHD code that calculated the time-dependent evolution of the three spatial components of magnetic field/velocity resulting in field line stretching. Winglee expressed that MHD detachment will be enhanced through self-focusing effects. He found four parameters critical in determining the nature of the flow and whether the frozen-in theory will remain valid, which are: Mach number, Alfvén Mach number, ratio of thermal beta to kinetic beta, and the ratio of the ion gyroradius to magnetic field scale length. Winglee's simulations showed the field line stretching and self-focusing effects to be valid, but the experimental results were less conclusive as limited diagnostics and non-ideal conditions may have been a factor.

Further experimentation was later performed by Deline[76, 98] et al. using the Detachment Demonstration Experiment (DDEX) at NASAs Marshall Space Flight Center (MSFC). The experiment involved hydrogen and helium plasmas over a variety of magnetic field configurations. The measured plume radius was compared to a general magnetic field scaling law ($R \sim 1/B^2$) and shown not to follow the scaling with the separation point located near the estimated sub-to-super Alfvénic transition point ($\beta_k \sim 1$). Despite this claim magnetic field line stretching was not presented, mentioned, or observed. There have been other experiments during this time frame that observed magnetic nozzle effects on flowing plasma but did not specifically treat or mention detachment from the applied magnetic field[97, 106, 112-114].

Despite its lack of popularity non-MHD related detachment studies did not stop. Gesto[90] et al. ran particle trajectory simulations stating that ions will become demagnetized when the ion trajectory has zero curvature while electron effects were not considered. A simulated plume radius compared well with experimental data but the effort did not attempt to test any other detachment mechanisms. West[100] et al. followed up with a similar experiment setup stating the projected ion gyroradii are on the order of the size of the chamber and assumed demagnetization based on weak magnetic field strength. Coletti[73] et al. model detachment in an Magnetoplasmadynamic (MPD) thruster using loss of adiabaticity and found outside experimental data in agreement with the model. Kawabuchi[88] et al. used a particle-in-cell (PIC) code called TRISTAN, based on Maxwell's equations, finite-difference methods, and Runge-Kutta, to find that ions lose adiabaticity and pull electrons along. Schmit[85] et al. extended Hoopers electron inertia based detachment theory by including plasma rotation and claims significant enhancement to the detached flow over the non-rotating case. Little[82] et al. ran simulations of a two-fluid model for cold ions and hot electrons and found that most acceleration occurs within 5 throat radii downstream. Some marginal field line stretching is observed but the separation point seems to be more inertial. Ahedo[81, 83, 84, 86, 87] et al. refutes the conclusions of MHD detachment theory from Arefiev using a variant of Hoopers theory with weakly magnetized ions. In this case the azimuthal currents in the nozzle create an accelerating J×B force and modest charge separation from ion streamlines set up a negative current along the nozzle edge where electrons return to the nozzle keeping the plume ‘current free’. Electrons are then able to leave with the ions near the axis. Terasaka[115, 116] et al. used measured ion velocity vectors in a very small scale experiment to claim separation aligns well when the parameter measuring loss of adiabaticity was of order unity.

More detailed descriptions of each type of detachment theory based on the literary survey above will be discussed further below.

Section 2.3: Detachment theories

Section 2.3.1: Recombination theory

For collisional plasmas one of the more straight-forward ideas for detachment involves the recombination of ions and electrons during inelastic collisions so long as the re-neutralized gas avoids being re-ionized (figure 2.1). In this case the neutrals are freely expanding having a random velocity distribution as they are not affected by the field and the flow is detached. The parameters most commonly looked at to determine the viability of this mechanism are the species recombination rate compared to typical transit times for particles in the nozzle. If the particles traverse through the region where recombination conditions are ideal in a shorter amount of time than it takes for an ion/electron pair to recombine this mechanism cannot account for full plume separation. Simpson provided a three body formulation for recombination rates of argon[117]:

$$\dot{n} = n_e^2 n_i \propto' \qquad \text{2-1}$$

The computed recombination rate coefficients are very low ($\alpha' \sim 10^{-41}$ m^6/s for a 1 eV plasma) and drop several orders of magnitude with increasing electron temperature. Using this rate coefficient and the peak densities found in this experiment ($n \sim 10^{19}$ m^{-3}),

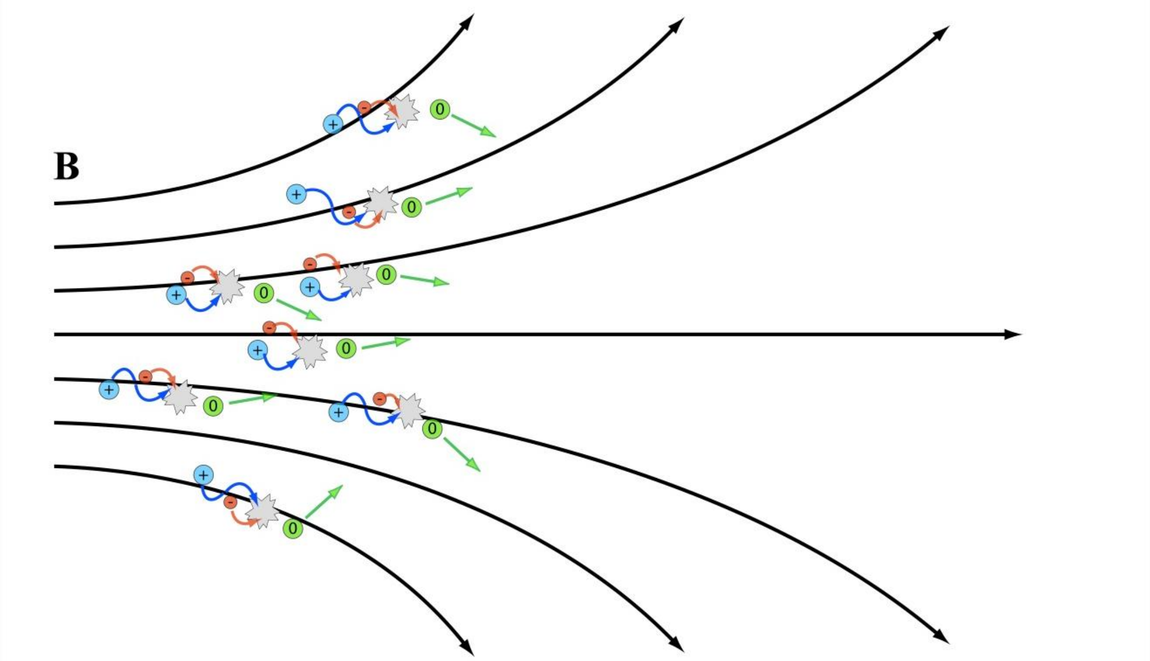

Figure 2.1: Detachment by electron and ion recombination. Particles gyrate about the field lines until colliding with a different charged particle which then becomes a neutral free of the magnetic field.

the time for recombination is estimated to be 10^2 - 10^3 s. The transit time for cold low velocity plasma in a magnetic nozzle (~ 10^4 m/s) over a distance of 1 m is several orders of magnitude less than the recombination time.

Since the transit time in many, if not all cases, of axially flowing plasma in a diverging magnetic nozzle is shorter than the recombination time, recombination to neutral species will not be a primary detachment mechanism and will not be scrutinized much further in this study.

Section 2.3.2: Diffusive/Resistive detachment

The other form of collisional plasma detachment is for the ions/electrons, through

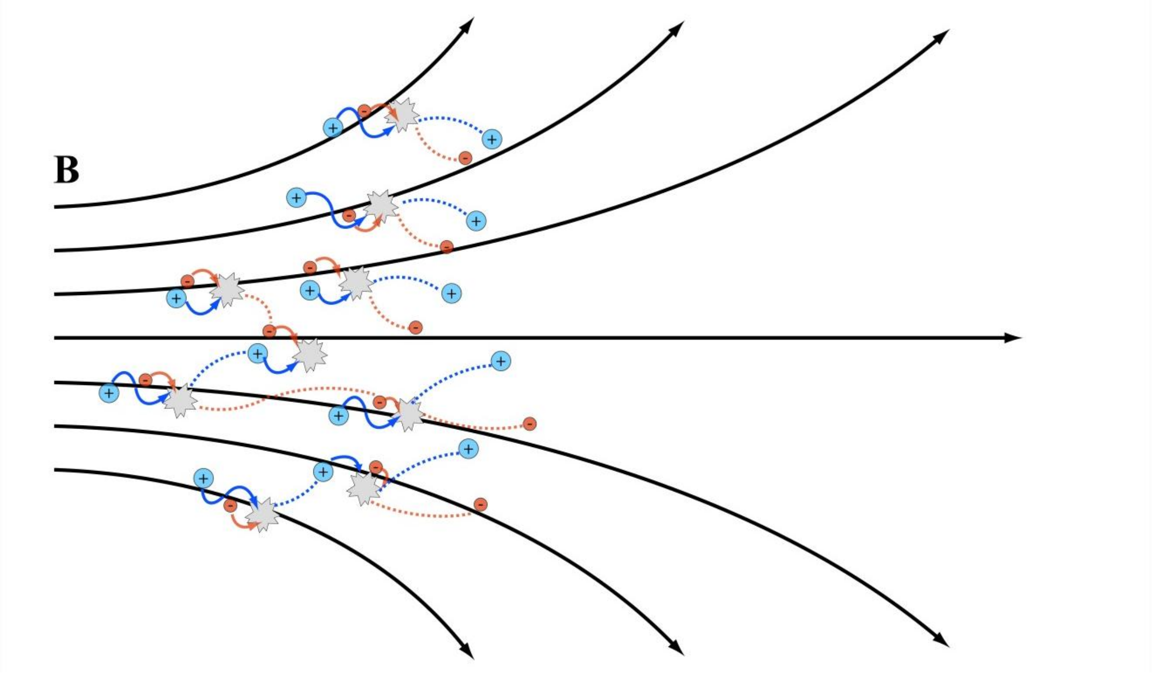

Figure 1.2: Detachment by collisional diffusion. Particles gyrating about the field lines undergo elastic collisions altering the position of their guiding center. After multiple collisions the particles have randomly 'walked' across the field lines and become demagnetized as the magnetic field strength drops.

elastic collisions, to diffuse across the magnetic field lines (figure 2.2). This 'random walk' crossing of the field lines would occur until the particles pass into weaker magnetic field regions where the plasma would simply become demagnetized.

Classical diffusion of particles is governed by Fick's law:

$$\Gamma = -\mathrm{D}\nabla \mathrm{n} \qquad 2\text{-}2$$

$$\mathrm{D} = \frac{kT}{m\nu_m} = \mu T \qquad 2\text{-}3$$

where the flux of particles is related by a density gradient and a diffusion coefficient, D, which is a function of particle mass, temperature, and momentum transfer frequency ν_m that can also be related to particle mobility, μ. These simple equations define free ion diffusion in the absence of magnetic fields. When magnetic fields are included the more mobile electrons are closely tied to the field lines, with a mean gyroradius of $r_{ce} = v_{th}/\Omega_e$, and the cross field diffusion coefficient becomes[118-120]:

$$\mathrm{D}_\perp = \frac{kT}{m\nu_m}\frac{1}{1+(\Omega_c\tau_m)^2} \approx \frac{kTm\nu_m}{q^2B^2} \qquad 2\text{-}4$$

This equation is commonly associated with classical diffusion as $D_\perp \sim 1/B^2$, and the parameter $\Omega_c\tau_m$ is important in the field of plasma confinement since large values will inhibit cross field diffusion. The time between particle momentum exchanges, τ_m, in this case is taken as $1/\nu_m$. The classical cross field particle velocity can be taken as[118-120]:

$$\mathrm{u}_\perp = \pm\mu_\perp E - D_\perp\frac{\nabla n}{n} + \frac{u_E + u_D}{1+(\Omega_c\tau_m)^{-2}} \qquad 2\text{-}5$$

where u_E and u_D are the perpendicular velocities from the E×B and diamagnetic drifts. As collisions decrease the drifts can cause instabilities to form that may trigger anomalously high cross-field transport. In practice, plasmas are not in thermal equilibrium and are subject to instabilities as well as turbulent diffusion with a proposed upper limit of the Bohm diffusion coefficient[61, 121]:

$$\mathrm{D}_B = \alpha \frac{T_e}{B} \qquad 2\text{-}6$$

which is proportional to 1/B as opposed to the classical $1/B^2$. The numerical factor α in the Bohm limit needs to be experimentally determined but is usually taken as 1/16.

Taylor and McNamara provided a theoretical treatment of instability enhanced diffusion resulting from fluctuations in the electric field[121]:

$$\mathrm{D}_\perp = \frac{c}{\sqrt{2\pi}B}\left(\int_a^b \frac{dk}{k}\langle|E^2(k)|\rangle\right)^{1/2} \qquad 2\text{-}7$$

which is integrated and wavenumber, k, averaged. Okuda and Dawson used this treatment to find that there are three regions of magnetic diffusion scaling, each determined by the ratio of the square of the ion plasma frequency to the cyclotron frequency[61]. In high density (collisional) plasmas with weak magnetic fields, $\omega_{pi}^2/\Omega_i^2 >> 1$, the cross field diffusion scales as $1/B^2$. For $\omega_{pi}^2/\Omega_i^2 \leq 1$ the diffusion scales like the Bohm type going as 1/B. In between lies an intermediate region with $1 \leq \omega_{pi}^2/\Omega_i^2 \leq (n\lambda_D^2)^{1/2}(m_i/m_e)^{1/2}$ where the cross field diffusion becomes roughly independent of the magnetic field. The main proponents of collisional diffusion as a detachment mechanism seem to favor the onset of turbulent instabilities to drive the diffusion rather than by classical ion diffusion alone[56, 107].

Although the ions in the present study are collisionless, the principals of turbulent driven diffusion may still be important as several authors have proposed effective collision rates due to plasma instability despite the absence of collisions[120, 122-126].

Section 2.3.3: Magnetohydrodynamic (MHD) detachment

The motivation for this detachment mechanism stems from the observation of the solar magnetic field being stretched or carried outward with the solar wind [127]. This theory preserves the frozen-in condition and alleviates any need for cross field transport as the field lines will become stretched out with the flow. The resulting stretched magnetic field will then be almost entirely generated from the plasma currents rather than the external applied field. The essence of this theory revolves around the ratio of plasma flow energy to magnetic energy[59, 60, 67, 69-72, 74, 76-79, 89, 93, 98, 109-111]:

$$\beta_k = \left(\frac{\mathrm{v}}{\mathrm{v}_A}\right)^2 = \frac{nM_i u_i^2}{B^2/\mu_0} \qquad \text{2-8}$$

which is the same as the ratio of the squares of the flow velocity to the Alfvén velocity. As the ratio approaches unity, and transitions to super-Alfvénic flow, there will be sufficient energy in the plasma to tear itself away from the magnetic field with the ability to distort or carry the magnetic field lines along with the bulk flow (figure 2.3).

In the MHD scenario electrons and ions are treated as combined into a single fluid. The MHD equations for a steady-state flow of cold, ideally conducting magnetized plasma are[70]:

$$\rho(\mathrm{v}\cdot\nabla)\mathrm{v} = -\frac{1}{4\pi}B\times[\nabla\times B] \qquad 2\text{-}9$$

$$\nabla\cdot(\rho\mathrm{v}) = 0 \qquad 2\text{-}10$$

$$\nabla\times[\mathrm{v}\times B] = 0 \qquad 2\text{-}11$$

$$\nabla\cdot\mathrm{B} = 0 \qquad 2\text{-}12$$

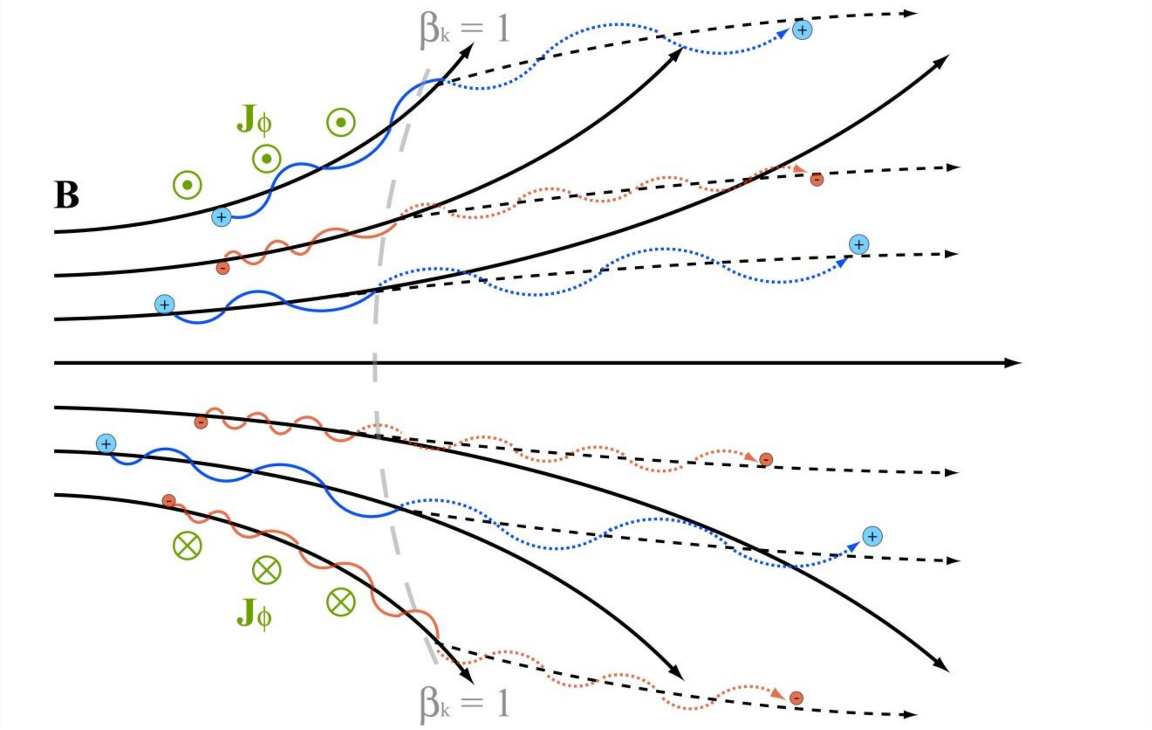

Figure 2.3: Detachment by magnetohydrodynamic (MHD) field line stretching. The ions and electrons behave as a single fluid and as the magnetic field lines expand and the field strength drops the plasma will reach a point where it is energetically capable (β_k = 1) of stretching out the weak field lines. Azimuthal plasma currents arise in the expanding field region creating a solenoidal addition to the field. Frozen-in flow is preserved as particles gyrate about the stretched field lines (black dashed) which are stretched to infinity and thus considered detached.

where v is the plasma velocity, ρ is the mass density, and B is the magnetic field created by both external and plasma currents. These equations can be solved for the field aligned flow to produce magnetic flux surfaces as functions of r = r(Φ, z)[70]:

$$\frac{\mathrm{r}}{2}\left(\frac{\partial B^2}{\partial \Phi}\right)_z = \left(\frac{\partial B_r}{\partial z}\right)_\Phi - \left[\frac{\partial}{\partial z}\left(\chi(\Phi)\frac{B_r}{B}\right)\right]_\Phi \qquad \text{2-13}$$

$$\mathrm{B}_r = 2\left(\frac{\partial r}{\partial z}\right)_\Phi \left(\frac{\partial r^2}{\partial \Phi}\right)_z^{-1} \qquad \text{2-14}$$

$$\mathrm{B}_z = 2\left(\frac{\partial r^2}{\partial \Phi}\right)_z^{-1} \qquad \text{2-15}$$

where $\chi = 4\pi\rho v^2/B$ is the flow profile and Φ(r, z) is a magnetic flux function. Equation 2-13 can be simplified by assuming a paraxial nozzle with an ideally conducting wall at r = R(z)[70]:

$$\delta \mathrm{B} = \mathrm{B}\left[\left(1 + \frac{\mathrm{v}^2}{\mathrm{v}_A^2}\right)\kappa R + \theta_0^2\right] \qquad \text{2-16}$$

where κ is the field line curvature and θ_0 is the nozzle divergence angle.

As the plasma expands in this nozzle, plasma currents induce azimuthal currents along the nozzle wall and cause small perturbations of the magnetic field. These perturbations give rise to a rarefaction wave at the edge of the outgoing flow. The azimuthal currents in this rarefaction layer act as a solenoid adding magnetic flux to the plume and allow the field lines to stretch. The distorted magnetic field in the main flow is found by solving for the magnetic flux surfaces for a paraxial nozzle geometry with a highly super-Alfvénic flow ($v \gg v_A/\sqrt{\kappa R}$). The magnetic field in the rarefaction wave comes from solving equation 2-13 for small perturbations of the magnetic flux which ends up being a hyperbolic PDE. The total solution for the magnetic field in the main flow, rarefaction region, and external regions are[70]:

$$\mathrm{B(r,z)} = \begin{cases} \dfrac{2\Phi_0}{z^2\theta_0^2}, & \mathrm{r} \leq \mathrm{r}_{rw} \\ \mathrm{B}_0 \dfrac{z_0^2}{z^2} \dfrac{\mathrm{v}^2}{9\mathrm{v}_A^2} \left[1 - \dfrac{z_0}{z}\right]^{-2} \left[\dfrac{r}{z} - \theta_0 - \dfrac{2\mathrm{v}_A}{\mathrm{v}}\left(1 - \dfrac{z_0}{z}\right)\right]^2, & \mathrm{r}_{rw} < \mathrm{r} < r_{pv} \\ 0, & r_{pv} \leq r \end{cases} \qquad 2\text{-}17$$

$$r_{rw} = z\theta_0 \sqrt{1 - \frac{2}{\theta_0}\frac{\mathrm{v}_A}{\mathrm{v}}\left(1 - \frac{z_0}{z}\right)} \qquad 2\text{-}18$$

$$\mathrm{r}_{pv} = z\theta_0 + 2z\left[1 - \frac{z_0}{z}\right]\frac{\mathrm{v}_A}{\mathrm{v}} \qquad 2\text{-}19$$

where Φ_0 is the total unperturbed magnetic flux, B_0 and z_0 are the magnetic field and axial location of the nozzles end. The interface subscripts r*w* and *pv* stand for the inner rarefaction wave boundary and plasma-vacuum boundary, respectively. It is a necessary consequence from the boundary conditions of the rarefaction wave that the magnetic field vanish at the plume edge, which corresponds to $\Phi = \Phi_0$. Another notable point is that the magnetic field lines are straight inside the flow out to the rarefaction wave inner boundary.

Considering the model by Arefiev assumes a cold ideally conducting plasma, similar solutions (equations 17 – 19) have been published by Breizman[78] using a Lagrangian solver with hot anisotropic ions and cold electrons, similar to what is found in the present experiment. Cassibry[72] arrived at similar conclusions using equations 2-17 to 19 for a resistive (non-ideally conducting) rarefaction layer. Additionally, Winglee[89] reports from simulation that an already super-Alfvénic flow entering the nozzle has the tendency to pull flank magnetic field lines into the center causing a ‘self-focusing’ of the entire plasma beam. Despite previous experimental claims, the MHD detachment scenario, including magnetic field line stretching, has yet to be explicitly demonstrated.

Section 2.3.4: Reconnection detachment

Another mechanism of plume detachment involving the preservation of the frozen-in condition is magnetic reconnection, where the field lines are perturbed to the extent that they become pinched off forming small scale magnetic ‘islands’ or annular rings (figure 2.4). Although not the main detachment theory of any paper dedicated to plasma detachment in an axial magnetic nozzle, there have been several authors willing to suggest this mechanism as an alternate possibility to their proposed theory[10, 26, 65, 94, 128-132]. The idea of magnetic reconnection and its affects in the acceleration of plasmas was popularized by Sweet[12] and Parker[8] in the 1950s while studying the merging of sunspot magnetic fields. The Sweet-Parker model relies on the magnetic field diffusing through resistive plasma flowing through a current sheet of specified dimensions and leaving at velocities near the Alfvén velocity at a rate proportional to the inverse square root of the Lundquist number[129]. This model sparked rather intense debate as the predicted reconnection rates were far too slow to explain observed solar reconnection events. Another approach was developed by Petschek[11] whose model included flow stagnation points and assumed two collisionless slow-mode shock waves mediated the conversion between magnetic energy into plasma thermal energy; the reconnection rates were much closer to observation. The theories remain controversial and each is compared to modern collisionless fast-reconnection models[9, 129, 133].

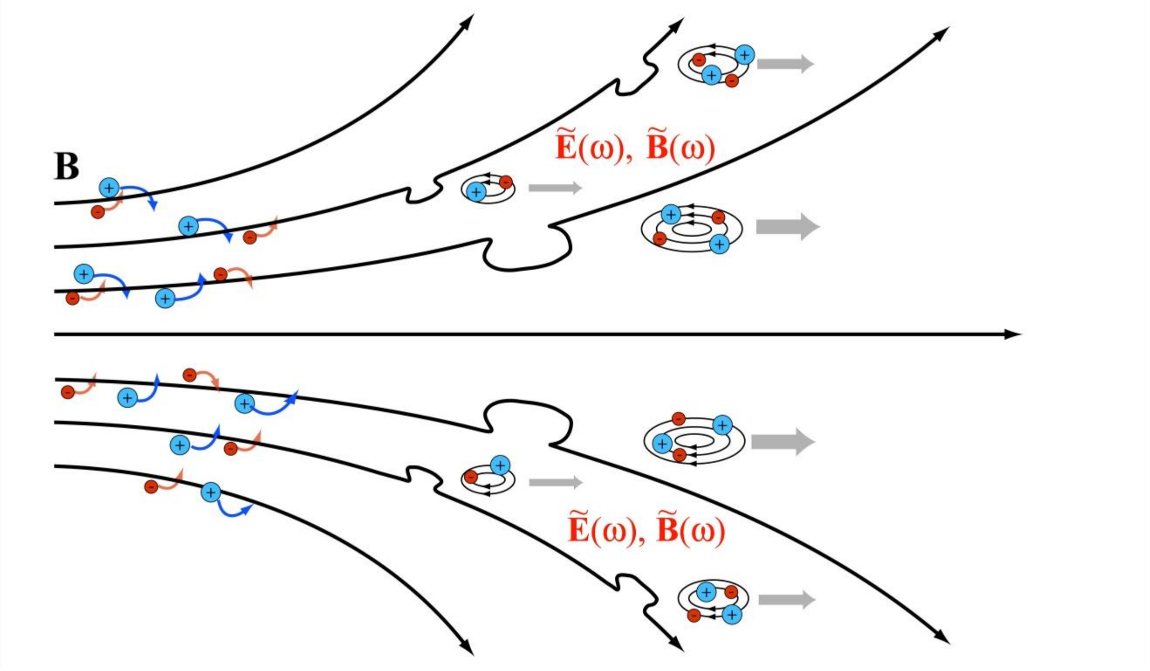

Figure 2.4: Detachment by magnetic reconnection. Particles remain tied to the magnetic field lines which become distorted by turbulence driven instabilities. The distorted field lines are pinched off during reconnection, creating magnetic islands or ringlets, allowing particles to remain on closed field lines. The frozen-in condition is preserved and allows collisionless plasma detachment from the external field as the islands stream away from the nozzle.

Most recent numerical models for magnetic reconnection have involved plasma turbulence where X line reconnection is brought on by a pair of plasma instabilities[129-131, 133]. In this mode ions are thought to be unmagnetized while electrons, tied to the field, are accelerated into the current sheets via the lower hybrid drift instability (LHDI) initiated by turbulent motion between ions and electrons[130, 131]. The thinning of the current sheet would also result in velocity shear that causes the Kelvin-Helmholtz instability to form and mediate the reconnection. What may be expected for low frequency magnetic reconnection are magnetic field line fluctuations up to the ion cyclotron frequency. For high frequency reconnection, one may expect magnetic fluctuation frequencies near the lower hybrid frequency and signatures of the LHDI.

Section 2.3.5: Demagnetization/Loss of adiabaticity

An entirely different detachment mechanism in the collisionless regime that doesn't require the frozen-in condition to be preserved is breakdown of the magnetic moment. Particles traversing across an expanding magnetic nozzle will conserve the first adiabatic invariant, μ, as gyration energy is converted into directed flow.

$$\mu = \pi r_c^2 \cdot \frac{q\Omega_c}{2\pi} = \frac{\frac{1}{2}m\mathrm{v}^2}{B} \qquad \text{2-20}$$

$$\frac{\mathrm{v}_{\perp i}^2 + \mathrm{v}_{\parallel i}^2}{B_i} = \frac{\mathrm{v}_{\perp f}^2 + \mathrm{v}_{\parallel f}^2}{B_f} \qquad \text{2-21}$$

The adiabatic invariant, also referred to as the magnetic moment, is a well conserved quantity until the magnetic field becomes weak and the static field changes with a scale length comparable to the particles gyroradius at which point the particle becomes effectively demagnetized.

This principle can be further understood by considering the action angle invariant averaged over a single gyro-orbit. If the gyro-orbit becomes too eccentric over a single gyroperiod, the magnetic moment will be lost as the line integral from Faraday's law due to the change in B becomes irrelevant. Taking r_c to be the average gyroradius during a gyroperiod, the orbit becomes demagnetized when $\Delta r_c \geq r_c$. This can be expressed as:

$$\frac{\Delta r_c}{r_c} = \left[\frac{\Delta\mu}{2\mu} - \frac{\Delta\Omega_c}{\Omega_c}\right] \approx -\frac{\Delta\Omega_c}{\Omega_c} \geq 1 \qquad \text{2-22}$$

where Ω_c is the gyrofrequency and Δ refers to a change in a quantity after a gyroperiod. The right hand side of equation 2-22 assumes that $\Delta\mu/\mu$ remains small until total μ breakdown. Since the particles spiral about a guiding center along the field line until μ is no longer conserved, $\Delta\Omega_c/\Omega_c$ can be estimated using the path along the field line[108]:

$$\frac{\Delta\Omega_c}{\Omega_c} \approx \Delta s\hat{b} \cdot \frac{|\nabla B|}{B} \qquad \text{2-23}$$

where Δs is the distance the particle travels along the field line during the gyroperiod, and $\hat{b}$ is the unit vector along the field line. If most of the energy is converted from perpendicular to parallel while the magnetic moment is still conserved, the distance can be approximated as[108]:

$$\Delta s \approx \frac{2\pi \mathrm{v}}{\langle\Omega_c\rangle} = \frac{\mathrm{v}}{\langle \mathrm{f}_c\rangle} \qquad \text{2-24}$$

Using this result along with equation 2-22, the approximate range where adiabatic invariance is valid is estimated as:

$$\frac{\mathrm{v}}{\langle \mathrm{f}_c\rangle}\frac{|\nabla B|}{B} = \mathrm{r}_c \frac{|\nabla B|}{B} \ll 1 \qquad \text{2-25}$$

Since the magnetic moment is conserved when equation 2-25 is less than unity, loss of adiabaticity occurs when the product of the gyroradius and change in magnetic scale length exceeds unity. This form of plasma detachment is illustrated in figure 2.5. Because the ion gyroradius is larger than the electron gyroradius, ion demagnetization will occur sooner than for electrons. A few authors postulate this method of detachment for both the ions and electrons[62, 67, 73, 82, 90, 100, 108]. This detachment method depends upon the magnetic topology and may be best suited for dipole expansions such as in natural plasmas whereas long narrow nozzles may favor the other detachment mechanisms.

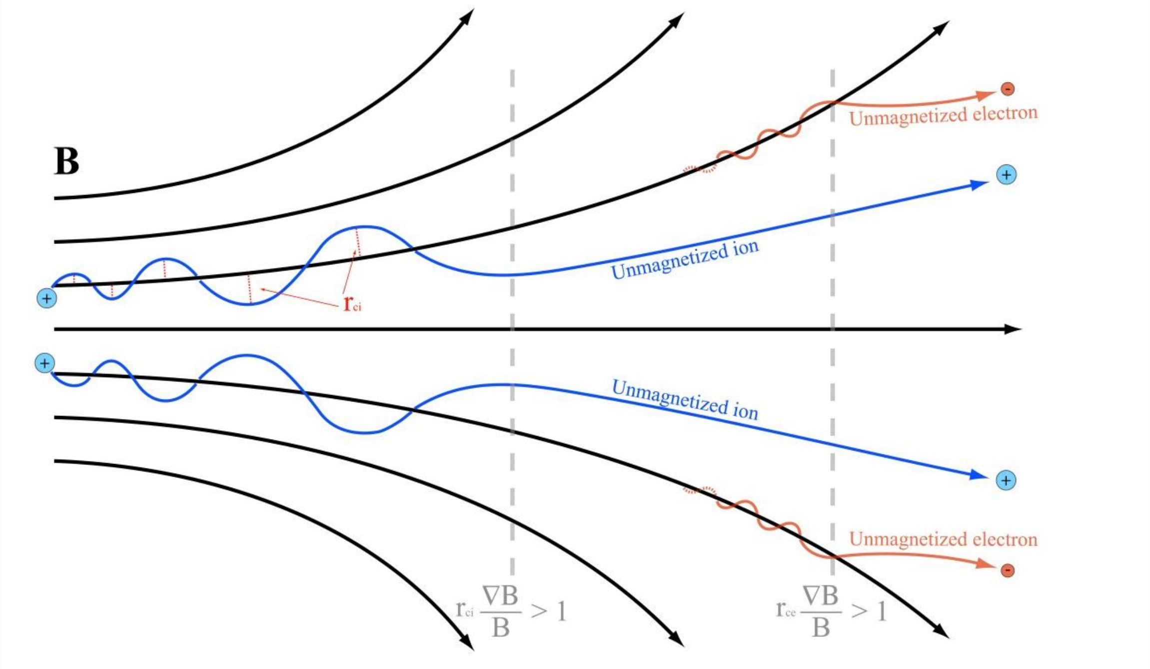

Figure 2.5: Detachment by breakdown of the first adiabatic invariant. The particle gyroradius increases in an expanding magnetic field and the perpendicular velocity is converted into parallel velocity. Once the change in the gyroradius, from one orbit to the next, is of the same scale as the gyroradius itself the particles become demagnetized and continue on the same trajectory at the moment of breakdown.

Section 2.3.6: Non-magnetized ions and electron inertia

Considering detachment of the plasma is not entirely complete unless both ions and electrons separate from the magnetic field, otherwise large electric fields would develop due to charge-separation. In the collisionless regime of weakly magnetized or non-magnetized ions and fully magnetized electrons, a particle based theory for plasma detachment based on electron inertia was developed by Hooper[60]. This particular study is considered a fundamental lower limit to detachment as several effects important in actual plasmas are ignored such as ionization, particle acceleration down the field gradient, dissipation, instabilities, and cross field currents. Other assumptions are that the magnetic field has no azimuthal component and that electric fields arise to prevent ions from deviating strongly from the electrons/flux surfaces essentially balancing the centrifugal force seen by an ion moving along the magnetic field.

The model starts with the momentum equation for each particle species in the form of the Lorentz force:

$$mu(r,z)\cdot\nabla \mathrm{u}(\mathrm{r},\mathrm{z}) = \mathrm{q}(E + u\times B) \qquad \text{2-26}$$

After employing local ambipolarity, the method of characteristics, and eliminating the azimuthal velocity for each species, the longitudinal plasma flow is found to order m_e/m_i[60]:

$$u(r,z)\cdot\nabla u(r,z) = -\nabla\left[\frac{q^2(\Psi_0-\Psi)^2}{2m_e m_i r^2}\right] \qquad \text{2-27}$$

where Ψ is the magnetic flux and the subscript 0 refers to parameters evaluated in the nozzle throat. This can be seen as flow that is determined by an effective potential which written using dimensionless variables, $\nu = u(r,z)/u_0$ and $\psi = \Psi/\Psi_0$, becomes[60]:

$$\nu\cdot\nabla\nu = -\frac{G}{2}\nabla\left[\frac{(1-\psi)^2}{r^2}\right] \qquad \text{2-28}$$

The parameter G, assuming uniform magnetic flux in the nozzle throat ($\Psi_0 \approx B_z r^2_0/2$), is essentially a hybrid ion-electron particle Larmor radius normalized to the throat conditions[60]:

$$G \approx \frac{1}{4}\frac{qB_z}{m_e}\frac{qB_z}{m_i}\frac{r_0^2}{u_0^2} \qquad \text{2-29}$$

This parameter is generally a large number and serves to quantify this second order cross field drift mechanism. The detachment of this hybrid particle is then determined by the curvature accelerations in that if the longitudinal velocity is much greater than the radial velocity, separation occurs. The characteristics equations of the hybrid (electron-ion) particle moving in a potential are[60]:

$$\frac{dv_r}{dt} = -\frac{G}{2}\frac{\partial}{\partial r}\left[\frac{(1-\psi)^2}{r^2}\right] \qquad \text{2-30}$$

$$\frac{dv_z}{dt} = -\frac{G}{2}\frac{\partial}{\partial z}\left[\frac{(1-\psi)^2}{r^2}\right] \qquad \text{2-31}$$

Once the magnetic flux functions in the nozzle can be defined, the limits between flows energetically able to detach from those that must remain attached can be determined. For this model it is found that only particle flows close to the nozzle axis are able to detach corresponding to lower values of G and more slowly diverging field lines (figure 2.6). Since this is a lower limit for particle based detachment, Hooper postulates that separation may be aided by dissipation, cross-field currents, or some form of turbulence[60].

One author has revisited this model employing non-zero angular velocity profiles

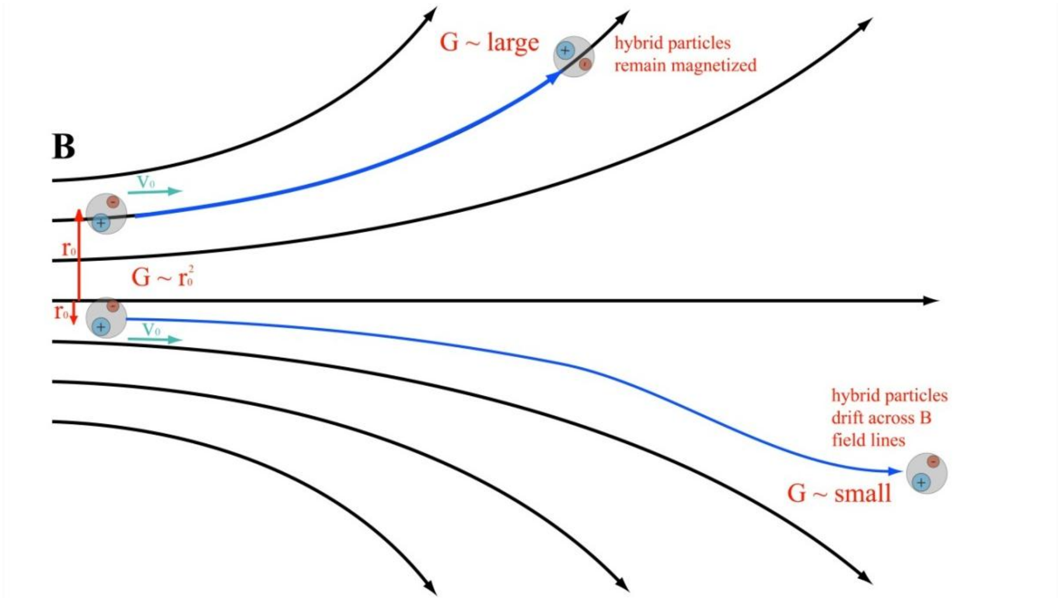

Figure 2.6: Detachment by electron inertia. Ions, already demagnetized, they are electrostatically tied to electrons forming a 'hybrid' particle. These particles drift across the field lines (detach) in regions where longitudinal velocity is larger than radial, i.e. close to the nozzle axis. If the hybrid particles begin near the edge, the radial velocity dominates and the particles will remain attached.

causing equation 2-27 to take the form[85]:

$$u(r,z)\cdot\nabla u(r,z) = -\nabla\left[\frac{q^2}{2(m_e m_i)^{1/2}}\frac{1}{r^2}\left((\Psi_m-\Psi)^2+\xi\right)\right] \tag{2-32}$$

$$\Psi_m \equiv \Psi_0 + \frac{m_i m_e r_0^2}{q(m_i+m_e)}\left(\dot\theta_{i0}-\dot\theta_{e0}\right) \tag{2-33}$$

$$\xi \equiv \frac{m_i m_e r_0^4}{q^2(m_i+m_e)^2}\left(m_i\dot\theta_{i0}+m_e\dot\theta_{e0}\right)^2 \tag{2-34}$$

where $\dot\theta_{i0}$ and $\dot\theta_{e0}$ are the initial angular velocity profiles for the ions and electrons respectively. These equations reduce to the Hooper limit in the case of zero rotation.

The effects of non-zero angular velocity are that the equilibrium magnetic flux surface, Ψ_m, shifts away from Ψ_0 without affecting r_0 and an always positive ξ adds a radially repulsive term with $1/r^2$ dependence. Detachment is then determined by the guide field geometry and aided by making $\Psi_m \leq 0$ and $\xi = 0$ as long as one may control of the rotation of the ions with respect to the electrons. Making Ψ_m negative effectively moves the hybrid particles equilibrium flux surface closer to the nozzle axis resulting in a smaller plume angle thus enhancing the probability of detachment. Minimizing the repulsive term, ξ, results in fewer closed equipotential surfaces. Simulations run under these conditions show plume angles reduced by over 50% and exhaust aperture increases by 100% over the Hooper model[85]. These effects are illustrated in figure 2.7. The one large issue with this type of detachment mechanism is the means by which rotation of the species may be introduced into the system which may be more possible in terrestrial plasmas (i.e. using RF or other HF EM wave coupling) than for space plasmas.

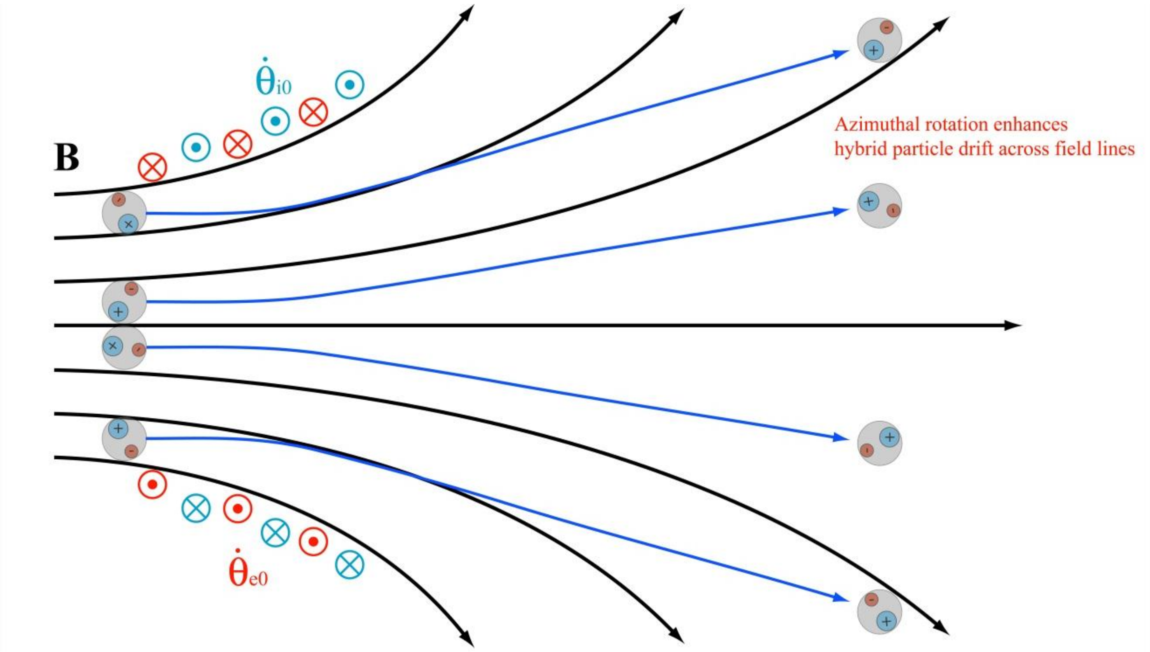

Figure 2.7: Detachment by electron inertia with the addition of azimuthal velocity profiles. This is similar to figure 2 of Schmit[85] et al. The azimuthal rotation aids the drift across field lines (detachment) for 'hybrid' particles beginning on essentially all radial starting points.

Another variant to Hooper's theory is that of Ahedo[84] et al. who employ angular momentum, barotropic functions, and conservation of the Bernoulli function along streamlines while ignoring the assumption of current ambipolarity. Equation 2-27 modified to include these effects becomes[84]:

$$m_j u_j(r,z) \cdot \nabla u_j(r,z) = -\nabla H(\Psi_j) + \frac{u_{\theta j}}{r} \nabla D(\Psi_j) \tag{2-35}$$

$$H(\Psi_j) = h_j + q_j \phi + \frac{1}{2} m_j u_{\theta j}^2 \tag{2-36}$$

$$D(\Psi_j) = r m_j u_{\theta j} + q_j \Psi_j \tag{2-37}$$

where $u_{\theta j}$ is the azimuthal component of velocity of species j, and $h_j = n_j^{-1} \nabla p_j$ is the barotropic function along the streamlines. The functions H and D correspond to the Bernoulli function along the streamtube and the total angular momentum, respectively. Hooper's version in this form corresponds to $h_j = 0$ and D = constant. The resulting ion and electron current densities, $j = j_i + j_e = qnu_i - qnu_e$, become important magnitudes to the plasma response. The azimuthal components of this current, $j_{\theta i}$ and $j_{\theta e}$, are referred to as the *swirl* and *Hall* currents which are positive and negative, respectively. The Hall current is generated from the E×B and diamagnetic drifts of the electrons and serves to accelerate the plasma. The swirl current is generated mostly from the conservation of total angular momentum rather than E×B drifts and acts to decelerate the plasma. These currents define the momentum gain as well as the magnetic topology induced by the plasma in the nozzle and can result in either convergent or divergent plasma detachment[84].

In Ahedo’s model the trajectories are found by similar methods to those from Hooper by combining model equations, numerical integration, and using the method of characteristics for a set of given throat conditions[84]. The modelled ion trajectories feature small differences in angle to the electron trajectories (along the magnetic field lines) and the ion streamlines more convergent than the electron streamlines. This angular difference causes a streamtube charge separation that, under the assumption of current-free plasma, drives a negative axially directed electron current back along the edge electron streamlines (figure 2.8). The negative electron current would rebound along the axis further upstream and leave the nozzle system near the center of the flow following the ions longitudinally.

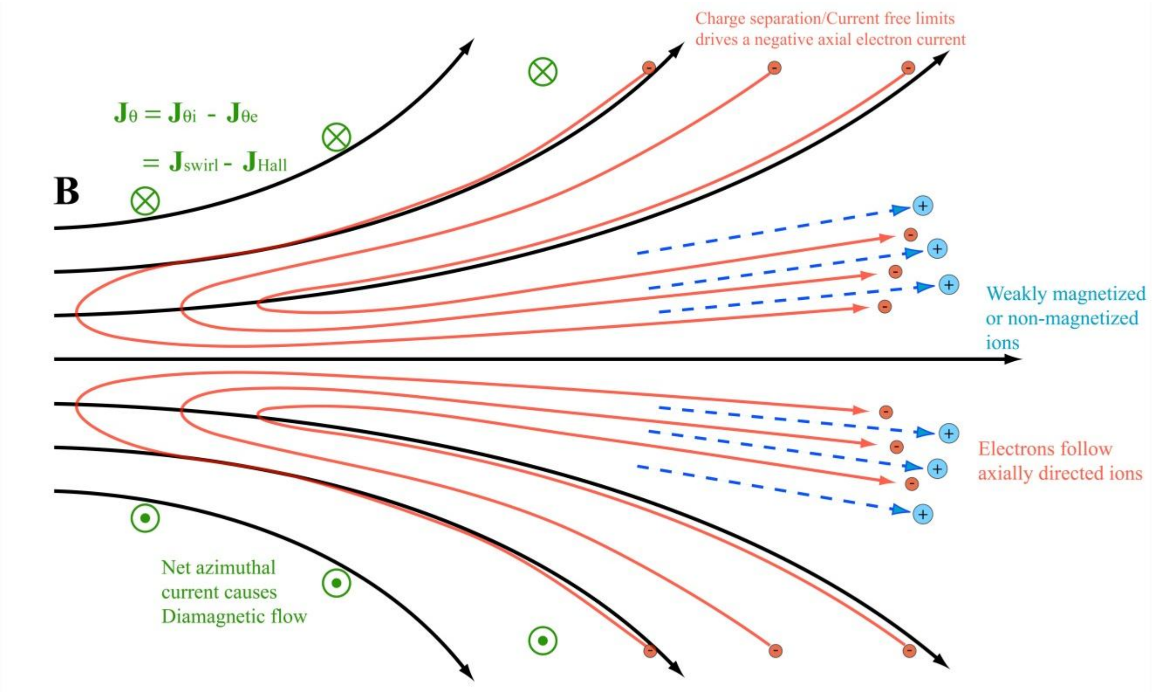

Figure 2.8: Detachment by electron inertia adding diamagnetic effects and counterstreaming electrons. Unequal azimuthal rotation both particle species cause a net current to flow in the expansion region of the nozzle. If ion current (swirl) dominates, an opposing diamagnetic field is set up resulting in a reduced axial magnetic field and enhanced radial magnetic field. A streamtube charge separation develops causing a negative axial electron current to form. Electrons rebound in the high field region to follow the ions more heavily concentrated closer to the nozzle axis.

Verification of any of these methods from Hooper, Schmit, and/or Ahedo requires the ability to measure/map the ion streamlines from the plasma response while comparing them to each model. Divergent detachment and ion streamlines largely following the field would tend to favor the Hooper model. Significant convergence of the ion streamlines would point to the Schmit model involving enhancement due to rotational velocity profiles. The Ahedo model would show small angle convergence of the ion streamlines over the magnetic field lines in addition to some magnetic field flaring from the swirl/Hall currents and a negative axial electron current. These have yet to be tested experimentally.

Section 2.3.7: Plasma turbulence and anomalous resistivity

Although not the main theory of any one author, plasma detachment from a magnetic nozzle via turbulence driven anomalous diffusion has been suggested by some as a plausible alternative[60, 69, 81]. In this case the ions are unmagnetized and the electrons are tied to the magnetic field in a collisionless plasma. The free-streaming ions with increasing axial distance, even at modest separation angles, will spatially diverge from the magnetized electrons and an electric field will develop. Plasma turbulence from current driven microinstabilities arise, possibly from ion/electron azimuthal currents (E×B drifts), gyrational motion of the particles, or differences in ion and electron temperatures, causing the electric field to become frequency dependent. Dominant modes of this wave field will have characteristic frequencies near the lower hybrid frequency, ω_{LH}, and the instability serves as the collisional transport analog in the collisionless regime; one form of this instability is known as the generalized lower hybrid drift instability (GLHDI)[126]. The GLHDI is a limiting case of the lower hybrid drift instability (LHDI) where wave number ($k_{\parallel} \rightarrow 0$) and relative electron-ion cross field drift trend to zero ($u_{dei} \rightarrow 0$)[134]. The LHDI itself has been presented as a fluid-like, T_e/T_i dependent, modified two-stream instability (MTSI) with characteristic frequencies and growth rate comparable to the lower hybrid frequency[135]. The plasma response to these fluctuating fields will be a fluctuating electron density in phase with the electric fields enhancing electron transport perpendicular to the external magnetic field.

One way to look at this is with the generalized Ohm's law, which in the form of Spitzer is[122, 136]:

$$\frac{m_e}{q^2 n_e}\frac{\partial J}{\partial t} + \eta J + \frac{J \times B}{q n_e} = E + \mathrm{v} \times B + \frac{\nabla p}{q n_e} \qquad \text{2-38}$$

where J is the current density, η is the plasma resistivity, and ∇p is the pressure gradient for each species. The wave, or high frequency, contribution from the fluctuating fields on the right hand side is associated with the resistive term, ηJ, on the left hand side. The classical Spitzer resistivity, η_c, is defined as the momentum exchange between ions and electrons, due to collisions, in the direction of the current:

$$\eta_c = \frac{m_e \nu_{ei}}{n_e q^2} \qquad \text{2-39}$$

The fluctuating wave fields cause a momentum exchange between the electrons and the field in a similar way giving rise to an effective 'collision' frequency[126]:

$$\left(\nu_e^p\right)_{AN} = \frac{q}{\langle \tilde{n}_e \rangle m_e \mathrm{v}_{de}} \langle \tilde{n}_e \tilde{E} + \tilde{n}_e \tilde{\mathrm{v}}_{de} \tilde{B}_r - \tilde{n}_e \tilde{\mathrm{v}}_{de} \tilde{B}_z \rangle \qquad \text{2-40}$$

where v_{de} is the relative drift velocity of the electrons in the ion rest frame. The tilde denotes a fluctuating quantity due to unstable waves and $\langle\rangle$ represents the time average of enclosed parameters. The resistivity due to this effective anomalous collision rate is known as anomalous resistivity[122, 123, 126]:

$$\eta_{AN} = \frac{m_e\left(\nu_e^p\right)_{AN}}{\langle\tilde{n}_e\rangle q^2} \qquad 2\text{-}41$$

The overall effective resistivity then becomes the sum of the classical resistivity with the fluctuating wave anomalous resistivity[122]:

$$\eta_{eff} = \eta_c + \eta_{AN} \approx \eta_c + \frac{\langle\tilde{n}_e\tilde{E}\rangle}{q\mathrm{v}_{de}\langle\tilde{n}_e\rangle^2} \qquad 2\text{-}42$$

The right hand side of equation 2-42 assumes electric field mode dominance to the fluctuating fields. If these instabilities vanish the resistivity returns to the classical Spitzer formulation. In the absence of collisions the anomalous resistivity may be the only resistive diffusion mechanism in the plasma, and will enhance transport in moderately collisional plasmas.

An anomalous mobility for electrons results from modification of the time between momentum exchanges mentioned in section 2.3.2. The new effective momentum transfer time is then[120]:

$$\tau_{eff} = \frac{m_e}{\eta_{eff} q^2 n_e} \qquad 2\text{-}43$$

and the cross-field mobility is[120, 124]:

$$\mu_{\perp} = \frac{1}{B}\left[\frac{\Omega_e \tau_{eff}}{1 + \Omega_e^2 \tau_{eff}^2}\right] \quad 2\text{-}44$$

while the anomalous diffusion rate is the product of the cross-field anomalous mobility with the electron temperature, $D_{\perp} = \mu_{\perp} T_e$. The cross-field mobility is also related to the traditional Pedersen conductivity.

Considering the electrons may have instability enhanced transport across the magnetic field there are still competing forces where the magnitude of the fluctuating electric field is important. The ion response to these fluctuating fields will be to follow the electrons along the field lines where the electric field may be large enough to balance or exceed the centrifugal force on the ions thus trapping them in the magnetic field[124]:

$$\langle \tilde{E}_{\perp} \rangle_{IT} = \frac{m_i \mathrm{v}_i^2}{q R_c} \quad 2\text{-}45$$

where R_c is the radius of curvature of the interacting magnetic field line. The electron response to the fluctuating fields, as discussed above, is to cross the field lines and follow the ions on a more axially directed ballistic trajectory. The electric field in this scenario is defined as the ratio of the cross-field electron velocity to the anomalous mobility[124]:

$$\langle \tilde{E}_{\perp} \rangle_{AN} = \frac{\mathrm{v}_{e\perp}}{\mu_{\perp}} = \mathrm{v}_i \sin\theta \, B \left[\frac{1 + \Omega_e^2 \tau_{eff}^2}{\Omega_e \tau_{eff}}\right] \quad 2\text{-}46$$

where the cross-field velocity of the electrons is the product of the sine of the separation angle, θ, and the ion velocity. This is a requirement for the electrons to follow the ions to prevent space-charge effects that would eventually cause a drag force on the ions. This process is illustrated in figure 2.9. Comparison of the competing particle responses to the electric fields will dictate which of the two processes will dominate over the other. This is shown as the ratio of the ion trapping (IT) electric field to the anomalous resistivity electric field (AN)[124]:

$$\frac{\langle \tilde{E}_\perp \rangle_{IT}}{\langle \tilde{E}_\perp \rangle_{AN}} = \frac{m_i \mathrm{v}_i}{q R_c B \sin\theta} \left[\frac{\Omega_e \tau_{eff}}{1 + \Omega_e^2 \tau_{eff}^2} \right] \tag{2-47}$$

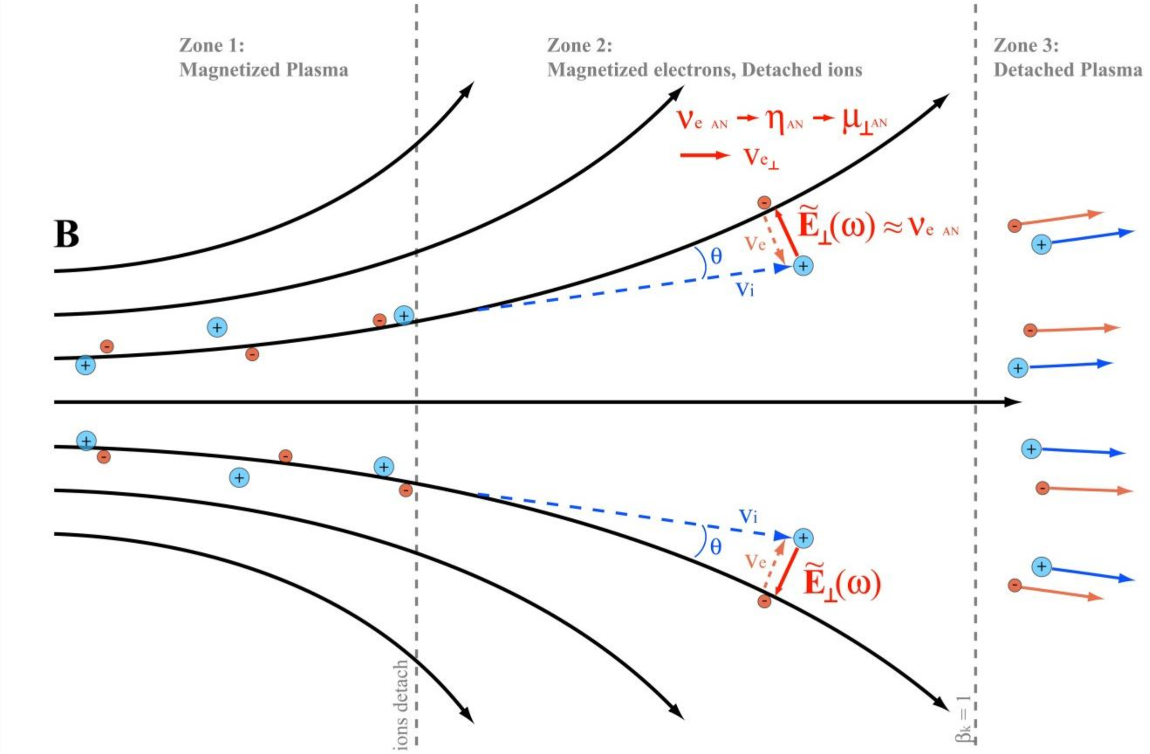

Figure 2.9: Detachment by turbulence driven anomalous diffusion. Charge separation between ballistic ions and magnetized electrons drive turbulent electric fields to form. These fluctuating electric fields will drive anomalous transport of the electrons across the field lines. If the ion velocity is large enough, electrons are pulled perpendicularly inward to follow the ions further downstream into regions where the electrons become demagnetized. If the ion velocity is too small (not shown), ions may be pulled outward by the electrons.

The process requiring the lower electric field strength will saturate and never reach the field strength necessary for the other process to operate. The electric field for anomalous resistivity to be the dominant process will saturate when this ratio exceeds unity and vice versa for ion trapping. One should expect, in turbulent plasmas, anomalous resistivity will drive the electrons to follow the ions for weak magnetic field regions, low field line curvature, heavier ion species, and/or high energy (velocity) ions. A larger T_i/T_e ratio will also increase the effective anomalous collision rate, shown here normalized to the lower hybrid frequency[126]:

$$\frac{(\nu_e^p)_{AN}}{\omega_{lh}} = -\frac{\mathrm{v}_{ti}}{\mathrm{v}_{de}}\left(\frac{T_i}{T_e}\right)^{1/2}\frac{m_i}{m_e}\int \frac{\varepsilon_{k_\perp}}{\langle\tilde{n}_e\rangle T_i} \times \Im\left\{k_\perp r_{ce}\left[R_{xx}^{(e)}\left(\frac{\tilde{E}_x}{\tilde{E}_y}\right)^2 + R_{yy}^{(e)} + R_{zz}^{(e)}\left(\frac{\tilde{E}_z}{\tilde{E}_y}\right)^2 + 2R_{yz}^{(e)}\frac{\tilde{E}_z}{\tilde{E}_y}\right]\right\}dk \qquad \text{2-48}$$

where v_{ti} is the ion thermal velocity, ε_k is the electric field energy density, and $R_{ij}^{(e)}$ represent elements of the electron dispersion tensor **R(ω,k)** insomuch that **R·E = 0**. Further details of the derivation and propagation of the dispersion tensor can be found in the reference by Choueiri[126]. On the other hand it can be expected that for light ion species, low energy (velocity) ions, large flaring nozzles (large R_c), and/or in regions of higher magnetic field strength ion trapping may be the dominant particle response to fluctuating electric fields.

Section 2.4: Experimental characterization of detachment mechanisms

In order to test any of the mechanisms described in Section 2.3 details of the experiment setup/environment as well as plasma diagnostics and their capabilities are important. In terms of the experiment setup it is highly important that the vacuum environment be acceptable in terms of pumping speed and pressure during the plasma discharge as these determine loss mechanisms and the quality of the data. Also important is the spatial scale of the measurement versus axial falloff rate of the magnetic field. Testing some of these detachment theories requires mapping the ion or electron streamlines allowing enough volume for plume expansion over the extent of the magnetic nozzle. Therefore the experiment should be capable of measuring $r_{max} > 2r_0$ and $z_{max} > z(B_0/10)$. The normalized axial falloff of the magnetic nozzle for this experiment is displayed in figure 2.10. This experiment measures radii out to $r > 5\ r_0$ and over an axial distance spanning nearly 2 orders of magnitude in the magnetic field strength. The rest of the experiment setup as pertains to the environment and measurement range will be described further in Chapter 3.

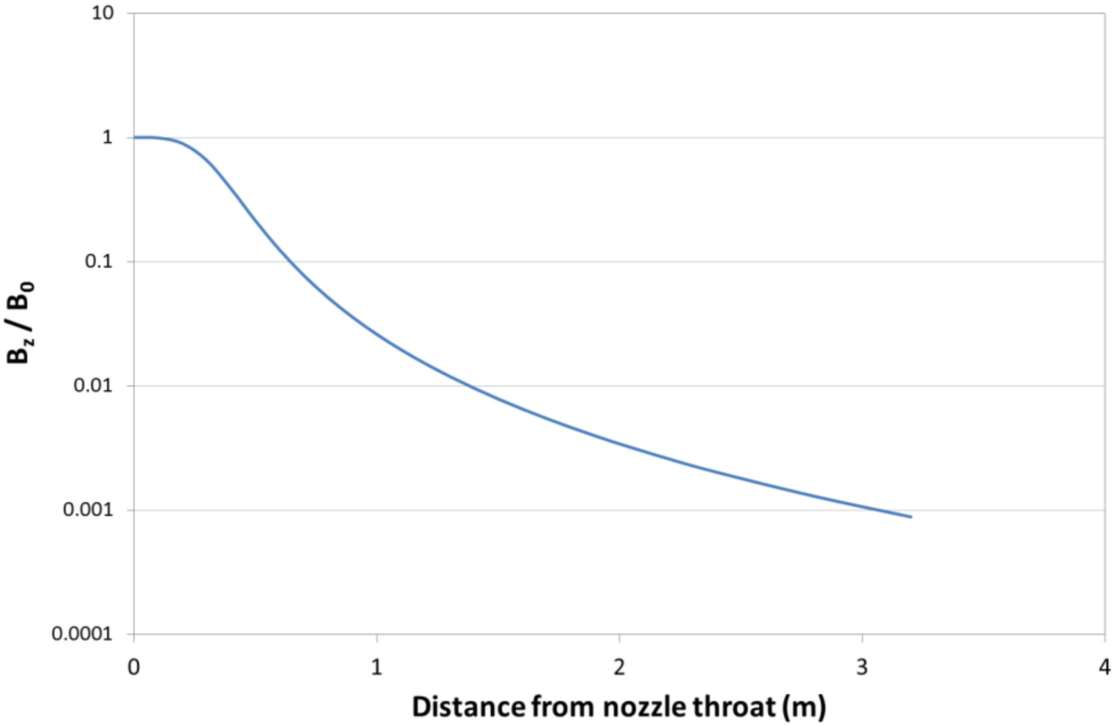

Figure 2.10: Axial magnetic field profile for this magnetic nozzle experiment normalized to the field strength at the nozzle throat.

The plasma diagnostics needed depends upon the individual theory. Verifying the collisional detachment theories would require neutral pressure measurement and a swept

Langmuir probe to measure the plasma density and electron temperature. A magnetometer would be needed further to test diffusion based detachment to get an estimate of the exact diffusion regime and degree of collisionality. If plasma were detaching by these mechanisms the flow would not necessarily be collimated or directed axially, as collisions are random, and have fairly even parallel and perpendicular ion/electron distribution functions. A Retarding Potential Analyzer (RPA) or some form of gridded energy analyzer taking measurements both parallel and perpendicular to the flow would confirm or exclude these mechanisms.

The detachment mechanisms preserving the frozen-in flow conditions can be verified using magnetic field diagnostics. A magnetometer measuring the local magnetic field strength before and during plasma flow will be able to detect any field line stretching or twisting. Mapping these vacuum and plasma magnetic fields throughout the spatial extent of the nozzle, specifically crossing through the Alfvén Mach transition point and beyond, while comparing the results to the models listed in equation 2-17 or similar references[70, 78] will indicate if MHD field line stretching applies for these conditions. Considering reconnection would create magnetic ringlets or islands, the reconnection rate should be near the same rate as the outflow of particles and cause 180° flips in the field. A power spectrum from a Fast Fourier Transform (FFT) of the magnetic field signal over this range should show these changes/flips in the magnetic field reflecting that of the particle bulk velocities. Higher frequency changes in the magnetic field due to lower hybrid instabilities would be detectable using ‘B-dot’ probes. The extent of these magnetic field fluctuations could then be mapped and shown to match up with a directed plasma flow.

Testing the idea of breakdown of magnetic moment and loss of ion magnetization, the ion flux as a function of radial and axial position should be compared to the location of the magnetic field lines (or at least a trusted magnetic field model). For the theory to hold the location where the ions begin to deviate from the magnetic field, to within uncertainty, must align with the location where the product of the magnetic field scale length and the ion Larmor radius exceeds unity. This adiabaticity parameter, from equation 2-25, can be calculated using ion velocity data, the cyclotron frequency, and B field scaling from magnetometer data (or a magnetic field model) and an RPA (or gridded energy analyzer). A similar treatment may be used for the electrons using the electron thermal velocity, v_{te}, assuming no significant heating/cooling prior to detachment in the same nozzle field. If the electron adiabaticity parameter exceeds unity prior to the location where the bulk of the plume has separated, the electrons will be detaching by this method as well.

The ion flux as a function of radial and axial position may also be used to test the validity of the electron inertia theories in that the ion flux may be integrated to compute the ion streamlines. It would be equally useful to map out the electron streamlines; however, the electron saturation current may be difficult to measure accurately considering the volatility in the electron sheath as the bias potential increases. Therefore it is still possible to use the ion streamlines and compare them with each electron inertia theory listed above. The limiting case of Hooper[60] with no azimuthal rotation would have the ion streamlines towards the edge of the plume following the magnetic field lines and a few of the inner ion streamlines showing some deviation. The addition of azimuthal rotation in the Schmit theory[85] may result in the ion streamlines converging towards the axis of the nozzle similar to figure 2-7. A magnetometer would be needed to test the Ahedo variant[81, 84] to show the magnetic field response to the azimuthal currents (Hall and Swirl currents) as well as the counter-streaming electrons. Also in the Ahedo model it is expected that the bulk of the ion flow will be located closer to the nozzle axis in order to drive electrons along the edge back upstream subsequently following the ions.

The final detachment theory to verify is plasma turbulence which requires high frequency (HF) probes able to measure in the expected range of the lower hybrid frequency and beyond. Similar probes have been designed and tested to measure high frequency components to plasma density and the electric field[137, 138]. These probes require extremely high sample rates to acquire data in the time domain or a spectrum analyzer to measure the power spectrum of the density/electric fields in the frequency domain. Signatures of large electric fields fluctuating near and exceeding the lower hybrid frequency would be a strong indicator of turbulent, instability driven, electron transport. These fluctuations along with little deviation of the ion streamlines and the magnetic field may indicate the ion trapping response. Conversely axially directed divergent ion streamlines would correspond to anomalous transport of the electrons as they are ‘pulled along’ by the ions. The electric field fluctuations should also have some spatial structure, being higher in regions where ion trapping or anomalous transport may be more favorable, while dispersing after complete plume detachment where the ions and electrons are flowing together.

Chapter 3: Experiment Configuration

Scaling results up to astrophysical plasmas with the intent to study electron and ion detachment from a magnetic nozzle requires an energetic flowing plasma source, a divergent magnetic nozzle, a large vacuum facility with high pumping capability, and an appropriate plasma diagnostics system. The argon plasma source, although designed as a research device for advanced electric propulsion, provides an ideal plume environment for studying the physics of plasma detachment. The plasma source, magnetic nozzle, vacuum facility, and data acquisition system are described in more detail below. The plasma diagnostics shall be described in chapter 4.

Section 3.1 - The VASIMR® VX-200 plasma source

Section 3.1.1: VX-200 components and operation

An ideal plasma source for the study of magnetic nozzle physics is the VASIMR® (**VA**riable **S**pecific **I**mpulse **M**agnetoplasma **R**ocket) thruster owned and operated by the Ad Astra Rocket Company. The VASIMR® concept has origins dating back to the late 1970s with inventor Dr. Franklin Chang-Díaz as a spinoff from fusion research[139, 140]. More than a decade later lower power versions of the electric rocket were studied and improved at NASA’s Advanced Space Propulsion Lab (ASPL)[69, 139, 141-148]. By 2005 the ASPL was closed due to program cutbacks allowing the formation of the Ad Astra Rocket Company, a privately funded version of the ASPL, and the further development of the VASIMR® engine[140, 149-155]. The two-stage thruster model VX-200 (**V**ASIMR®

e**X**periment **200** kW class thruster) was used for the duration of this experiment (figure 3.1). A simplified schematic of the thruster operation is presented in figure 3.2.

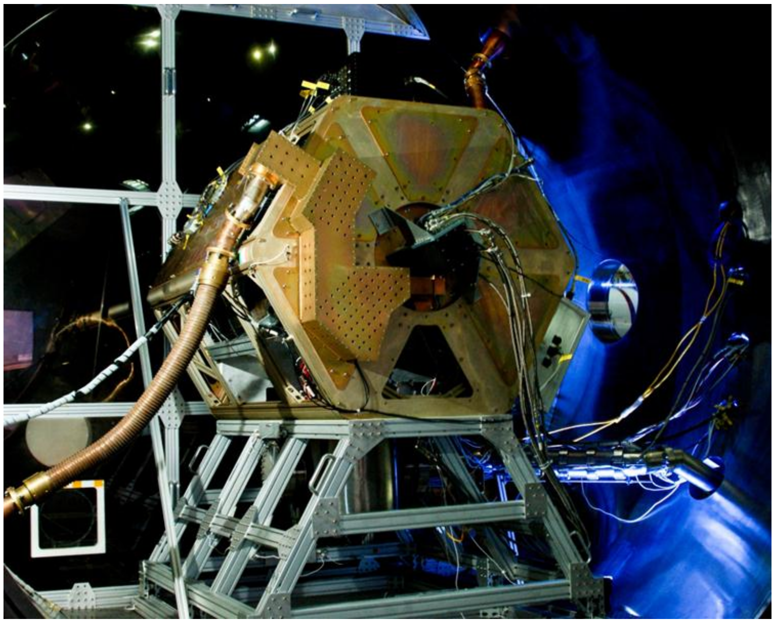

Figure 3.1: VX-200 Electric Rocket on its mounting stand inside the AARC Space Simulation Chamber. The rocket measures 1.8 m end to end (axially).

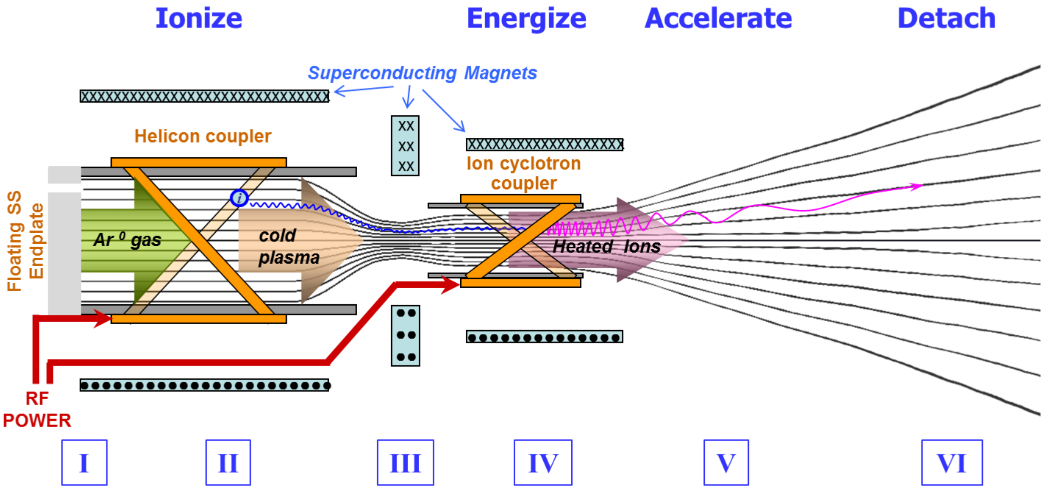

Figure 3.2: Simplified schematic of VASIMR® operation

The function of the VASIMR® can be divided into six operational phases. Room temperature neutral argon gas enters an ionization chamber via an electrically floating stainless steel cover plate (figure 3.2 I). A helicon wave coupler launches m = +1 helicon waves along parallel magnetic field lines ionizing the gas creating a population of cold ions (figure 3.2 II)[156-164]. The electric field for various helicon wave modes is displayed in figure 3.3. The VX-200 Helicon is capable of producing 10 – 40 kW of coupled RF power into the gas producing ~ 100% ionized plasma for a given RF power/gas flow rate. A magnetic choke compresses the flow and increases the plasma density prior to entering the Ion Cyclotron Heating[75, 110, 111, 139, 155, 165-171] (ICH) stage (figure 3.2 III). An ion cyclotron wave coupler launches left-handed circularly polarized waves causing an increase in pitch angle and tangential velocity (figure 3.2 IV). The VX-200 ICH coupler is capable of transmitting up to 175 kW of RF power into the ions while leaving the electrons relatively unaffected. A diagram of this principle is shown in figure 3.4. The heated ions enter the magnetic nozzle and the diverging field enables the conversion of perpendicular ion motion into directed (parallel) ion motion effectively accelerating the flow (figure 3.2 V). The final phase of VASIMR® operation is detachment of the plasma from the applied magnetic field via mechanisms studied in this paper (Figure 3-2 VI).

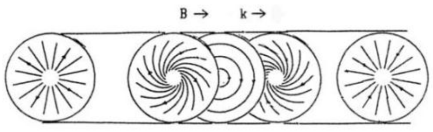

a) Helicon Mode m = 0

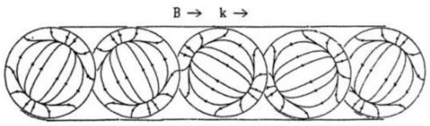

b) Helicon Mode m = +1

Figure 3.3: An example of the axial wave electric field propagation for two Helicon modes[158-160]

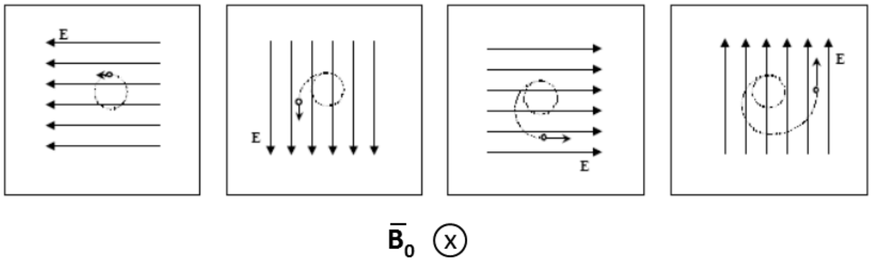

Figure 3.4: Ion cyclotron wave resonance principle[111, 139, 172]. The ion response to the rotating electric field results in an increase in pitch angle as well as tangential velocity.

Section 3.1.2: Gas feed system

The neutral argon gas was fed into the ionization chamber via an electrically isolated tube to the upstream endplate of the Helicon section of the VX-200. The gas was supplied by 99.999% purity research grade argon stored in a ‘K’ bottle. The flow rate is metered using a MOOG Inc. proportional flow control valve operating in a PID control loop using a Taber Ind. low pressure transducer as feedback device. The pressure upstream of a 0.041” orifice is measured and the valve throttle level, via a control current, is adjusted to the flow equation assuming choked flow[173]:

$$Q = AP_1C'\left(\frac{kT}{m}\frac{2\gamma}{\gamma+1}\right)^{1/2}\left(\frac{2}{\gamma+1}\right)^{1/\gamma-1} \qquad \text{3-1}$$

$$\text{for } P_2/P_1 \leq (2/(\gamma+1))^{\gamma/(\gamma-1)}$$

The variable Q is the gas flow through the orifice, A is the orifice cross-sectional area, P_1 is the orifice upstream pressure, P_2 is the orifice downstream pressure, C’ is the vena contracta correction factor (typically ~ 0.85), γ is the adiabatic index, k is the Boltzmann constant, T is the gas temperature, and m is the mass of the gas molecules. This condition of choked flow is verified for every plasma firing and the flow rate is checked against an inline calibrated MKS 179A Thermal Mass Flow meter. Gas flow rates of 107 mg/s (3600 sccm) and 100 mg/s were used in this experiment. These flow rates have been previously verified to produce approximately a 100% ionization fraction for the 30 kW Helicon RF power setting[140, 152].

Section 3.1.3: RF power generation

Each stage of the VX-200 is powered by a separate solid-state RF generator, based on frequency range and power capability[144, 152], manufactured by Nautel Ltd. of Canada. The generators used for this experiment are shown in figure 3.5. The operational frequencies are proprietary and ITAR protected. The generators convert 375 VDC input into a programmable range of tens to hundreds of kilowatts of RF power using solid-state high power switching circuitry common to the radio transmission industry. This RF power is then fed into an impedance matching circuit matching the impedance load into the generators at 50 ohms. RF power data are measured using factory calibrated sensors located in each generator as well as sensors located on the transmission lines to measure current, voltage, and phase. These solid state RF generators use an FPGA controller for closed loop feedback of impedances and are capable of producing smooth power output with low line loss (> 95 % efficient). For this experiment it is important to have repeatable, steady power during plasma generation & heating to minimize uncertainty and ensure high quality data. The RF power during the magnetic nozzle study during each shot varies less than 1% of the programmed control value and is repeatable to within 2%.

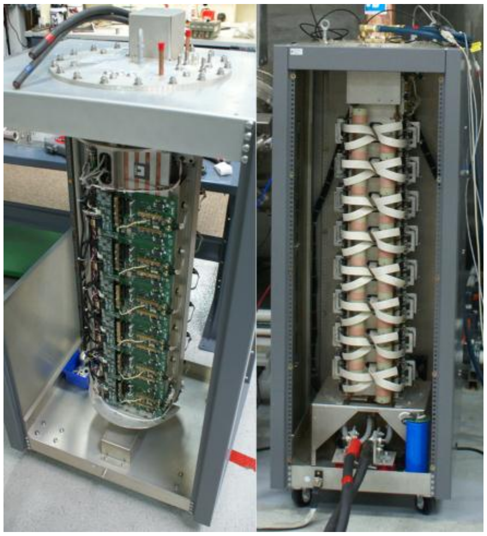

Figure 3.5: VX-200 RF Generators. (*left*) First stage Helicon generator (0 – 40 kW). (*right*) Second stage ICH generator (0 – 170 kW).

Section 3.2 - Magnetic nozzle

The magnetic nozzle for this experiment follows a general dipole expansion from the 'throat' located at the end of the plasma sources ICH section. The magnetic field creating this nozzle is generated by a set of type 1, Nb-Sn, superconducting magnet coils with a peak field strength exceeding 2 T. These coils are mounted inside of a separate cryostat that surrounds the plasma source and creates the magnetic conditions for Helicon plasma ionization and ICH resonance. Exact magnetic field magnitudes, coil current settings, and profiles within the rocket core are proprietary and ITAR restricted. The magnet coils are conductively cooled by a pair of Sumitomo Industries cryocoolers that utilize the Gifford-Mcmahon refrigeration cycle to ultimately achieve a base coil temperature of ~ 6 K. The magnet was built by Scientific Magnetics of England and acceptance testing is shown in figure 3.6. The plume magnetic field is modeled in figure 3.7. Magnet current is supplied by custom power supplies provided by Scientific

Magnetics and is stable to ± 1 mA. Current is persistently left on for the duration of the experiment keeping the magnetic field strength and topology constant.

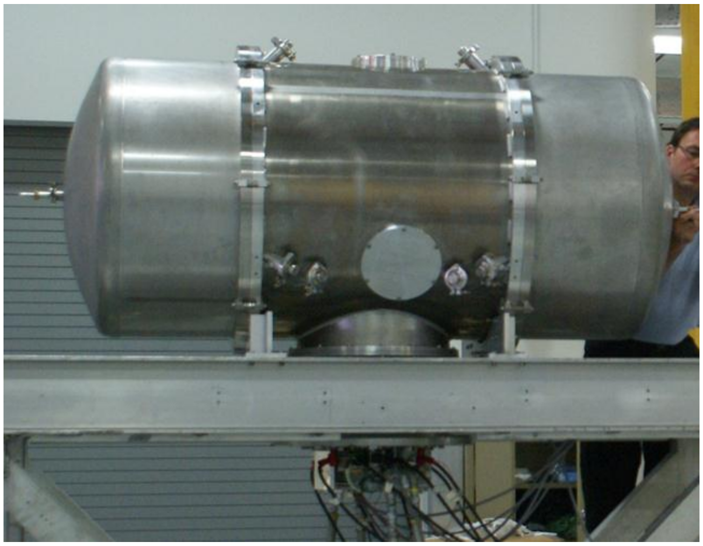

Figure 3.6: VX-200 Superconducting Magnet. Magnet coils are inside this cryostat shown during acceptance testing which required vacuum sealed endcaps and radial access tubes. An operator on the right is shown for scale.

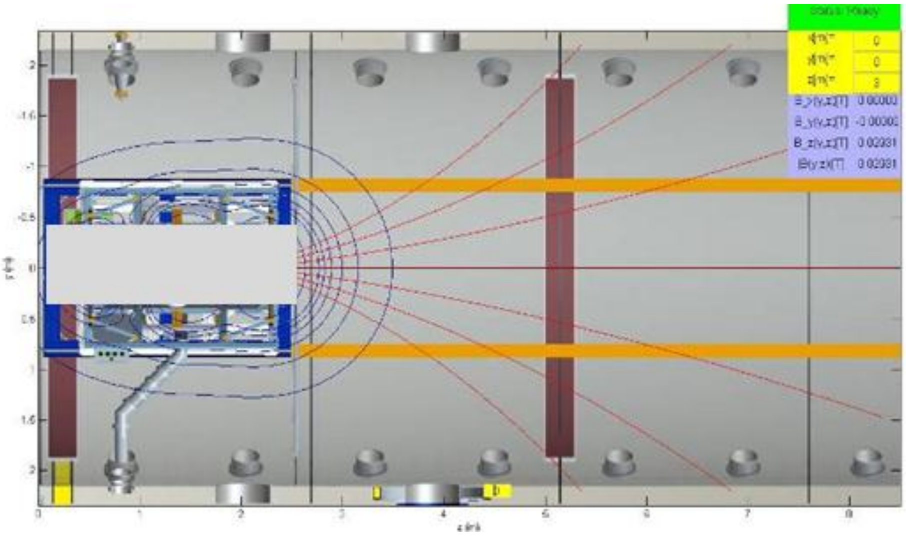

Figure 3.7: Modeled magnetic field (red lines) in the plume/nozzle region for the dipole field setup. The effects of Earth's magnetic field (0.47 G in Houston) are found to be negligible to the applied magnetic field throughout the measurement region (Z = 2.8 m - 5.5 m).

Section 3.3 – Vacuum environment and translation stage

Section 3.3.1: Vacuum facility

Studying the physics of flowing plasma in a magnetic nozzle, while obtaining high quality data, requires a large vacuum chamber with ample pumping capability. The chamber should be large enough to allow the plume/nozzle to expand unimpeded by any physical structure in order to take measurements over a broad range of nozzle strengths (B/B_0). The pumping rate needs to be high enough to maintain a good base vacuum level before and during plasma operation to minimize interaction with neutrals. The charge-exchange mean free path should be at least on the order of the scale length of the experiment if not larger than the largest chamber dimension.

Figure 3.8: (left) Preparing the experiment at the 150 m^3 vacuum facility located at the Ad Astra Rocket Company. (*right*) The VX-200 Plasma source mounted coaxially to the chamber in the front end of the chamber. Copper coaxial RF transmission lines are fed from either side into RF matching networks for each stage of the rocket. Onboard sensors, data, and pressurized helium (for cooling the superconductor) are fed out to the right.

The vacuum facility used for the experiment work presented in this paper was the 150 m^3 ‘El Monstruo’ chamber located at the Ad Astra Rocket Company in Webster Texas (figure 3.8 *left*). The VX-200 plasma source, superconducting magnet, and accompanying onboard diagnostics are mounted within the chamber (figure 3.8 *right*). A vacuum baffle has been installed to isolate the plasma and recombined neutrals from the high-voltage RF components to prevent loss of vacuum dielectric isolation and arcing. A top view cutaway model of the total system is displayed in figure 3.9 showing the coordinate system used for data analysis. The axial origin (Z = 0 m) is located at the door flange while the radial origin (r = 0 m) lies along the chamber central axis. The vacuum baffle, or wall, is located at Z = 2.61 m while the closest measurement location is at an axial position of Z = 2.79 m and the furthest located at Z = 5.09 m for the first data set and Z = 5.49 m for the second data set. The first data mapping area is outlined in figure 3.9 with a blue dashed rectangle.

The chamber was roughed down using a Pheiffer WKP 4000 Combiline pumping station. This pump evacuated the system to crossover where the high vacuum pumps took over. These pumps include three liquid nitrogen assisted TM1200i cryopanels

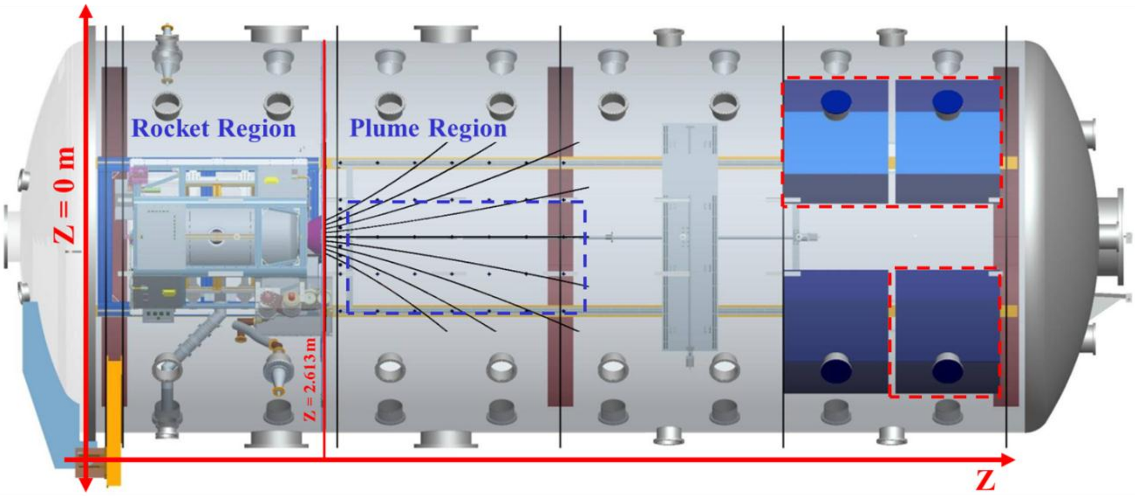

Figure 3.9: Top view the chamber and experiment region. The coordinate system is axially defined from the chamber door flange and radially from the chamber axis. The first data measurement region is marked with a blue dashed rectangle. The three active high vacuum pumps for this experiment are marked with red dashed rectangles.

(figure 3.9), two TM250 cryopumps, and a single Leybold TMP1000 turbopump for a total system pumping rate greater than 200,000 liters/s. This pumping speed resulted in base vacuum levels on the order of $1\text{x}10^{-8}$ torr and below. Pressures at the end of a 1.5 second plasma pulse would end up $1 – 2\text{x}10^{-4}$ torr. The pressures were measured and digitized using a pair of Bayard-Alpert ion gauges: Granville Phillips 356 Micro Ion Plus and a Granville Phillips glass tube ionization gauge with GP270 controller. Also used was an MKS e-series residual gas analyzer to check for impurities and partial pressures of various gases, up to 100 amu, during the firings. As expected argon was the dominant gas in the chamber at any given time during these experiments.

Section 3.3.2: Translation stage

The experiment data were taken on two separate occasions totaling over more than 1500 plasma firings, or shots as they will be referred to for the remainder of this thesis. Various plasma diagnostics, which will be covered in more detail in chapter 4, were positioned at a separate plume location for each shot completing a comprehensive mapping of the plasma and magnetic nozzle. A custom 2-axis translation stage with a range of 2 m x 5 m was built and used to reposition the probes (figure 3.10). Each translation stage axis features a ball screw coupling driven by a high-precision, high torque step motor with an optical encoder and microstepping control. The resolution for each axis is less than ±0.1 mm. Positions are taken relative to the chamber coordinate system and are calibrated using a set of inductive limit sensors on each axis. Probes are raised up to the axial plane of the chamber and mounted on top of an ‘optical bench’ like

Figure 3.10: (*left*) Two-axis translation stage during construction. The range of travel is 2.5 m in the Y direction and 5 m in the Z direction. Each axis is ballscrew driven controlled by high precision step motors and limited by inductive limit switches. Leading edges are covered by grafoil^{TM} to limit sputtering from the aluminum frame. (*right*) Translation stage shown installed in the exhaust region of the vacuum chamber looking upstream.

plate and each given offset coordinates with respect to the leading central position on the translation stage mounting plate.

Figure 3.11 displays a grid of translation stage positions for the first data set. Each point represents a separate shot with recorded data (positions, signals, etc.). Radial scans were taken at an interval of $\Delta Z = 10$ cm for the first 1 m, 20 cm for the next 0.5 m, and 40 cm for the last 1 m. Greater axial resolution was given for the higher density/higher magnetic field region than for the low density/low magnetic field region. Also at each axial position only radial scans for all diagnostics were possible. Two full diameter scans were made in order to verify azimuthal symmetry, one at the closest axial approach of $Z = 2.9$ m and the other at $Z = 3.6$ m. The shot density is irregular near the chamber centerline which is due to the offset position of the plasma diagnostic mounted on the translation stage and that each diagnostic had a dedicated shot while positioned on nozzle axis (Y = 0 m). Owing to a magnetometer sensor malfunction (B_Z), it became necessary to repeat the original data set with a recalibrated sensor in order to have accurate magnetic field data. The second data set was taken at higher spatial resolution at intervals of 10 cm along the Z axis and 5 cm along the Y axis and this grid is displayed in figure 3.12. Not all diagnostics were used or available during the second data set.

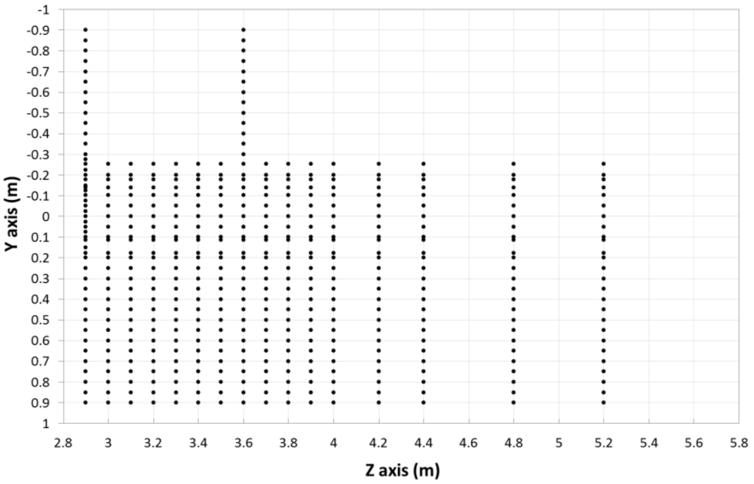

Figure 3.11: Plume mapping grid displaying the location of the translation stage for each shot in the first experiment map.

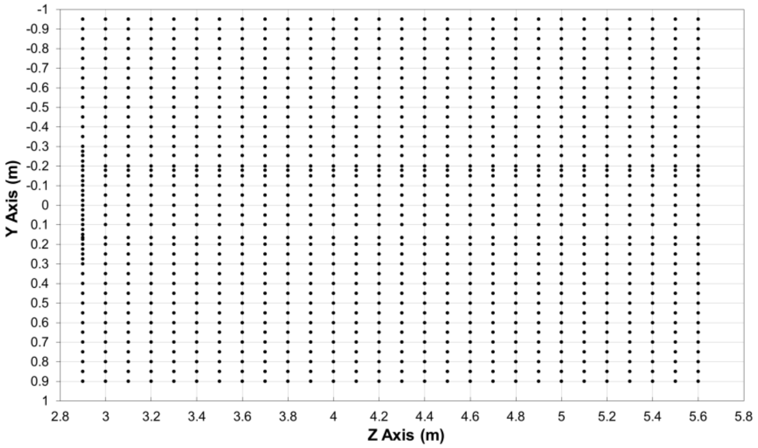

Figure 3.12: Plume mapping grid displaying the location of the translation stage for each shot in the second experiment map.

Section 3.4: Charge-Exchange considerations

Great effort has been extended to minimize the interaction of the argon ions with recombined neutrals. These efforts included increasing the vacuum pumping speed, advanced data and power synchronization techniques, and achieving steady high power very early in the shot before the chamber pressure became too high. Should the background pressure become high the probability of an ion receiving an electron from a slower neutral atom rises resulting in a slow ion and a fast neutral. This two-body effect is commonly referred to as a charge-exchange interaction[31, 118, 119, 174-180]. An elevated charge-exchange rate is effectively a reduction of unimpeded ion flux from the plume. The change in uncollided ion flux, $\Gamma_i = n_i v_i$, can be thought of as being proportional to the number of neutrals, n_n, in a volume of thickness dx[119]:

$$d\Gamma = -\sigma_{Cex}\Gamma n_n dx \qquad 3\text{-}2$$

The parameter σ_{cex} is the charge-exchange cross section and is dependent upon the type of interaction, species, and ion energy (figure 3.13). This differential equation is easily solved and takes the form[119]:

$$\Gamma(x) = \Gamma_{i0}\left(1 - e^{-x/\lambda_{mfp}}\right) \qquad 3\text{-}3$$

$$\lambda_{mfp} = \frac{1}{n_n \sigma_{Cex}} \qquad 3\text{-}4$$

where λ_{mfp} is the e-folding distance for the uncollided flux, Γ_{i0}, and is referred to as the charge-exchange mean-free-path.

For high quality data the spatial scale length over which data is taken for a given experiment should be less than this value. A heavily charge-exchanged plume will appear to broaden according to particle conservation as a reduction in ion flux would require a larger integration area. A graph plotting charge exchange mean free path versus chamber background pressure is displayed in figure 3.14 for four different ion energies. In this experiment the charge-exchange mean-free-path has been computed to range from 12.2 to 77.3 m during Helicon operation and from 1.24 to 3.12 m during ICH. These distances (during Helicon operation) are larger than the chamber itself and the total expanse of the data (ΔZ ~ 2.7 m, ΔY ~ 1- 2 m) are within acceptable limits during the majority of ICH operation. These may be considered worst case scenarios since the above equations neglect the motions of the neutrals assuming stationary target gas which is not the case. The ability of the plasma itself to act as a 'particle pump' is also ignored which effectively clears neutrals out of the plume through elastic collisions.

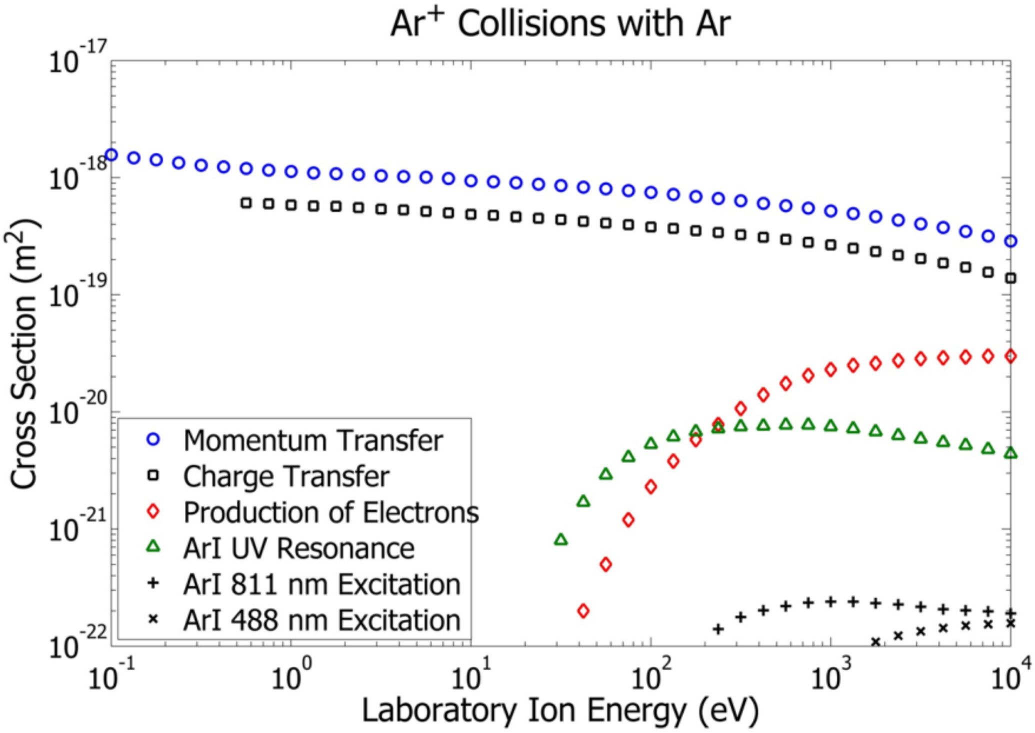

Figure 3.13: Interaction cross sections for argon ions incident upon argon neutrals[176].

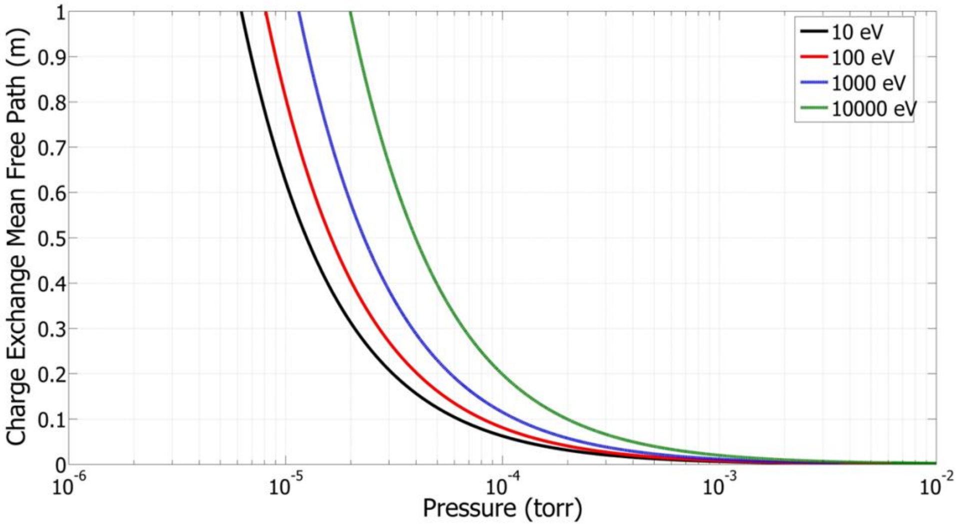

Figure 3.14: Computed charge-exchange mean free paths in argon on a log scale ordering of ion energies. For a given background pressure (assuming room temperature neutrals), the distance that an ion beam will travel before decreasing to ~ 37% of its initial flux can be estimated if the ion energy is known. Steady power at low pressures helped ensure that charge exchange mean free paths were large for this experiment.

Section 3.5: Experiment setup and data acquisition

The shot setup displaying the total RF power, gas flow rate, and resulting chamber background pressure versus time for the first data set are shown in figure 3.15. Each graph computes the shot-averaged value versus time over every shot in the data mapping (450 shots). The shot setup for the second data set is nearly identical to the first shown in figure 3.15 with the exception being the gas flow rate being slightly lower (100.75 mg/s as opposed to 107.3 mg/s). Outside of this small difference in flow rate the shot profile and repeatability are identical between the first and second data sets. The red boxes highlight the time windows where data were analyzed, each are 100 ms in duration. These times were selected as being the earliest time window, due to pressure, that the programmed RF power level was steady. The dashed curves in each graph display the

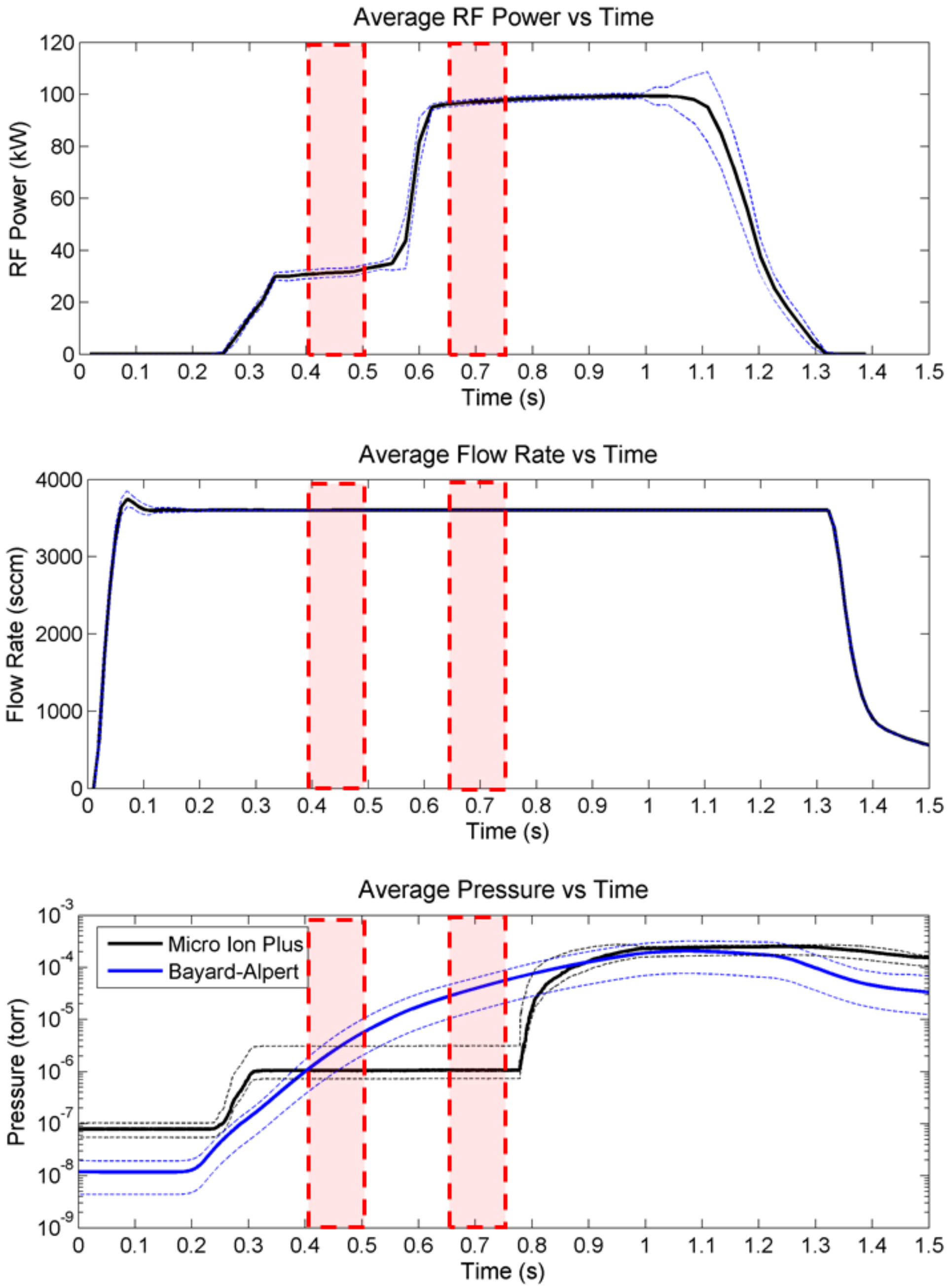

Figure 3.15: RF power, flow rate, and chamber pressure vs. time profiles. The data is averaged over all of the shots in the experiment map. The dashed curves present upper and lower uncertainty bounds for each data curve.

uncertainty bounds calculated from systematic uncertainty. The two series in the chamber pressure graph refer to the two separate gauges measuring pressure in the downstream section of the vacuum chamber. Although the gauges are mounted at different locations the GP Micro Ion Plus gauge includes internal filtering electronics, ranging features, and a slow response time (160 ms) that results in unrealistic, flat pressures during certain periods of the shot. The traditional glass tube Bayard-Alpert ion gauge is more representative of the chamber pressure. Two RF power settings were used: A constant 30 kW applied to the Helicon coupler and 70 kW to the ICH coupler from 0.575 s – 1.175 s (100 kW total) corresponding to two distinct ion energies flowing through the magnetic nozzle. The differences with regards to the plasma are noteworthy and are shown in figure 3.16. Each image was taken during steady RF power.

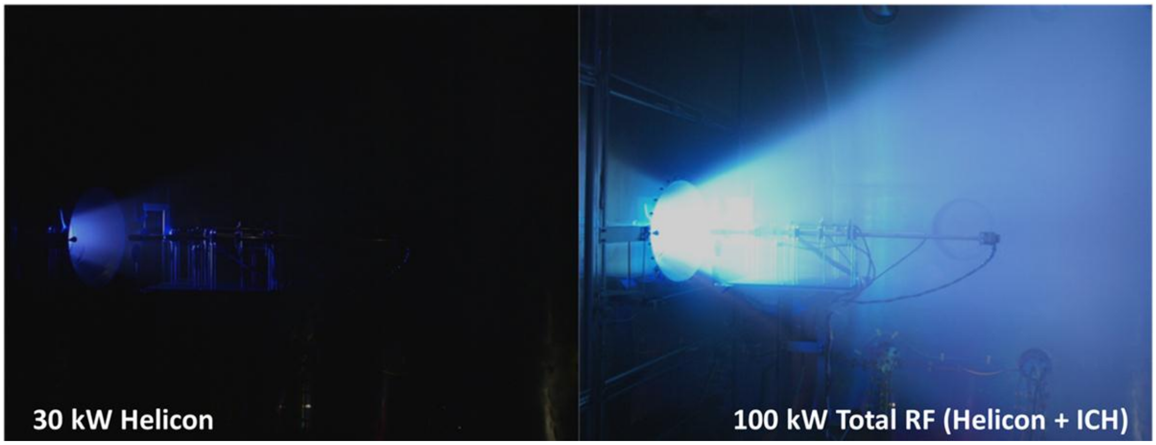

Figure 3.16: Images showing the first stage Helicon operating alone (*left*) and together with the second stage ion cyclotron heating (ICH) (*right*) during periods of steady RF power.

Each shot is initiated when the experiment operator presses a ‘pulse’ button as depicted in the DAQ block diagram (figure 3.17). The ‘pulse’ button sends a fiber optic linked pulse to both of the RF power generators as well as a pair of National Instruments PXI chasses configured with multiple analog to digital conversion cards (NI-PXI series

6200). This pulse synchronizes the devices by initiating the RF power profiles, starting the data acquisition sample clocks, and triggering the PID controlled gas flow. The sample rates can be varied on each NI PXI-6200 series card. The RF power and gas flow sensors sample at 100 Hz.

The plasma diagnostics take measurements at two sample rates: 40 kHz for the Langmuir probes, force target, and pressure gauges while a higher sample rate (100 kHz) is used for the RPA and magnetometer. The electric field probe signal is fed into an SRS brand SIM910 JFET voltage preamplifier prior to being sent into an Agilent 4395A network analyzer. The network analyzer was functioning in spectrum analyzer mode and taking frequency domain spectra at a rate of 2 Hz from a frequency range of 0 – 10 MHz. Even though the spectra rate is every 0.5 s, it takes only a few ms to complete the individual spectra. All of the other probe data are taken in the time domain.

The Langmuir probes and RPA require voltage bias that is provided by both Kepco and Xantrex brand power supplies. The Langmuir probe planar arrays are at a fixed DC bias of -20 V. The RPA and guard-ring Langmuir probe use the triangle wave output from the function generator to vary the bias voltage to the RPA discriminator and guard-ring collector, respectively. The triangle wave frequency was set at 200 Hz for the RPA and 70 Hz for the guard-ring probe. Data are taken for 2 s, buffered, and then sent via Ethernet to an MDSPlus server, which is a shot based open-source data management program that has roots in fusion research. MDSPlus then interfaces with computation software such as Matlab and IDL for future analysis. After all data are sent to the MDSPlus server, the time domain data and power spectra are displayed on computer monitors using custom National Instruments LabView GUIs. It is then at the discretion of the experiment operators to verify the quality of the data and determine whether the shot must be repeated or move on to the next setpoint/location. A summary of experiment parameters and settings is displayed in table 3.1.

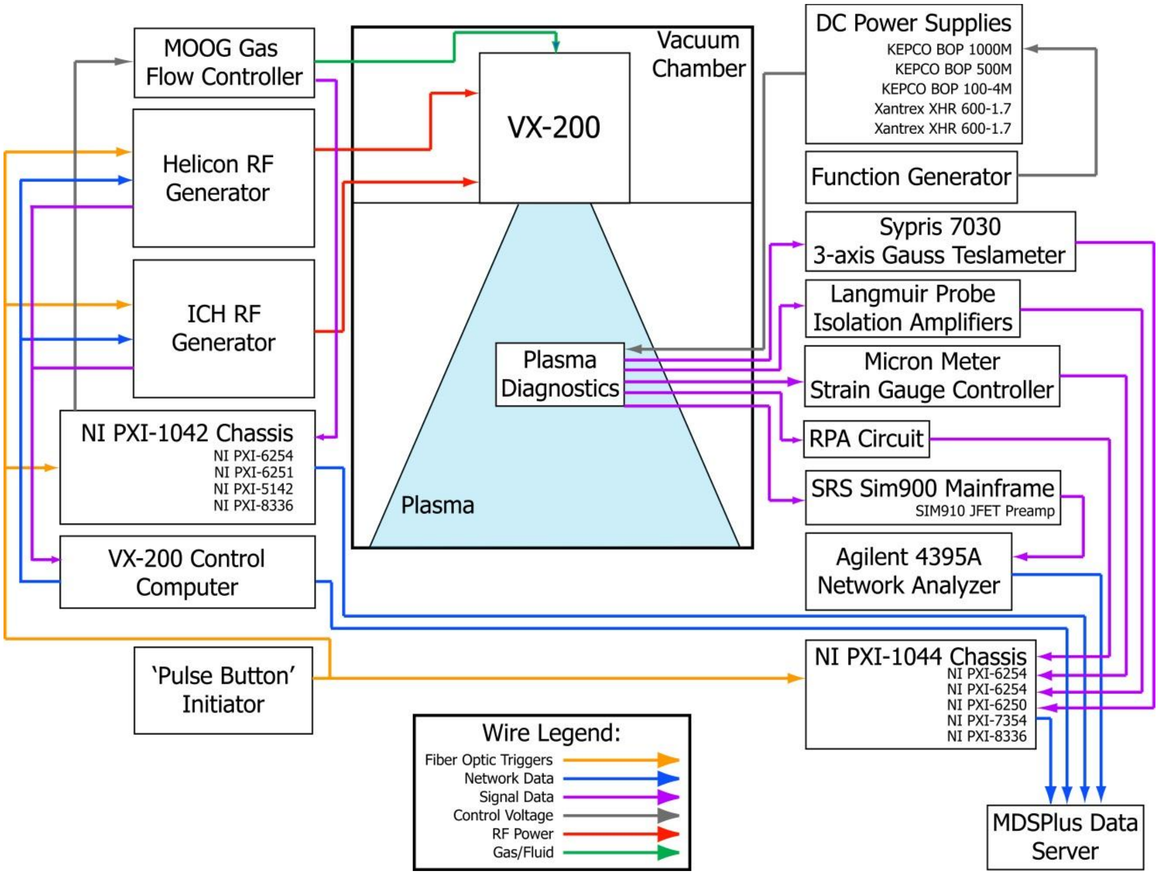

Figure 3.17: Operational block diagram for the VX-200 plasma source, timing and control network, and data acquisition hardware.

Parameter/Setpoint	Experiment #1 Values	Experiment #2 Values
Gas Species	Argon (99.999%)	Argon (99.999%)
Flow Rate	107.28 +/- 0.015 mg/s	100.75 +/- 0.10 mg/s
Plasma Source Power (Helicon RF)	31.1 +/- 0.7 kW	31.0 +/- 0.5 kW
Plasma Heating Power (ICH RF)	68.9 +/- 0.9 kW	70.7 +/- 2.1 kW
Helicon Wave Frequency	6.78 MHz	6.78 MHz
Peak Magnetic Field Strength	> 2 T	> 2 T
Measured Nozzle Field Strength (on axis)	10 - 740 G	10 - 740 G
Ion Energy	50 - 280 eV	50 - 280 eV
Translation Stage Y range	-0.254 - 0.9 m	-0.95 - 0.9
Translation Stage Z range	2.9 - 5.2 m	2.9 - 5.6 m
Nozzle 'Throat' Location	2.04 m	2.04 m
Vacuum Baffle/Wall Location	2.61 m	2.61 m
# of Shots per mapping	450	1103
Shot Duration	2 s	2 s
Helicon Data Window	0.4 - 0.5 s	0.4 - 0.5 s
ICH Data Window	0.65 - 0.75 s	0.65 - 0.75 s
Chamber Volume	150 m^3	150 m^3
Chamber Background Pressure	10^{-8} - 10^{-4} torr	10^{-8} - 10^{-4} torr
Charge Exchange mean free path (Helicon)	12.6 - 78.1 m	12.6 - 78.1 m
Charge Exchange mean free path (ICH)	1.3 - 3.2 m	1.3 - 3.2 m
Argon Pumping Speed	188,000 liters/s	188,000 liters/s
Gas Flow Sample Rate	100 Hz	100 Hz
RF Power Sample Rate	100 Hz	100 Hz
Langmuir Probe/Force Target/Pressure Sample Rate	40 kHz	40 kHz
RPA/Magnetometer Sample Rate	100 kHz	100 kHz
Langmuir Probe DC Bias	-20 V	-20 V
Guard Ring Probe Bias	-40 V - +40 V @ 70 Hz	-40 V - +40 V @ 70 Hz
RPA Discriminator Bias	-200 - +600 V @ 200 Hz	N/A
RPA Collector Bias	-30 V	N/A
RPA Primary Electron Suppressor Bias	-180 V	N/A
RPA Secondary Electron Suppressor Bias	-200 V	N/A

Table 3.1: VX-200 Magnetic nozzle experiment settings for the original experiment campaign (data set #1) and the repeat experiment campaign (data set #2).

Chapter 4: Plasma Diagnostics and Probe Theory

An experimental Investigation of plasma detachment requires the measurement and mapping of various plasma parameters in the plume using several forms of plasma diagnostics. Most of the diagnostics used in this magnetic nozzle experiment were mounted on top of the translation stage and positioned at multiple locations in the plume (Section 3.3.2). An image of the various probes used during this experiment is presented in figure 4.1. These probes, from left to right are: A retarding potential analyzer (RPA) with an articulating head, electric field probe (recessed), backup plasma momentum flux sensor (PMFS), primary plasma momentum flux sensor (PMFS), 3-axis magnetometer, swept guard ring Langmuir probe, azimuthal flux probe, ion flux probe array (lower), and ion flux probe array (upper). Each probe offset position with respect to the translation stage reference point is listed in table 4.1. Not shown is an IR heat sensor focused on the downstream side of the backup PMFS. Other diagnostics not mounted to the translation stage are an optical spectrometer, a 70 GHz microwave interferometer, and various firewire digital camcorders for filming the shots fired.

Considering many traditional plasma diagnostics are fundamentally invasive requiring physical insertion into the plasma, it is important to minimize the line-of-sight area that ‘sees’ the plasma to avoid altering the very plasma being measured. One worry is that large surface area contact with the plasma enhances the ion-electron recombination rate creating a local population of neutrals. These neutrals may then affect the amount of uncollided flux incident upon the probes (Section 3.5). In order to minimize the surface area in direct contact with the plasma, all of the probes have been offset away from the

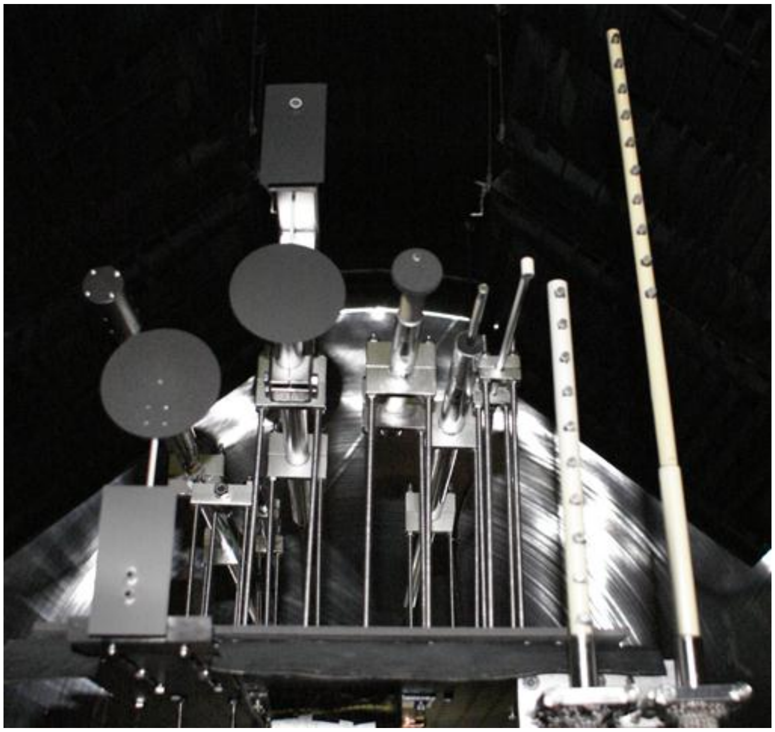

Figure 4.1: Image of plasma diagnostics mounted on the translation stage. From left to right the diagnostics are an RPA, electric field probe (recessed far back), backup PMFS, primary PMFS, magnetometer, guard-ring Langmuir probe, azimuthal flux probe, lower flux probe array, and upper flux probe array.

translation stage structure and given as much separation as possible with respect to adjacently mounted diagnostics. Each probe, with exception of the electric field probe, is mounted on a plane at an axial offset of Z = 4.2” (106.7 mm) in front of the leading edge of the translation stage. Most of the probes have also been raised above the surface of the translation stage to the central plane of the nozzle/vacuum chamber, unless intentionally positioned off-axis, using threaded rods. Taking data at high sample rates (40 kHz & 100 kHz) in these experiments will also help minimize this concern.

The rest of this chapter will focus on the probes used for the magnetic nozzle

Diagnostic	X offset (mm)	Y offset (mm)	Z offset (mm)	Angle (Deg.)
Ion Flux Probe Array (Lower)	-257.2 - 0	177.8	-106.7	0
Ion Flux Probe Array (Upper)	0 - 270	254	-106.7	0
Plasma Momentum Flux Sensor (Primary)	0	-50.8	-106.7	0
Plasma Momentum Flux Sensor (Backup)	-85.7	-0.127	-106.7	0
Magnetometer	0	50.8	-106.7	0
Guard-Ring Probe	0	101.6	-106.7	0
Retarding Potential Analyzer	0	-177.8	-106.7	0 - 90
Electric Field Probe	0	-114.3	333.4	0

Table 4.1: Listing of probe offsets with respect to the translation stage reference point. This point is located at the center of the leading edge of the translation stage.

experiment in the plume of the VX-200 device. Each section highlights the physics involved in a specific type or group of plasma diagnostics, discusses any specifics to each of the probes including design and geometry, and provides a sample of data taken along with a brief overview of the analysis methods used. It is important to establish this precedence in order to lend credibility to the resulting analysis and conclusions that are reached using the data from these measurements. The sections shall be arranged discussing each probe in the following order: Langmuir probes, force targets, magnetometer, RPA, electric field probe, and other supporting diagnostics.

Section 4.1: Langmuir probes and ion flux measurement

Section 4.1.1: Langmuir probe overview

Langmuir probes are one of the most frequently used plasma diagnostics due to their long history and simplicity. The probe dates to 1926 from the oft referred paper by Langmuir and Mott-Smith[181, 182] bearing the name of the famed scientist. In its most basic form a Langmuir probe is nothing more than a bare wire inserted into plasma where the probe is electrostatically biased with respect to the plasma potential. Different probe arrangements and circuits exist in the form of double, triple, and emissive Langmuir probes that are better suited at measuring specific plasma properties such as electron temperature, density, and plasma potential respectively. The main function of any Langmuir probe is to measure the amount of current collected or emitted as a function of the probe bias. This measurement of current versus bias results in what is known as the plasma I-V *characteristic* (figure 4.2) from which plasma properties such as electron temperature, density, plasma potential, and floating potential may be extracted.

The characteristic may be divided up into three separate regions: Electron saturation (I), transition region (II), and ion saturation (III). A negatively biased probe will collect more ion current, hence ion saturation, while reflecting electrons and vice versa for a positively biased probe. An equal number of ions and electrons are collected at the floating potential, V_f, drawing zero current. The transition region is where the

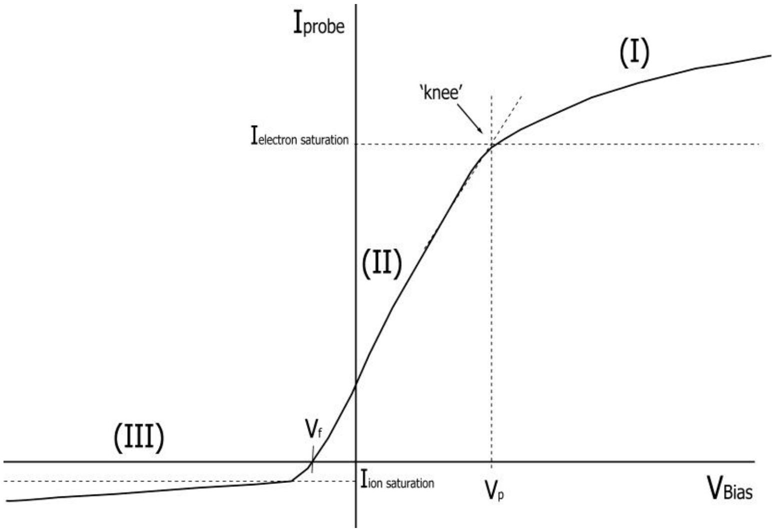

Figure 4.2: Schematic of a typical Langmuir probe I-V characteristic from measured current over a wide voltage bias range[140].

probe will effectively collect both ions and electrons. The potential where neither electrons nor ions can be accelerated into a sheath is known as the plasma potential, V_p, and is typically located at the union of the transition and electron saturation regions, or the 'knee' of the characteristic. A difference in potential between V_p and the potential at the probe surface (V_B), known as a sheath, develops and quasineutrality breaks down. The sheath is a relatively thin layer[119, 183-186]. The ion or electron current collected will depend upon the area of the sheath and saturates when the probe exclusively collects one particle species. The area of the sheath can grow by further increasing the probe bias thus allowing the collected current to increase proportionally. The mobility of the particles causes the difference in the magnitudes of the current with the more mobile electrons accounting for a much larger saturation current than the ions. An estimate of the electron temperature can be found from the I-V characteristic[183]:

$$\mathrm{T}_e = e\frac{|I - I_{ion\ saturation}|}{\frac{dI}{dV_B}} \qquad 4\text{-}1$$

which is the same as the slope of a line fit to a semi-log plot of $|I - I_{\text{ion saturation}}|$ versus V_B.

One of the main reasons for the use of plasma diagnostics and Langmuir probes in general is to be able to measure the details of the ion or electron distribution function. If the distribution function were assumed to have the same form as a Maxwellian distribution, it would be expressed as[118, 119, 187, 188]:

$$f(x, \mathrm{v}, t) = n\left(\frac{m}{2\pi kT}\right)^{3/2} e^{-\frac{m\mathrm{v}^2}{2kT}} \qquad 4\text{-}2$$

where n is the density, m is the mass, T is the temperature, v is the velocity, and k is the Boltzman constant. The first and second moments of the distribution function describe the particle number density and particle current density, respectively. These parameters may then take on a similar form:

$$n(x,t) = \int f(x,\mathrm{v},t)\,d\mathrm{v}_x d\mathrm{v}_y d\mathrm{v}_z \qquad 4\text{-}3$$

$$\mathrm{J} = \int f(\mathrm{v})\mathrm{v} \cdot \hat{n} d^3\mathrm{v} \qquad 4\text{-}4$$

The particle current density J, being the number of particles flowing per unit area, is related to the total electrical current, I, collected by a probe of area A[183]:

$$\mathrm{I} = \mathrm{eJ} = \mathrm{eA}\left(\frac{1}{4}n\mathrm{v}\right) = eA\Gamma \qquad 4\text{-}5$$

where Γ = nv is the particle flux, the number of particles per unit area per unit time.

A Langmuir probe is an invasive diagnostic in that the biasing electric potential can perturb the local plasma properties. The charge carriers within the plasma have the tendency to redistribute themselves to shield out this perturbation. This shielding is governed by Poisson's equation whose solution is dependent upon electron temperature as well as plasma density and is known as the Debye length[119, 183]:

$$\lambda_D = \sqrt{\frac{\varepsilon_0 T_e}{e^2 n_e}} \qquad 4\text{-}6$$

This equation states that the redistributed charges will shield out a perturbing electric field based on the values of the electron temperature and electron density to an approximate distance of λ_D. For the range of plasma densities (10^{15} – 10^{19} m^{-3}) and electron temperatures (2 eV – 6 eV) seen in this experiment, we can expect the Debye length to vary between 3 μm and 575 μm. It is within λ_D that charge neutrality breaks down and a potential difference, hence electric field, forms creating a plasma sheath. The sheath will be a few Debye lengths wide as the electrostatic potential will transition from the probe potential to the plasma potential. Ions incident upon the probe will enter the sheath giving rise to a current known as the Bohm current[183, 184]:

$$\mathrm{J}_i = n_i q A_s \sqrt{\frac{qT_e}{m_i}}\, e^{-1/2} \qquad \text{4-7}$$

where A_s is the effective area of the probe sheath. If the electron temperature can be extracted from the I-V characteristic, the plasma density can then be estimated by equating the measured probe current to the Bohm current despite possibly lacking information on the ion velocity.

There are some effects that can alter the analysis of the simple Langmuir probe theory listed above and should be taken into account. These effects are most notably due to collisional plasmas, magnetized plasmas, and plasmas created using RF sources. Collisional plasmas require the particles diffuse to the probe collector rather than reaching it by free flight. The parameter governing this effect is the collisional mean free path, may be defined as $\lambda_{MFP} = D_{\parallel}/v_{ti}$, where $D_{\parallel}$ is the parallel diffusion coefficient and v_{ti} is the ion thermal velocity. Comparing the collisional mean free path to the probe dimension provides a rule of thumb. If $\lambda_{MFP} >> r_p$, then collisions are considered negligible, but in the case that $\lambda_{MFP} << r_p$ current drawn by the probe will be reduced by the factor of λ_{MFP} /r_p and the equations governing the sheath physics such as the Child-Langmuir current and sheath thickness require modification[183]. Collisional mean free paths in this experiment have been estimated, dominated by electron→electron and electron→ion collisions, to range from 3 mm to 26 mm during Helicon operation and from 30 mm to 55 mm during ICH operation. The mean free paths for the other particle interactions are much longer on the order of meters. All of the Langmuir probes utilized in this experiment have a radius of 3.18 mm. Comparing this to the collisional mean free paths indicate that collisions may be considered negligible for the purposes of data analysis.

Magnetized plasma can alter the effective collecting area of the probe/sheath. Ions and electrons bound to the magnetic field lines would limit the probe to collecting current from particles whose flux tube lies within a projected area ($A_{projected} = \pi(r_{sheath} + r_{Larmor})^2$). This includes particles either created within the magnetic flux tube or diffused across the field lines into the flux tube. This effect would tend to decrease the current drawn by the probe and require the exponential in equation 4-7 (~ 0.61) be replaced/modified to 0.49[183, 184]. The same arguments apply to collimated or flowing plasma. For this experiment, which studies the transition from magnetized plasma to ballistic non-magnetized plasma, the density computed using the Bohm current (equation 4-7) has been modified to incorporate the corrected factor of 0.49.

Langmuir probes inserted into RF plasmas can easily be misinterpreted. RF sources can cause the plasma potential and floating potential to fluctuate as the RF voltage capacitively divides across the plasma. The probe data is then mistaken as the oscillations average out resulting in a higher V_p, and thus T_e, than in a similar non-RF plasma[189]. Probes intended for higher accuracy measurements of plasma potential and electron temperature should be designed with RF compensation[190].

Probes biased solely in ion or electron saturation are negligibly affected by RF oscillations. None of the Langmuir probes used in this magnetic nozzle experiment were

RF compensated as all probes, except the swept guard-ring probe, were biased into ion saturation. An attempt to quantify this effect was made using an oscilloscope to measure the magnitude of fluctuations in the floating potential for the guard-ring probe (section 4.1.3). These fluctuations were measured previously[153] for this exact probe where RF compensation was not used as it can result in shifts in the measured plasma and floating potentials. It was found that the floating potential had a ±0.2 V pk-pk signal during Helicon operation and a ±4.0 V pk-pk signal with the addition of ICH. This translates to an uncertainty in the electron temperature of ±0.3 eV during Helicon and ±3.2 eV during ICH. Propagating this uncertainty using the Bohm current formula (equation 4-7) the uncertainty in density is ±4% for the Helicon and ±20% for the ICH. These values are typically acceptable for swept, non-RF compensated and invasive plasma probes. Since this uncertainty is an estimate, the plasma density can be better bounded using non-invasive plasma diagnostics to verify the values measured by the guard-ring probe. One such non-invasive diagnostic is a 70 GHz microwave interferometer (MWI) and is considered to provide a more reliable measurement of plasma density than swept Langmuir probes. The problems in strictly using an MWI to map the electron density are that they are more expensive and difficult to implement on devices such as the translation stage. More details will be given about the MWI in section 4.6.

Section 4.1.2: Ion flux probes

The majority of the Langmuir probes used in this study were constantly biased to -20 VDC, well into ion saturation with the intent to collect only ions. These ion flux diagnostics consisted of two probe arrays (figure 4.1), each array positioned to measure the ion current above and below the axial plane of the chamber/nozzle. The upper probe array was positioned at a Y offset of +10” (254 mm) with respect to the translation stage coordinate reference while the lower probe array was offset to Y = +7” (177.8 mm). Both arrays were positioned on the same axial Z plane; offset -4.2” (-106.7 mm) with respect to the Z reference plane of the translation stage (leading edge). This information is summarized in table 4.1. Each probe array consists of ten 0.25” planar disk Langmuir probes featuring a terraced design[140] (figure 4.3) that have been used with good results.

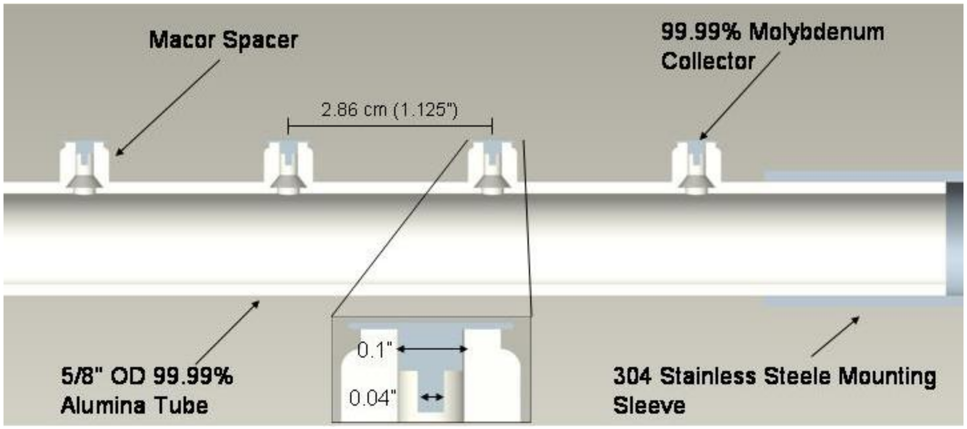

Figure 4.3: Lower ion flux probe array cross-section[140]. Both probe arrays are nearly identical with the exception that the upper probe array collectors are spaced 3 cm apart along a 0.5” OD tube. The collector disks are brazed to the signal wire and potted into the Macor™ spacers as well as the alumina tube using Varian Torr-Seal ceramic adhesive.

Each probe disk was machined out of high purity molybdenum, a common Langmuir probe material, selected for its high melting point, general machinability, and reasonable sputter yield (0.63)[119, 140, 191-193]. RF plasma sources impinging upon metal-to-ceramic joined surfaces can produce arcs or small static discharges across these small gaps in RF breakdowns. The ‘top-hat’ design minimizes this interaction by effectively increasing the gap distance between the ceramic and molybdenum collector. The insulating shaft is made out of high purity alumina (99.99% pure) while the spacers are fabricated out of Macor^{TM}, an easily machined ceramic. The signal for each planar probe was fed out of the vacuum chamber using an RG-188 coaxial cable and through well-shielded LEMO® or Fischer Connectors® feedthroughs.

The electric circuit for each Langmuir probe channel, including the swept guard-ring probe, is a variant of the simplest Langmuir probe circuit[119, 184, 185, 194]. The complete printed board circuit is displayed and described in greater detail in Appendix B. A convenient quantitative parameter used with ion flux probes is the measured current density. The current density is calculated from the signal when the probes were biased into ion saturation; measured as the voltage drop across a precision gain resistor over the area of the probe:

$$\mathrm{J}_i = \frac{V_{signal}}{R_G A_p} \tag{4-9}$$

The gain settings were selectable between 1, 10, 100, and 1000 Ω resistors whose values were measured to 0.1% with a milli-ohmmeter, tabulated, and stored in the MDSPlus database. The logarithmic scaling permitted a wide range of measured current densities in the plume. For a 0.25” diameter probe the maximum and minimum current densities measured ranged from 4000 A m^{-2} down to 0.05 A m^{-2}. An example of the signal versus time for one of these probes is shown in figure 4.4. The graph shows a raw data trace as the voltage measured across the gain resistor as well as the result filtered with a 50 sample wide boxcar filter. Details of the RF power profile can be seen in the probe voltage as the Helicon power begins at 275 ms and reaches the full 30 kW at 350 ms. The erratic signal is indicative of instabilities in the plasma which are calmed as ICH power is applied at 575 ms. The power, gas flow, and ion current are stable for the duration of the ICH power. The instabilities return for a brief period as the ICH shuts off and returns to solely Helicon operation at 1175 ms. The mapped data for both power levels are averaged for every shot during the respective time windows listed in chapter 3 (0.4 – 0.5 s for Helicon and 0.65 – 0.75 s for ICH). The current density is then computed according to equation 4-9 and tabulated creating a matrix of current densities vs. spatial positions. Further analysis using the current density, which includes fitting routines and numerical integration, will be discussed in chapter 5.

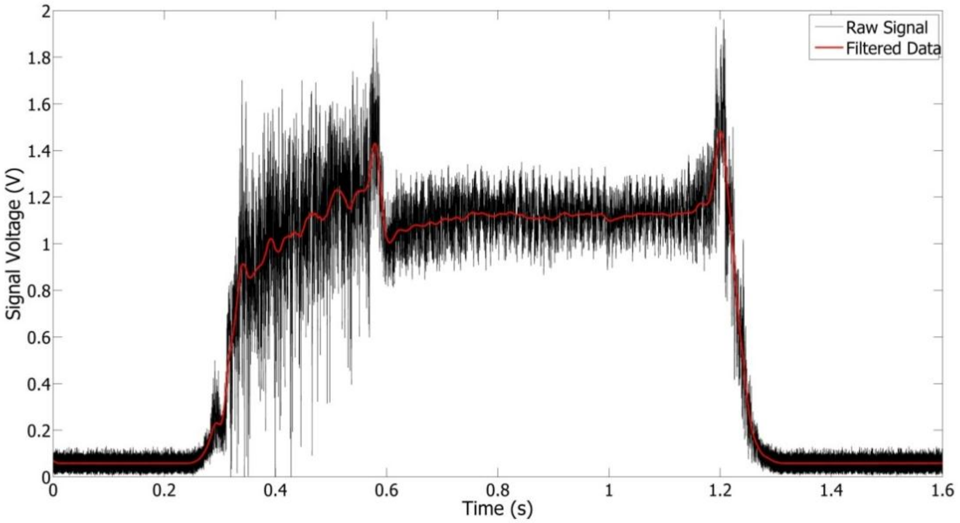

Figure 4.4: Signal from one of the upper flux probe array collectors biased at -20 VDC. The collector was located on the nozzle centerline (Y = 0 m) and at the closest axial position (Z = 2.79 m). The signal was passed through a 10 Ω sense resistor.

Section 4.1.3: Guard-Ring probe

The variable bias Langmuir probe used in this experiment is a guard-ring probe. One of the issues surrounding swept Langmuir probes is that the probe sheath expands with increasing bias voltage never allowing the current to ideally saturate. Guard-ring probes use a metal ring/cylinder around the collector to limit or cap the expansion of the sheath as the bias is increased and have been used with positive results on spacecraft[194]. A cross-section drawing of the guard-ring probe used in this experiment is shown in figure 4.5. The same probe has been used in RF plasma sources previously with good success[153].

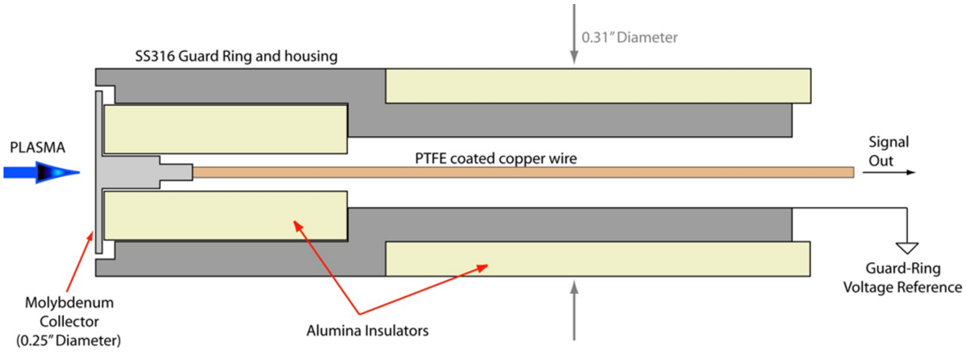

Figure 4.5: Cross section diagram of the guard-ring probe used in this experiment. Langmuir probes with guard-rings minimize radial sheath expansion. The collector uses the same 'top hat' design as the ion flux probes.

The collector is made out of high grade molybdenum and is of a similar design to the ion flux probe collectors. The collector is isolated from the stainless steel guard-ring using an alumina bead. The gap between the guard-ring and collector is 0.005 inches. A second alumina tube is used to isolate the guard-ring from the translation stage mounting hardware giving users the ability to control the guard-ring bias, although it was referenced to ground of the biasing power supply for the entirety of the experiment. The signal and guard-ring reference were led out of the chamber on PTFE coated, twisted-shielded pair wire. The probe was located at a Y offset of 4" (101.6 mm) with respect to the translation stage Y reference and a Z offset of -4.2" (-106.7 mm) to the Z reference, as listed in table 4.1.

The electronic circuitry is identical to the other ion flux probes mentioned in section 4.1.2. The electronic circuit is described in greater detail in Appendix B. The bias voltage ranging from -46 V to +48 V was supplied by a Kepco BOP-100-4 bipolar power supply and swept using the triangle wave output at a frequency of ~ 70 Hz from a typical function generator. A sample of the bias voltage sweep and collector signal presented in figure 4.6.

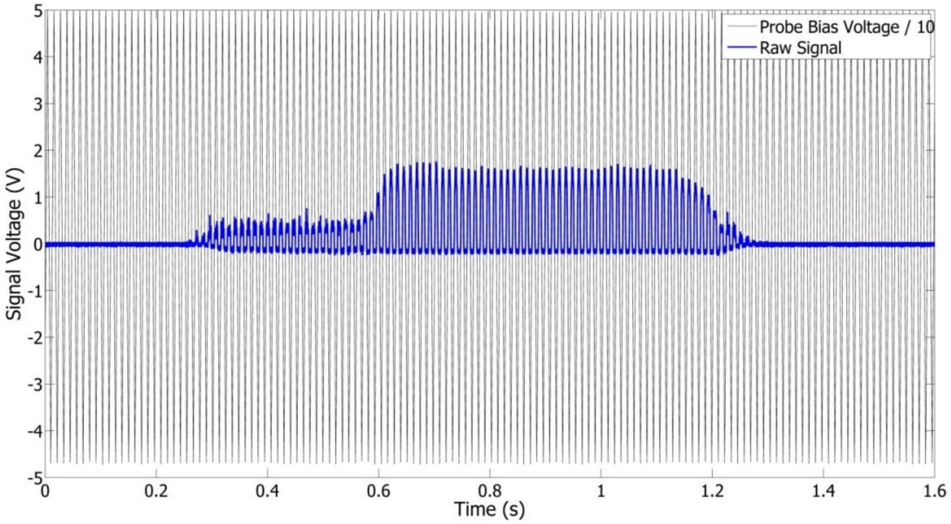

Figure 4.6: Example signal from the guard-ring probe swept at ~ 70 Hz between -46 V to 48 V. The DAQ has a range of ±10 V so the voltage bias must be sent through a 10:1 voltage divider prior to digitzation.

Similar to the sample signal from the ion flux probes (figure 4.4), the RF power profile can be seen in the raw signal from the guard-ring collector. The Helicon power phase begins at 275 ms and reaches the full Helicon power (~30 kW) at 350 ms. The ICH stage begins at 575 ms reaching full power (~100 kW total) from 625 ms to 1125 ms before returning briefly to Helicon only. The electron current increases by more than a factor of 2 when ICH is initiated. The data time-windows again are 0.4 – 0.5 s for

Helicon and 0.65 – 0.75 s for ICH. A zoomed in view for this shot during ICH is displayed in figure 4.7 with the collector signal converted from digitized voltage into current. Both the measured bias voltage and current are filtered using a low-pass Butterworth filter of order 8 and a cutoff frequency of 1 kHz. It was determined that a Butterworth filter provided the best gain versus frequency response in terms of flatness and cutoff frequency as opposed to other linear filters. The results are then sorted according to bias voltage and plotted in figure 4.8 showing the I-V characteristic.

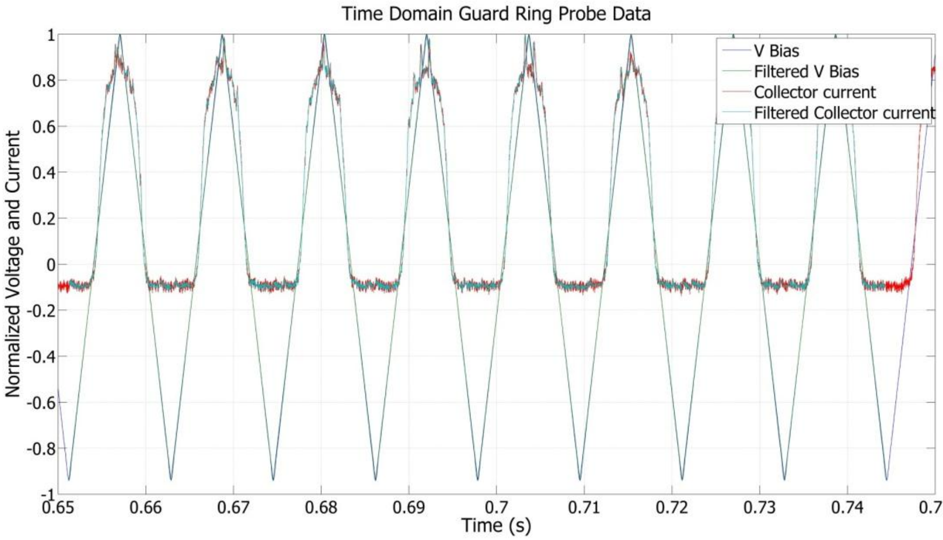

Figure 4.7: Data zoomed in and normalized from figure 4.6 for the ICH data window including the filtered signals which use an 8th order Butterworth filter.

The general trend is clear with the knee around 16 – 17 V but the logarithm of the current must be taken before accurately knowing the plasma potential. Both the linear and semi-log characteristics are plotted in figure 4.9. The linear characteristic also displays an averaged trace with uncertainty bounds based on the standard deviation over all the sweeps in the time window. In the semi-log plot of the current, the linear portions

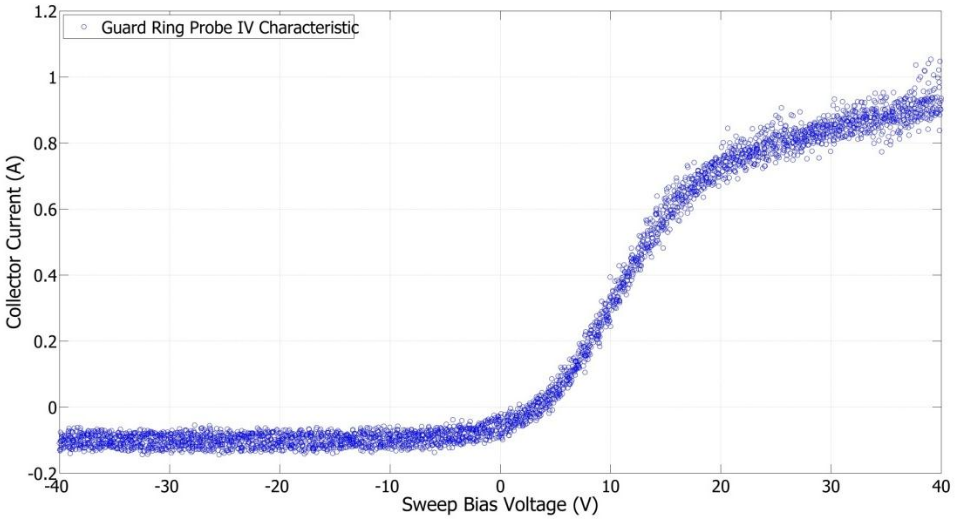

Figure 4.8: Guard-ring probe I-V characteristic from the ICH data window (0.65 s – 0.75 s) of the signal shown in figure 4.6. The data have been filtered and sorted according to bias voltage. The overall trend is clear and each region including the 'knee' is easily identified.

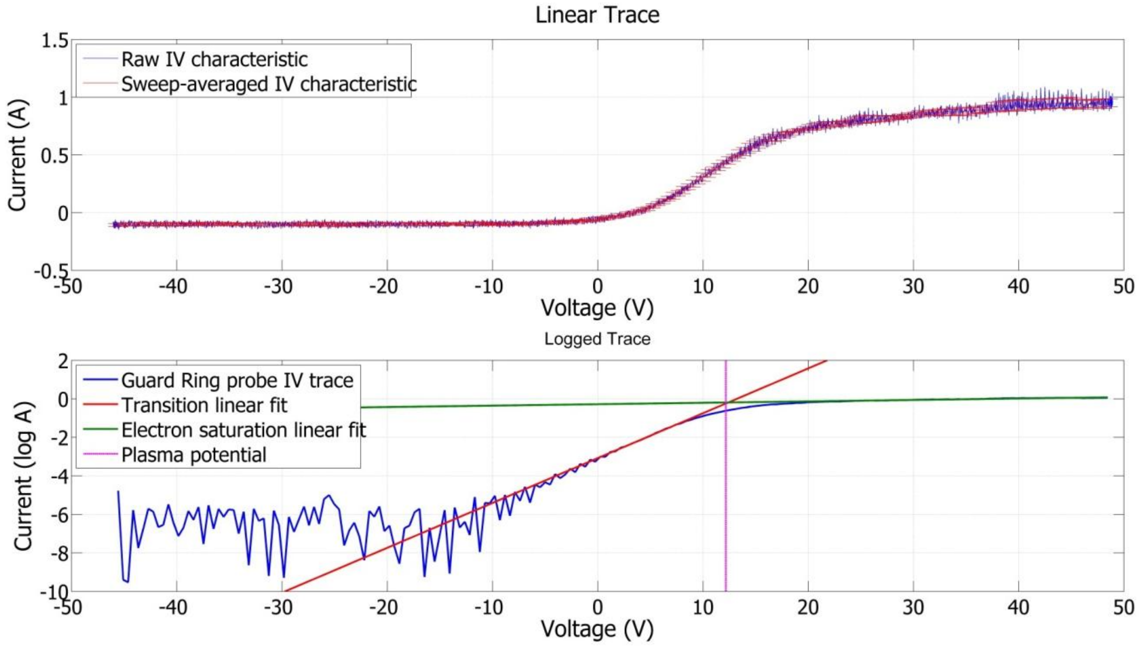

Figure 4.9: (*top*) Guard-ring probe I-V characteristic including the sweep-averaged value with vertical error bars. (*bottom*) Semi-log plot of the characteristic with lines fit to different regions to find the plasma potential and solve for the electron temperature.

of the transition region (figure 4.9 *bottom*, red line) and electron saturation (figure 4.9 *bottom*, green line) region are user selected. The intersection of these lines reveals the plasma potential to be ~12 V (Figure 4-9 *bottom*, pink line). The slope of the red line is used to compute the electron temperature according to equation 4-1. This temperature is inserted into the Bohm current (equation 4-7) to compute the electron density. This process is repeated for each time window for every shot in the experiment and tabulated/recorded according to probe location.

Section 4.2: Force density measurement

An interesting quantity to measure when exploring plasma detachment from a magnetic nozzle is momentum flux, or force density. While electrostatic probes are useful in measuring charged particle flows in plasma, the data can be skewed by charge-exchange. Momentum flux probes can measure fluxes from both neutral and charged particles in flowing plasma. This quantity used alongside the ion flux measurements can confirm the integrated ion trajectories that may show detachment as well as differentiate whether the flow is recombination or charge-exchange detached. The concept of using a momentum flux paddle began with Chavers, et. al., with the intent of using the probe in magnetized plasma[195, 196]. The paddle probe could be used to infer thrust when placed in the plume of an electric thruster. Many electric thrusters utilize some mechanism to measure the thrust or total integrated momentum exiting the device, most commonly an inverted pendulum thrust stand. The Plasma Momentum Flux Sensor (PMFS) used in this experiment had been previously tested in conjunction with a thrust stand and found to agree to within 2.8%[197]. Similar targets have been used in other plasma plumes[198].

The momentum flux at the surface of the target can be computed using the momentum equation[196]:

$$\frac{d}{dx}(m_i n_i \mathrm{v}_i^2 + p_i + p_e + m_n n_n \mathrm{v}_n^2) = 0 \qquad 4\text{-}10$$

where the last term in the left hand side is the energy from fast neutrals resulting from charge-exchange. The drift electron energy is neglected since the thermal velocity is larger (up to ~ 10^2) than the drift velocity. Since the target disk is floating, the sheath electric field will reflect most of the electrons leaving $p_e \approx 0$. From the conservation of momentum flux the change in momentum of the target disk will be equal to the plasma parameters just upstream of the sheath, which is the net force on the target given by[196]:

$$F = A_p(n_e k_B T_e + m_i n_i \mathrm{v}_i^2 + m_n n_n \mathrm{v}_n^2) \qquad 4\text{-}11$$

where the force caused by the surface charge density of the target is equal and opposite to the change in momentum of the sheath electric field. Thus it is expected that the momentum flux will deviate from the ion flux when charge-exchange or other interaction with neutrals start to become non-negligible.

The PMFS uses uniaxial strain gauges to measure the force imparted by plasma incident upon a target disk. The concept is drawn in figure 4.10a. A 9 cm diameter (0.8 mm thick) graphite disk is attached to a titanium beam with an 11.65 cm long square (3.1 mm x 3.1 mm) shaped alumina rod. Any deflection of the disk causes a buildup of the bending stress, σ, given by[196]:

$$\sigma = \frac{My}{\mathrm{I}} = \frac{FLy}{\mathrm{I}} \qquad 4\text{-}12$$

$$\mathrm{I} = \frac{bh^3}{12} \tag{4-13}$$

where M is the bending moment, F is the force from the plasma, L is the length of the alumina shaft, y is the deflection, and I is the moment of inertia over the area (b*h) of the titanium beam. The bending stress is converted into strain using Hook's law:

$$\epsilon = \frac{\sigma}{E} \tag{4-14}$$

where E is Young's tensile modulus and for titanium is $1.14\text{x}10^{11}$ Pa. Strain is concentrated by adding holes (figure 4.10b) to reduce the dimensions of the moment of inertia from b = 12.7 mm to 2 mm (h = 1.6 mm). This gives a reduced moment of inertia $I \approx 6.83 \text{ x } 10^{-13} \text{ m}^4$. Assuming a force of 10 mN and a deflection of 0.8 mm, $\sigma \approx 1.23$ MPa which gives a presumed strain of $\varepsilon \approx 11.97$ microstrains (1 microstrain = strain of

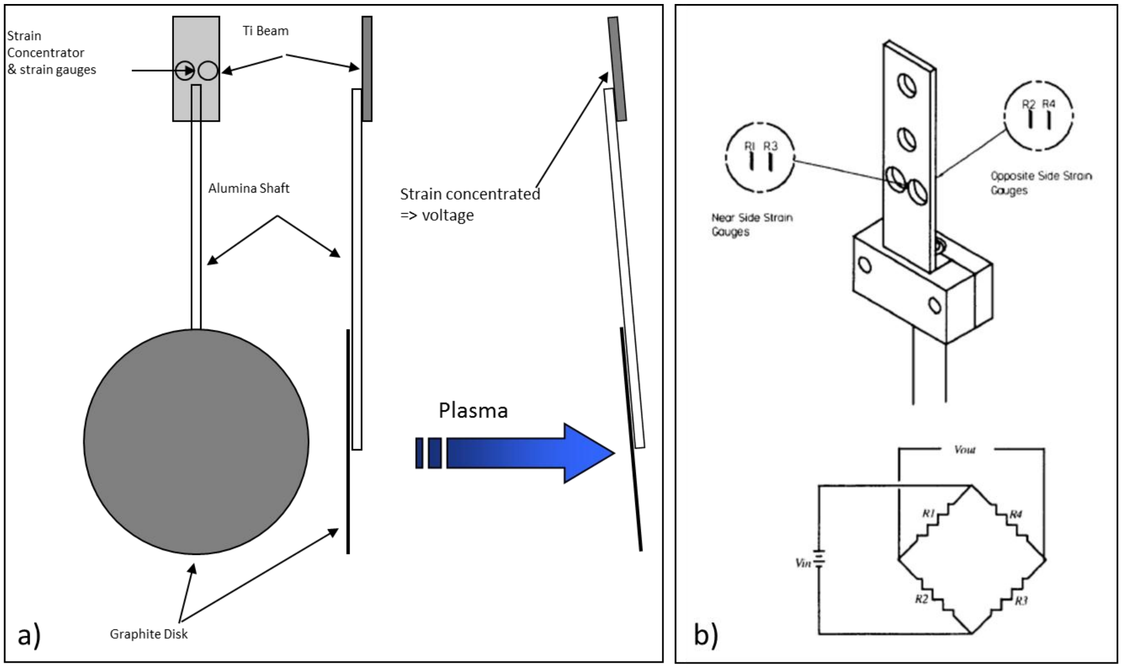

Figure 4.10: a) Concept drawing of the Plasma Momentum Flux Sensor (PMFS). The force from plasma and neutrals incident upon the graphite disk causes the pendulum to bend and induce strain in the titanium isthmus. b) The strain is concentrated and the output voltage is measured using miniature strain gauges arranged in a Wheatstone bridge configuration. Courtesy of D. Chavers[196].

10^{-6} meters/meter). Then it would be expected that a force of 1 mN will produce a strain of 1.2 microstrains. The use of this relation depends upon an accurate measurement of the deflection, which is difficult for these small ranges of deflection. Instead strain is measured from the voltage output from strain gauges.

There are four strain gauges, made of Czochralski pulled boron doped silicon, connected in a Wheatstone bridge configuration (figure 4.10b). The output voltage is related to the input voltage by[196]:

$$V_{out} = V_{in}\left(\frac{R_3}{R_3 + R_4} - \frac{R_2}{R_1 + R_2}\right) \qquad 4\text{-}15$$

The input voltage is supplied and regulated by a Micron meter strain gauge readout, manufactured by Micron Instruments, who also produced the strain gauges. Although the strain gauges themselves are shielded from the plasma flow, the Micron meter also provides thermal compensation to account for voltage drift as the strain gauges become hot. Any change in resistance due to strain is governed according to[196]:

$$\Delta R = GR\epsilon \qquad 4\text{-}16$$

where G is a constant known as the gauge factor (~ 155) and R is the resistance of the strain gauges which at room temperature and under no stress is 1125 Ω.

Since the measurement of the momentum flux on the target produces an output voltage and not a measure of the actual deflection, calibration is required to correlate the output voltage to the incident force. This calibration was performed prior to the experiment using a fixture that mounted onto the translation stage. The fixture converted gravitational force, from very small precision masses (0.5 g – 50 g), into a line tension connected to the rear of the graphite target similar to a weight/pulley system. The weights were able to calibrate the primary PMFS to a force range of 0.9 – 491 mN. The calibration curve is displayed in figure 4.11 and is shown to be linear with an uncertainty under 2%. Using the calibration curve:

$$\mathrm{F} = 1.7745V_{signal} - 0.0011\,N \qquad 4\text{-}17$$

the measured signal from the Micron meter is filtered by a 20 sample wide boxcar filter, converted into Newtons, which is then converted into momentum flux by dividing by the area of the probe before being tabulated according to probe position.

A sample of data is presented in figure 4.12 when the probe was positioned at a (Y, Z) of (0 m, 2.79 m). This data is from the primary PMFS. Two momentum flux sensors were used during the experiment, although only the data from the primary PMFS will be used. As shown in table 4.1, the primary PMFS is positioned on the translation stage at a Y offset of -2” (-50.8 mm) and a Z offset of -4.2” (-106.7 mm) with respect to

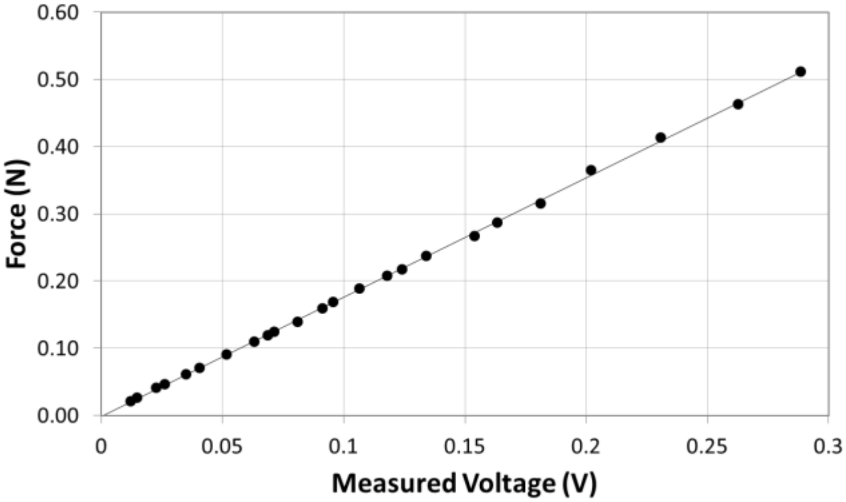

Figure 4.11: Force calibration curve for the primary PMFS. The linear fit correlating force end to end with measured voltage on the data acquisition system is displayed in equation 4-17.

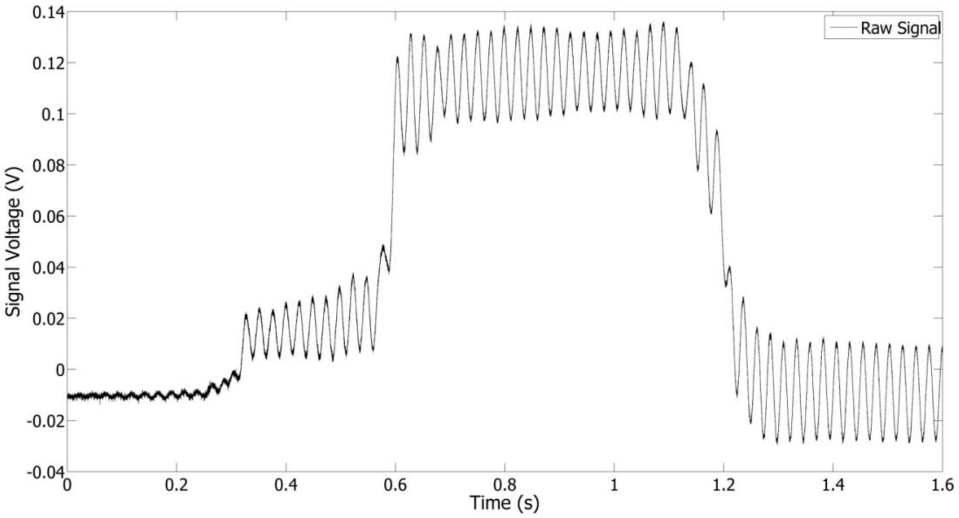

Figure 4.12: Sample data from the primary PMFS. The ringing in the signal is a function of the length and rigidity of the alumina shaft. The ringing continues after the shot is over becoming damped out before start of the subsequent shot.

the table reference point. The secondary PMFS is located at an offset of -5” (-127 mm) in Y, and -4.2” (-106.7 mm) in Z, but is positioned below the central plane at X = -3.375” (-85.7 mm). As reflected in the Langmuir probe raw data, the RF power profile is evident in the PMFS signal although the gas flow is detected prior to any RF power being delivered to the couplers. Also important to these types of probes is the natural frequency of the sensor which is determined by the size of the target disk, length of the alumina shaft, as well as the stiffness of the shaft. The natural frequency for this probe is ~ 40 Hz giving a time resolution of 25 ms. Despite this limitation it is still proper practice to average over at least 3-4 periods, if not many more. This ‘rule of thumb’ is satisfied by the 100 ms long Helicon and ICH data windows with approximately 4 pendulum periods.

Section 4.3: Magnetic field measurement

Magnetic fields in plasma are measured in a variety of ways ranging from inferring the magnetic field strength based on how the field deflects the motion of charged particles to measuring the amount of spectral broadening to sampling the amount of current induced in a coil of wire. A mass spectrometer tuned to a specific particle mass can measure the deflection of particles and correlate this to the field strength. Another type of device that relies on charged particle deflection is the Hall Effect sensor. Hall sensors are solid state devices where current flows across a pnp junction. When a magnetic field is perpendicular to the face of this semi-conductor, the charges in the flowing current experience a deflecting Lorentz force creating an electric potential across the sensor proportional to the field strength. Spectral measurements can reveal broadened absorption and emission lines from Stark and Zeeman effects as a result of charged particles interacting in a magnetic field. These previous mechanisms for measuring magnetic fields work well for measuring the vacuum field including any changes in the field during plasma operation. The method of using a coil of wire are useful only when the field is changing or there is a steady current (from the plasma) and are based on the total magnetic flux being proportional to an induced current. A Rogowski coil is an example of a very simple device that measures the magnetic field from the induced current as a result of plasma flow through the center.

The magnetic field measurements in this experiment were made using a 3-axis Hall Effect probe made by F. W. Bell. The magnetometer is a model 7030 Gauss/Tesla Meter using a ZOF73-3208-30-T 3-axis Hall probe. The Hall sensor elements are arranged orthogonally at the end of an 8” long plastic structure housed within an aluminum fixture (figure 4.13). According to manufacture specifications the measurement range for each Hall sensor is 0 to 30 kG with a resolution of 0.1 mG and is accurate to within 2%. The sensors are temperature compensated correcting for a typical -0.05% / °C change. The magnetometer itself was thermally protected from the plasma being mounted inside of a round capped alumina sleeve and shadowed by a 1.5" diameter graphite disk. The temperature of the probes never exceeded 40 °C. The mounting offsets for the magnetometer were +2" (50.8 mm) in the Y offset and -4.2" (106.7 mm) in the Z offset of the translation stage as listed in table 4.1.

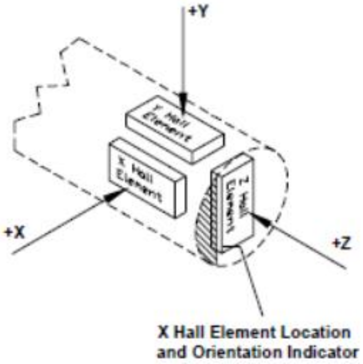

Figure 4.13: Layout of the Hall Effect sensors in the magnetometer probe[199] (Courtesy of F.W. Bell)

The magnetometer electronics unit featured two analog output modes: uncorrected and corrected output. The uncorrected output is representative of the magnetic flux density as measured by the Hall probe. The corrected analog output features additional compensation for temperature, frequency variations, and effects from non-linearity inherent in Hall probes. For this reason the corrected output is listed as higher accuracy than the uncorrected output up to a frequency bandwidth of 200 Hz (due to filtering electronics). The uncorrected output is used for higher frequency response measurements up to 50 kHz. For this experiment the uncorrected output was sampled at 100 kHz to satisfy the Nyquist criterion and search for fluctuations up to 50 kHz. The corrected output was sampled at the lower 40 kHz sample rate. The analog output is set to 0 – 3 V full scale and the range settings are logarithmic in that the conversion from signal volts to magnetic field strength is[199]:

$$B = V_{signal} B_{scale} \tag{4-18}$$

$$B_{scale} = \begin{cases} 10\ G/V \\ 100\ G/V \\ 1000\ G/V \\ 10000\ G/V \end{cases} \tag{4-19}$$

In addition to the accuracy of the probe, the accuracy of the analog output must also be considered given the signal conditioning that takes place in the electronics. The manufacture states the accuracy of the corrected analog output is certain to ±0.15% while the uncorrected analog output is 0.25% ±40 mV. The overall uncertainty in the magnetometer data for this experiment is then ±2.15% for the corrected analog output. The uncorrected output can have more extreme uncertainty in regions where the signal is weak; up to 100% for the uncorrected B_y axis and up to 40% for the uncorrected B_z axis. In normal signal regions the uncorrected output uncertainty ranges up to 11% for the B_y axis and 5% for the B_z axis. For this reason the uncorrected signal data was not used except to explore high frequency magnetic phenomena (up to 50 kHz).

Analysis of the magnetometer data from the first dataset revealed a malfunction in the B_z sensor of the magnetometer probe. This malfunction made it necessary to have the manufacturer calibrate the sensor and retake the magnetic field data. The 3-axis probe, full cable assemblies, and electronics were calibrated to the ISO/EIC 17025 standard which is the highest, most rigorous, and most legally traceable calibration standard offered for this instrument. The original tests with near identical (slightly lower gas flow rate) experiment settings were repeated at a higher spatial resolution (figure 3.12) with fully functional magnetometer sensors.

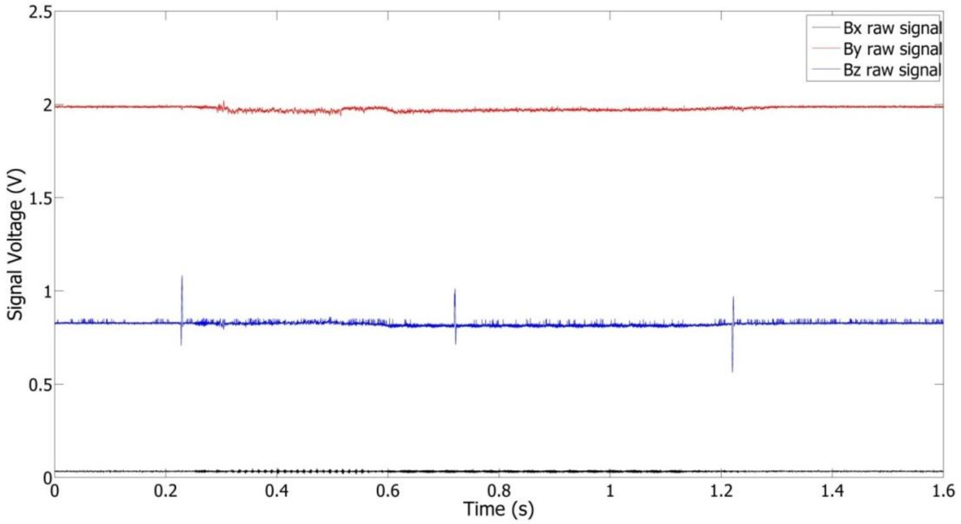

Figure 4.14: Example of raw data output from each Hall Effect sensor in the magnetometer. The signal is from the corrected analog output for a random shot in the map.

Representative data from the magnetometer is displayed in figure 4.14 for one of the shots in the map. The RF power profile is more difficult to distinguish from the data but small signal changes can be seen starting at around 325 ms when power to the Helicon is initiated and ends at ~ 1200 ms after all RF power has been shut off. For this particular shot the plasma does not influence any large-scale DC magnetic field changes. Given that the magnetometer was mounted on the horizontal plane bisecting the nozzle, the B_x axis data stays near zero for all practical purposes. The DC data are filtered using a 50 sample wide boxcar averaging filter and averaged over each data time window prior to being tabulated and stored according to (Y, Z) position for every shot in the map.

Section 4.4: Retarding potential analyzer

A Retarding Potential Analyzer (RPA) is a device that falls into the class of gridded energy analyzer, an electrostatic probe that can be used to gather information about the ion distribution function (equation 4-2); much like a Langmuir probe is used to measure properties of the electron distribution function. Some gridded analyzers employ a single grid that may be used to selectively repel particles while a collector measures the current that is permitted to pass through. The grid potential that completely repels or retards the particles, ions in this case, is referred to as the retarding potential. The single grid approach can have issues with secondary electron emission that can alter the measurement and introduce uncertainty.

One solution is to use multiple grids in the probe as shown in a schematic of the RPA used in this experiment (figure 4.15). The first double grid is biased negatively to repel all electrons from the incident plasma and is known as the primary electron suppressor. This repulsion results in an ion beam, and thus a space-charge limited region, between the first and second double grids. The sweep grids, or discriminator, are swept in bias voltage so that ions with energies less than the grid potential will be repelled while those with energies in excess of this potential are permitted to pass through to the collector. This current and discriminator voltage when plotted against each other will produce an I-V characteristic similar to a Langmuir probe but without the saturation regions. A third set of grids, known as the secondary electron suppressor, are biased negatively and are needed to repel secondary electrons liberated during particle collisions with the primary suppressor and sweep grids. The collector, made out of molybdenum, is biased to -30 VDC to collect ion current.

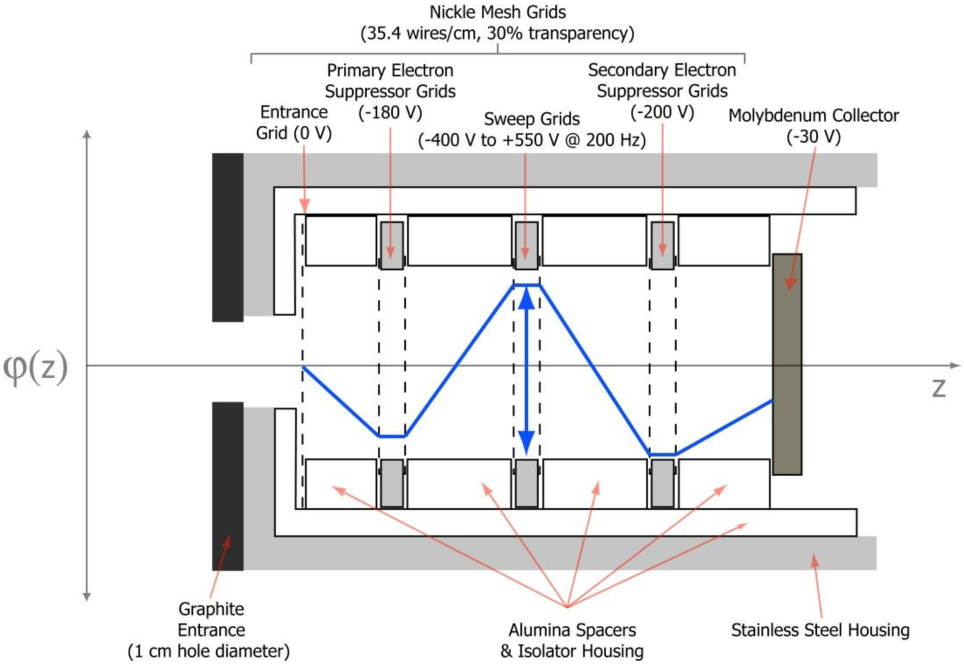

Figure 4.15: Schematic of the RPA used in the experiment. This RPA was designed by Dr. E. A. Bering of the University of Houston and his research group. A graph of the electric potential versus relative distance in the RPA head is overlain.

The wire spacing of the nickel-mesh electron suppressor is an important parameter as the Debye length (equation 4-6) must be greater than the wire gap or else the plasma will electrostatically shield out these grids entirely. Some common ways to accomplish this requirement are to use very fine mesh, decrease the incident density using attenuation grids, or a combination of both as were used for this case. A mesh density of 35.4 wires/cm has a 0.28 mm wire gap. This suggests that the electron density, for 2 – 11 eV plasma, would have to be reduced to $1.4 \times 10^9 - 7.7 \times 10^9$ cm^{-3} in order to effectively screen out electrons. This reduction is accomplished using a graphite entrance orifice and a pair of attenuation grids. The practice of using of double grids and a large negative bias can help alleviate the Debye length to wire gap requirement[200]. As mentioned above, quasineutrality is violated between the primary electron suppressor and sweep grids in the form of a space-charge limited ion beam. The space-charge effects will change the electric potential so that it may become larger than the greater or smaller than the lesser of the sweep grid potential limits. If this occurs the ions may be unexpectedly repelled causing erroneously lower ion current than would be anticipated. To minimize this effect the spacing between the grids should satisfy a condition based on ion energy and density[172]:

$$L \leq \sqrt{\frac{4}{9}\frac{\varepsilon_0 E_i}{e^2 n}} \qquad \text{4-20}$$

This criterion, derived by Green[201] and reiterated by Glover[172], state that the grid spacing to minimize space-charge related effects should be less than the square root of the ratio of ion energy to plasma density. Assuming ion energies up to 500 eV at densities on the order of $1\text{x}10^9$ cm^{-3}, L ≈ 3.5 m; the 1.5 mm grid spacing used for this probe is more than sufficient to bridle charge-limited errors. The grids are isolated from each other using alumina spacers and are also isolated from the RPA body and mounting hardware using an alumina sleeve. Signal and control voltages are fed out on RG-188 coaxial cable and twisted-shielded cable bundles, respectively.

Due to the low densities reaching the collector, measuring current at such reduced levels, ranging from microamps to a few tens of microamps, is difficult using common current to voltage converters; such as the Langmuir probe circuit mentioned above. A preamplifier circuit is necessary to measure currents of that range. A transimpedance amplifier is a useful circuit having zero input impedance that measures the current while proportionally amplifying an output voltage. The transimpedance circuit used for this RPA is discussed in greater detail in Appendix B.

An RPA will measure discriminated current based largely on the direction the entrance to the probe is facing. Should the probe be aligned with the magnetic field for magnetized plasma or along the axis of flow the RPA will measure the parallel velocity distribution. Likewise if the RPA is rotated orthogonal to the primary flow axis or magnetic field, the probe will measure the perpendicular velocity distribution function. The RPA used in this experiment is unique in that the probe head containing the biasing grids and collector have been mounted on a gear driven goniometer (figure 4.16). The angle that the RPA faces is controlled by a step motor that rotates a worm gear located at a pivoting joint that turns the probe. The probe head then has an angular range/resolution from 0° - 90° ±0.1°. This articulation permits a full measure of the magnetic nozzle effect in the conversion of perpendicular particle gyromotion into bulk parallel flow, hence the efficiency of the nozzle. To accommodate for the additional space required to pivot the probe head, without interfering with other diagnostics, the RPA could only be placed on the far left edge of the translation stage at a Y offset of -7” (-177.8 mm) and Z offset of -4.2” (-106.7 mm) as summarized in table 4.1.

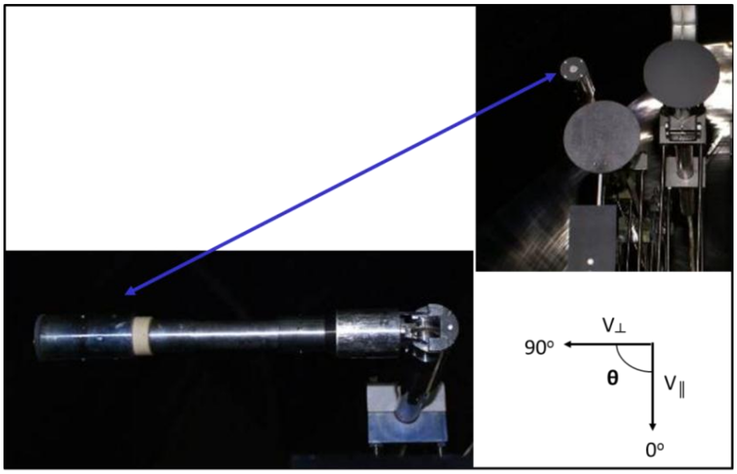

Figure 4.16: The articulating RPA can pivot the sensor head precisely up to 90° to measure both components of the ion velocity. Views of both of those position extremes are demonstrated.

The collected current is related to the velocity distribution function by means of the differential current measured by the collector[172]:

$$dI(\mathrm{v}) = n_i q A \eta \mathrm{v} f(\mathrm{v}) d\mathrm{v} \qquad \text{4-21}$$

where n_i is the ion number density, q is the electric charge, A is the aperture area of the probe, η is the net transmission of the grids, and f(v) is the distribution of velocities entering the probe. In terms of the discriminator potential, V_R, and the ion energy distribution, the characteristic can be defined as[172]:

$$I(V_R) = n_i q A \eta \sqrt{\frac{2q}{m_i}} \int_{V_R}^{\infty} \sqrt{V_R}\, f(V_R) dV_R \qquad \text{4-22}$$

where the relation $\frac{1}{2} m\mathrm{v}^2 = qV_R$ has been used. It is important to note that the velocity in this equation does not reflect the ion velocity in the external plasma but the velocity where the ions are at an electrostatic potential of zero and the kinetic energy is the total energy. The velocity of the ions in the plasma can be known using the measured plasma potential and taking the derivative of the characteristic[172]:

$$\frac{dI}{dV_R} = \frac{n_i q A \eta}{m_i} \sqrt{\frac{2q}{m_i}} \sqrt{V_R} f(V_R) \qquad \text{4-23}$$

and solving equation 4-23 for the ion energy distribution gives[172]:

$$f(E) = \frac{\sqrt{2} A \eta}{n_i} \left(\frac{q}{m_i}\right)^{3/2} \frac{1}{\sqrt{V_R}} \frac{dI}{dV_R} \qquad \text{4-24}$$

These equations state that the distribution function is proportional to the derivative of the I-V_R characteristic. The distribution for the ions in the external plasma will then be represented by shifting this distribution by the value of the plasma potential.

These equations are useful when the ion density and plasma potential are well known quantities. If they are not, another useful method for determining the distribution function is to assume the ion velocity is drifting, similar to the analysis of satellite based electrostatic probes[202-204] requiring the form of a drifting Maxwellian distribution[203]:

$$f_\infty = n_i \left(\frac{m_i}{2\pi k T_i}\right)^{3/2} e^{-\left(\sqrt{\frac{m_i}{2kT_i}}\mathrm{v}_\infty - M\right)^2} \qquad 4\text{-}25$$

where v_∞ refers to the velocity of particles originating from infinity and M contains an offset based on the velocity of the spacecraft. Similar to equation 4-22, this distribution function is related to the probe characteristic through integration[202]:

$$I = n_i q A \eta \left(\frac{\mathrm{v}_d}{2}\big(1 + erf(x)\big) + \sqrt{\frac{kT_i}{2\pi m_i}}\, e^{-x^2}\right) - I_e \qquad 4\text{-}26$$

$$x = \sqrt{\frac{m_i}{2kT_i}}\left(\mathrm{v}_d - \sqrt{\frac{2q(V_R - V_P)}{m_i}}\right) \qquad 4\text{-}27$$

where the drift velocity, v_d, represents the velocity of the ions in the external plasma. By fitting equations in the form of equations 4-26 and 4-27 to the RPA characteristic each parameter may be extracted from the fit coefficients. An example using this fitting technique is shown below.

Figure 4.17 shows RPA data for the sweep grid potential (black line) and collector current (blue line) during one of the shots from the map. As is the case with many of the other probes signal data shown in this chapter, the RF power profile is reflected in the collector current versus time signal. The voltage of the sweep grids are supplied by a Kepco BOP-1000-4 bipolar power supply controlled by a 200 Hz triangle wave.

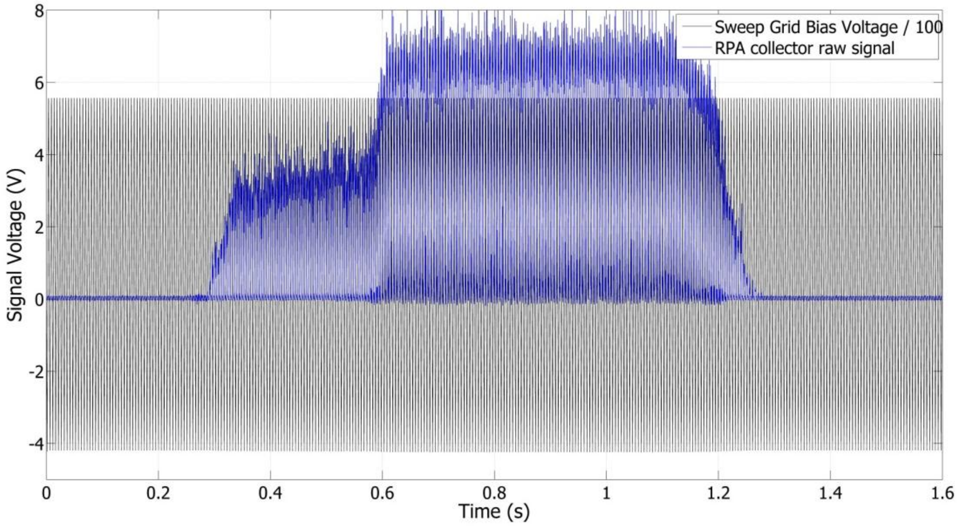

Figure 4.17: Example of raw data from the RPA where the sweep grid was swept at 200 Hz between -400 V to 550 V. Similar to the guard-ring probe, the bias voltage signal must be sent through a 100:1 voltage divider prior to being sent to the data acquisition system. This shot took place when the RPA was on the nozzle centerline (Y = 0 m) and at the closest axial location (Z = 2.79 m).

The characteristic is taken by plotting the collector current against the sweep voltage over both data windows. Figure 4.18 shows the RPA characteristic for the Helicon (figure 4.18 *left*) and ICH (figure 4.18 right) data windows. Also shown in both plots are the fits using the form of equations 4-26 & 4-27 for both the upsweep (blue) and downsweep (green), referring to the sweep voltage either trending up or down, respectively. The trends of the sweep voltage, either up or down, must be analyzed separately because a separation of the signal develops due to parasitic capacitance from the grids as well as the influence of the ions being attracted or repelled over the course of a sweep. The end result is taken as an average of the upsweeps and downsweeps fits. The fits to the characteristic for each data window, for every shot in the map, were performed using built in fitting routines using IDL analysis software written by Dr. Edgar Bering III. The fits are a form of nonlinear least squares using the Levenberg-Marquardt algorithm and adjustments can also be made manually. The velocity is extracted from the resulting fitting coefficients and is tabulated and stored according to RPA position/angle. Ion temperature and number density are also parameters extracted in the coefficients but density is not taken with a high degree of confidence. The densities extracted from the guard-ring probe will be used instead. RPA data were taken for only the first data set because the probe was being serviced during the repeated experiment campaign.

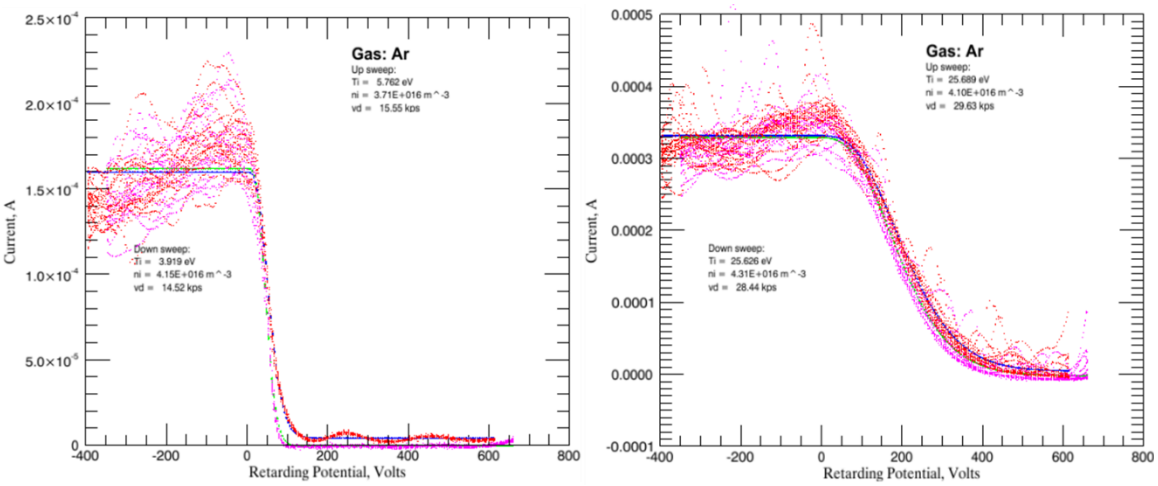

Figure 4.18: RPA I-V characteristics along with fits to the data according to equations 4-26 & 4-27 for the Helicon data window (*left*) and ICH data window (*right*).

Section 4.5: Electric field measurement

In addition to measurements of the magnetic field in the plasma, knowledge of the electric field, whether steady or oscillating, is important when dealing with flowing charges. Knowing the range of frequencies associated with large electric fields is telling to both particle/wave transport and instabilities that may exist in the plume and nozzle system. The DC electric field may be computed using plasma potential data from the guard-ring probe by taking the gradient over some spatial distance. If the data were sampled fast enough it is feasible to take an FFT of this DC electric field to look further into the AC components. The first approach is a valid method to find the DC electric field so long as the relative plasma potential, rather than the absolute, results can be trusted and assuming the RF affects the data uniformly. For this experiment the relative plasma potential data are consistent, although noisy, and this method will be used for the DC electric field analysis. The second method is not viable since the data acquisition hardware was not able to make time series measurements fast enough to sample frequencies of interest near the lower hybrid frequency.

Instead, to measure the fluctuating electric field at high frequencies, an Agilent 4395A Network/Spectrum/Vector Analyzer[205-209] was used to measure the power spectrum between two floating Langmuir probes. The spectrum analyzer uses a stepped FFT technique in repeated bursts of 100 ms/spectrum using a time gated function over a capable frequency range of 10 Hz to 500 MHz[206]. Based on estimations of the lower hybrid frequency in the nozzle regions, the frequency scans used in this study were capped at 10 MHz. Each power spectrum data array was 801 points long giving a frequency step of 12500 Hz and was repeated every 500 ms. Due to this limitation, the shot length during each operational phase, in a separate lower-spatial resolution mapping (92 shots), was increased to 1.5 s producing at least 3 spectra during each power phase. The data output is a power ratio in units of dBm, which is the measured power referenced to one milliwatt. Converting the power ratio into units of power gives:

$$dBm = 10Log_{10}(1000P) = 10Log_{10}P + 30 \qquad \text{4-28}$$

$$P = 10^{(dBm-30)/10} \qquad \text{4-29}$$

where power, P, is in watts. Since the electric field and, hence, voltage are time varying this measured power is an averaged value. The time varying voltage as a function of the average power is found using the nominal impedance of an unbalanced transmission line:

$$V_{rms} = \sqrt{PR} = \sqrt{50 \cdot 10^{(dBm-30)}/_{10}} \qquad 4\text{-}30$$

where R represents the impedance of the transmission line, 50 Ω, which is the most common coaxial transmission line standard and has aged roots in RF and microwave technology. This voltage is a root-mean-square value and assuming the fluctuations are sinusoidal the true voltage is $V = \sqrt{2}\, V_{rms}$. The electric field, E(f), is then the voltage divided by the separation distance between the electrodes, Δx.

The probe electrodes used are displayed in figure 4.19. These probes, constructed by Nils Brenning and colleagues at the Alfvén Institute in Stockholm[137], are a combination of an electric field probe and a B-dot probe. The electric field probe

Figure 4.19: Probes designed to measure high frequency plasma phenomena. The top and bottom probes are identical in design featuring two tungsten electrodes spaced ~ 12 mm apart with a small B-dot coil in between. An individual B-dot probe is shown in the middle, but was not used in this experiment. The power spectrum is measured between the two electrodes.

electrodes are made of tungsten wire, 0.012” (0.31 mm) in diameter, covered by alumina capillary tubes and fed through multi-bore alumina rod into a common transistor socket. This mounting architecture allows for easy setup and swapping between varieties of probes. The separation distance between the wires is 0.47” (11.94 mm). The B-dot probe is consists of fine copper magnet wire wound in a small loop resting between the tungsten electrodes. This wire is covered by Torr-Seal, an epoxy like compound commonly used in vacuum/ceramic applications. Because this sealant contains organic binders and is not ideal for high-temperature plasma environments, the probe has been recessed towards the back end of the diagnostics table to minimize the heat flux on the probe. The Y offset is -4.5” (-114.3 mm) and the Z offset is +13.125” (333.4 mm) with respect to the table reference point (table 4.1). The signals are fed out on a twisted-shielded pair wire.

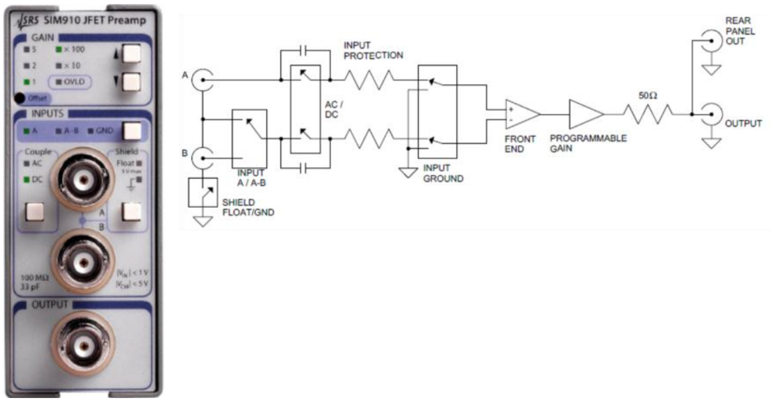

Figure 4.20: Preamp circuit used to measure the power spectrum of the plasma between the pair of electrodes. The output is unbalanced, referenced to an impedance of 50 Ω, and is sent to the spectrum analyzer (Courtesy of Stanford Research Systems, www.thinksrs.com).

The probe signal, prior to being fed into the spectrum analyzer, is fed into an SRS SIM910 JFET based voltage preamp as a balanced signal (figure 4.20). The output is an unbalanced signal referenced to the standard 50 ohm impedance which is then fed into the spectrum analyzer. This preamp features a selectable gain and has a bandwidth of 1 MHz. This circuit is not useful for the B-dot probe which requires a current-sensitive preamp; thus the B-dot probe was not used in this experiment. In order to make use of bandwidth limitations in this circuit, a calibration was performed over the entire 10 MHz frequency range by applying a 1 $V_{p\text{-}p}$ sinusoidal signal across the electrodes using an Agilent 33220A waveform generator. The calibration was performed in place using the full cable lengths. The resulting calibration curve and corresponding gain function is displayed in figure 4.21. The measured amplitude of the sine wave as a function of frequency (figure 4.21a) is used to compute the attenuation (gain) of the signal (figure 4.21b) passing through the filtered preamp and cable assemblies. This gain function can then be used to back out the corresponding voltage signal at higher frequencies.

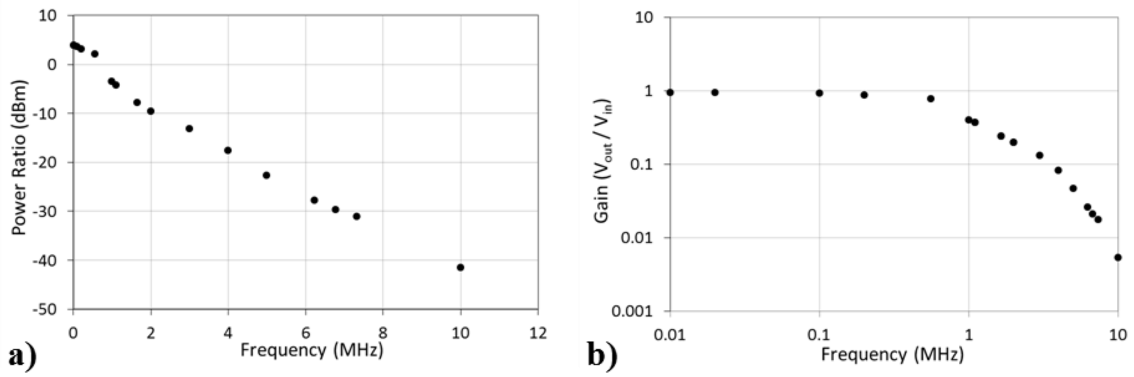

Figure 4.21:   Calibration curves used for high frequency probes. The peak of the power ratio (a) measured as a function of frequency is used to calculate the precise gain (b) as a function of frequency. The test setup placed a 1 $V_{p\text{-}p}$ sine wave across the electrodes, using full cable assemblies, at various frequencies and measuring the resulting power ratio on the spectrum analyzer.

A sample of spectral data from one of the mapped shots is shown in figure 4.22. Here the spectra are arranged top to bottom in time sequence during the extended shot.

The first spectrum is taken before plasma is initiated. The second and third spectra represent the Helicon operational phase while spectra 4 – 8 are at full power. The spectra during each power stage are then frequency averaged prior to subtracting off RF pickup in the signal wires. The representative RF pickup, used for the entire map, is the signal taken during an active shot where the probe is entirely out of the plasma; in this case at a translation stage position of Y = -900 mm, Z = 2900 mm. After this noise is subtracted off of the average spectrum from each data window, V_{rms} is found using equation 4-30. A linear interpolation of the gain function (figure 4.21b) to the frequency sweep is used to back out the true amplitude. The electric field is then found by dividing this voltage by the separation distance and preamp gain. This frequency dependent electric field is calculated for each position in the reduced resolution, extended shot length, map and can reveal ion energy dependent spatial irregularities.

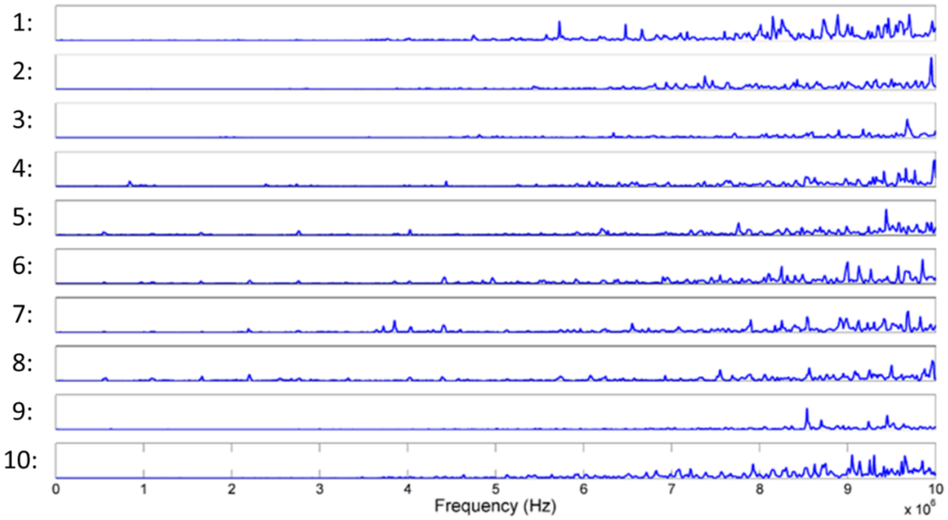

Figure 4.22: Example of electric field spectra taken with the probe on nozzle centerline (Y = 0 m) and at the closest axial location of the electric field probe (Z = 3.23 m). Spectra are taken every 0.5 s ranging between 0 and 10 MHz and are shown normalized (V_{rms}).

Section 4.6: Other diagnostics

Some of the other diagnostics used during this experiment were a Quinstar 70 GHz microwave interferometer (MWI) and an Ocean Optics USB4000 optical spectrometer. These remained stationary for the duration of the experiment and served as 'standard candles' for plasma density and impurity species in the plume.

Section 4.6.1: Microwave interferometer

Microwave interferometers are used as a non-invasive plasma diagnostic that measure line integrated density based on index of refraction changes proportional to the density between the antenna horns. MWI have been used in many instances on similar electric propulsion devices to get a more accurate measurement of plasma density[76, 210]. An oscillator creates microwaves which are split sending one part of the beam across a reference leg while the other is sent through the plasma. The index of refraction from the plasma alters the phase, creating a phase difference, with respect to the reference leg before the signals are recombined at the detector known as the I-Q mixer. This phase difference, $\Delta\varphi$, is dependent upon the electron density and may be defined as[183]:

$$\Delta\varphi = \frac{-\omega}{2cn_c}\int n_e dl \tag{4-31}$$

where ω is the frequency of the wave and n_c is the cutoff density. This cutoff is the point where the plasma refractive index becomes imaginary and the wave propagation becomes evanescent, effectively giving the MWI a maximum detectible density[183]:

$$n_c = \frac{\omega^2 m_e \varepsilon_0}{q^2} \tag{4-32}$$

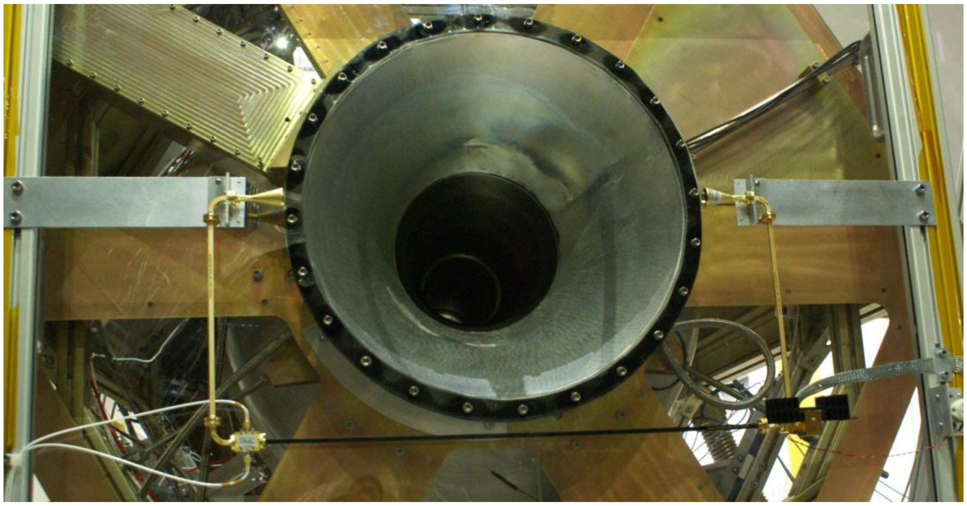

Figure 4.23: The microwave interferometer used during this experiment is mounted on the vacuum wall at an axial location of Z = 2.654 m. The waves propagate between the antenna horns aligned with the horizontal plane of the nozzle. The I-Q mixer is seen on the bottom left with coaxial signal wires being fed out. The oscillator and power supply are seen in the bottom right.

which for f = 70 GHz, $n_c \approx 6.08 \times 10^{19}$ m^{-3}.

The MWI used was mounted on the downstream side of the vacuum wall (figure 4.23) at an axial location of Z = 2654 mm having a spacing between the horns of 53.6 cm. The data for each shot in this experiment when mounted at this location were cutoff (figure 4.24) where the phase difference is saturated and essentially non-detectable. Normal phase differences, or fringe shifts, would appear as complete polar circles when plotting I (In-phase) versus Q (Quadrature)[210]. Instead the plot is compressed to a back and forth line indicating plasma is cutoff. Because the MWI was in a fixed location for all of the shots and the RF power/gas flow were identical and highly repeatable, it is reasonable to expect all of the shots were equally cutoff. This assertion has been confirmed by examining a handful of various shot data. Despite not having an accurate estimate of the plasma density at this location, the cutoff plasma can still be useful to verify the order of magnitude of the density from guard-ring probe data. As shown in section 4.1.3, assuming the cutoff density at the axial location of the MWI and magnetized electrons, the plasma should expand proportionally to the drop in magnetic field strength according to[98]:

$$\frac{R(z)^2}{R_0^2} \approx \frac{B_0}{B(z)} \tag{4-33}$$

The magnetic field is ~ 1320 G at the MWI and ~ 740 G at the closest measurement location of the guard-ring probe. This corresponds to an effective area increase of 0.176 m^2 and thus a drop in density to 3.42 x 10^{19} m^{-3}. This is still about a factor of 2 higher than the peak density as measured by the guard-ring probe. This can be considered to be in relative agreement to within the uncertainty of swept Langmuir probes thereby lending confidence to its data.

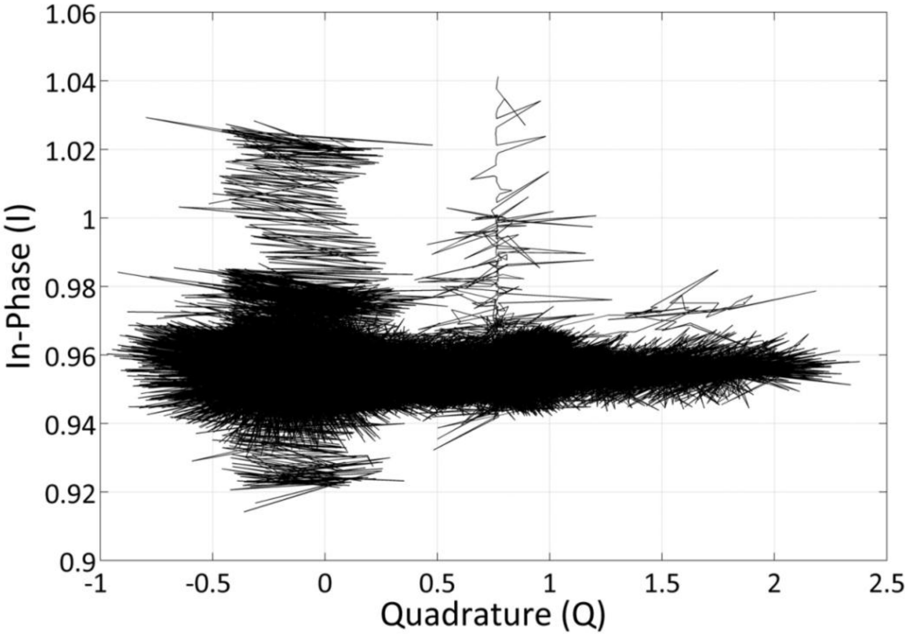

Figure 4.24: The output signals from the I-Q mixer shown on an I-Q plot. Normal phase shifts that are counted appear as open circular ellipsoids. These ellipsoids collapse upon plasma cutoff and is the case for each of the shots measured at this location.

Section 4.6.2: Optical spectrometer

An optical spectrometer was used to measure emitted light via a fiber optic cable mounted on the endplate of the Helicon core. The type of spectrometer used is an asymmetric crossed Czerny-Turner that uses a diffraction grating of 600 lines blazed at 400 nm, an entrance slit of 5 μm, has a measurement range of 200 – 850 nm, and a FWHM resolution of 0.03 nm. This instrument is useful in ensuring that the plasma is near completely ionized as well as to investigate any impurities introduced into the plasma. A sample spectrum from one of the shots is presented in figure 4.25. Also plotted with the sampled data is a normalized NIST reference spectrum for Ar II. This spectrum demonstrates that the Helicon ionization stage produces near 100% ionization of the argon input gas. Spectrometers calibrated to known source intensities may be used to measure electron temperature. This device was not calibrated in this manner and any electron temperatures inferred will not be comparable to those from the guard-ring probe.

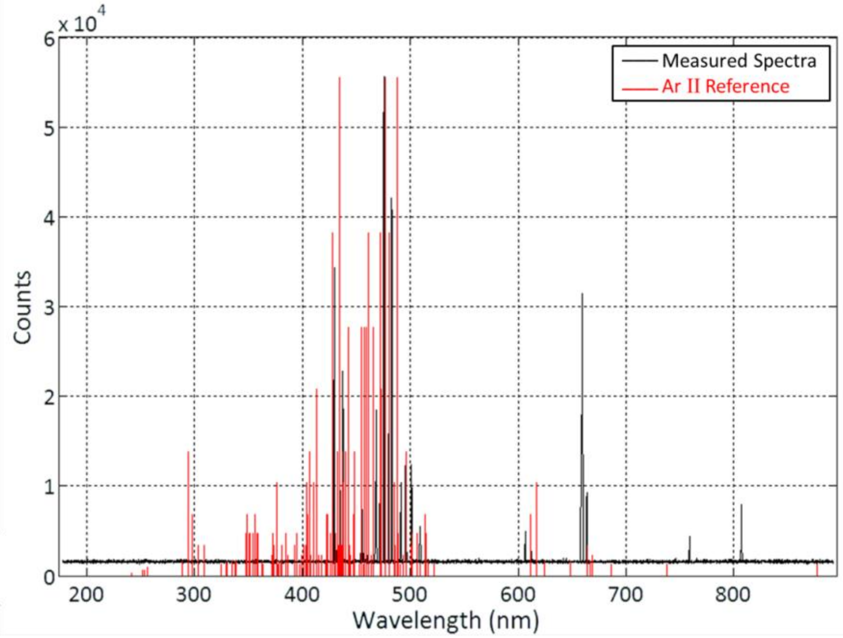

Figure 4.25: Sample spectrum of light collected within the Helicon section of the plasma source.

Chapter 5: Presentation of Data, Methods, and Results

The emphasis of this chapter will be to present much of the reduced plume data and analytical methods that demonstrate, characterize, or indicate ion and/or electron detachment from a magnetic nozzle. Further analysis and comparison to the presently accepted theories will come in the following chapter. Section 1 will present a qualitative overview on the behavior of the plasma, plume structure, and nozzle environment during both operational phases as indicated by the diagnostics using compiled data in the form of contour maps. Section 2 will discuss and compare the axial data trends with respect to the magnetic field and demonstrate that the flow does not expand at the same rate as the magnetic field. A new method for following and tracking ion/momentum flux based on the mapped data will be detailed in section 3 providing further evidence for ion detachment. Section 4 will discuss data taken from an angular scan of the ion velocity vector from five different regions of the plume using the articulating motion of the RPA. Section 5 will present the plasma electric field, both steady state and oscillating, and its implications for cross field diffusion and drifts motion of the electrons. Lastly, in Section 6, a summary of the findings from this chapter will be given.

Section 5.1: Contour map representation of data

Perhaps the simplest and most straightforward way of presenting a large amount of plume data is in the form of contour maps considering the data were taken over a large spatial range (figure 3.11). This format gives an idea of the overall structure of each parameter in the plume and serves as a low-level confirmation prior to further examining any additional trends. The measured data, typically in analog voltage form, were converted into meaningful quantities according to the reduction methods described in chapter 4. The data handling was accomplished mostly using common analysis software programs such as Matlab™. The averaged values from each time window, corresponding to specific power levels, were stored in Microsoft® Excel for each diagnostic according to (R, Z) coordinates. The native Matlab™ function *griddata* was used to interpolate between the data points along a regular grid spanning from R = 0 – 0.7 m and Z = 2.79 (~ 70 cm downstream of the nozzle throat) – 5.09 m as measured in the vacuum chamber coordinate system. The grid spacing interval was 5 mm in both R and Z. Interpolation between data points used either a biharmonic spline interpolant common in satellite image reduction[211] or a linear interpolant. The biharmonic spline produces smoother transitions than the linear interpolants but can insert false data relics when there is a lack of ample boundary data. Unless otherwise specified the reader may assume the interpolation method was linear.

Contour maps representing the ion flux are presented in figure 5.1. The current was measured by the lowest collector, positioned along the horizontal plane of the nozzle, of the upper Langmuir probe array which was steadily biased at -20 VDC. The images are plotted using a logarithmic scale to improve the contrast of the plume structure to the vacuum signal (~ ±0.06 A m^{-2}). All of the contour maps presented in this chapter display the plasma plume propagating from left to right and viewed from above as data are taken along the horizontal plane of the chamber. First observation indicates the plume slightly broadens and becomes smoother on the left hand side (yellow contours) during ICH

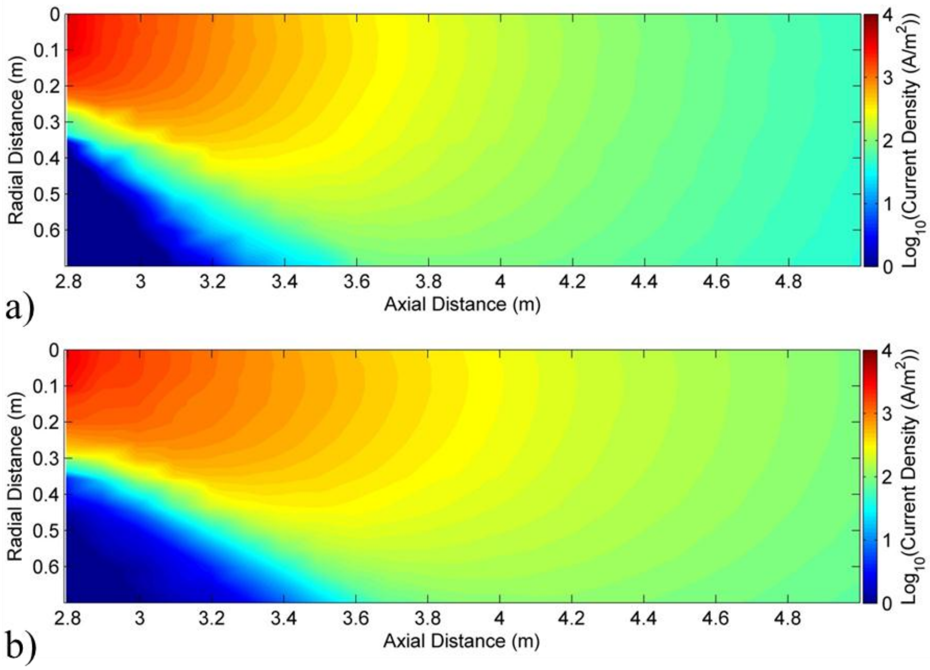

Figure 5.1: Contour maps of the measured ion flux during the a) Helicon and b) ICH time windows. Maps are taken along the horizontal plane of the nozzle and viewed from above. Despite the similarities in the plume structure during both power phases, the high power phase (b) is smoother along the edges of the plume.

operation (b) than during Helicon operation (a) with a smaller divergence angle further downstream along the edges (cyan contours). The higher current density portions of the plume have a greater extent during the ICH phase (b) than for the Helicon phase (a) indicating a more focused and directed flow given both emerge under identical magnetic nozzle configurations. Some charge-exchange related effects begin to emerge as the low density/energy coma along the edges expands radially outward with a large angle of divergence. This outer layer may have difficulty fully separating from the field, the extent of which may be the subject of a future study. During both phases the axis of the flow is seen to be slightly off-center with a low (~ 5 – 7 cm/m) divergence rate. At present the reasons for this off-nozzle axis flow are not well understood but may have to do with the absorption patterns and power deposition profiles under each RF coupling antenna, which is beyond the scope of this thesis.

Considering these maps show a measure of current density which is an ion flux collected over the area of the disk, the radial profiles of these plots may be integrated to quantify the total ion flux contained within some pre-defined bounding surface. These are one of two separate ‘flux densities’, along with momentum flux, that will be used to track lines of constant integrated flux described in section 5.3.

The electron density, taken from the analysis of a voltage swept guard-ring probe, mirrors the structure of the ion flux contours (figure 5.2). The data was reduced according to the methods detailed in section 4.1.3. The measurable plasma density range was slightly less than 10^{15} m^{-3} to slightly greater than 10^{19} m^{-3}. At densities much lower than 10^{15} m^{-3} the signal to noise ratio becomes too low to provide reliable results and positions corresponding to these areas are displayed in white. Comparison of the plasma density during ICH operation (b) to that during Helicon (a), much like the ion flux, show smoother organization and less irregularity. Although the peak densities are higher during Helicon power, due to the reduced ion velocity and under the assumption of quasineutrality, they spread out more and drop off faster than the higher energy ICH phase. This trend is best observed when comparing the light-orange colors in the far plume where the darker-orange permeates further during ICH (b) than for Helicon (a) which is mostly yellow indicating nearly a factor of 2 less. These falloff rates are indicative of a more axially directed flow at higher ion energies and faster radial expansion at lower ion energies.

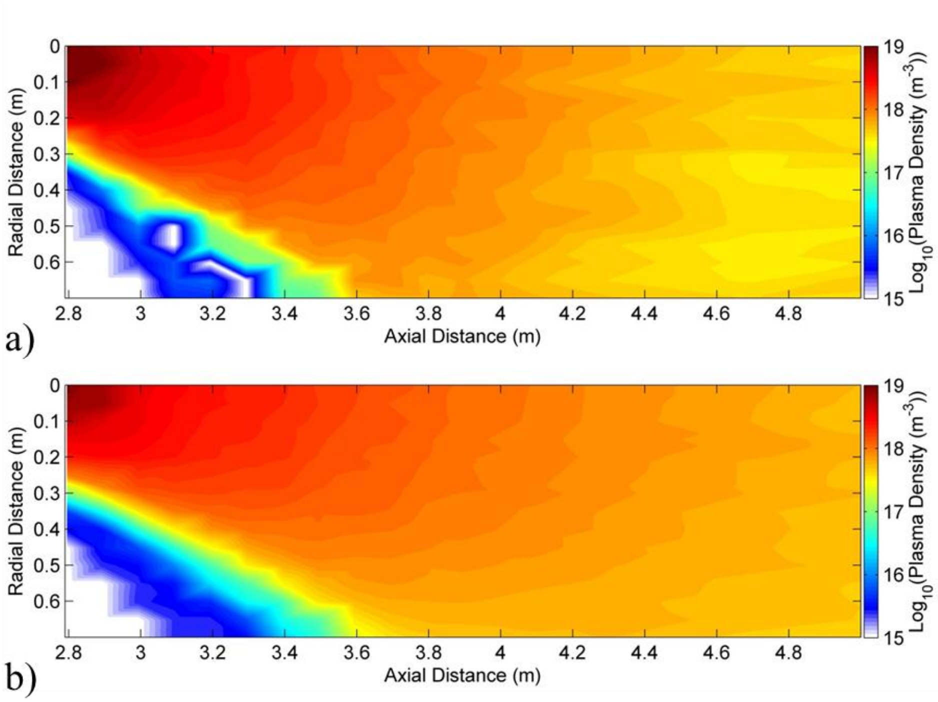

Figure 5.2: Contour maps of the measured electron density during the a) Helicon and b) ICH time windows. Maps are taken along the horizontal plane of the plume and viewed from above.

As mentioned in section 4.2, it is prudent to measure and compare the momentum flux trends in the plume. Considering the contour maps presented above were taken from Langmuir probes, either swept or held at constant bias voltage, they are susceptible to the effects of charge-exchange in terms of a reduction in collected ion flux. Despite efforts or other preparation in the setup to minimize the overall effects of charge-exchange, it is impossible to eliminate entirely and the result would be an artificial broadening of the ion plume. This broadening would appear as if the plasma were still magnetized as the newly formed ions may become re-magnetized and then follow the field lines. The plasma diagnostic that is sensitive to both ion flux and neutral flux is the plasma momentum flux sensor (PMFS) whose contour plots are presented in figure 5.3.

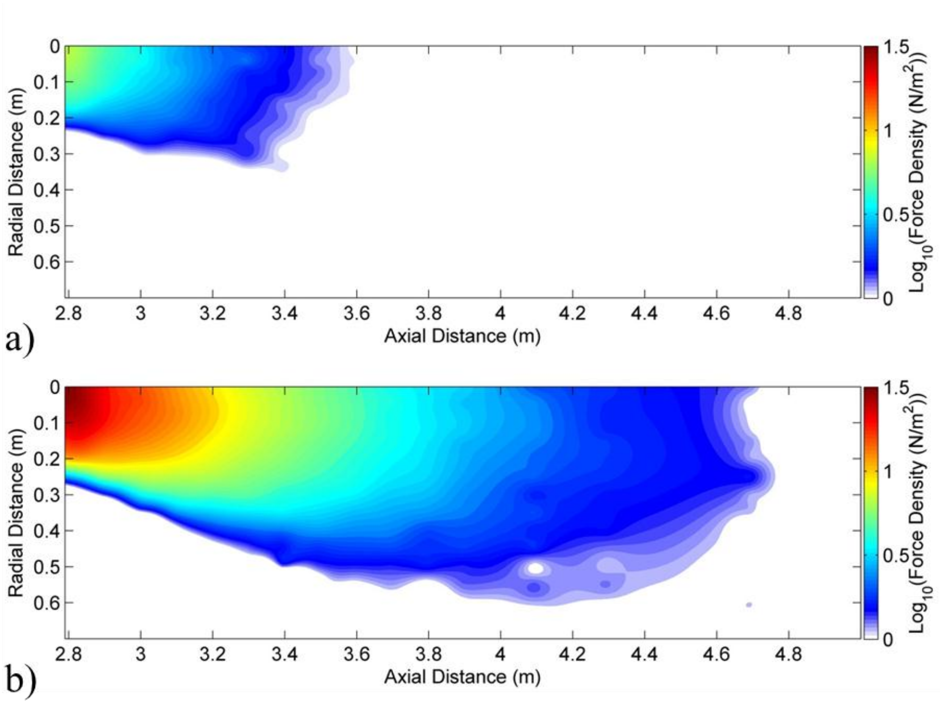

Figure 5.3: Contour maps of the measured momentum flux during the a) Helicon and b) ICH time windows. Maps are taken along the horizontal plane of the plume and viewed from above. A smooth biharmonic spline interpolation method was used on the data.

The data were taken from the primary PMFS, a 9 cm diameter pyrolitic graphite disk mounted along the horizontal plane of the nozzle. The graphite disk is attached to sensitive strain gauges via a 3.1 mm x 3.1 mm alumina tube. This force target is described in greater detail in section 4.2. The analog voltage signal from the micron meter strain-gauge readout was converted into units of force using the calibration curve presented in figure 4.11. Considering the natural frequency of the target/beam system is about 40 Hz, the time window of 100 ms for each time window provides 3 – 4 oscillations of the pendulum. The representative force during each operational phase is the average value over this span. This was done for each position in the map and interpolated using the biharmonic spline interpolant mentioned above and is plotted on a logarithmic scale (figure 5.3). The Helicon operational phase (a), in terms of momentum flux, dissipates rapidly with increasing axial distance. Much like the electron density displayed in figure 5.2, regions where the signal-to-noise ratio is small are too difficult to analyze with certainty and have therefore been colored white in both images. For this strain gauge the lowest detectable force density before the signal blends with the noise is about 0.14 mN/m^2. For the higher power (~ 100 kW) ICH operational phase (b) the momentum flux/force density extends more than 1 m further downstream. The PMFS maps also confirm that the plume is observed to be slightly off-nozzle axis with a small divergence rate (~ 5 – 7 cm/m).

As stated above, one can obtain a qualitative understanding of the effects of charge-exchange by comparing the ion flux contours with the momentum flux contours (figures 5.4 & 5.5). It is useful to overlay lines marking the divergence angle for both the ion and momentum flux. For the ion flux, lines following the denser portion of the plume, along the yellow-green interface, are more appropriate than measuring the divergence of the less dense, lower energy fringe regions. Figure 5.4 compares the ion flux (a) to the momentum flux (b) during the Helicon operational phase. The divergence angles differ by 8° that a first impression may imply the plume is heavily charge-exchanged. To see if this is the case, one must consider the nature of the force target along with its limitations. Given the purpose of the 9 cm diameter graphite disk is to increase the sensitivity to very weak plasma flows, it can cause discrepancies along the plume edge where the target only partially intercepts the flow. Due to this effect, radial PMFS data is only reliable out to 80% of the plume radius (0.8r_p) before significant momentum collection area ‘sees’ vacuum. This will become an important consideration

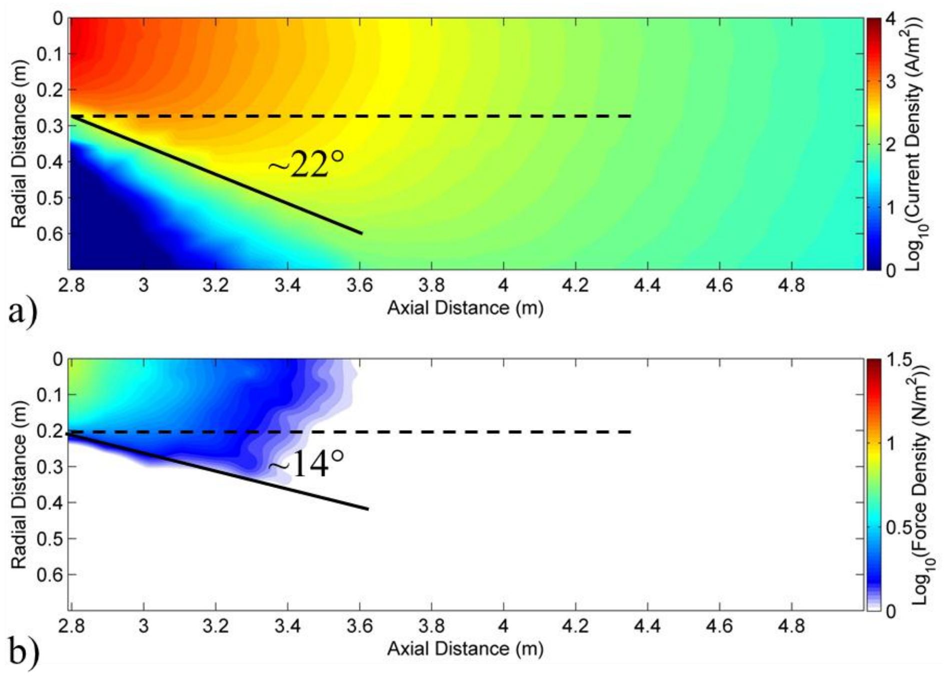

Figure 5.4: Comparison of ion flux (a) and momentum flux (b) contours and plume divergence angles during the Helicon time window.

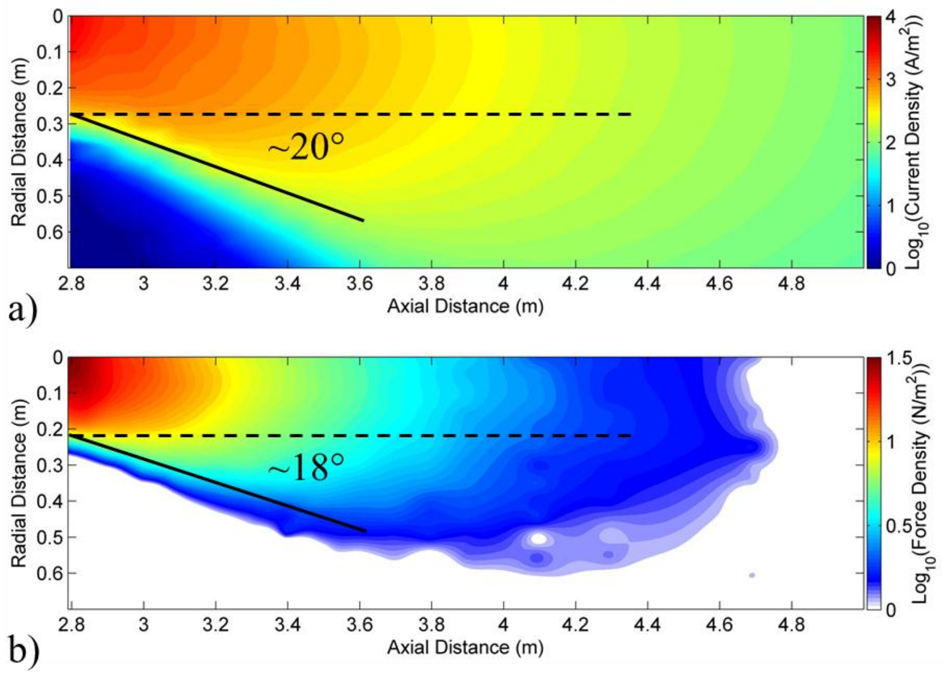

Figure 5.5: Comparison of the ion flux (a) and momentum flux (b) contours and plume divergence angle during the ICH time window.

for the flux tracking methods listed in Section 5.3. Another contributing factor to the large difference in angle during Helicon is that the strain gauge signal may be too small to provide an accurate measure of the divergence angle. The argument is deferred to the estimates based on neutral pressure, ion energy, and charge-exchange cross sections for argon ions incident upon argon neutrals to presume charge-exchange is negligible during this operational phase (Appendix A).

Figure 5.5 shows the contour maps of the ion (a) and momentum flux (b) during the ICH time window and the estimated plume divergence angles. The overlain angles for the ion flux were again chosen based upon bulk flow rather than fringe regions. Here the momentum flux signals were higher making it is easier to approximate a divergence angle of ~ 18°. This value is within 2° of the estimated divergence of the ion flux plume indicating that, between 650 – 750 ms, charge-exchange seems to be having minimal effect on the ion flux plume structure. With this understanding it is reasonable to state that the force target measurement is mostly representative of momentum exchange with ions rather than fast neutrals. Radial integration later will offer a different conclusion. The ion momentum structure during this time window does not appear to non-linearly broaden with increasing axial distance indicating the momentum of the ions does not spread out with the magnetic field as would magnetized plasma. The signal and structure is too weak to make this claim for the low power Helicon stage.

The RPA, described in section 4.4, is able to measure ion velocities by screening out electrons and tracking the collected ion current against a voltage swept discriminator grid. The resultant contour maps of measured ion velocity are presented in figure 5.6.

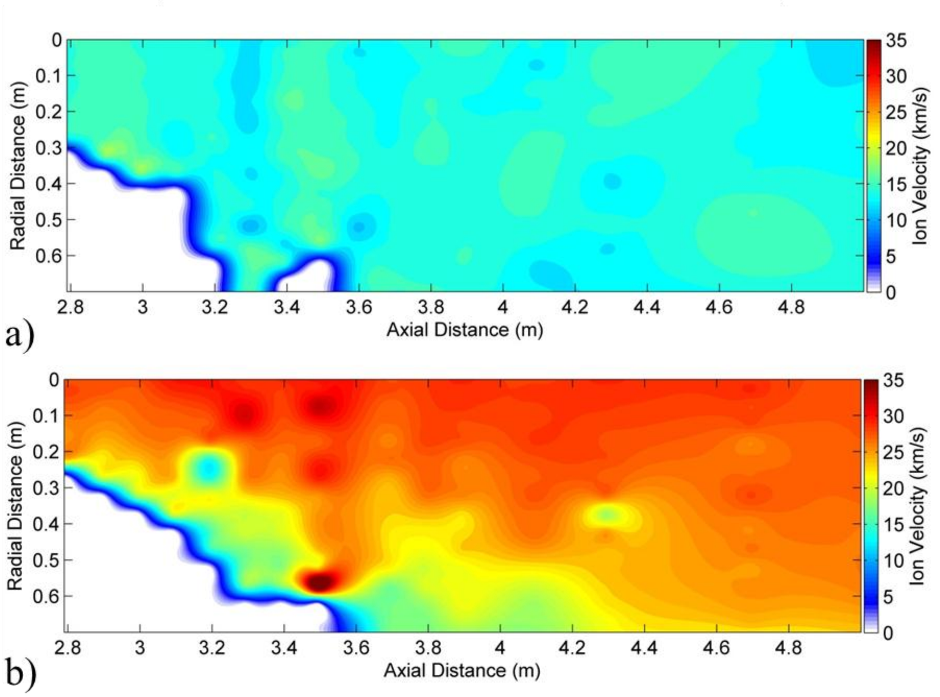

Figure 5.6: Contour maps of the measured parallel ion velocity during the a) Helicon and b) ICH time windows. Maps are taken along the horizontal plane of the plume and viewed from above. A smooth biharmonic spline interpolation method was used on the data.

As was the case for the momentum flux, the interpolation method used was the smooth biharmonic spline method ushered by Sandwell[211]. Unlike the other mapped data, the post-processed velocity data from the RPA, in terms of spatial coherence, is much noisier. Despite these spatial variants, the trends in the parallel ion velocity structure are clear. During the Helicon time window (figure 5.6a), the ion velocity is fairly uniform and flat across the plume with velocities ranging from ~ 13 – 17 km/s. The trends during the ICH time window (figure 5.6b) are even more pronounced. The red-orange regions define a fairly uniform broad peak before rolling off at a divergence angle of approximately 16°. The velocity during the ICH phase range up to ~ 35 km/s. The green to dark blue regions extending out to the white areas, where the collector signal became too weak to properly analyze, represent either a low energy region where the velocity is smaller or the velocity vector is changing as the curvature of the magnetic field decreases. In the case of the former, a decrease in the parallel velocity component may correspond to the fringe/halo region where the plasma density is lower and/or the effects of charge-exchange are more prominent. The divergence angle along the outer edge is approximately ~ 27° during both time windows.

With regards to ion detachment one would expect that if the ions were perpetually magnetized and bound to the magnetic field the peak of the parallel ion velocity would spread out with a uniform radial drop-off. Considering the relative radial velocity profiles for each time window are reasonably flat across the central regions, one may conclude that the majority of the plume is not magnetized. The red-orange peak during ICH (figure 5.6b) is fairly well directed, expanding at rates similar to, within uncertainty, the expansion of the ion and momentum fluxes. Stated in another way, based on these qualitative images alone, the denser portions of the plume carrying the more axial momentum are detached from the applied magnetic field; whereas for the less dense, lower energy regions the state of plasma magnetization is unclear.

At this point it seems appropriate to discuss the structure of the measured magnetic field in the plume and how it may correlate to the other measured parameters. Measurements were taken using a 3-axis magnetometer discussed in section 4.3. Colored contour maps representing the interpolated vacuum (no plasma) magnetic flux, Helicon window magnetic flux, and ICH window magnetic flux for the radial magnetic component are displayed in figure 5.7. These data were taken from the second data set after the magnetometer had been recalibrated. Systematic uncertainties based upon

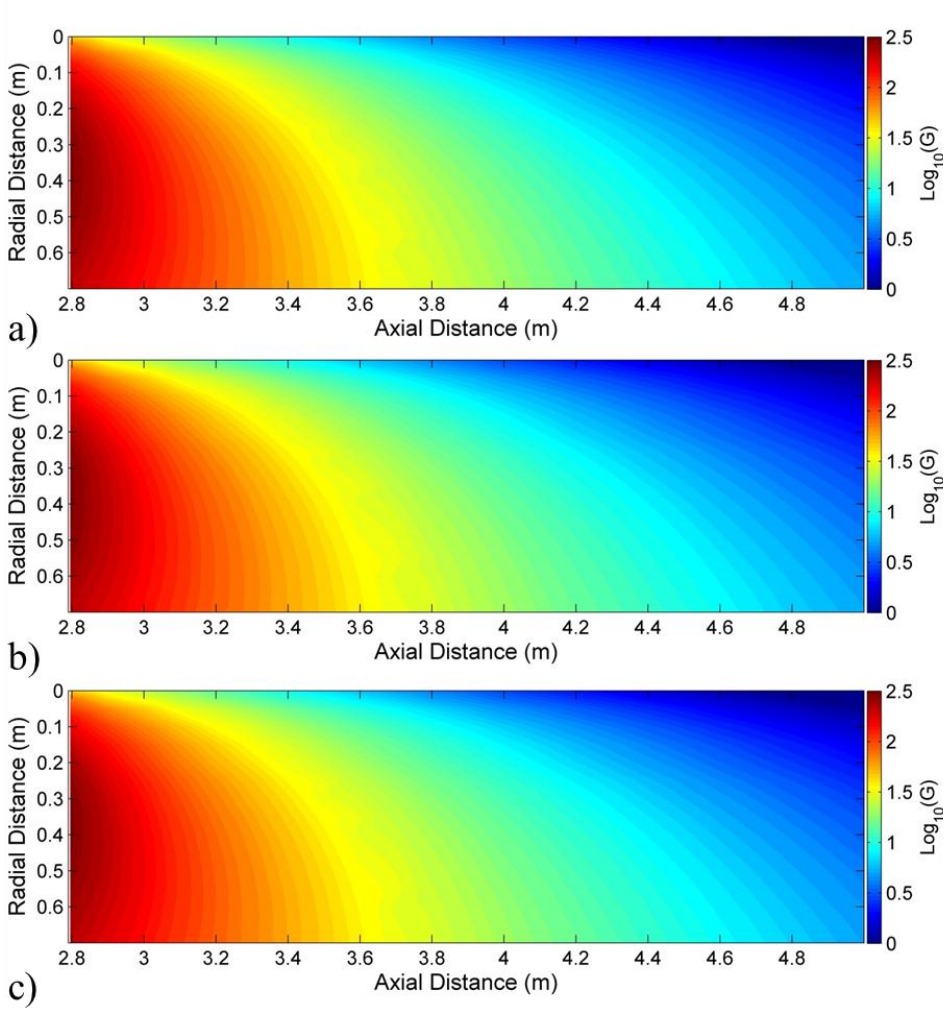

Figure 5.7: Logarithmic contour plots of the radial component (B_r) of the vacuum magnetic field (a), as well as during the time windows for the Helicon (b) and ICH (c). The compiled data were taken from the second experiment data set. The differences in radial magnetic fields from vacuum to plasma are minimal.

repeated shots range up to ±1.6%. The presented trends are clear and the comparisons show that the changes in the radial component of the magnetic field from the vacuum field during both phases of firing are negligible. Post-processing analysis of the data show that the changes in the magnetic field, normalized to the local vacuum field strength, is negligible outside of the areas where the radial field is weak (along the magnetic axis) and approaches the magnitudes of the fields produced by the flowing plasma.

The axial component of the magnetic field taken from the first experiment data set is unusable as post-experiment analysis revealed a faulty B_z sensor. The data for this axis were incoherent, random, and did not match any of the expected vacuum field models for the magnet coil currents. Inspection of the sensor revealed no visible damage but required further calibration and electronic inspection by the manufacturer. This repair has since been done and the functional calibrated sensor was used extensively in the repeat experiment campaign. The axial component data for each operational phase of the firings is compiled and presented in figure 5.8. Much like the radial magnetic component there is little noticeable change in the magnitude or structure of the field in the presence of flowing plasma. There is one irregularity in the B_z contour plot spanning the range of Z = 4.0 – 4.3 m where three of the contours appear jagged and may likely be due to residual effects from the linear interpolation algorithm. This feature is not a cause for concern given it is present during all phases of the shot. The axial data are very repeatable as the systematic uncertainty for the measured B_z data, as indicated from repeated shots, range up to ±0.1%. In terms of the change in magnetic field due to flowing plasma, when normalized to the local magnetic field component, the differences have been measured only as high as ±0.2%. This leads to the conclusion that the plasma flow is not having a large effect on either the radial or axial magnetic components.

Considering the negligible changes from either magnetic component, comparing data from the other probes in the first experiment to the magnetic field may then be done using previously verified models of the axial magnetic component[212]. This model

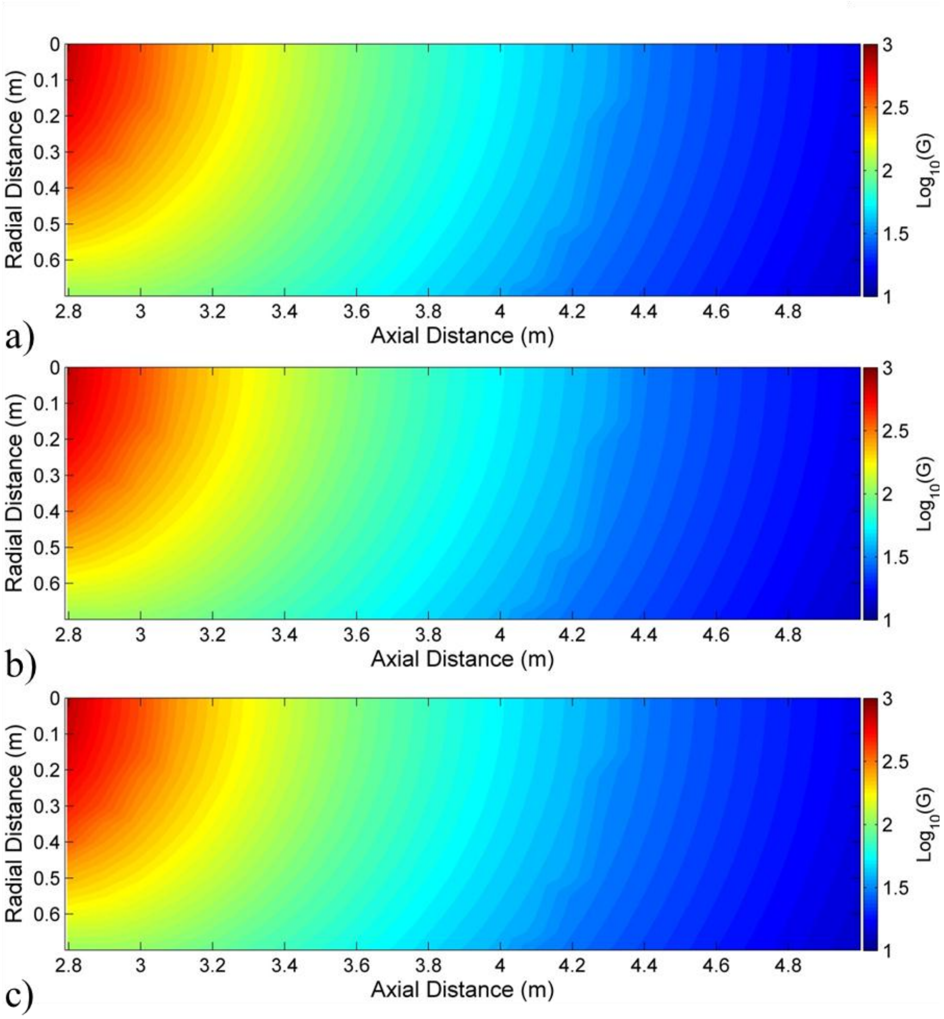

Figure 5.8: Logarithmic plots of the measured axial (B_z) component of the magnetic field for the the vacuum magnetic field (a), as well as during the time windows for the Helicon stage (b) and ICH stage (c). This data was taken from the second data set from the repeated experiment.

should offer sufficient comparison to the applied field during the first dataset to understand the effects of ion and electron detachment with respect to the magnetic structure in the plume.

While comparisons of these several colored contour maps of the various plasma properties are not quantitative in their descriptions of ion or electron detachment, they do offer a qualitative overview of what may be occurring in the plume during the various phases of the discharge. It may be concluded that during the Helicon time window the plume is overall broader in terms of ion flux, electron density, and velocity distribution, while the momentum flux of the ions dissipates rapidly downstream. With the addition of additional energy to the ions via ICH the velocity increases by more than a factor of 2. The plume also becomes more focused downstream in terms of ion flux, plasma density, velocity distribution, and had a greater axial extent in terms of momentum flux. All of these plume structural changes occur with little change to the magnetic field topology. These data all suggest that the flowing plume, during ICH, is not following the magnetic field and is a low-level indication of detachment.

Section 5.2: Axial profiles

A more quantitative conclusion for particle detachment from the magnetic nozzle is a comparison of the measured plasma parameters along the nozzle axis. One would expect for a magnetized plume that ion and momentum flux should assume a similar axial drop-off as the magnetic field. This falloff trend is manifest by comparing power law fits to the data trends and should be proportional to ~ z^n where n represents the extent of the axial falloff. Any trends diverting from the axial magnetic falloff may serve as an indication that the flow is not magnetized.

Data taken along the nozzle axis (Y = 0 m) for measured ion flux, momentum flux, magnetic flux, and ion velocity for both Helicon (blue) and ICH time windows (red) are presented in figure 5.9. The ion flux, momentum flux, and magnetic flux are taken from the repeat (second) experiment data set while the parallel ion velocity data are from the first data set. Ion flux data were taken with the center plane collector from the upper Langmuir probe array, biased at – 20 VDC which was verified to be 3T_e less than the floating potential into ion saturation ensuring the efficient collection of ions while reducing the creation and reflection of secondary electrons[140]. Ion flux, measured as a current density in A/m^2, is taken as the measured current over the collection area of the probe (section 4.1.2). The momentum flux data are taken from the primary PMFS target mounted along the central plane of the magnetic nozzle and measured in N/m^2 according to pre and post experiment calibration (section 4.2). The magnetic flux data were taken from the ISO/EIC-17025 calibrated z-axis hall probe which corresponds to the positive z

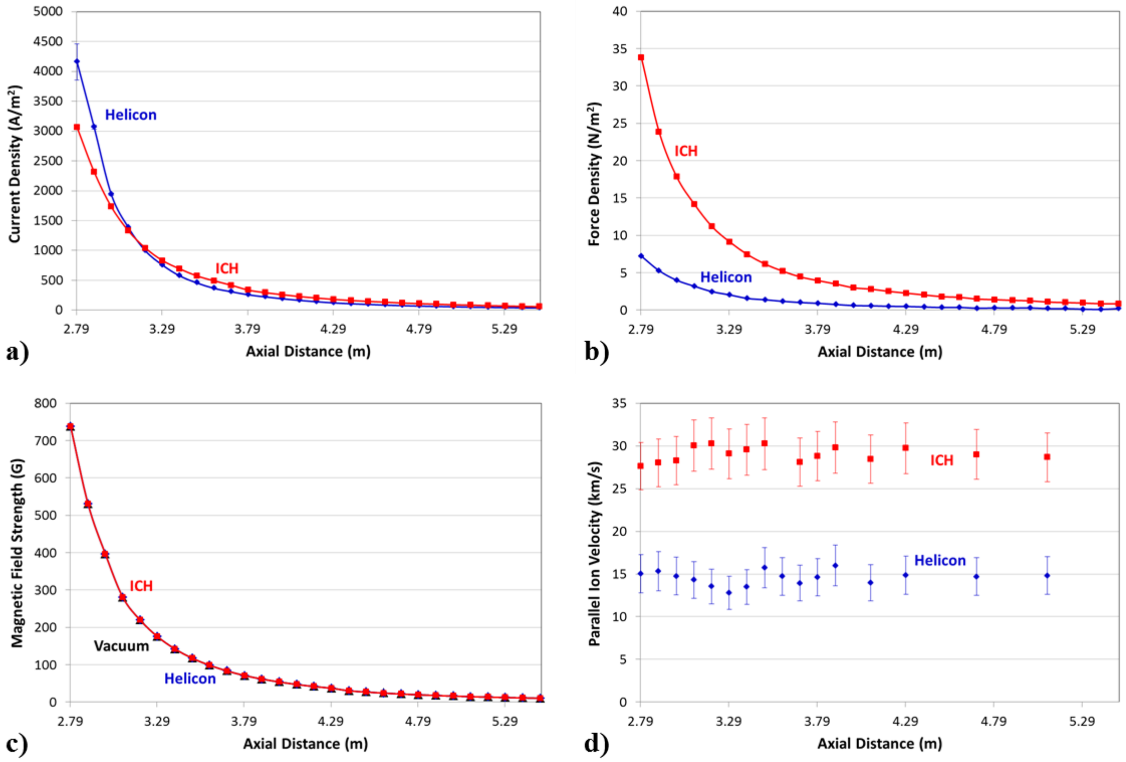

Figure 5.9: Axial trend data of a) ion flux, b) momentum flux, c) magnetic flux, and d) parallel ion velocity for both the Helicon (blue) and ICH (red) time windows. All data, except ion velocity, were taken from the second data set. The measured vacuum magnetic field is also presented (black).

axis of the magnetic nozzle and is measured in Gauss. The ion velocity data, although from the first data set, should be representative of the ion velocity in both experiments given the differences in experiment setup/conditions are minimal being only a slight increase in neutral propellant flow rate. These data were taken from the RPA oriented parallel to the nozzle axis. Error bars are presented for each datum point and are calculated using the relative systematic uncertainty from repeated firings. Several of the values were quite repeatable to the extent that magnification of the error bars would be necessary to resolve them.

Analysis of the ion flux data shows a rapid falloff with increasing axial distance during the Helicon time window along the first 0.6 m in Z. This trend corresponds to a proportional power law falloff of $\Gamma \sim z^{-10.1}$. Over the next 2 m this decline shallows out to $\sim z^{-5.5}$. With the addition of energy to the ions in the form of ion cyclotron resonance the ion flux falloff over the first 0.6 m follows a power law scaling of $\sim z^{-7.8}$. The scaling changes to $\sim z^{-4.9}$ over the following 2 m. The falloff of the momentum flux during the Helicon time window doesn’t take as large of a falloff as it trends $\sim z^{-7.7}$ over the initial 0.6 m and $\sim z^{-5.0}$ for the final 2 m. Similarly during ICH the momentum flux falloff is $\sim z^{-7.7}$ and $z^{-4.4}$ for the initial 0.6 m and following 2 m respectively. These trends are consistent with the qualitative analysis of the contour maps presented in section 5.1 that with an increase in ion energy the plume becomes more directed and focused with increasing axial distance.

The axial magnetic field data shows no discernible difference, at this scale, in magnetic field strength over the vacuum levels during plasma operation. This non-difference helps confirm the conclusions drawn from the comparison of the contour maps presented in figure 5.8. Using the vacuum field data, the axial component of the magnetic field falls off over the same initial 0.6 m at a rate of $B_z \sim z^{-8.6}$ and $B_z \sim z^{-5.4}$ for the following 2 m. The trends from this first region reveal that over the initial 0.6 m, where the change is greatest, neither the ion flux nor momentum flux, during the Helicon nor ICH time windows, matches the falloff rate of the magnetic field. The large falloff of the ion flux during the Helicon time window is likely revealing of strong radial forces driving the expansion. The falloff of the ion flux closely matches the magnetic flux falloff over the final 2 m (-5.5 to -5.4) for plasma during the Helicon time window. The momentum flux during this same time and region is slightly less (-5.0) which may be attributed to the lower signal-to-noise ratios involved.

Adding momentum to the ions via ICH causes the axial falloff trends of the ion and momentum flux to diverge from rate of the magnetic flux falloff (-4.9 and -4.4 compared to -5.4). These rate constants are indicative that the ion flow is not following the magnetic flux in this region and may be considered detached. The differences in the ion and momentum flux may be attributed to interactions with neutrals given that the plume, in regards to ion flux, falls off at a faster rate when the distances become comparable to the charge-exchange mean free path. Aside from these effects the plume expansion, between 1.5 m to 3.5 m downstream of the nozzle throat, are expanding at a lower rate than the magnetic field and is an indication of detached flow.

The ion velocity curves are essentially flat over the entire range of the downstream nozzle region. The ion flow appears to have been completely converted from perpendicular motion to parallel flow through conservation of the first adiabatic invariant further upstream. There are also no indications of slowing down effects or retarding of the flow of the ions. The changes in the power law scalings of the ion and momentum fluxes in the far plume during high power operation indicate the existence of an ion velocity threshold between 17 and 25 km/s.

Observation of the axial behavior for other plasma properties may also be informative. Axial data of electron density, electron temperature, plasma potential, and floating potential for both Helicon (blue) and ICH (red) time windows are displayed in figure 5.10. The data were extracted using the guard-ring Langmuir probe through methods described in section 4.1.2. The error bars displayed represent the relative systematic uncertainty measured over repeated firings. Although not as smooth as the data presented in figure 5.9, the overall trends are discernible. The electron density

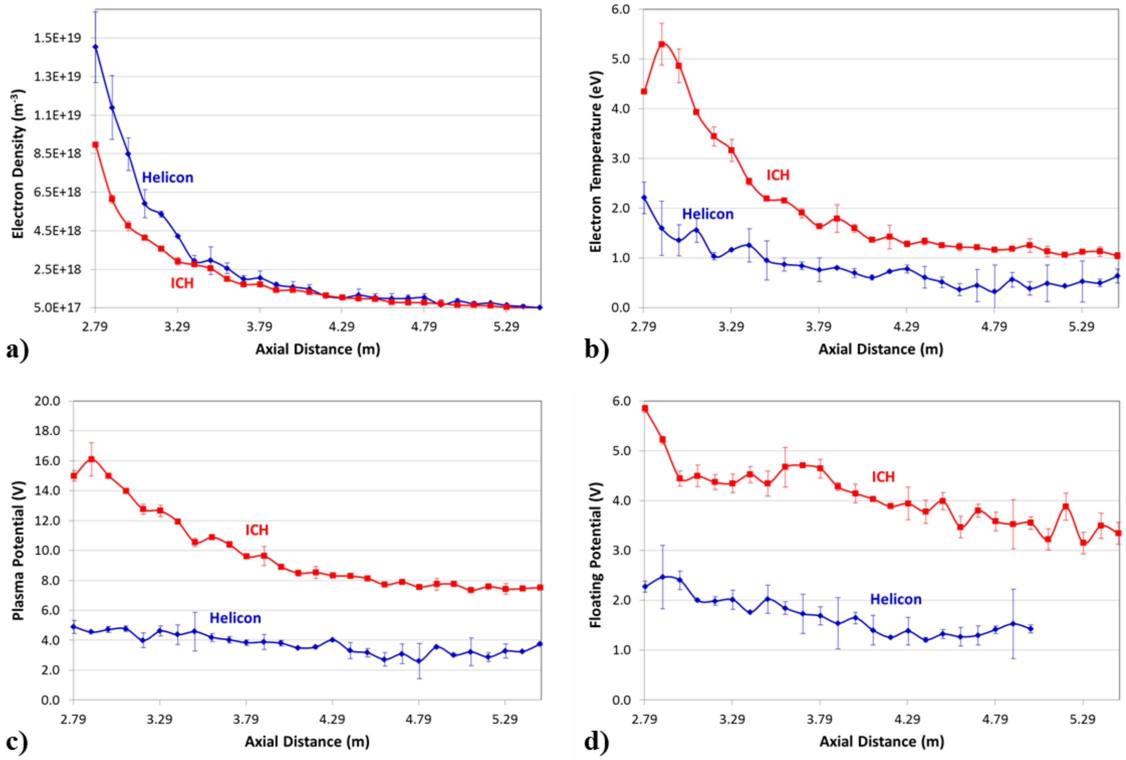

Figure 5.10: Axial data for the a) electron density, b) electron temperature, c) plasma potential, and d) floating potential during both the Helicon (blue) and ICH (red) time windows. The data shown were taken from the second experiment data set.

(figure 5.10a) peaks at a little over 1.4 x 10^{19} m^{-3} during the Helicon time window and drops to about 8.5 x 10^{18} m^{-3} as the ion velocity approximately doubles (figure 5.9d). The density measured during ICH is consistent with conservation of particle flux ($\Gamma \sim nv$), within uncertainty, and assuming quasineutrality. The density drops off more rapidly during Helicon than ICH over the first 0.6 m but merges to approximately the same value at around ~ Z = 4.0 m.

The Helicon plasma source produces relatively cold plasma with an electron temperature ranging from 0.5 – 2.1 eV at distances more than 1.5 m downstream of the source (figure 5.10b). The axial expansion provides a gradual cooling before leveling off at approximately Z = 4.5 m. The addition of energy to the ions during the ICH time window appears to also warm up the electrons. The ion cyclotron resonance antenna launches waves specific to energize ions at a given magnetic field and cyclotron frequency; it is difficult in practice to couple 100% of that energy into solely ions. Some parasitic waves or reflections may occur and permit some heating of electrons as well. This effect is seen as the electron temperature range from 1.0 eV to 5.2 eV. There is a small bump across the span of Z = 2.8 – 3.1 m which at present is believed to be related to a small axial ambipolar electric field. Apart from this bump, the electron temperature also experiences cooling as the plume expands downstream.

The plasma potential (figure 5.10c) and floating potential (figure 5.10d) are relatively flat along the extent of the nozzle during the Helicon time window. The plasma potential spans approximately +5 V to + 3 V over a distance of ~ 2.5 m. The floating potential is even more gradual dropping approximately 1 V over the same span. The final five data points from this set were outliers, having values greater than 6σ from the mean, and have been intentionally removed. Contrasting these trends in potential to those during ICH shows the plasma potential ranging from +16 V down to approximately +7.8 V. The small bump in the electron temperature between Z = 2.8 – 3.1 m is also reflected in the plasma potential and may be the cause of the bump in T_e. Also like the electron temperature falloff, the plasma potential gradually decreases before leveling out at about Z = 4.5 m. This gradient would indicate that a DC electric field forms during ICH. There do not appear to be any sharp changes after approximately 0.6 m (Z = 3.5 m), the location where the trends changed in ion, momentum, and magnetic flux. The floating potential during ICH is similarly decreasing from +6 V down to + 3 V over a distance of 2.5 m. This gradient reflects the axial trends seen in the plasma potential and electron temperature.

All of the axial data may be plotted and summarized for conditions in the magnetic nozzle during both time windows (figure 5.11). All units have been normalized to the value of the closest measured data point and systematic error bars have been scaled accordingly. Error bars that are not seen are too small to pass beyond the font size of the data point. The ion flux, Γ_i, is decreasing much faster than the axial magnetic flux, B_z, over the same distance during the Helicon time frame. The momentum flux, N/m^2, and electron density, n_e, have about the same axial falloff rate for this same discharge period until the signal-to-noise becomes too low to accurately measure strain on the PMFS (Z = 4.5 – 5.5 m). The ion velocity, v_i, plasma potential, V_p, and electron temperature, T_e, are relatively flat or have a gradual slope indicating no dramatic DC electric fields or electron pressure structures are being setup. Figure 5.11b represents ion flows with about 4x the kinetic energy Helicon only discharge (figure 5.11a). The ion flux generally follows the

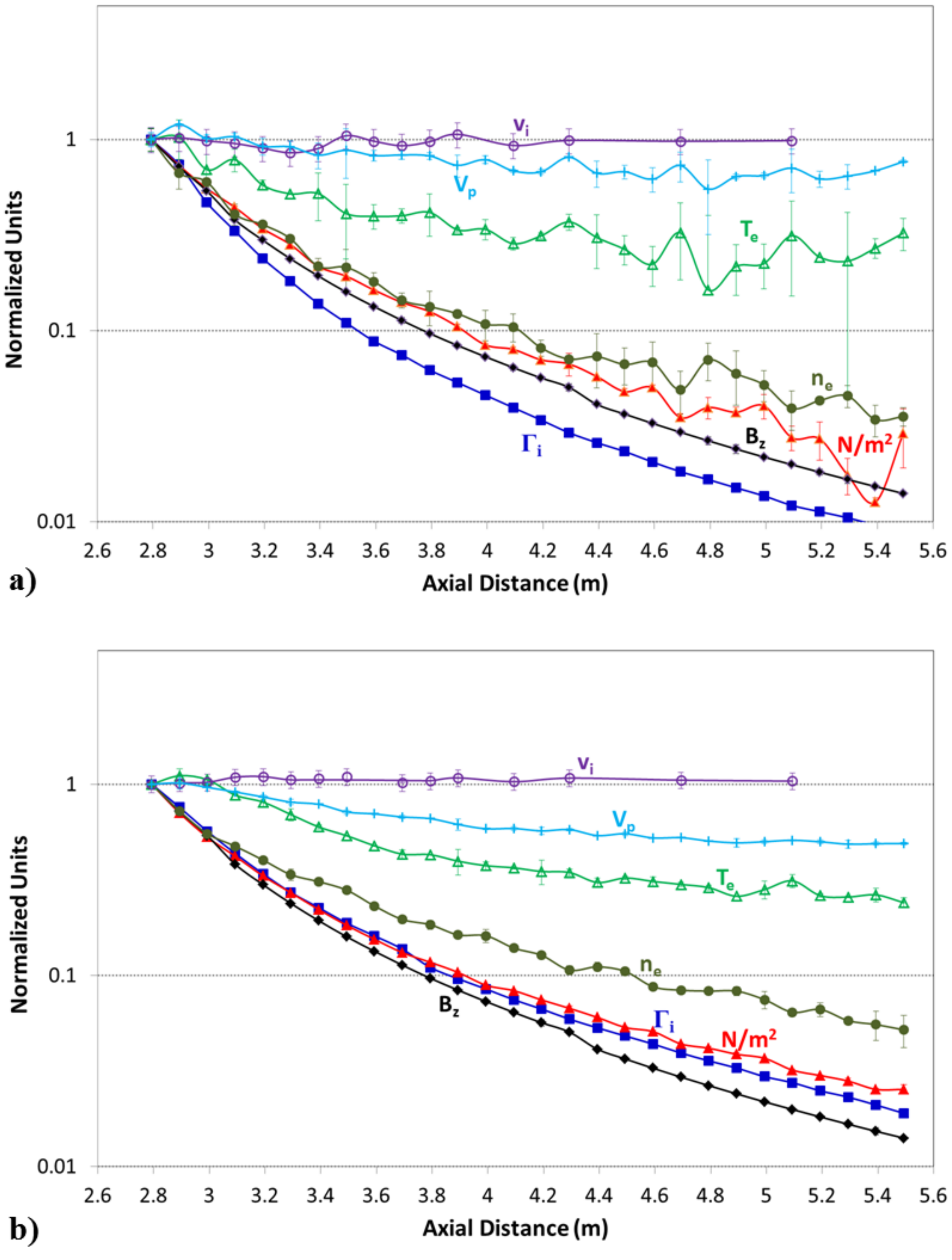

Figure 5.11: Comparison of the rates of axial expansion for various plume parameters during the Helicon (a) and ICH (b) time windows. Each parameter is normalized to the closest measured value (~ 0.7 m downstream of the nozzle throat) and plotted on a logarithmic scale. Systematic error bars taken from repeated shots are scaled accordingly.

momentum flux until Z = 4.1 m where the two quantities diverge slightly. Both fluxes drop off less than the magnetic flux which is indicative of a detached ion beam. The other quantities measured by the guard-ring probe resemble the falloff rates of those measuring during the Helicon case; but with less spatial variation as the flow becomes less erratic and better defined. Much of the plume in both cases follows approximately the same rate of axial magnetic expansion only for the first 0.3 m. Beyond this point it is difficult to argue the idea of a collectively magnetized/attached ion flow in the plume.

Section 5.3: Plume streamline analysis

Section 5.3.1: Defining the method

The previous analyses of the contour maps and the axial expansion trends are approximate indicators for ion detachment but still lacking in definitive confirmation that ions and electrons have separated from the applied nozzle field. A more conclusive approach is to map out the paths of the ions in the expanding nozzle and compare them to the magnetic field lines as the plasma flows downstream. This method has not been implemented in as detailed a manner or over the scale lengths of this experiment in previous detachment studies. The approach developed for this nozzle study involves mapping out both the ion flux and momentum flux over the extent of the plume and comparing numerically integrated paths to the magnetic flux contained within this same region. The justification for this method begins with the conservation of mass under the assumption of negligible secondary sources or losses for the ions:

$$\frac{\partial \rho}{\partial t} + \nabla \cdot (\rho \bar{u}) = S - L \approx 0 \qquad 5\text{-}1$$

where ρ is the mass density, u is the ion velocity, and S/L represent the ion sources and loss mechanisms in the plume. The partial derivative on the left hand side may be eliminated since the data were taken over time windows at steady state RF power and mass flow rate. The equation then states that the divergence of the plume is conserved and may be integrated in order to track out quantities of ion and momentum flux as a function of Cartesian space. The mapping of these conserved fluxes is accomplished by taking radial profiles of the z-component from each parameter at fixed axial locations (figure 5.12).

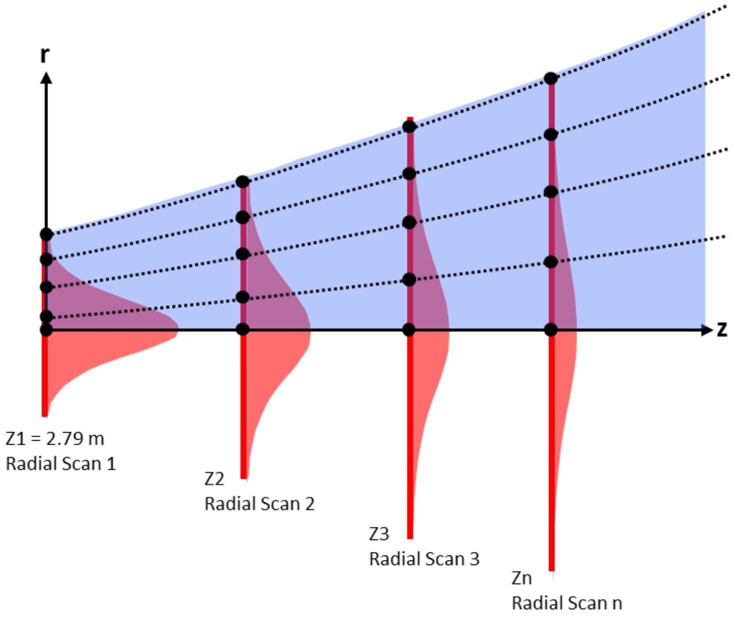

Figure 5.12: Concept diagram of following radially integrated flux as the plume expands downstream.

Ideally one would use measurements of both the axial and radial components of each probe to create mathematical streamlines, but that was not possible for these diagnostics given the probes only orientation was in the axial Z direction. The Z component should be a suitable representative of the bulk flow since most of the flow is in the Z direction, and under the assumption of azimuthal symmetry, with respect to the peak of the profile, changes in the radial component would be manifest in the axial data. Each radial profile may then be numerically integrated radially outward from the peak of the plume:

$$\Gamma_{iz}(r) = 2\pi \int_0^r \frac{J_{iz}}{q} r dr \qquad 5\text{-}2$$

$$\mathrm{F}_{iz}(r) = 2\pi \int_0^r P_{iz} r dr \qquad 5\text{-}3$$

$$f_i = \frac{\Gamma_{iz}(r)}{\Gamma_{iz1}(r_{edge})} = \frac{P_{iz}(r)}{P_{iz1}(r_{edge})} \qquad 5\text{-}4$$

Equations 5-2 and 5-3 represent a typical integration of the measured current density, $J_{iz}(r)$, and momentum flux, $P_{iz}(r)$, to produce values for ion flux, $\Gamma_{iz}(r)$, and force, $F_{iz}(r)$, respectively. The integration is performed in the coordinate reference frame of each measured profile and then offset accordingly to take into account the plume axis is not exactly aligned with the nozzle axis. Equation 5-4 describes an integer quantity referred to as the plume fraction, f_i, which takes the ratio of integrated ion flux or force from equations 5-2 & 5-3 to a reference flux/force taken along the radial profile measured closest to the beginning of the magnetic nozzle (Z1 as in figure 5.12) and serves to represent 100% collection of the plume. The reference value for ion flux or force is integrated out to r_{edge}, a position determined from a projection of the magnetic field line from the edge of the plasma core, effectively enclosing the plasma, and is a firm boundary condition. The projected magnetic field lines from along the wall of the plasma core from both the Helicon and ICH regions are shown in figure 5.13. The ICH core edge projection, r_{edge} = 0.387 m, was used as the upper limit for integration as the edge projection from the Helicon core region would not capture the entire profile during both time windows (figure 5.14).

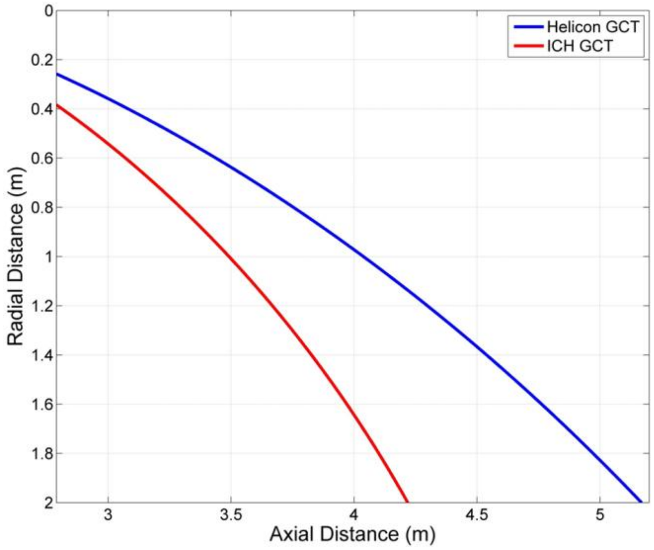

Figure 5.13: Projected magnetic field lines referencing the wall location of the gas containment tube (GCT) from both the Helicon (blue) and ICH (red) regions of the plasma core. The ICH projection (r_{edge} = 0.387 m, Z = 2.79 m) was used as an upper limit of integration for the reference flux/force values to ensure the entire plume profile was captured.

The numerical integration process begins by taking the raw axial component data along the radius (positive Y direction) of the plume. This radial profile of the data is then smoothed out using a 2nd order Savitzky-Golay smoothing filter that uses a local polynomial regression about each data point[213-215]. This smoothing will help clarify the trends in the axial expansion despite introducing some additional uncertainty, which is accounted for and propagated using[216]:

$$\sigma_x^2 = a\sigma_{\mathrm{u}}^2 + b\sigma_{\mathrm{v}}^2 \pm 2ab\sigma_{\mathrm{uv}}^2 \qquad \text{5-5}$$

where a and b are constants of proportionality, σ_u represents the systematic uncertainty of the measured value, σ_v is the uncertainty introduced by the smoothing filter, and σ_{uv} is the covariance (assumed to be negligible). The smoothed data points are then interpolated over a radial array vector using Matlab's piecewise cubic Hermite polynomial (PCHIP) function. The PCHIP interpolant is used because it results in less spatial variance than traditional splines while being smoother than simple linear interpolation. The radial array subdivides the measured radial positions into 2000 equal parts resulting in sub-millimeter resolution of the integration. The measured data, smoothed Savitzky-Golay filter, and PCHIP interpolation are shown as an example of this process in figure 5.14.

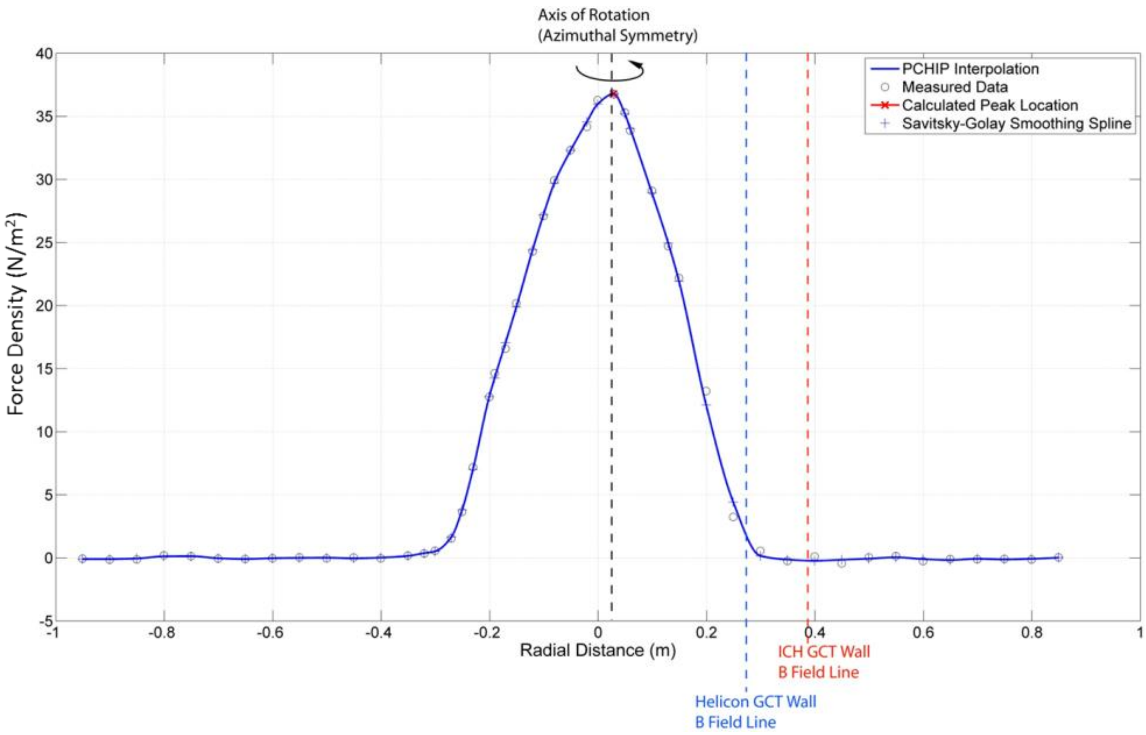

Figure 5.14: Example of a radial profile (in this case a diameter scan) of the momentum flux demonstrating the measured values, the new smoothed values, and the resulting interpolated profile. The calculated peak about which the integration is performed is displayed as well as the upper limit in the ICH field line projection.

The smoothed data array is the numerically integrated along the radial array using equations 5-2 and 5-3 and corresponding (r, z) coordinates are produced when plume fractions (equation 5-4), ranging from 5% to 95% in intervals of 5%, become equal to that fraction of total integrated reference flux/force. Similar treatment is extended to the magnetic flux, Φ_z, using:

$$\Phi_z(r) = 2\pi \int_0^r B_z r dr \qquad 5\text{-}6$$

$$f_\Phi = \frac{\Phi_z(r)}{\Phi_{z1}(r_{f_i})} \qquad 5\text{-}7$$

where B_z is the magnetic flux and f_Φ is the enclosed plume fraction representing the enclosed magnetic flux contained within each ion plume fraction along the beginning profile, r_{fi}. In other words the magnetic flux enclosed within each corresponding ion plume fraction will be measured and tracked as the plume expands in the magnetic nozzle. The plume trajectory mapping was performed using the ion flux and momentum flux from the first data set along with the previously verified modeled magnetic field [212].

Performing this radial integration over several axial positions provides expansion trends of the plume up to 95% of the reference profile. Comparing the rates of expansion of the ion and momentum flux to that of the enclosed magnetic flux is a definitive indication of the state of magnetization for the plume as a function of axial position. It is argued that if the rate of ion or momentum flux expansion matches the expansion rate of the magnetic flux, the plume may be considered to be magnetically bound to the applied nozzle field. Conversely if either fluxes expansion diverges from the enclosed magnetic flux, resulting in either a convergent or divergent plume, the flow may be considered

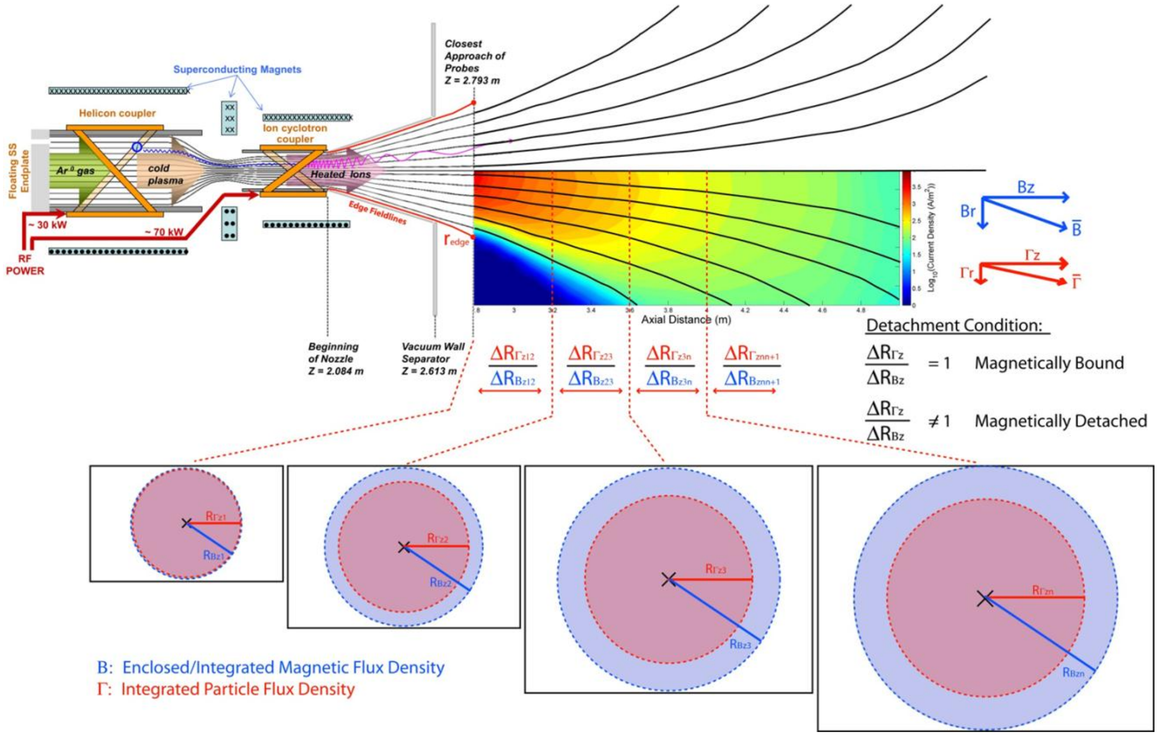

Figure 5.15: Summary of the method for mapping out the flow of ions compared to the magnetic field in order to verify detached flow. A logarithmic map of the ion flux is shown, to scale, along with the VX-200 plasma source on the left. The circles shown below represent the azimuthally symmetric cross-sections of both the magnetic flux (blue) and particle (red) as both ion and momentum flux.

separated or detached from the magnetic field. This value is taken as a ratio of the (r, z) coordinates for each plume fraction to those of the enclosed magnetic plume fraction. A summary of this method along with several scale lengths in this experiment are presented in figure 5.15. A schematic of the VX-200 plasma source is shown on the left with magnetic field lines emerging towards the right creating the magnetic nozzle. An ion flux contour map is underlain to illustrate the measurement region as well as to highlight a few of the system limits such as r_{edge} (red). The circles below represent cross-sections of the plume, magnetic flux (blue) and ion/momentum flux (red), expanding as the flow continues downstream. Comparing these spatial rates of expansion define the detachment condition.

Section 5.3.2: Mapping lines of constant integrated flux

The streamline expansion analysis for the ion flux data, as a result of the integrations are presented in figure 5.16. Lines of constant integrated ion flux for the Helicon (figure 5.16a, blue lines) and ICH (figure 5.16b, red lines) time windows are shown with corresponding ion plume fractions. The integrations were performed for ion plume fractions for every 5% up to 95% but only increments of 10% were plotted to avoid excessive clutter in the graphs. The data points displayed along each of the trends are where the integration was able to measure the value of the ion plume fraction. Some of the plotted series having fewer points as a result of the integration failing to measure certain values of the ion plume fraction within the radial limits of the translation stage.

Resultant error bars are also displayed (in black), computed and passed through the integration, assuming the maximum and minimum error bars of the reference profile. The large error bars for the Helicon case are a result of the numerical integration failing to measure the ion plume fraction values for the upper error value in the profile, giving instead the maximum radial position. Lines of best fit are presented for the downstream features for each ion plume fraction (solid black lines). The fits are mostly quadratic for the Helicon (the 90% line is a 3rd order polynomial) and entirely linear for the ICH plume. Ions along the edges (40% - 90%) during Helicon rapidly spread out and those plume fractions are not able to be mapped downstream to the final radial profile. The inner plume (10% - 30%) is still spreading more rapidly than the ICH counterpart.

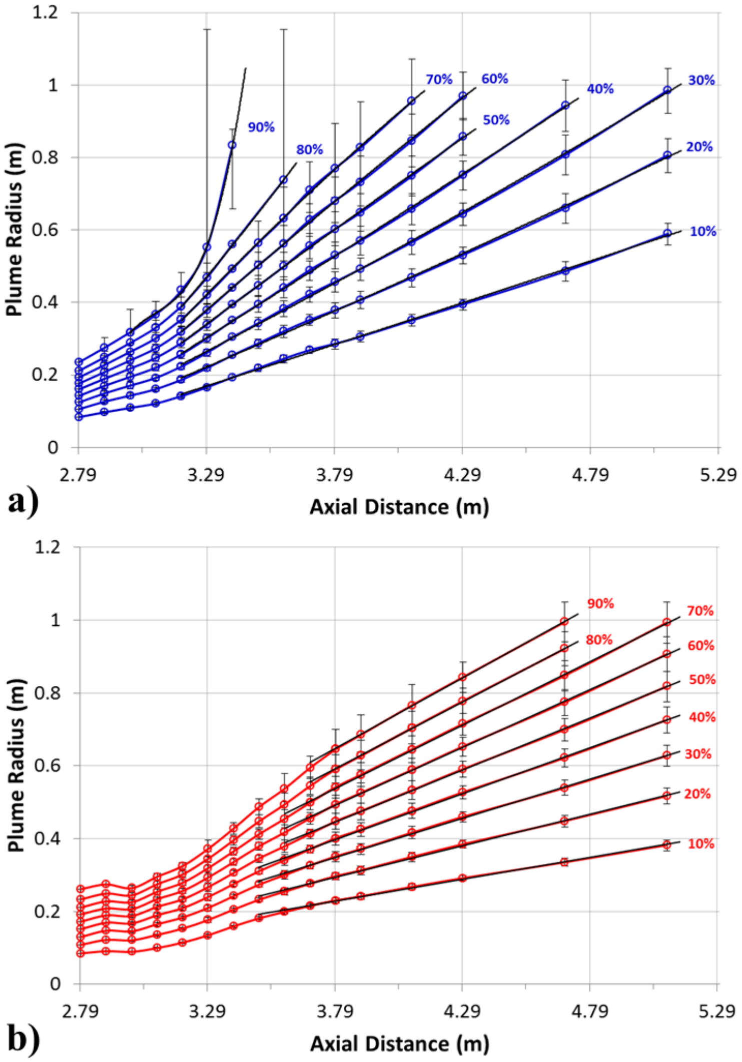

Figure 5.16: Lines of constant integrated ion flux in terms of ion plume fraction (10% - 90%) for the plasma from the Helicon (a) and ICH (b) time windows. Error bars (black) have been carried through and are shown for each datum point. Overlain lines (black) represent fits to the downstream features of the plume.

The integrations for the ICH time window were able to follow most of the data series downstream (10% - 70%) within the same translation stage limitations. This is indicative of a more focused and directed plume consistent with the analyses of sections 5.1 and 5.2. Each ICH ion plume fraction series can be broken up into three regions based on behavior and points of inflection: The first 0.2 m (Z < 3.0 m) where the plume does not expand much, Z = 3.0 m – 3.9 m where the plume integrations follow a more quadratic fit, and Z ≥ 3.9 m where the trajectories are linear or ballistic. The transition to the linear flow seems to gradually occur over the span of 3.6 m < Z < 3.9 m where the inner plume fractions linearize sooner (10%) than the outer plume (90%).

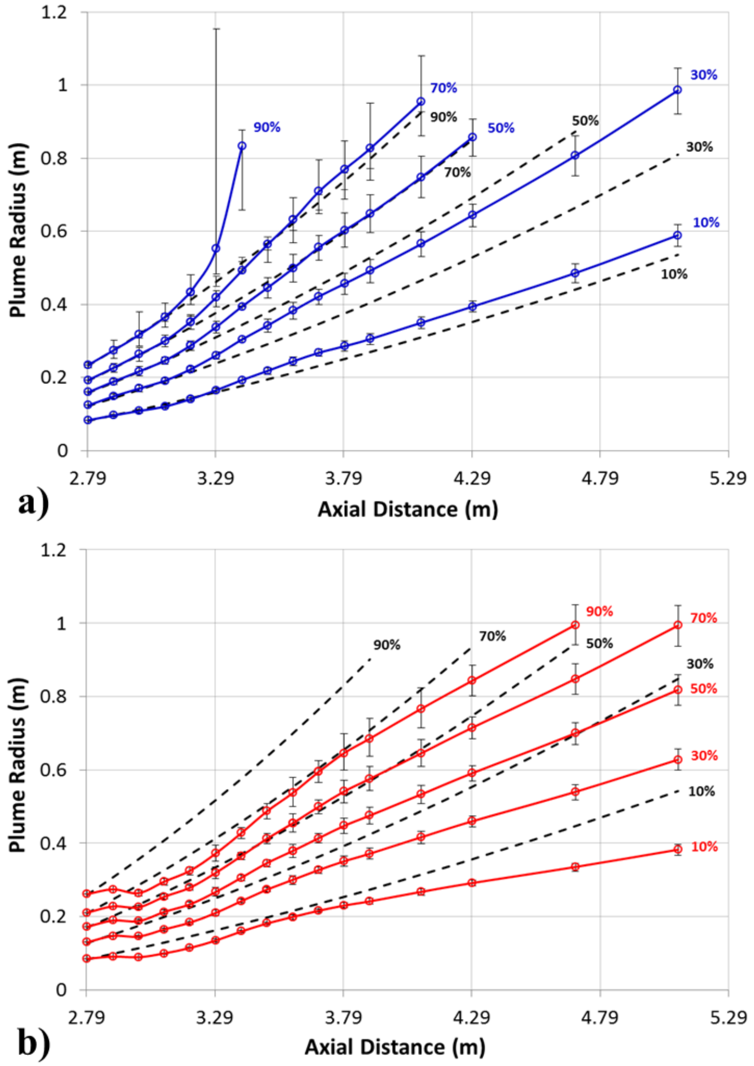

Figure 5.17: Comparison of the lines of constant integrated ion flux to the lines of constant integrated enclosed magnetic flux (black dashed) for the Helicon (a) and ICH (b) time windows.

The trends become clearer when the lines of enclosed magnetic flux (black dashed lines) and corresponding plume fractions are also displayed together (figure 5.17). Only the odd ion plume fractions (by 10%) are plotted to avoid excessive clutter on the graphs. Comparing the expansion of the ion plume during both time windows to that of the enclosed magnetic flux confirms the data trends seen in the previous sections. The ions created during the Helicon discharge expand faster than the magnetic flux while those energized by ion cyclotron resonance expand slower than the magnetic flux. Ion detachment is occurring in the sense that the integrated ion flux is not expanding at the same rate as the magnetic flux in both cases. For the Helicon window, the ions expand at approximately the same rate as the magnetic field for the first 0.3 – 0.4 m before separating divergently. One surprising aspect of this divergence is that it is observed across the plume radius for all ion plume fractions rather than those on the outer edges of the plume (60% - 90%) where the magnetic field curvature is smallest. One may expect at least partial detachment where the inner plume (10% - 40%) would follow the field lines for a greater distance downstream or have the axial ion momentum cause convergent detachment; neither of which occurs.

The higher energy ions during the ICH time window do not seem to follow the magnetic field expansion outside of the first 0.1 m. This distance corresponds to the first region mentioned above. The ions begin to deviate from the magnetic flux shortly downstream where a gradual expansion, radially outward, occurs for approximately $\Delta Z = 0.6 – 0.8$ m, nearly crossing over the expanded magnetic flux for the inner plume (10% - 20%). The ions in this region are possibly being affected by radial ambipolar forces, perhaps from the still magnetized electrons, causing this non-ballistic expansion. This effect on the ion plume expansion ceases approximately 0.8 – 1.0 m downstream of the first measurement plane marked by an inflection point where each series begin to follow a linear trajectory. It is estimated that the electrons become demagnetized or cross over the field lines near this point following a similar trajectory to the ions. Either effect would result in a reduction of any large-scale electric forces driving outward expansion.

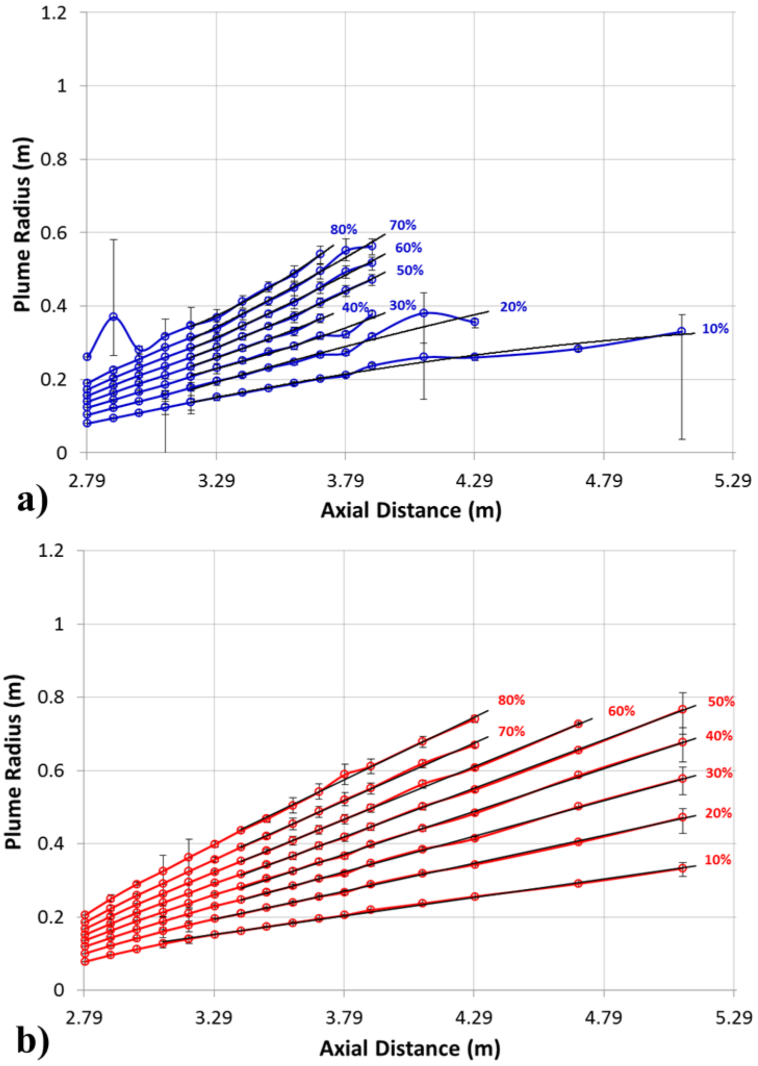

Figure 5.18: Lines of constant integrated momentum flux in terms of force plume fraction (10% - 80%) for the plasma during the Helicon (a) and ICH (b) time windows. Error bars (black) have been carried through and are shown for each datum point. Overlain lines (black) represent fits to the downstream features of the plume.

In that sense the plume, ions and electrons, are effectively detached or otherwise ballistic.

The ion momentum flux is integrated in a similar manner to the ion flux and the force plume fractions are presented in figure 5.18. The primary difference between the two integrations is the spatial resolution is lower for the PMFS than for the ion flux collectors (90 mm vs. 6 mm) at the expense of increased sensitivity. For this reason it is difficult to integrate force plume fractions close to the edge of the plume since part of the target disk is out of the plume, causing a torque about the shaft, and increases the uncertainty beyond acceptable limits. Therefore force plume fractions for the PMFS target are only reliable up to 80% of the integrated plume where the entire target is known to completely intercept the reference profile. The symbols and notation in figure 5.18 are similar to 5.16 including the overlain lines of best fit for the downstream plume trends.

The measured force during the Helicon window, figure 5.18a, is only able to be integrated downstream to ~ Z = 3.8 m because the signal-to-noise becomes too low and is essentially lost a little more than 1 m downstream of the reference profile. Despite the dropout, some of the trends are still noticeable and fits to the lines from Z = 3.2 – 3.9 m best follow a 2nd order polynomial. During the ICH window the same trends, similar to the ion flux, follow a linear trend but begin ~ 0.2 m upstream near Z ~ 3.5 m. Another difference is that the integrated force lines are separable into difference regions based on trends and multiple inflection points, as were the ion flux lines. The change to ballistic flow is smoother and more subtle.

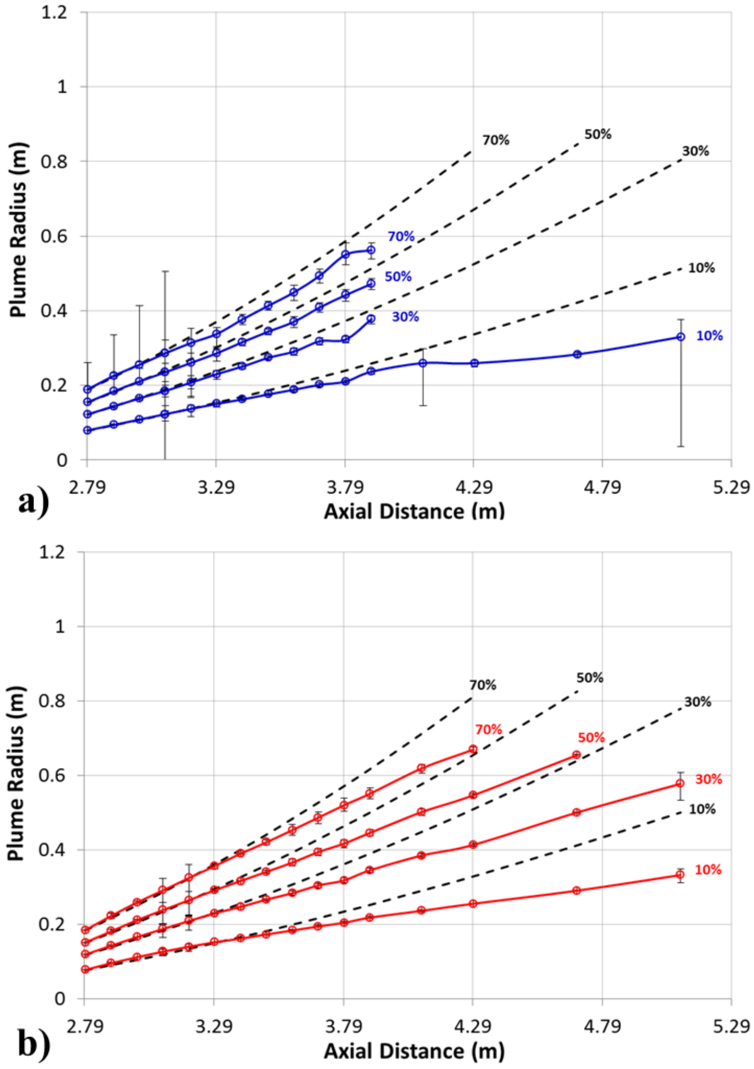

Figure 5.19: Comparison of the lines of constant integrated momentum flux to the lines of constant integrated enclosed magnetic flux (black dashed) for the Helicon (a) and ICH (b) time windows.

A comparison of the enclosed magnetic flux expansion to the integrated momentum flux is presented in figure 5.19 where the notation and symbols are similar to figure 5.17. The resulting lines of constant force, from both Helicon (figure 5.19a) and ICH (figure 5.19b), separate from the magnetic flux converging towards the nozzle axis. Because the PMFS is sensitive to both ions and neutrals the integration trends are different from the integrated expansions of the ion flux probes. The trends in the momentum flux, downstream of the separation point (Z ~ 3.2 m) during the Helicon window, behave more consistently like a signal dominated by interactions with neutrals; otherwise a more divergent detachment would be observed similar to figure 5.17a. Neutrals, not being bound to the field or affected by magnetized electrons, will seemingly continue on a linear trajectory as the magnetic flux curves away. The small component of force due to the ions will give each blue series their slight quadratic trend up and away from the axis, but overall will still be convergent. Even when the ions are energized during the ICH window, the trends of the first two ion flux regions are masked by the influence of the neutrals, and the separation point from the magnetic flux appears further downstream. Both Helicon and ICH momentum flux appear to follow the magnetic flux for at least ΔZ ~ 0.6 m before diverging. The higher velocity ions become the dominant component further downstream as the trajectories linearize similar to the ion flux. Expansion due to neutral dominated flow would continue in a straight line from the separation point (Z ~ 3.3 m), effectively bisecting the black dashed and red lines. Instead the lines curve more towards the nozzle axis. The momentum flux results at the higher ion energies then agree with the ion flux results indicating detached ion flow.

Section 5.3.3: Slope ratio analysis

A means of extending the analysis of these flux line trends is to employ the method, illustrated in figure 5.15, where a ratio of the spatial derivative of the line trend to the spatial derivative of the enclosed magnetic flux is plotted with increasing distance. This dimensionless quantity is referred to as the slope ratio, SR, and may be expressed as:

$$SR = \frac{\mathrm{m}_{\Gamma_n}}{m_{B_n}} = \frac{\left(\frac{dR_{\Gamma_n}}{dz}\right)}{\left(\frac{dR_{B_n}}{dz}\right)} = \frac{R_{\Gamma_{n+1}} - R_{\Gamma_n}}{R_{B_{n+1}} - R_{B_n}} \qquad 5\text{-}8$$

where the ion flux, Γ, may be freely interchanged with the force F, and n an the integer representing each radial profile beginning with the reference profile at Z = 2.79 m. The slope ratios for the integrated ion flux and corresponding enclosed magnetic flux are plotted according to axial position in figure 5.20 during both time windows. In each plot all of the ion plume fractions are included and range in color from black (5%) to blue (55%) and green (60%) to red (95%) over a scaled color gradient. The detachment condition indicating an equivalent expansion rate is also plotted as a thick red line. Error bars are propagated along using a combination of equation 5-5 as well as[216]:

$$\frac{\sigma_x^2}{x^2} = \frac{\sigma_{\mathrm{u}}^2}{\mathrm{u}^2} + \frac{\sigma_{\mathrm{v}}^2}{\mathrm{v}^2} \pm 2\frac{\sigma_{\mathrm{uv}}^2}{\mathrm{uv}} \qquad 5\text{-}9$$

where the covariance, σ_{uv} is assumed to be negligible, and u/v are the corresponding components of the slope ratio equation and their associated uncertainties. It is interesting to point out that for both time windows the slope ratio trend is similar along the span of Z = 3.0 – 3.8 m where the SR increases at first (Z ~ 3.0 m) before rolling back over (Z ~ 3.3 m) and leveling out (Z > 3.8 m). This is the region where ambipolar electric forces appear to be significant influencing the motion of free ions. Beyond this region the Helicon (figure 5.20a) SR has a nearly constant gradient indicating free expansion of the plume. The bulk ion flow lies above the convergent detachment threshold and the plume may still be influenced by the magnetized electrons or the magnetic field lines are starting to turn back. The vertical spread in SR indicates a greater spread of the plume and results in lower nozzle efficiency and a larger pitch angles distribution. During ICH (figure

5.20b) the SR gradient at the inflection point (Z = 3.8 m) and beyond indicate ballistic ion trajectories as the magnetic flux slope increases and the ion flux slope remains the same. The vertical spread in SR narrows showing a more directed bulk flow, higher nozzle efficiency, and suggests a more concentrated pitch angle distribution.

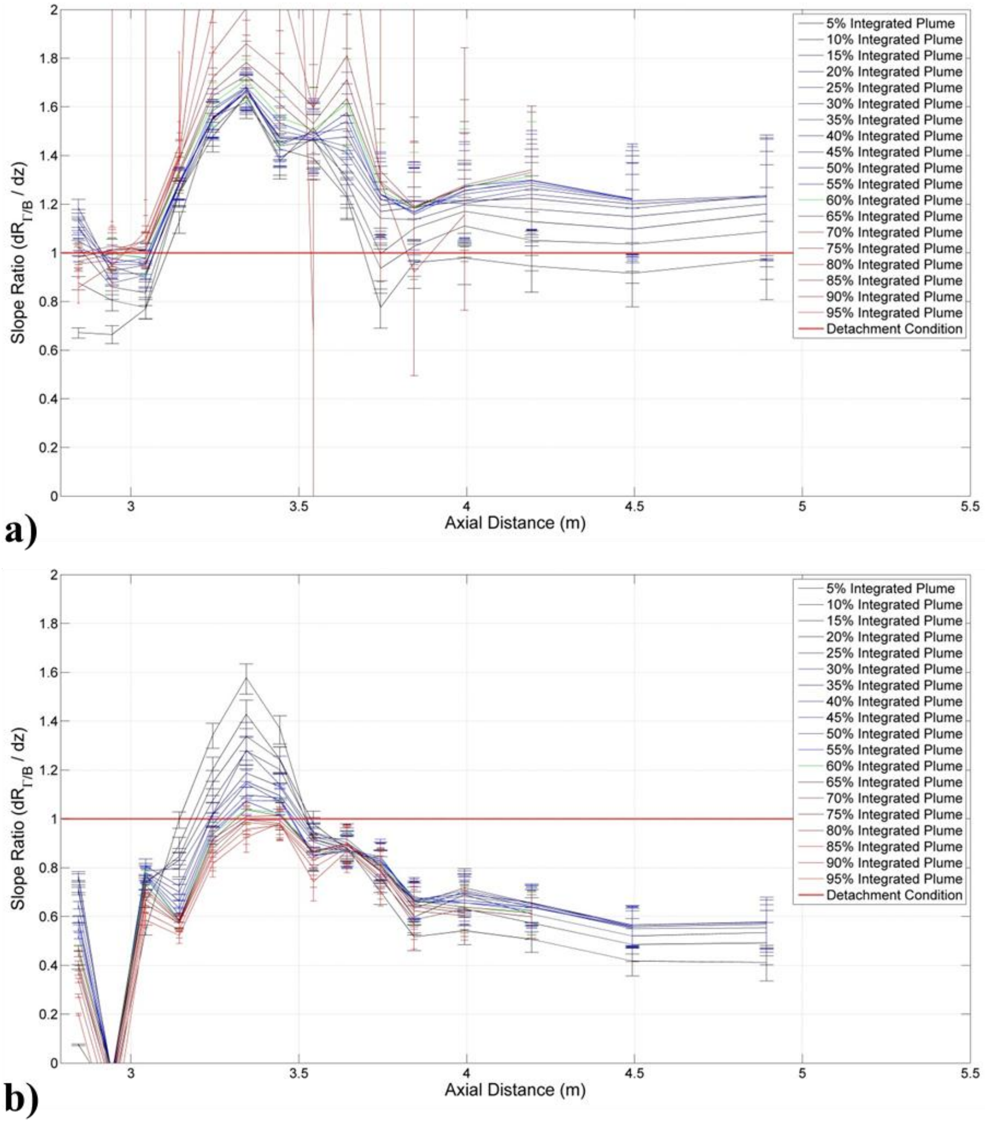

Figure 5.20: Plots of the Slope Ratio trends for all of the ion flux plume fractions during both Helicon (a) and ICH (b) time windows. A value of 1 indicates expansion at the same rate as the magnetic flux while values higher or lower than unity confirm divergent or convergent detachment respectively.

The slope ratios for the integrated momentum flux are plotted in a similar manner as the ion flux and are displayed in figure 5.21. During the Helicon (figure 5.21a) time window, the data beyond Z ~ 3.6 m are too noisy for clear trends to emerge and are essentially useless. Upstream of that point (Z < 3.6 m) the SR trend is clear such that it has a negative, nearly linear gradient confirming a ballistic, neutral dominated signal and

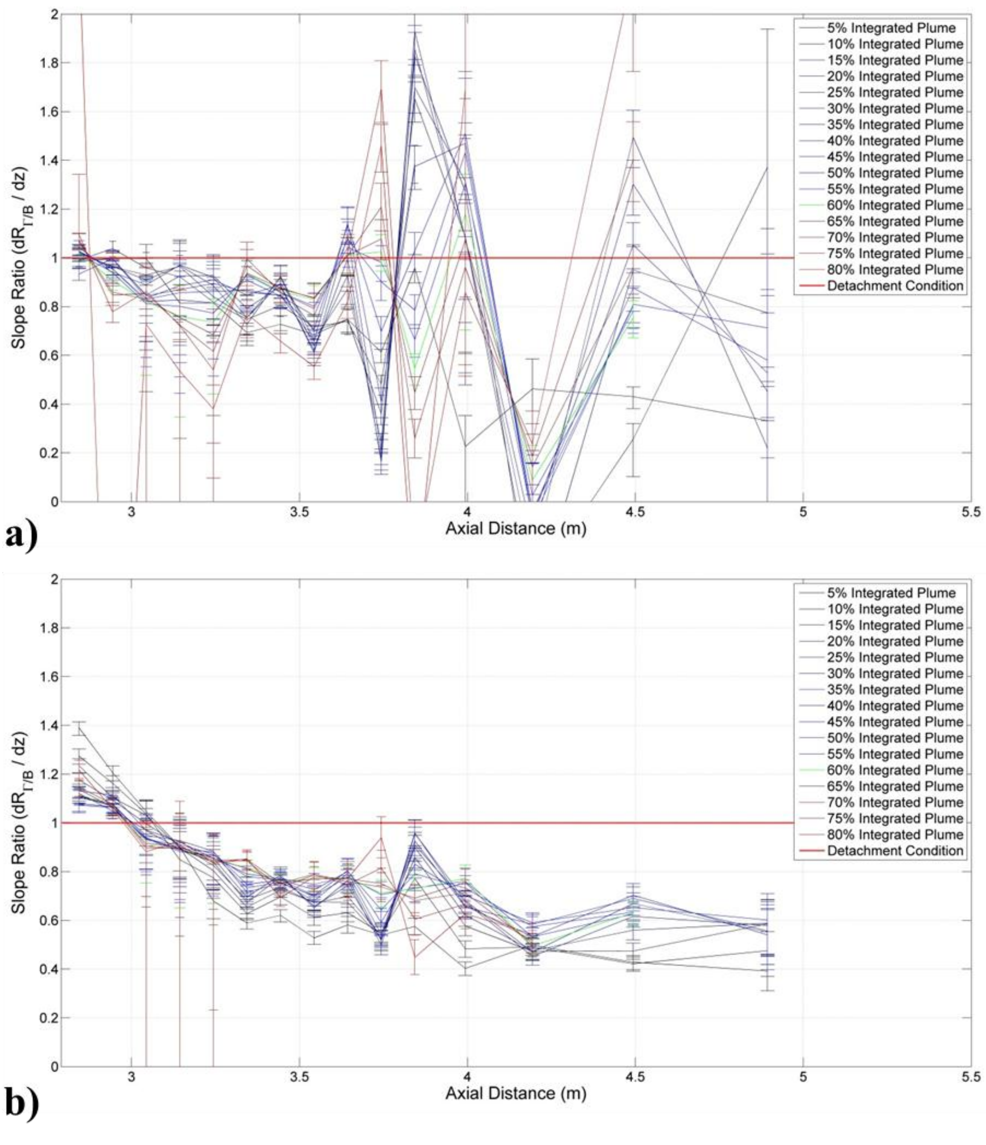

Figure 5.21: Plots of the Slope Ratio trends for all of the force plume fractions (up to 80%) during the Helicon (a) and ICH (b) time windows. A value of 1 indicates expansion at the same rate as the magnetic flux while values higher or lower than unity confirm divergent or convergent detachment respectively.

is expected given the nature of the probe. When ICH power is applied (figure 5.21b) the SR gradient is steep and negative from Z = 2.8 – 3.3 m before folding over to a gradual yet still declining trend for Z > 3.3 m. The far plume SR trend (Z > 3.8 m) is nearly identical to the ion flux SR confirming that the ions have separated from the magnetic nozzle and are following a ballistic, freely-expanding trajectory.

Section 5.3.4: Detachment angle analysis

It is useful to quantify the separation further by looking at the angle formed between the each of the ion plume layers, for both the ion and momentum flux, and the magnetic flux. This angle can be expressed as:

$$\theta_n = \tan^{-1}\left(\frac{m_{B_n} - m_{\Gamma_n}}{1 + m_{B_n} m_{\Gamma_n}}\right) \qquad \text{5-10}$$

where m_{Bn} and $m_{\Gamma n}$ are the slopes of the n^{th} axial point of the magnetic flux and ion flux respectively. These angles are plotted for the ion flux, over all of the ion plume fractions, during both Helicon (a) and ICH (b) time windows in figure 5.22. Similar to the computations involving the slope ratios, the uncertainty is taking into account in equation 5-10 using equations 5-5 & 5-9. The ions during the Helicon window appear to follow the magnetic flux for the first 0.3 m (Z ~ 2.8 – 3.1 m), then spread rapidly to angles greater than -20° (Z ~ 3.1 – 3.8 m), before leveling out with a nearly constant angular spread of 0° to -7° (Z > 3.8 m). The negative angles correspond to divergent detachment where the difference between the slopes of the magnetic flux and the ion flux is negative. The ions during the ICH window follow a similar trend up to Z ~ 3.8 m except that the angular range has been shifted about 10° more positive. At greater distances ($Z \geq 3.8$ m), in the region where the ion plume fractions expand linearly, the detachment angles range from 4° to 10°+, indicating convergent detachment, and appear to be trending gradually upward. These angles may seem modest but only small deviations from the nozzle field are sufficient to confirm detached flow.

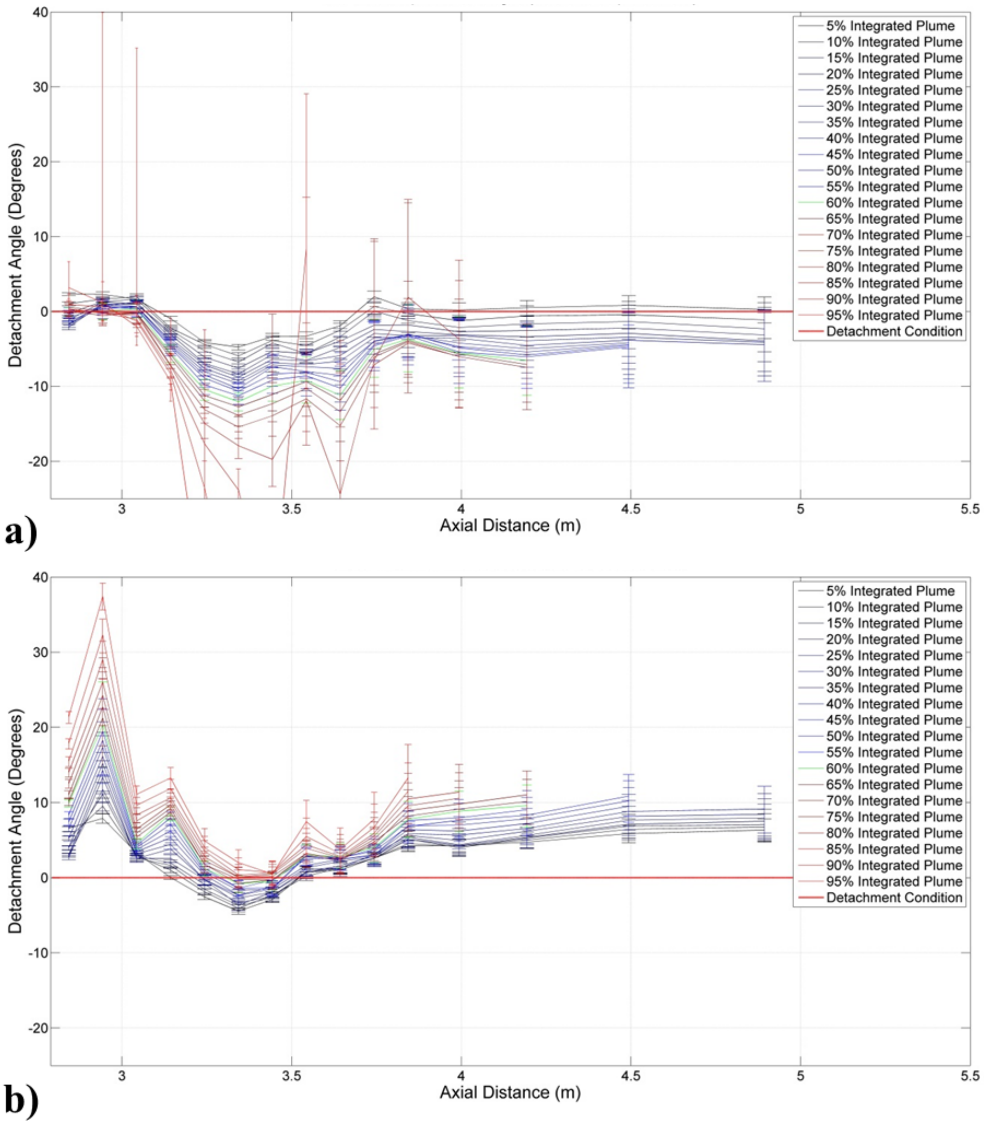

Figure 5.22: Plots of the angle between ion flux plume fractions and expanding magnetic flux as a function of axial position for the Helicon (a) and ICH (b) time windows. A positive angle indicates convergent separation while negative corresponds to divergent separation.

The same analysis performed on the momentum flux lines are displayed in figure 5.23. Similar to the slope ratio plots (figure 5.21), the detachment angles during the Helicon time window (figure 5.23a) reflect a signal dominated by the free expansion of neutrals, shown as a linear trend from 0° to 3.5° over the span of Z = 2.8 – 3.6 m. Beyond Z = 3.6 m the data are no longer usable. When the ions are accelerated (figure

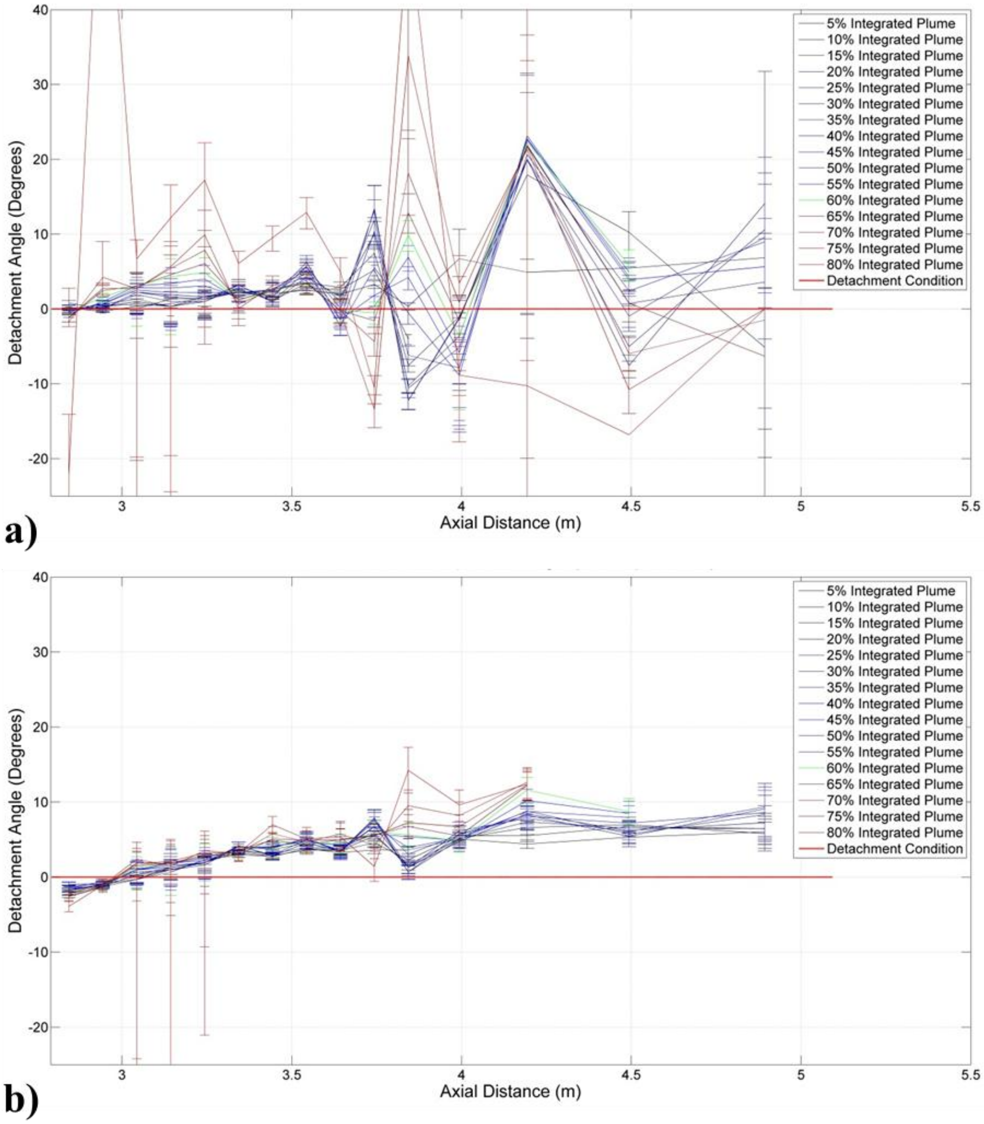

Figure 5.23: Plots of the angle between force plume fractions (up to 80%) and expanding magnetic flux as a function of axial position for the Helicon (a) and ICH (b) time windows. A positive angle indicates convergent separation while negative corresponds to divergent separation.

5.23b) and parallel ion energy increases, the axial trends in the detachment angle do not change significantly (~ 1°) from the low ion energy case over the same span. The far plume (Z > 3.8 m) angles line up well with the ion flux detachment angles having a slight upward trend and angular span of 4° - 10°. If the translation stage were able to move further outward being able to collect the entire plume at the large axial distances, it is reasonable to expect detachment angles nearing 15° for the higher plume fractions. Never-the-less the detachment angles for the momentum flux data, in the 'linear' region (Z > 3.8 m), are indicative of convergent ion flow separated from the applied magnetic field of the nozzle.

To summarize the results of this section, a new method has been developed to follow the expansion of the ion, momentum, and magnetic flux as the plume flows along the axis of the magnetic nozzle. Both the ion flux and momentum flux, along with the enclosed magnetic flux density, were integrated producing lines of constant ion flux, force, and magnetic flux for discrete increments (5% to 95%) of the upstream measured plume reference. This procedure was done for the plasma during both experiment data windows. The constant ion flux lines revealed there are up to three distinct plume regions and the plume at low ion energies (Helicon) expands *more* (divergent detachment) than the magnetic flux while the plume at higher ion energy expands less (convergent detachment). The ion trajectories in the convergent detachment scenario follow a linear/ballistic trend at separation angles up to and exceeding 10°. These results are validated by force target data despite additional sensor interaction from neutrals not affected by the magnetic field. Divergence of the ions from the magnetic flux for both ion energy levels is confirmed, although the trajectory of the low energy ions may be affected more by radial electric forces.

Section 5.4: Ion velocity vector analysis

In certain regions of the plume ion detachment can be confirmed by measuring the pitch angle distribution of the velocity vectors which for magnetized plasma will be directed along the magnetic field line vector. This pitch angle distribution can also serve to validate parts of the slope ratio trends described in the previous section. This distribution is measured with the RPA using methods discussed in section 4.4. In an RPA the ion velocity distribution is proportional to the first derivative of the current versus voltage signal and can be quantified if the transmission function/alignment of the grids is known. Once the velocity distribution is measured for one orientation, with respect to the nozzle axis, a stepper motor is used to rotate a goniometer at the base of the probe causing the probe to pivot to a new orientation (figure 4.16). This process was repeated over several angles ranging from $\alpha = 0°$ to 90°, in increments of 10°, for five radial locations between R = 0 – 0.4 m. Each of these five pitch angle distributions were taken with the RPA located at Z = 3.9 m. These particular data were reduced and plotted by Dr. Edgar Bering III, professor of physics and electrical and computer engineering at the University of Houston.

The ion velocity pitch angle distribution at (r, z) = (0 m, 3.9 m) is presented in figure 5.24. These graphs display the perpendicular ion velocity versus parallel ion velocity, referenced to the nozzle axis, as a logarithmic contour map of the ion distribution function. The components of the magnetic field are listed in the legend and the cumulative field vector is overlain (black arrow). The plume during the Helicon time window (figure 5.24a) features a wide angular distribution where the bulk of the low ion energy flow ranges from α = 0° – 50° and drops off to lower energies approaching the

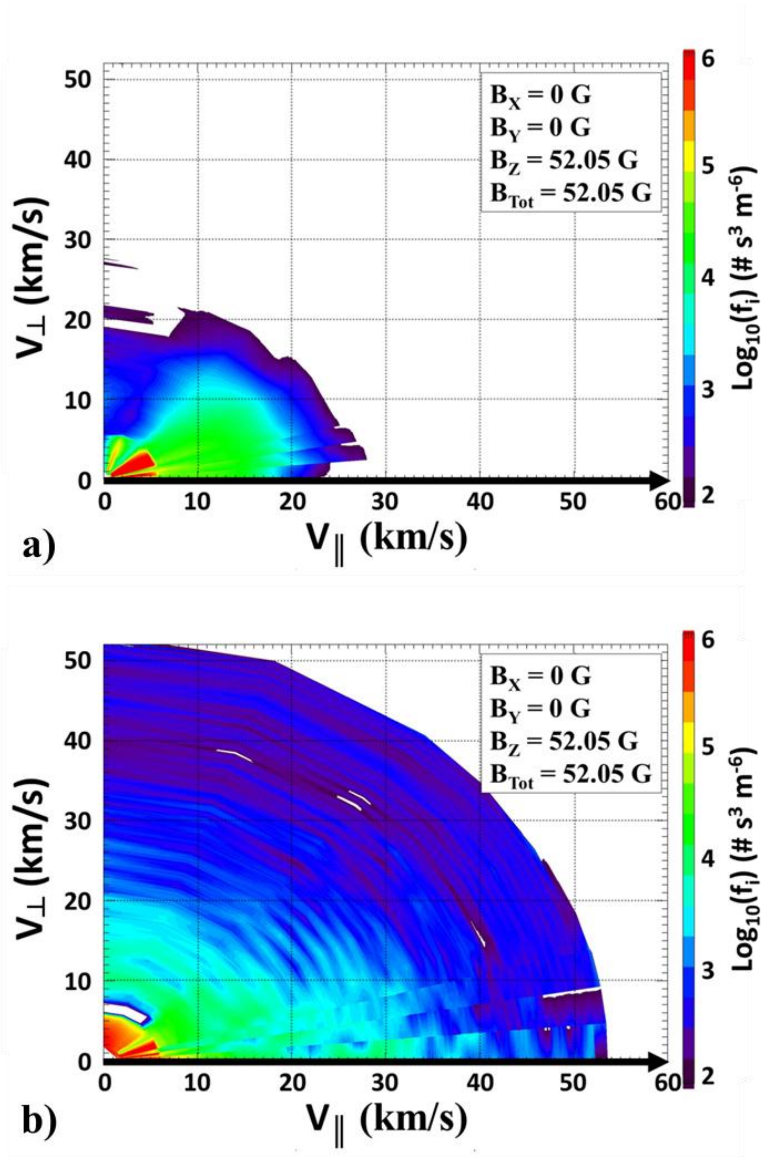

Figure 5.24: Pitch angle distribution contour map for (r, z) = (0 m, 3.9 m) during the Helicon (a) and ICH (b) time windows. The ion distribution function, displayed logarithmically, was interpolated linearly between the parallel and perpendicular velocity components. The local magnetic field vector is displayed (black arrow). Neither flow is concentrated primarily along the magnetic field but is spread out.

larger angles. The bulk of the ion flow during ICH (figure 5.24b) similarly is spread out over a broad angular range with flows up to 20 km/s up to α = 90°. The difference is that the higher energy flow is directed more along the parallel velocity component up to α ~ 20°. Neither of the two cases support that the flow is still magnetized, where if true the angular spread would be narrower and preferentially concentrated near the magnetic field vector.

To confirm these flow effects it is useful to contrast the distribution along the nozzle axis with a similar pitch angle distribution taken at a larger radial position (0.4 m) where the magnetic field vector is not parallel to the nozzle axis (figure 5.25). The bulk of the ion flow during the Helicon window (figure 5.25a) in not limited to solely follow the local magnetic field vector. The spread in the pitch angle is greater at R = 0.4 m than at R = 0 m ranging up to α ~ 75° (opposed to α ~ 50°). This larger spread is similarly reflected in the outward vertical trend of the ion flux slope ratios, shown in figure 5.20a. The simple conclusion is that with increasing radius the pitch angle distribution for lower velocity ions broadens. This effect is not necessarily the case with higher velocity ions seen during the ICH window (figure 5.25b). Along the nozzle axis a non-negligible fraction of ions had perpendicular velocities up to 20 km/s, whereas at larger radial distances this fraction is reduced, the bulk flow is mostly parallel to the axis (α < 45°), and extends to higher tail end velocities (v_i > 50 km/s). A similar conclusion is that larger radii the pitch angle distribution for higher velocity ions narrows becoming more axially directed or focused.

The other important conclusion to draw from figure 5.25 is that the flow for both high and low velocity ions do not show any signs of predominant magnetization, even at larger radial distances where the magnetic field is beginning to curve away. The bulk flow does not display any preferential organization near the angle of the magnetic field. This claim is validated for any of the ion energies across this radial scan. A graphical summary of these pitch angle distributions is presented in figure 5.26 with each subplot

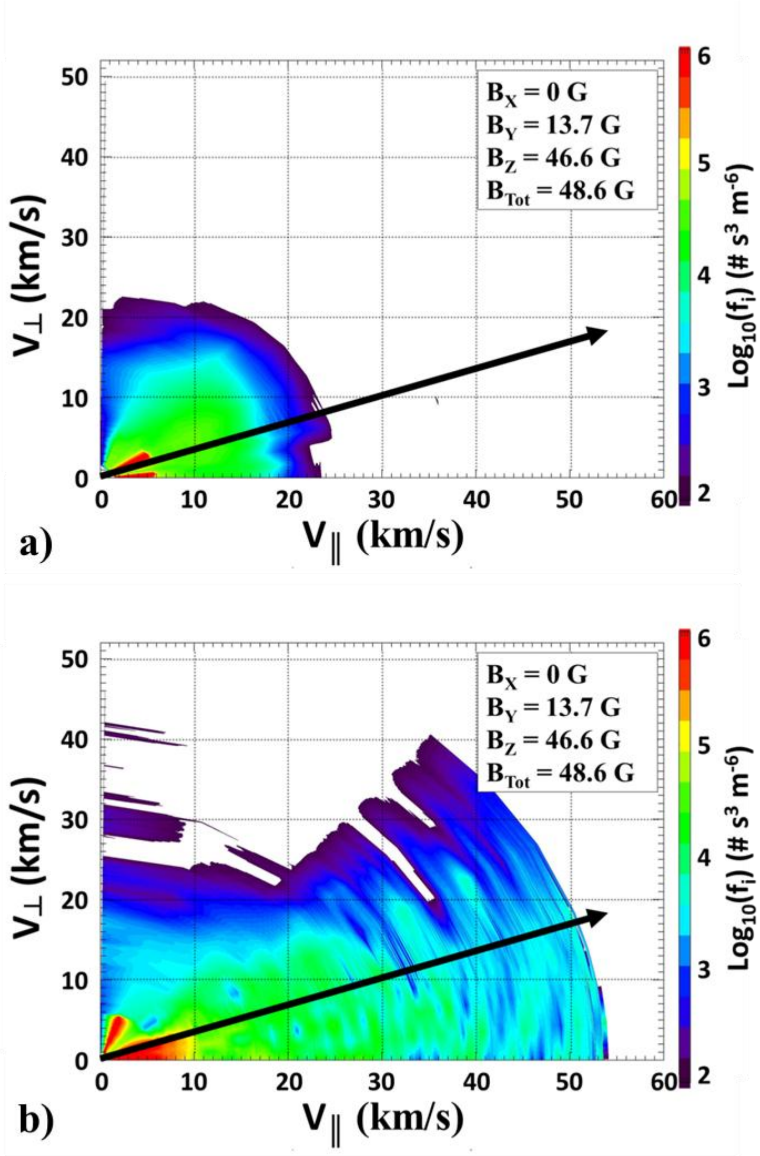

Figure 5.25: Pitch angle distribution contour map for (r, z) = (0.4 m, 3.9 m) for the Helicon (a) ICH (b) time windows. The ion distribution function, displayed logarithmically, was interpolated linearly between the parallel and perpendicular velocity components. The local magnetic field vector is displayed as a black arrow. The magnetic field is directed further away from parallel and neither case organizes about the field line. The flow is not magnetized.

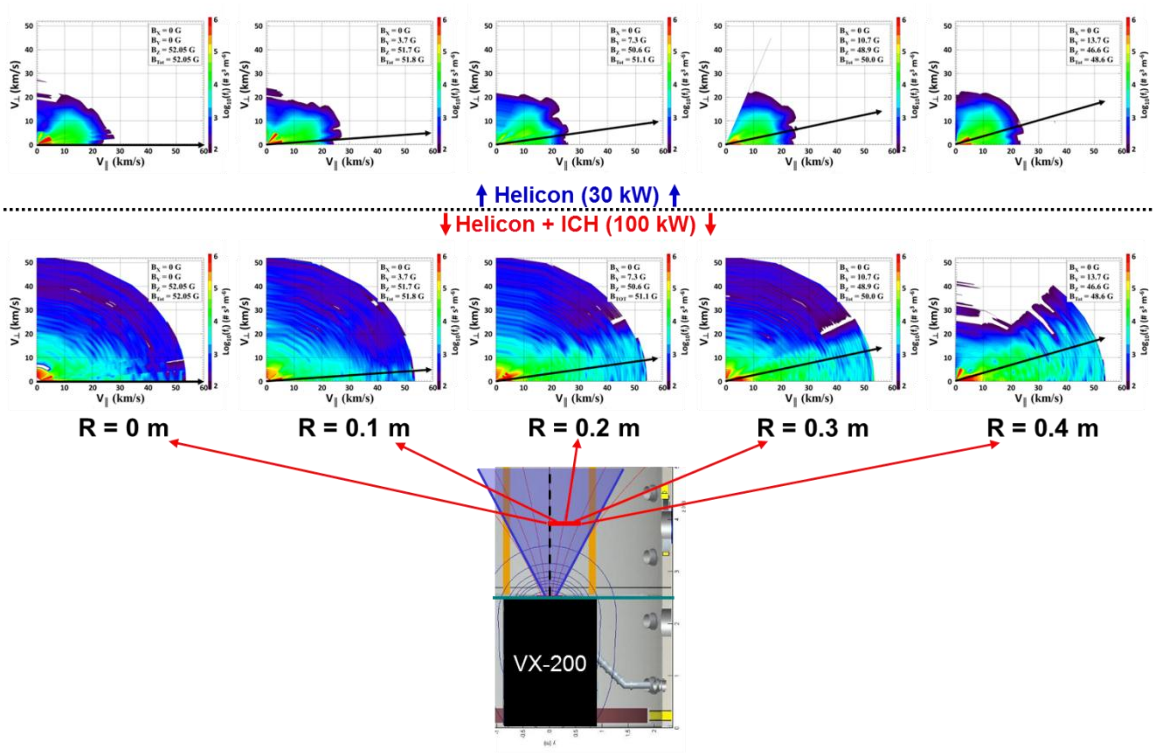

Figure 5.26: Graphical summary of pitch angle distributions across the radial section R = 0 – 0.4 m at a constant Z = 3.9 m. The contours along the top row represent the low energy ions during the Helicon power window while the bottom row similarly show the higher energy ions accelerated during ICH. The radius increases by 0.1 m from left to right with each displaying the local magnetic field vector. None of the cases indicate bulk magnetized flow or organization about the field vector.

setup similarly to figures 5.24 & 5.25. The radius increases by 0.1 m from left to right, from 0 – 0.4 m, and the local magnetic field vector is displayed as a black arrow. The same conclusions may be drawn in regards to the pitch angle spread and extent of the ion energy as a function of radius. At an axial distance ~ 1.9 m downstream of the nozzle throat, the trend is that the pitch angle broadens at larger radii for low energy ions. At higher ion energies the pitch angle distribution becomes narrowed and extends to higher parallel velocities. The ions are detached from the magnetic field and confirm the ion and momentum flux data along this axial plane (Z = 3.9 m). The physical limits of the translation stage prevented the acquisition of pitch angle distributions at radii larger than

0.4 m. The RPA pivot mechanism seized during a second radial scan leaving the above data as the lone successful set. A more detailed radial mapping of the pitch angle distributions at multiple axial planes may be the focus of future experimentation and will play an important role in measuring the velocity conversion efficiency (nozzle efficiency) for a given magnetic nozzle topology.

Section 5.5: Plasma electric field analysis

Measurement of the plasma electric field, whether steady state (DC) or time varying (AC), is informative of the electric forces that may influence electron motion/transport which are important in understanding the complete detachment scenario. The DC electric field, as a simple estimate, may be found from plasma potential measurements over the extent of the plume despite the uncertainty introduced by the RF plasma source. The AC electric field is measured by taking the power spectrum between a pair of electrodes and converting the voltage signal to a frequency dependent electric field as described in section 4.5. Each type of electric field for this magnetic nozzle setup will be described in the following sub-sections.

Section 5.5.1: DC Electric field

As mentioned above the steady state (DC) electric field is derived from the plasma potential data acquired from the guard-ring probe measurements from the second experiment data set. Color contour maps showing these plasma potential measurements for each time window is displayed in figure 5.27. The white areas are regions where the signal-to-noise ratio was too low to get reliable measurements. Plume features are enhanced using a logarithmic scale. The plasma potential during the Helicon window (figure 5.27a) is fairly flat and generally uniform from Z = 2.8 – 4.2 m ranging from 3 – 7 V with a peak of 8.1 V. Recalling from Section 4.1.1, plasma potentials measured in RF plasma sources, using non-compensated probes, are susceptible to fluctuations that introduce uncertainty to the measurement. The fluctuations induced during Helicon plasma were characterized to be minimal (± 0.2 V) but are an order of magnitude larger during ICH (± 4.0 V). Despite the larger uncertainty, the overall trends are clear and a structure emerges that resembles the velocity contour map from figure 5.6b. It is then reasonable to assume that the relative spatial gradients in the plasma potential remain

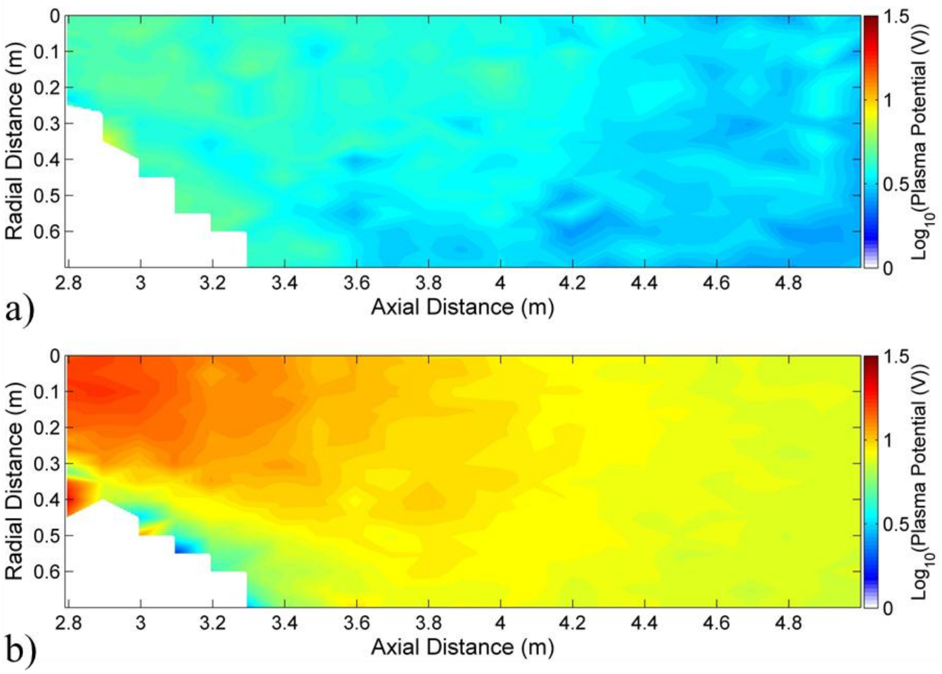

Figure 5.27: Color contour maps of the plasma potential during the Helicon (a) and ICH (b) time windows. The data were interpolated linearly and plotted on a logarithmic scale to visually enhance the plume structure. Areas displayed in white represent regions where no data are possible due to low signal-to-noise ratio and therefore unable to be interpolated. Data are taken from the second experiment data set.

valid and that the electric field will be accurate. The plasma potential ranges as low as 5 V to as high as 17 V with a peak of 21.2 V.

The electric field vectors are computed by taking the negative gradient of the plasma potential from figure 5.27 along both the radial and axial directions. It is understood that taking the derivative of a noisy signal tends to amplify the noise, but valuable trends still emerge. The radial component of the electric field is displayed in figure 5.28. The low ion energy plasma during the Helicon time window (figure 5.28a) is fairly uniform with a few scattered 'hot' spots having electric fields greater than 15 V/m.

These hot spots may be attributed to noise from the plasma potential. Also misleading are values along the edge of the region where no reliable data exists, white

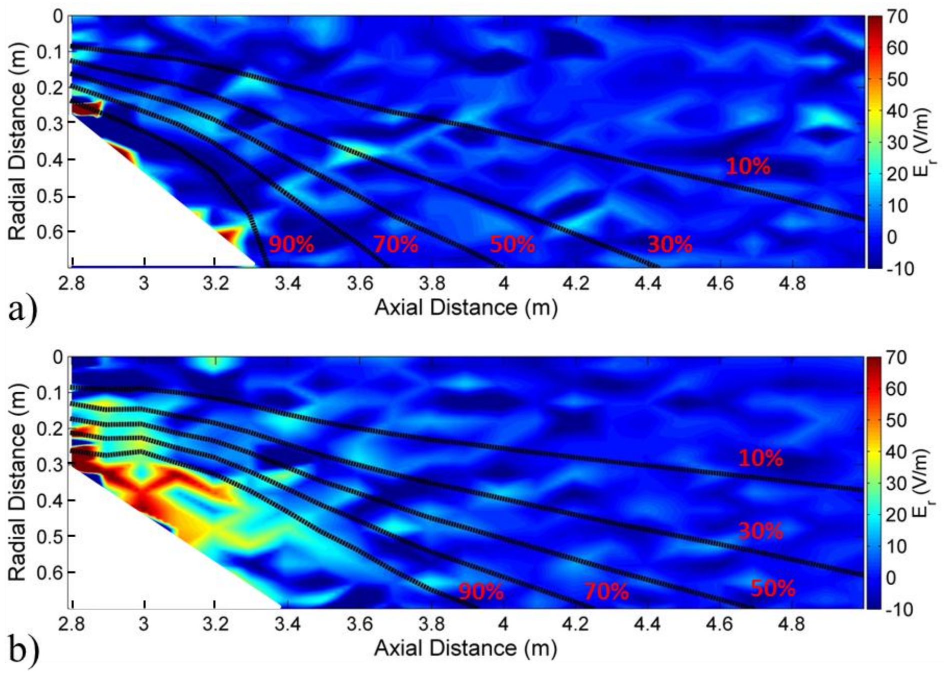

Figure 5.28: Contour maps of the radial component of the DC electric field vector for plasma during the Helicon (a) and ICH (b) time windows. Lines of constant integrated ion flux (black dashed) and corresponding ion plume fraction (red labels) have been displayed for reference. Regions with no data are shown in white.

areas, as the derivative may take a sharp jump. The integrated lines of constant ion flux from the corresponding plume fractions are displayed for reference. This flat radial field does not indicate the existence of any large-scale force that would cause low energy ions to diverge more than the applied magnetic field. This claim could be presumptive as the data may not be taken far enough in radius or erroneously assuming the effects at the plasma vacuum interface are negligible. The electric field during the ICH window (figure 5.28b) may be more informative since the plasma potential has more radial structure. The electric field structure is essentially flat within the flow, closely similar to the values during the Helicon case, but much higher along the edges of the flow (up to 75 V/m). The 90% integrated ion flux line tracks along this edge confirming data between two separate plasma diagnostics by defining an effective plume boundary. This boundary serves to answer the question of causality as the radial electric field is a result of the flow from the higher energy plume and not the other way around. The positive radial field in this region will contribute to an azimuthal E×B drift on magnetized electrons which will be discussed in the next chapter. The radial electric field along the plasma boundary drops off with increasing Z where by Z ~ 3.8 m the magnitude merges with the inner-plume electric field, aligning with the location where the plasma potential flattens out. This point also aligns with the same location that the ion flux transitions to linear flow trajectories as was discussed in section 5.3.

The axial component of the DC electric field is displayed in figure 5.29 and is presented similar to figure 5.28. The axial fields are similarly noisy and the overall magnitudes are lower than the radial counterparts ($\mathbf{E_z} \sim 8 - 10$ V/m on average) with maxima slightly greater than 30 V/m. For this component the positive electric field is largely concentrated in regions where the plume is flowing. During the first data time window (figure 5.29a) the plume is widely spread out as marked by the 90% ion plume fraction line and the axial electric field matches this spread. With the addition of ICH (figure 5.29b) and more energy to the ions, the axial electric field outside of the 90% integrated ion flux for Z < 3.8 m drops off. An axial gradient forms (for Z< 3.6 m) during the high ion energy case and is not present at low ion energies. The gradient during the ICH window drops off in magnitude to the levels observed during Helicon plasma alone between Z ~ 3.6 – 3.8 m.

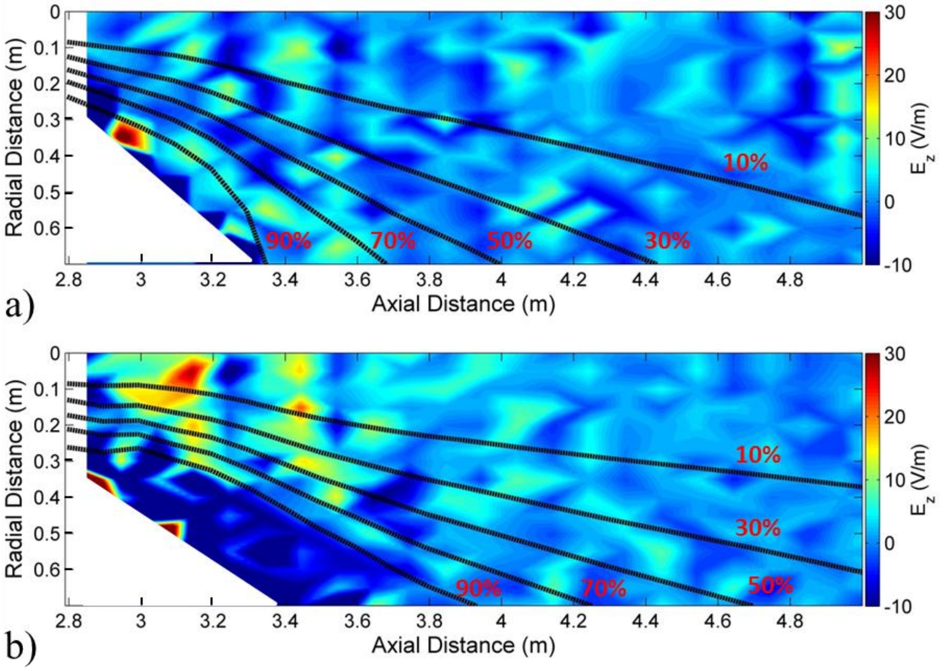

Figure 5.29: Contour maps of the axial component of the DC electric field vector. The plots are displayed similar to figure 5.28 showing the field during the Helicon (a) and ICH (b) time windows. Lines of constant integrated ion flux (black dashed) and corresponding ion plume fraction (red labels) have been displayed for reference. Regions without data are shown in white.

The axial and radial electric field components may be combined to show the magnitude of the DC electric field during each phase of plasma operation and is presented in figure 5.30. The radial component is the dominant component in the total electric field influencing the field along the boundary to the flow. The electric field during low ion energy flow (figure 5.30a) is small (< 20 V/m), essentially flat, and spread out over the plume. At higher ion energies larger (> 50 V/m) electric fields become concentrated outside of the 90% integrated ion flux. It may then be stated that for axial positions less than Z ~ 3.8 m (1.8 m downstream of the nozzle throat) and higher flow velocities the resulting electric field, dominated by the radial component, is shaped by the ion flow and will cause magnetized electrons to experience azimuthal E×B drifts. For Z > 3.8 m there is virtually no distinction between the DC electric field in the plasma for either high or low ion flow velocity. This lack of distinction suggests the macroscopic charge separation has minimized and is a signature of the transition to detached flow for the high ion velocity case.

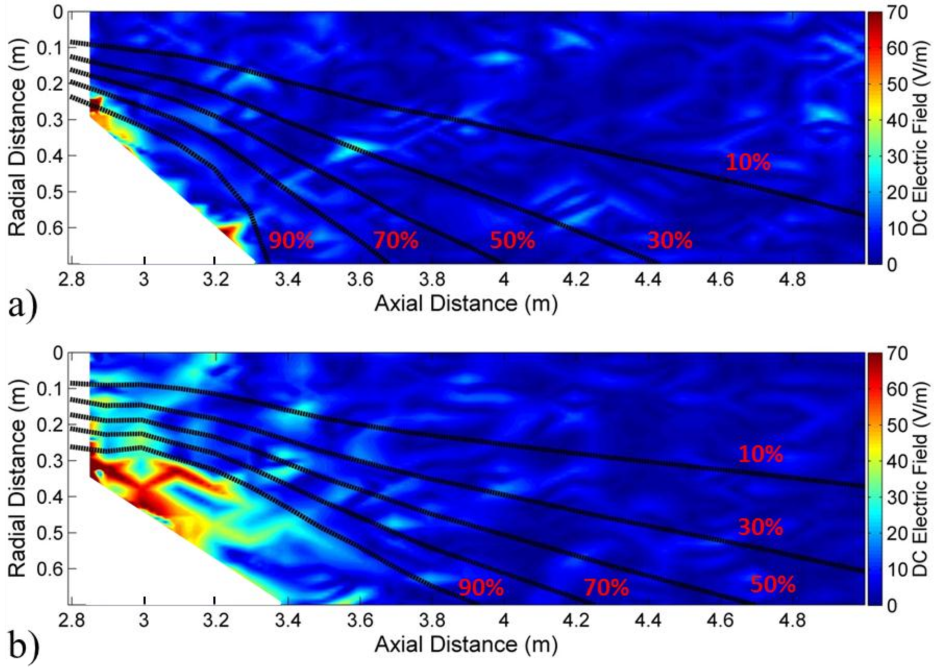

Figure 5.30: Contour maps of the magnitude of the total DC electric field vector during the Helicon (a) and ICH (b) time windows. The plotted lines and labels are arranged similarly to figures 5.28-29.

Section 5.5.2: AC Electric field

The high frequency (HF) or AC electric field is useful to the study of plasma waves and other transport phenomena in magnetic nozzles. As discussed in section 2.3.7, oscillating electric fields, in phase with density fluctuations, serve as a means of cross magnetic field transport for electrons[122, 123, 125]. Knowledge of the magnitudes, frequencies, and wave numbers of these turbulent fluctuations will shed light on instabilities playing a role in the detachment process. For this research a single electric probe consisting of a pair of tungsten electrodes was used and oriented such that the electric field vector measured ($\tilde{E}_r$) was perpendicular to the nozzle axis. The probe was measured using a spectrum analyzer scanning frequencies up to 10 MHz over steps in frequency space of 12.5 kHz. This range was selected to measure frequencies near the lower hybrid frequency across the plume, as well as an order of magnitude more. The methods of spectral data analysis and calibration for this probe were discussed in greater detail in section 4.5.

The spectra, taken in dBm and subtracting baseline spectral noise, are first converted to V/m and scaled according to the calibration before being plotted according to the position of the probe. RZ maps of these spectra will determine if any logical structure forms in the plume. A 3D graph of these compiled frequency spectra are taken over the range of R = 0 – 0.785 m at Z = 3.23 m and displayed in figure 5.31. There is little difference between the electric field spectra in the plasma opposed to out of the plasma during the Helicon time window (figure 5.31 *top*). The 'edge' of the plume for this axial location, in terms of ion flux according figure 5.1a, is between 0.4 m and 0.5 m. There does not appear to be any organized electric field structure, as a function of frequency, at this location for the lower velocity ions. There is a small trend as frequency increases for electric field strengths up to ~ 100 V/m. The spectra during the ICH data window (figure 5.31 *bottom*) are both larger in amplitude (up to ~ 700 V/m) and localized within the plasma boundary. There is a noticeable gap between the largest peaks, found mostly within 0.2 m from the edge of the plume, and the smaller spectra closer to the axis. This gap suggests that a ring-like or conical (assuming axisymmetry) HF electric field structure forms in this region of the plume where higher velocity ions have begun to deviate from the field lines. It is worth noting that none of the frequency peaks of the spectra match either of the RF drive frequencies of the plasma source (Helicon ~ 6.78 MHz), acceleration mechanism (ICH ~ 100's kHz), or associated harmonics. The effects of RF noise into the probe have been isolated and subtracted off with the baseline spectral values so that the data then represents the actual frequencies found across the plasma.

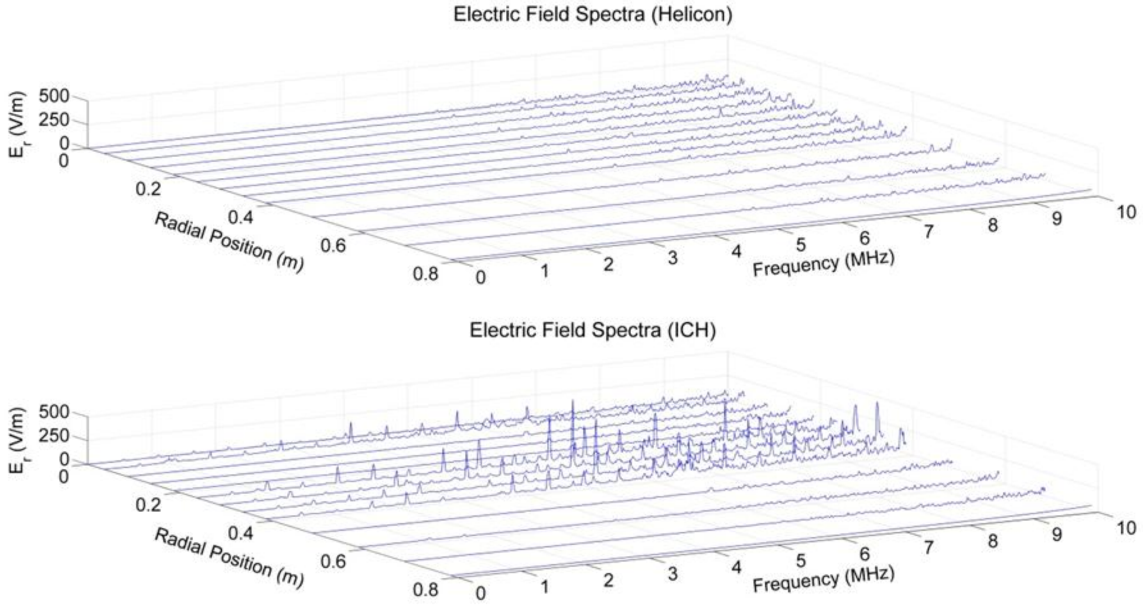

Figure 5.31: Electric field frequency spectra as a function of radial position at an axial position of Z = 3.23 m. Spectra during the Helicon time window (*top*) show modest amplitudes both in and out of the plasma compared to the ICH window (*bottom*) where magnitudes are not only much larger but at specific locations within the plume.

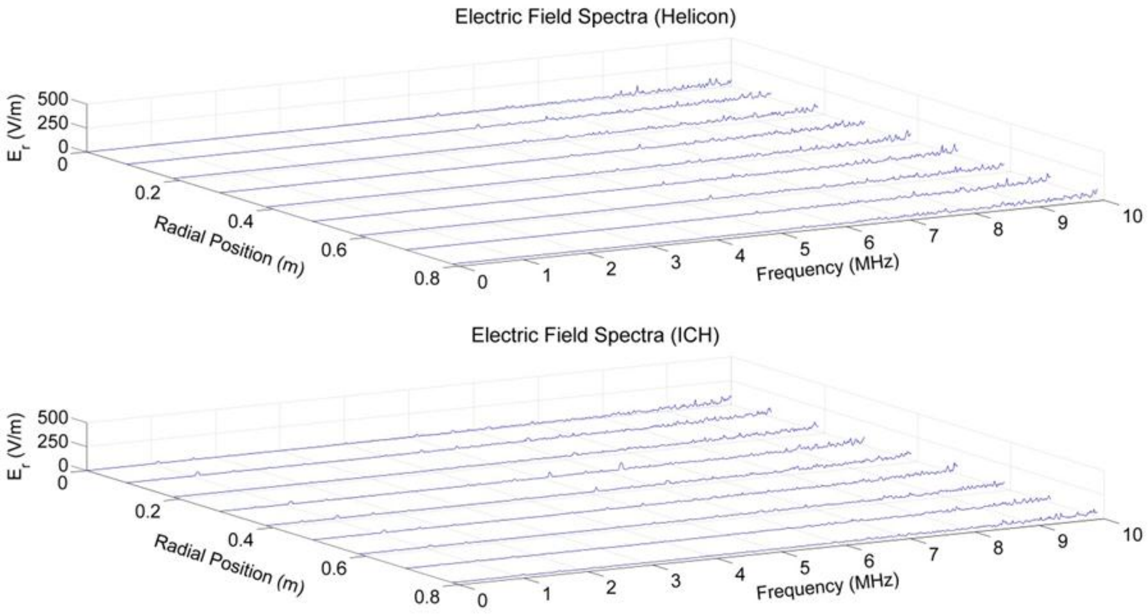

Figure 5.32: Electric field frequency spectra as a function of radial position at an axial position of Z = 4.13 m. The modest amplitudes of the spectra during the Helicon time window (*top*) are essentially indistinguishable from those of the ICH window (*bottom*) at the larger axial locations.

To investigate if this HF field structure during the ICH phase persists throughout the entire nozzle or is a localized feature, similar radial measurements of the spectra were taken at different Z locations. A 3D graph, similar to figure 5.31, taken at an axial location of Z = 4.13 m ($\Delta Z = 0.9$ m) is presented in figure 5.32. Along this plane there is virtually no difference between the spectra during either time window. All of the spectra across the radius of both of these plots fall within the boundaries of the plume; which has expanded to $R_{90\%} \sim 0.81$ m. The wave electric field appears to have been damped out over the course of 1 m where conditions are no longer favorable to drive the oscillations (i.e. instabilities).

To clarify the extent of this spatial structure and dissipation of the driving mechanism, the 3D radial plots of the electric field spectra are converted into color contour plots and arranged in a composite image as a series of plasma power level and axial position (figure 5.33). Contour plots during the Helicon data window are on the left while the ICH data are on the right displaying several discrete axial positions (increasing bottom to top). Each plot is scaled logarithmically over a wide range of electric field strengths to better define any structural organization within the plume. From this data it is verified that no consistent high frequency electric field structure forms in the plume during the Helicon discharge, at least within these limits of measurement. The low ion velocities may be unable to produce the instabilities to create such electric fields at this characteristic frequency range. The spectra are essentially identical with increasing distance in the plume. The transition to higher ion velocity during ICH results in a wide conical-shaped, electric field structure along the plume boundary. This structure broadens with increasing axial distance before dissipating to the background (or Helicon only) electric field levels between Z ~ 3.93 – 4.13 m.

This data is consistent with the trends of the integrated ion and momentum flux observed in section 5.3. It was observed that during the ICH time window the ion flux plume fractions, although not following the magnetic flux, expand at a non-linear rate along the second region ($3.0 \text{ m} < Z < 3.9 \text{ m}$). This non-linear expansion region aligns well with the axial bounds of the wave electric field structure. The region where the ion flux plume fractions transition to a linear/ballistic, trajectory ($Z \geq 3.9$ m) also aligns with the axial location where electric field dissipates to background levels. This effect is perhaps best described by instabilities, caused by flowing charge-separation, which produce the turbulent electric field and the ions/electrons respond through particle transport. Charge separation will be greatest along the edges of the plume where the

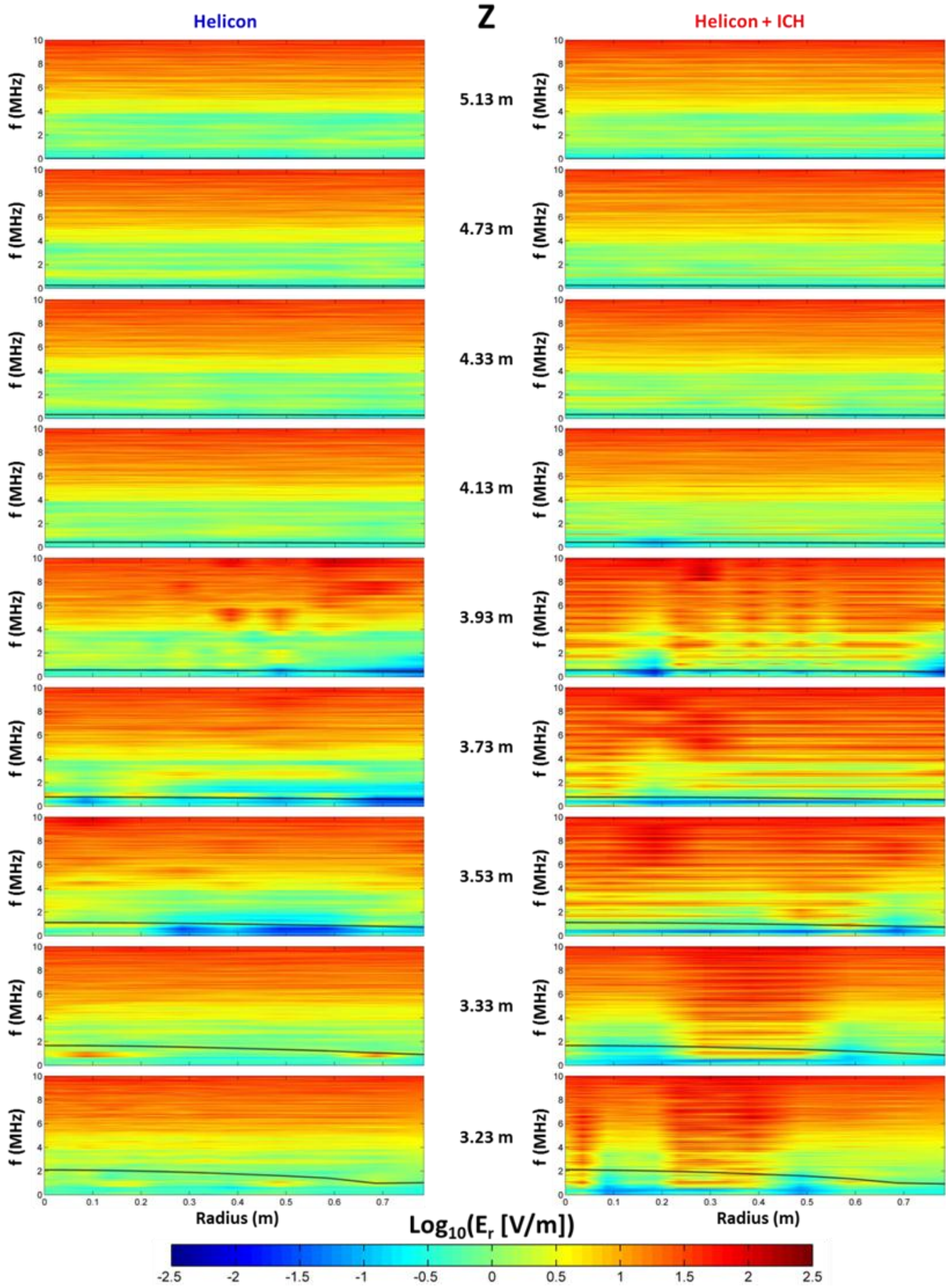

Figure 5.33: Compilation of contour plots for the radial electric field (V/m) as a function of frequency and radial position. The plots have been arranged according to the plasma source power level (Helicon stage vs Helicon + ICH) as well as the axial location for each radial scan. Each plot is scaled logarithmically and overlays the local lower hybrid frequency (black line).

curvature of the magnetic field is least allowing the instability driven electric fields to grow. Similar drift wave instabilities are commonly found on the edges of plasmas in Tokamak reactors enhancing cross-field transport of particles, heat, and momentum[217-220]. The location where these instabilities have dispersed would indicate that the charges are no longer separated. Considering the ions follow a linearly expanding trajectory in the far plume, during ICH, the electrons must be following the ions as detached particles. The electrons must then be able to cross the magnetic field lines along this electric field region ($3.0 \text{ m} < Z < 3.9 \text{ m}$) and balance the flow of departing ions.

Supporting this claim for instability driven turbulence, the radial electric field is composed of frequencies near the lower hybrid frequency (figure 5.33 black lines) as well as near integer multiples of the lower hybrid frequency. The Lower Hybrid Drift Instability (LHDI), or a variant discussed in chapter 2, appear to be the best candidate to fit the observations. More analysis will be presented in the next chapter regarding the possibility of these instabilities contributing to sufficient cross-field electron transport and electron detachment.

Section 5.6: Chapter summary

A large amount of data have been presented in this chapter providing both qualitative and quantitative results, observations, and/or signatures that the flowing plasma are no longer attached to the field lines of this dipole shaped magnetic nozzle. Section 1 presented several contour maps of compiled and interpolated data taken at many separate locations within the nozzle. The mappings presented contrasts between a lower energy (~ 47 eV) and higher energy (~ 188 eV) argon population created during a Helicon discharge and energized using ion cyclotron resonant heating (ICH). This qualitative comparison showed that the plasma within the nozzle transitioned into a better defined, more axially directed, and narrower plume that extended farther downstream during the high energy scenario for identical magnetic field conditions as the low energy case. This trend was observed in measurements of the ion flux, electron density, momentum flux, and ion velocity. The measured magnetic field components were compared and found that the magnetic field during plasma flow, during both Helicon and ICH time windows, were minimally different from the vacuum field. This result suggests that magnetic field line ‘dragging’ is not occurring.

The second section discussed the results from measuring and comparing data expansion trends along the nozzle axis. The data confirmed some of the qualitative observations from section 1 while showing that neither the ion nor momentum flux follow the same expansion trends as the axial magnetic flux. The axial expansion trends were compared using power law fits along separate regions of the plume. The ion flux during the Helicon time window was found to expand *faster* than the magnetic flux while the momentum flux, although noisy at low energy levels, expanded *slower* than the magnetic flux. During the ICH time window, the expansions of both the ion and momentum fluxes were comparable expanding at rates *slower* than the magnetic flux. Over these same distances the other plasma properties such as electron temperature, density, plasma potential, and ion velocity were found to be nearly flat or gradually decreasing as the plume expanded.

A new method for mapping and tracking fluxes in the expanding plume was implemented in section 5.3. This process involved organizing the plume into conical layers, according to fractions of the total integrated value emerging from the closest measurement/reference plane. These lines of constant integrated ion and momentum flux were compared to similarly integrated magnetic flux enclosed within each fractional layer. It was observed that the plume, according to these flux lines, may be divided into at least two regions, separated by trajectory and/or inflection points of the lines. For the low energy flow during the Helicon time window, the ion flux lines follow the magnetic flux for a short distance (first region) before diverging *more* than the enclosed magnetic flux (second region). Some of the plume fraction lines farther from the nozzle axis begin to diverge immediately. The momentum flux, due to noisy/low amplitude signals, was only valid over a small range ($Z < 3.6$ m) but was consistent with a linear expansion dominated by neutrals.

For higher energy flows during the ICH time window, the ion flux lines appear to follow the magnetic flux for 0.1 – 0.2 m ($Z \sim 2.8 – 3.0$ m) in the first region. The lines then converge inside the flux but expand quadratically (3.0 m $< Z < 3.9$ m) in the second region. The third region is defined by a steady linear expansion ($Z \geq 3.9$ m) over all plume fractions. The quadratic expansion suggests radial forces are playing a role in the second region. The momentum flux first follows the magnetic flux in the first region before diverging into a linear trajectory similar to the ion flux.

The latter parts of the third section go into detail describing trends of two quantities defined as the slope ratio (SR) and detachment angle. The slope ratio is a ratio of the slopes of the integrated ion/momentum flux line to the integrated magnetic flux line as a function of axial position. The detachment angle is a measure of the angle between the ion/momentum flux vectors to the enclosed magnetic flux vector. The values for both of these variables reflect the regions and conclusions from the mapped integrated flux lines. The slope ratio/detachment angle trends during the Helicon time window indicate the plume does not follow the magnetic flux, separating divergently at angles up to ~ 7°. During ICH the slope ratios measure less than unity with detachment angles ranging from 4° – 10° indicating convergent detachment.

Further confirmation of detached ion flow was presented in section 5.4 where the pitch angle of the ion velocity was plotted across a radial plume segment. This was done using a goniometer mounted RPA capable of measuring pitch angles from $\alpha = 0° - 90°$ relative to the nozzle axis. It was found that the pitch angle distribution for low energy ions spreads out (from $\alpha \sim 50° - 75°$) with increasing distance from the nozzle axis. Over this same distance the pitch angle distribution narrows for higher energy ions (during ICH) and is directed more paraxial at $\alpha \leq 45°$. This narrowing of the high energy flow is a reflection of the nozzle efficiency in that higher velocity ions experience a greater parallel conversion than the low velocity ions. There does not seem to be any collective organization of the velocity pitch angle about the local magnetic field vector suggesting the ions are demagnetized and simply ignoring the magnetic field.

The electric field responses to the plasma during each stage of operation were presented in section 5. The DC electric field was produced from the negative gradient of the plasma potential and found that the radial component was the more dominant component. The field magnitude was found greatest (as high at 70 V/m) during ICH and outside of the 90% integrated ion flux line (for $Z < 3.8$ m). This field location is consistent with the expansion region (second) of the ion flux. The DC electric field will contribute to azimuthal E×B drift motion and will be discussed in chapter 6.

The high-frequency electric field data consisted of the radial electric field measured between a pair of electrodes by a spectrum analyzer scanning near the lower hybrid frequency. Organizing these spectra according to (r, z) position showed that the difference in the frequency dependent electric field in the plasma compared to in vacuum was negligible for low energy ions. The amplitude of the field was small and relatively flat, trending gradually only at higher frequencies. The electric field spectra, for higher ion energies during ICH, were much larger in amplitude (up to 740 V/m) and structurally organized along the edges of the plume. This structure was seen to follow the edge further downstream and broaden out before dissipating completely ($3.93 \text{ m} < Z < 4.13 \text{ m}$). The trends of this field structure are consistent with the transition regions of the ion flux lines and provide another confirmation of plume detachment.

Chapter 6: Analysis of Detachment Mechanisms

In the previous chapter it was shown that there are regions of the plume where the ions are diverging from the applied magnetic field. It was also shown, indirectly, that the electrons had detached ~ 1 m downstream of this ion divergence region through the correlation of the dissipation of the high frequency and DC electric fields, and the location of the transition to linear ion flux trajectories. The next step of this research is to analyze which of the proposed detachment mechanisms are most applicable and align best with the observed data. Each of the theories discussed in chapter 2 will be tested individually in the following sections of this chapter. The first section will cover collisional detachment mechanisms as a means for detaching both ions and electrons. The second section will revisit the theories dealing with preservation of the frozen-in condition to see if the applied magnetic field is being carried away with the plasma. The third section will look into the fundamental lower limits of detachment along the lines of electron inertia theories. The fourth section will investigate the possibility of particle demagnetization through loss of adiabaticity for both particle species. The last section will explore plasma turbulence as a detachment mechanism. All of the contour maps presented in this chapter utilized gridded linear interpolation between data points similar to those described in chapter 5.

Section 6.1: Collisional detachment analysis

Section 6.1.1: Resistive diffusion

It is often necessary to analyze the effects of inter-particle collisions and their role in the macroscopic behavior of the plasma. As explained briefly in section 2.3.2, cross-field transport due to elastic particle collisions is the basis for the resistive diffusion of magnetized plasma. In a simplified classical collision scenario the particles gyrating about the field lines collide and begin to gyrate about a new field line, up to one gyroradius ($r_c = v/\Omega$) from the original, giving rise to a random walk perpendicular to the magnetic field. The diffusion coefficient has dimensions of $(\text{length})^2/\text{time}$ and in the limit of a strong magnetic field ($\Omega >> \nu_c$) becomes $D_\perp \approx r_c^2 \nu_c$. Diffusion along the magnetic field lines is unaffected by the field and is dependent upon the collisional mean-free-path, $D_\parallel \approx \lambda_c^2 \nu_c$. In the weak field limit ($\Omega/\nu_c \rightarrow 0$) the cross-field diffusion tends to the parallel or unmagnetized result governed by the collision mean-free-path. These heuristic approximations apply to diffusion across a uniform magnetic field. For an inhomogeneous magnetic field, such as an expanding magnetic nozzle, these assertions change and the diffusion coefficient defined in equation 2-4 may be used so long as appropriate collision parameters are used.

To get a rough estimate for the role collisions play in the VX-200 plume it is useful to employ a simple test particle model of the distribution function in the Fokker-Planck equation. For a uniform, field-free plasma in thermal equilibrium the Fokker-Planck equation becomes[188]:

$$\frac{\partial f}{\partial \mathrm{t}} = -\Gamma \frac{\partial}{\partial \mathrm{v}} \cdot \left(f \frac{\partial \mathrm{H}}{\partial \mathrm{v}} \right) + \frac{1}{2} \Gamma \frac{\partial^2}{\partial \mathrm{v} \partial \mathrm{v}} : \left(f \frac{\partial^2 \mathrm{G}}{\partial \mathrm{v} \partial \mathrm{v}} \right) \qquad 6\text{-}1$$

where f is the distribution function of the test particle, Γ is the particle flux, G/H are the Rosenbluth potentials, and the colon operator is the dyadic dot product of the matrices.

The first term on the right hand side produces a deceleration of the test particle while the second term produces a spreading effect on a beam; they are often referred to as the coefficients of dynamical friction and diffusion respectively. The distribution functions for the test particle (*f*) and field/scattering particles (f_s) are then defined as[188]:

$$f(\mathrm{v},\mathrm{t}) = \delta[\mathrm{v} - \mathrm{V(t)}] \qquad \text{6-2}$$

$$f_s(\mathrm{v}_s) = \frac{n_s a_s^3}{\pi^{3/2}} e^{-a_s^2 \mathrm{v}_s^2} \qquad \text{6-3}$$

$$a_s^2 = \frac{m_s}{2k_B T_s} \qquad \text{6-4}$$

where V(t) is the test particle velocity at any given time but in many cases the collision parameters are estimated by evaluating velocity moments at time t = 0[188]. For cross-field transport the collision frequency, ν_c in the conventional form, is taken as the reciprocal of the time for a particle to be deflected through a right-angle. In the test particle model ν_c is found by taking the $\mathrm{v}_\perp^2$ moment of equation 6-1, which is the sum of the squares of v perpendicular to V(0)[188]. The only non-zero contribution to the collision frequency, through integration by parts of equation 6-1, turns out to be the coefficient of diffusion term involving only the G Rosenbluth potential and is written as[188]:

$$\frac{\partial \mathrm{V}_\perp^2}{\partial \mathrm{t}} = \frac{2\Gamma}{V}\frac{\partial \mathrm{G}}{\partial V} \approx \sum_s \nu_s V^2 \qquad \text{6-5}$$

$$\mathrm{G} = \sum_s z_s^2 \int |\mathrm{v} - \mathrm{v}_s| f_s(\mathrm{v}_s) d\mathrm{v}_s \qquad \text{6-6}$$

Inserting the field particle distribution function from equation 6-3 into equation 6-6 and evaluating equation 6-5 will produce estimates of the collision frequencies for the test particles and field particles alike. For electrons and singly charged ions, the collision frequency may be written as[188]:

$$\nu_{\alpha\beta}(V) = \frac{n_\beta q^4 \ln\Lambda}{2\pi\varepsilon_0^2 m_\alpha^2 V^3}\left[\phi\left(a_\beta V\right) - \psi\left(a_\beta V\right)\right] \tag{6-7}$$

$$\phi(x) = \frac{2}{\sqrt{\pi}}\int_0^x e^{-y^2}dy \tag{6-8}$$

$$\psi(x) = \frac{\phi(x) - x\phi'(x)}{2x^2} \tag{6-9}$$

where the subscripts α and β refer to the test particle and field particles respectively, ln Λ is the Coulomb logarithm, and ϕ(x) is the error function.

The collision frequency from equation 6-7 may be simplified by using the limiting or asymptotic values for the error function and derivatives (x→0: $\phi(x) \sim 2x/\sqrt{\pi}$, $\psi(x) \sim 2x/3\sqrt{\pi}$; x→∞: $\phi(x) \sim 1$, $\psi(x) \sim 1/2x^2$). For charged particle collisions within the range of parameters in this experiment, the asymptotic limits are valid. These limiting values for the collision frequency, in the form of Trubnikov, were used to estimate charged transport perpendicular and parallel to the nozzle magnetic field[37, 221]. For collisions of charged test particles scattering off of neutral argon atoms, the estimated collision frequency was calculated using[37]:

$$\nu_{\alpha 0} = n_0 \sigma_s^{\alpha 0}\left(\frac{k_B T_\alpha}{m_\alpha}\right)^{1/2} \tag{6-10}$$

where the subscripts α and 0 refer to the test particle and neutral atom respectively and $\sigma_s^{\alpha 0}$ is the effective scattering cross section which is dependent upon the test particle energy. Previously published scattering cross section vs. energy curves for electrons[222, 223] and ions[176] scattering off of neutral argon atoms were used to interpolate the cross section values and are typically on the order of ~ 5 x 10^{-15} cm^2.

Values for the estimated collision frequency and collisional mean-free-path (v_{th}/ν_c) along the nozzle axis for electrons and ions as test particles incident upon electrons/ions/neutrals as field particles are displayed in figure 6.1. It is convenient to use axial plume data as a broad characterization to narrow the focus on a particular form of transport. The test particles are represented by symbols (o for electrons, + for ions) while the field particles are indicated by line color (**blue** for electrons, **red** for ions, and **black** for neutrals). These data effectively demonstrate that the ions may be considered collisionless while the electrons are fairly collisional when interacting with other electrons and ions. Hazelton and Meiss describe the 'collisionality parameter' as a ratio

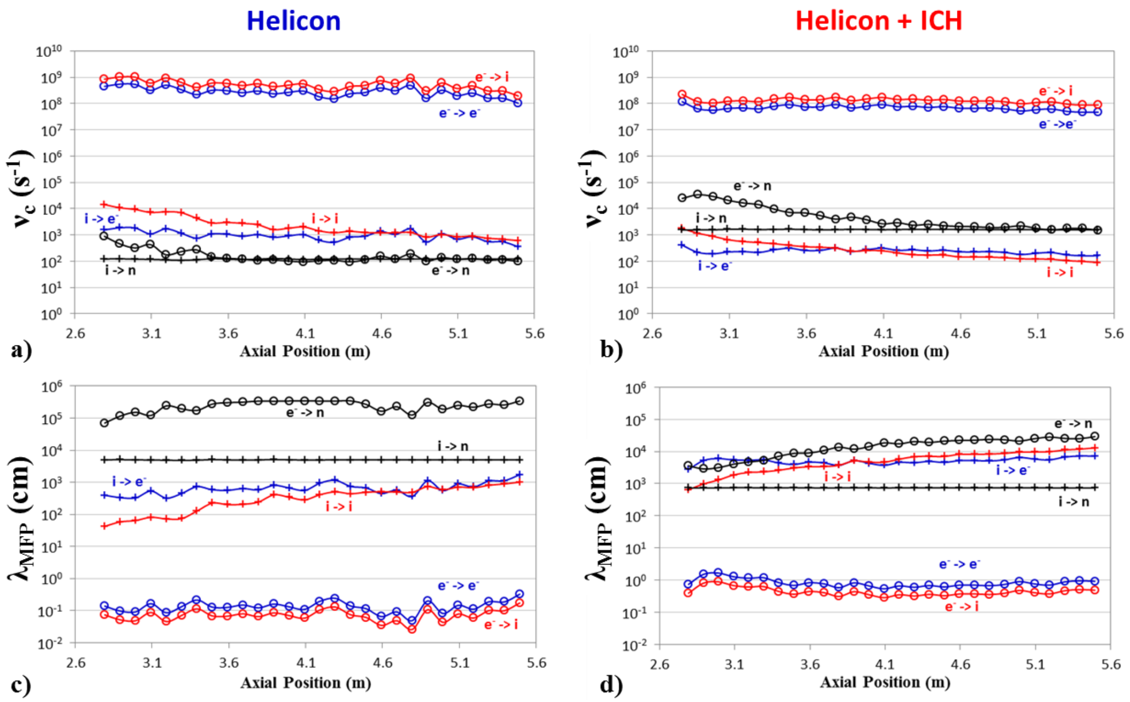

Figure 6.1: Collision frequency and collisional mean-free-path as a function of distance along the nozzle axis for both the low energy Helicon (a, c) and high energy ICH (b, d) cases. Electrons as test particles are orders of magnitude more collisional than the ions. The strongest interactions are with other electrons and ions rather than neutrals. The mean-free-paths for these interactions are also much shorter than the scale lengths in the nozzle. There is a small dependence on energy as increasing the energy reduces the collision frequency and increases the mean-free-path.

of the collision frequency to the transit frequency, ω_t, which is defined as the thermal velocity over the scale length[31]. For $\nu_c/\omega_t << 1$ the system is said to be collisionless whereas the opposite is collision dominated. The transit frequency for electrons during all phases of this experiment, for scale lengths of ~ 30 cm (plume radius) and ~ 200 cm (approximately the axial extent of measurements), is always much less than the collision frequencies indicating electrons are collision dominated throughout the plume. Both test particles do not strongly scatter off of neutrals although the rates do increase during the ICH time window (figure 6.1b) due to the expected pressure rise later in the firing sequence. Increasing the ion energy, and electron energy to a lesser degree, results in a small decrease in collision frequency and an increase in mean-free-path. The mean-free-paths for the electron→electron and electron→ion collisions are much shorter than the scale lengths for measuring detachment, thus reflecting the conclusion of the collisionality parameter.

Often when considering collisions in plasma it is useful to compare the collision frequency to the cyclotron frequency and plasma frequency as shown in figure 6.2. The inverse of the collision frequency to the cyclotron frequency is commonly referred to as the Hall parameter[126]. Figure 6.2 is setup in the same symbol/color format as figure 6.1. The inverse Hall parameter reveals the number of collisions per gyro-orbit where a large number indicates that collisions may affect net particle transport through random walk processes, especially when the Larmor radius is small. For lower ion energies (figure 6.2a) all of the particles are able to make several gyrations about the magnetic field lines before a collision (up to Z ~ 3.2 m), where the electrons begin colliding at least once per gyration. At higher ion energies (figure 6.2b) this location is extended out to Z ~ 4.0 m.

This axial location lines up well with those mentioned in chapter 5 where the ion trajectories became linear and the electric field dissipated along the plume edges. It is worth noting that the shape of the rising trend is consistent with the growth of the Larmor radius as the magnetic field decreases.

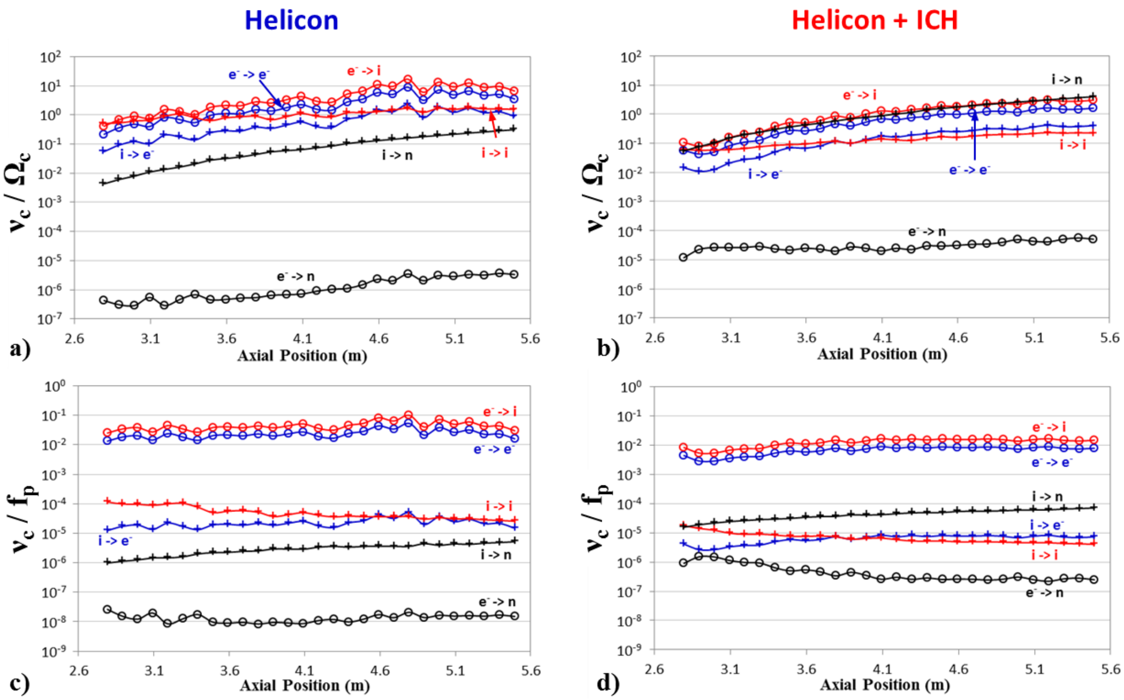

Figure 6.2: Collision frequency ratios to cyclotron and plasma frequency as a function of distance along the nozzle axis during both Helicon (a, c) and ICH (b, d) time windows. The increasing trend of collisions per orbit is consistent with increasing Larmor radius in the expanding nozzle. The collision frequency is less than the plasma frequency indicating the collisions are weakly coupled.

Comparing the collision frequency to the plasma frequency is a useful indication whether the collisions are able to affect plasma oscillations. In a weakly coupled plasma, where $\nu_c << f_p$, the collisions essentially have no effect on the large scale oscillations on the plasma. The opposite is a strongly coupled plasma, $\nu_c >> f_p$, where collisions may prevent plasma oscillations from developing and the system no longer follows conventional plasma dynamics. It is evident from figure 6.2c,d that the plasma may be considered weakly coupled for both ion energy regimes. The electron→electron and electron→ion collision rates come closest to the plasma frequency but are still 1-2 orders of magnitude less.

Given these trends it is valid to assume that the ions may be treated further as collisionless while the electron→electron and electron→ion collisions are not able to be ignored. Therefore, the ions in this setup do not detach by means of collisional diffusion but the possibility remains that electrons may diffuse across field lines to follow the non-magnetized ions. If this were the case it would be necessary for the cross-field drift velocity of the electrons to approximate the ion velocity to prevent an unstable accumulation of space-charge and large electric fields. It is understood that net electron cross-field transport is not likely via electron→electron collisions since the effects tend to cancel out, but will still be presented below for the sake of comparison to electron→ion collisions where net transport is more probable.

To estimate and compute the cross-field velocities from electron collisions, the neoclassical model of diffusion is assumed as briefly described in chapter 2[118, 119, 224]:

$$\mathrm{u}_{\perp} = \pm\mu_{\perp}E_{\perp} - D_{\perp}\frac{\nabla n_{\perp}}{n} + \frac{u_E + u_D}{1 + \left[\frac{\nu_e}{\Omega_c}\right]^2} \qquad \text{6-11}$$

$$\mathrm{D}_{\perp} = \frac{k_B T_e}{m_e \nu_e}\frac{1}{1 + \left[\frac{\Omega_c}{\nu_e}\right]^2} \qquad \text{6-12}$$

$$\mathrm{u}_E = \frac{E \times B}{B^2} \qquad \text{6-13}$$

$$\mathrm{u}_D = \frac{k_B T_e}{qB^2}\frac{\nabla n \times B}{n} \qquad \text{6-14}$$

The mobility is taken as the diffusion coefficient over the electron temperature, $\mu_\perp = D_\perp/T_e$. The electric field, E, is the DC electric field presented in chapter 5 and the magnitude perpendicular to the magnetic field is used to estimate the velocity component due to electron mobility. It is found by taking the sine of the angular difference between the electric and magnetic field vectors, i.e. $E_\perp \approx |\mathbf{E}|\sin(\Delta\theta_{\mathbf{EB}})$. A similar treatment is done to find the magnitude of the density gradient perpendicular to the magnetic field. The E×B and diamagnetic drift velocities are by definition perpendicular to the gradients in potential and density. For this system, with cylindrical coordinates and assuming symmetry about the nozzle axis, these drifts are along the azimuthal direction which does not contribute to the net axial/radial cross-field transport. Therefore contribution from the final component of the right hand side of equation 6-11 will be ignored in this study; but the associated drifts will be briefly presented in the following sub-section.

Also useful for the purposes of studying transport is to compare the collisional drift velocity to that of the Bohm drift velocity which follows a B^{-1} scaling instead of B^{-2} and has been verified experimentally multiple times in Stellerators[118]. The Bohm diffusion coefficient is defined as[37, 118, 119, 188, 224]:

$$D_B = \frac{1}{16}\frac{k_B T_e}{qB} \qquad 6\text{-}15$$

The resulting drift velocity is found by replacing the diffusion coefficient in equation 6-11 with the Bohm value from equation 6-15. Although the factor of 1/16 has no theoretical foundation, but rather is a traditional empirical value, it will be used as such for a benchmark comparison in this study.

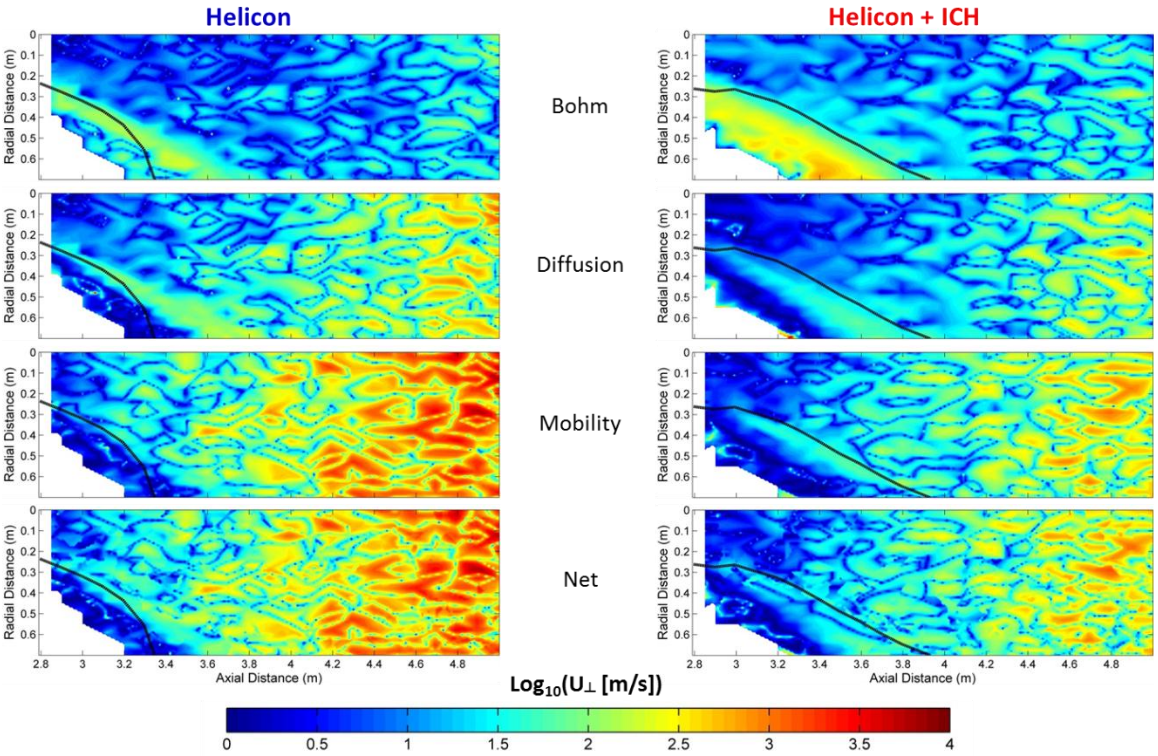

Figure 6.3: Comparison of the contributions to cross-field electron velocity due to *electron→electron* collisions for the Helicon (*left*) and ICH (*right*) time windows. The contour plots are arranged according to the specific velocity calculated ranging from the Bohm diffusion coefficient, collisional diffusion coefficient, mobility, and the net sum. An effective plume edge is plotted for reference (black line) which is taken from the 90% integrated ion flux line.

Maps of the cross-field electron velocity are created using overlapping measurements of plasma density, electron/ion temperature, plasma potential, ion velocity, and magnetic field strength to estimate collision frequencies, calculate gradients, and compute values corresponding to equation 6-11 as a function of position. The resulting color contour maps are presented in figure 6.3 showing the transport velocity due to electron→electron collisions. As stated in the previous chapter when the DC electric field was computed, taking the spatial gradient of directly measured plasma data is typically noisy and here is no exception. The data have not been smoothed, yet trends appropriate for analysis still emerge. Plotted in figure 6.3, in columns of ion energy level (Helicon *left*, ICH *right*), are maps of the cross-field electron velocity as a function of radial and axial position. The rows correspond to different contributions to the cross-field velocity (equation 6-11), namely from Bohm diffusion, collisional diffusion, electric field mobility, and the net sum of the collisional components. The white areas represent regions of no data or low signal-to-noise data and the black line marks a reference to an effective plume edge given by the 90% integration of the ion flux from chapter 5.

It is seen from electron→electron collisions that the transport resulting from diffusion along the density gradient is less than that of the Bohm case except in the far plume region where the magnetic field is much weaker; this is true for both ion energy cases. The transport due to mobility along the electric field is greater than the diffusion contribution but only in the far plume where detachment is not expected according to results in chapter 5 (i.e. $Z < 3.9$ m). The increase in mobility for the far plume region is due to the electron temperature decreasing as the plume expands. The reverse effect occurs in the high ion energy (ICH) case where the resonance increases the electron temperature slightly, corresponding to a drop in mobility. The mobility term is the stronger form of transport for both ion energy cases. Under a requirement that the electron cross-field velocity match that of the departing ions, 13 – 17 km/s during Helicon and 27 – 32 km/s during ICH, the values fall short by more than an order of magnitude. The peak values for net transport are only a few km/s while in the region of interest (3.0 m $< Z < 3.9$ m) only achieve a few 100 m/s. Transport due to electron→electron collisions is insufficient to account for electron detachment in this plume.

A more plausible electron detachment scenario is carried out with electron→ion collisions where electron gyro-trajectories are altered without significant impact to the ions. This scenario is mapped out in figure 6.4 and presented in a similar format to figure 6.3. The Bohm diffusion values are identical to the previous scenario since the dependence is only on electron temperature and magnetic field rather than collision frequency. For both ion energy levels a more significant transport structure is setup along the edge of the plume where the density gradient is greatest. The collisional diffusion values exceed the Bohm estimate but share a similar structure suggesting the experimentally determined coefficient assumed to be 1/16, may be too low by a factor of 2 – 5. Unlike electron→electron collisions, the diffusion contribution is larger than the mobility component for electrons scattering off of ions. The increase in ion temperature, as values initially during Helicon ($T_i \approx 6 – 10$ eV) rise to ICH levels ($T_i \approx 27 – 37$ eV), is seen in the maps on the right side, and transport is enhanced within the bulk of the plume. The edge transport structure during ICH appears to dissipate near Z ~ 3.8 m, again consistent with the transition location for linear ion trajectories. Despite this promising result, the magnitude of the net-cross field electron transport falls short of the required values needed to match the axial departure velocity of the ions. These values would need to be increased by at least an order of magnitude for electron→ion collisional diffusion to be considered as a valid detachment mechanism.

It is concluded for this setup with heated ions and cold-magnetized electrons flowing through a dipole magnetic nozzle that collisional diffusion alone is insufficient as

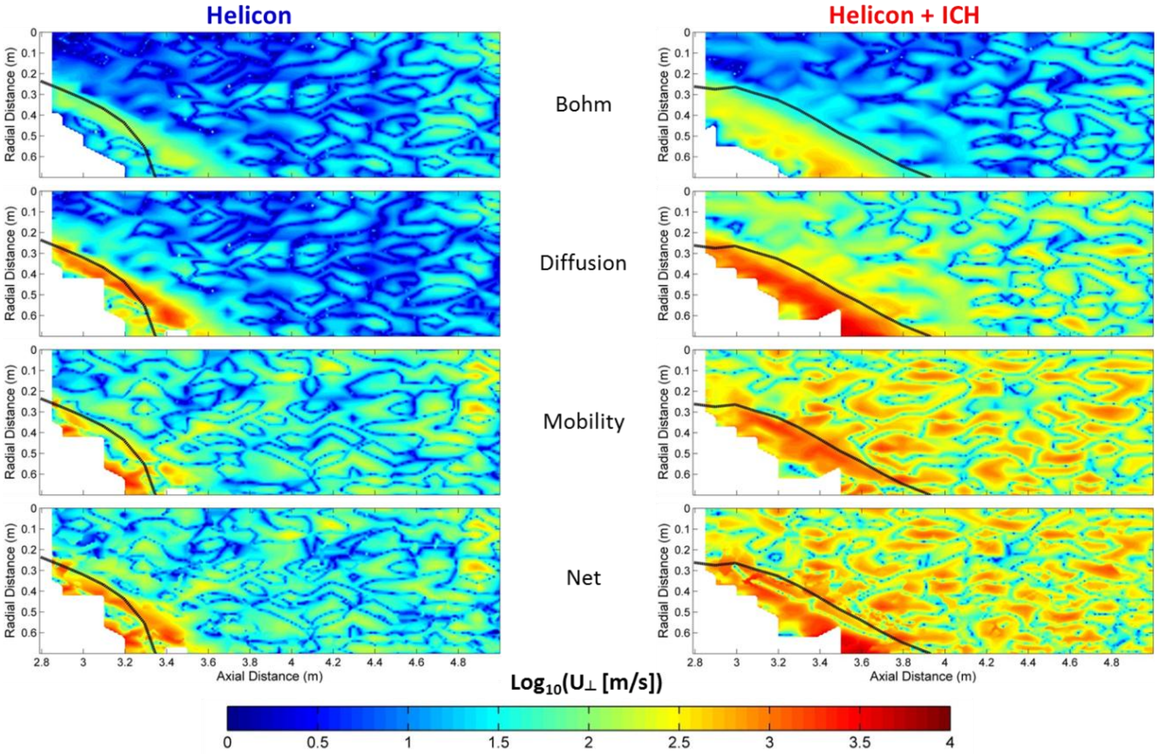

Figure 6.4: Comparison of contributions to cross-field electron velocity due to *electron-ion* collisions for the Helicon (*left*) and ICH (*right*) RF power levels of this experiment. The contour plots are arranged according to the velocity calculated from the Bohm diffusion coefficient, collisional diffusion coefficient, mobility, and the net sum. An effective edge of the plume is plotted for reference (black line) which is taken from the 90% integrated ion flux.

an electron detachment mechanism. It is possible that some other mechanism may enhance or otherwise play a role to increase the transport velocity to the degree that electrons are able to flow along with the ions. Anomalous resistivity is commonly mentioned as another possible way to enhance transport and achieve electron detachment[60, 69, 81, 125].

Section 6.1.2: Guiding center drifts

The motion of charged particles in electric and magnetic fields is complex and guiding center drifts may result if the particles behave as a collective of individual particles rather than as a combined fluid. Each of these prescribed drifts are maximized under particular conditions and many of the more common drift motions are described by F. Chen[118]. Most of the drifts mentioned involve the cross product of a particular force with the magnetic field vector or gradient. In this axisymmetric magnetic field these drifts result in azimuthal currents. The drifts most probable to occur in the plume are the E×B drift, the diamagnetic drift, non-uniform electric field drift, curved magnetic field drift, and the polarization drift. Although not likely to directly contribute to the radial or axial cross-field transport of electrons, in terms of detachment, it is still useful to understand some of the other plume dynamics involved in this system.

The E×B and diamagnetic drifts were defined in equations 6-13 and 6-14. The non-uniform electric field, curved magnetic field, and polarization drifts are then[118]:

$$\mathrm{u}_{nuE} = \left(1 + \frac{1}{4} r_c^2 \nabla^2\right) \frac{E \times B}{B^2} \tag{6-16}$$

$$\mathrm{u}_{B} = \frac{m}{q} \left(\mathrm{v}_{\parallel}^2 + \frac{1}{2} \mathrm{v}_{\perp}^2\right) \frac{R_c \times B}{R_c^2 B^2} \tag{6-17}$$

$$\mathrm{u}_{P} = \pm \frac{1}{\Omega_c B} \frac{dE}{dt} \tag{6-18}$$

Contour plots of the E×B and diamagnetic drifts are displayed in figures 6.5 and 6.6 for the Helicon (a) and ICH (b) time windows, respectively. These plots, like others presented, involve spatial derivatives of the plasma potential and density that introduce noise and have not been filtered. Both drifts set up azimuthal velocity structures along the outer edges of the bulk flow. The E×B drift (figure 6.5) velocities are approximately equivalent within the plume for both ion energy regimes with a slight increasing trend in the far plume as B decreases. The structure along the edge grows significantly when the ions are heated forming a current cone surrounding the outbound flow. The magnitude of the velocity peaks ~ 7 – 9 km/s, which is less than the ion velocity and much less than the electron thermal velocity. The diamagnetic drift (figure 6.6) is mostly governed by the density gradient shown by the well-defined edge structure and relative lack of significant organization within the plume. Like the E×B drift, there is little difference within the plume in terms of cold versus hot ions. The peak velocity for this drift approaches ~ 10 km/s. Combining the contributions of both drifts allows the net velocity to approach that of the ions (cold and hot) to within a factor of 2.

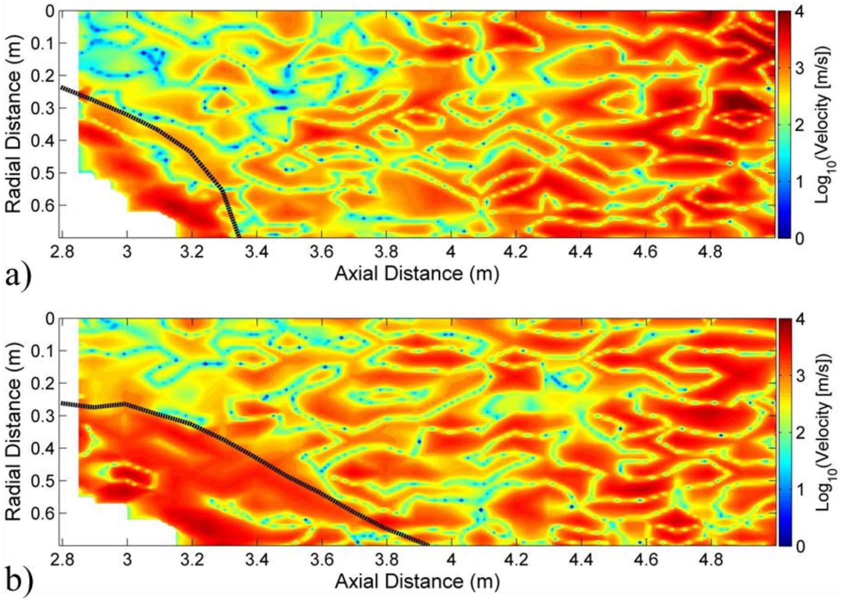

Figure 6.5: Contour plots of the azimuthal velocity from the E×B drift in the plume during the Helicon (a) and ICH (b) time windows. A black line representing an effective plume edge, using the 90% integrated ion flux line, is presented for reference.

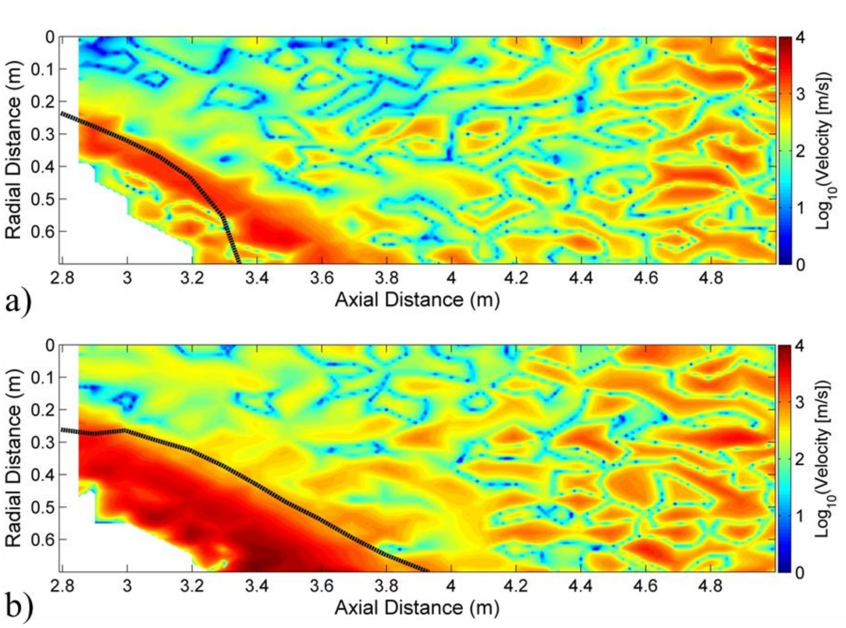

Figure 6.6: Contour plots of the azimuthal velocity from the diamagnetic drift in the plume during the Helicon (a) and ICH (b) time windows. A black line representing an effective plume edge, using the 90% integrated ion flux line, is presented for reference.

When considering the impact of an azimuthal current structure such as these surrounding the majority of the plume, one must be reminded that the density in this region is rather low (10^{15} – 10^{16} m^{-3}). Assuming the azimuthal velocity matches that of the outbound ions, the current density within this structure ranges between ~ 5 – 50 A/m^2. This range is far below the peak current densities, ~ 4000 A/m^2, as measured with the ion saturation biased Langmuir probes.

The effects of the other guiding center drifts may also contribute to the net azimuthal velocity but not necessarily to the degree of the previous two. The non-uniform electric field drift in equation 6-16 is essentially the E×B drift with second order terms included. Given that the maximum cyclotron radius is on the order of meters for ions (millimeters for electrons) combined with the presumably small second order derivatives, it is reasonable to ignore these higher order effects. The curved magnetic field drift, which includes the contributions of the Grad-B drift and curvature drifts, is also a relatively small addition to the net azimuthal velocity. The mass-to-charge ratio (m/q) is minuscule and the only region where the drift may have any effect is beyond the plume edge where the radius of curvature is small. Assuming electrons along the plume edge with thermal velocity are the dominant component, a radius of curvature of $R_c \approx 1$ m, and a magnetic field of 100 G, the curved magnetic field drift velocity is ~ 260 m/s which is nearly 2 orders a magnitude smaller than either the diamagnetic and E×B drifts. The polarization drift should also have a negligible effect when compared to the other drifts. A time dependent electric field was shown to be present along the edges of the plume in section 5.5.2 with peak magnitudes above 700 V/m at frequencies of ~ 5 MHz. Again assuming the effects are on the magnetized electrons in a 200 G field (for the location of the peak AC electric field), the cyclotron frequency is 3.5×10^9 s^{-1} and the azimuthal polarization drift velocity is ~ 50 m/s. All of these additional guiding center drifts do not significantly enhance or reduce the main azimuthal drift velocities and are therefore ignored.

It is worth restating that while these drifts are not likely to be a sole mechanism for particle detachment from the magnetic nozzle, the resulting currents are important when considering the processes and system responses for creating thrust from J×B forces. There may be a small radial/axial component, due to non-perfect axial symmetry, to these drifts that contribute to the collisional cross-field electron transport, but this was not able to be measured with the current setup. The main result of these drifts, with regards to magnetic nozzle physics, is that they form a well-defined azimuthal velocity structure along the boundaries of the plume that approximate the velocities of the departing ions. Heating the ions as done during ICH, results in a larger current (by amplitude and area) bounding the plasma which will serve to increase the volumetric Lorentz force (J×B) effectively increasing the thrust from the magnetic nozzle.

Section 6.2: Preserving frozen-in flow

In general there are two approaches to the problem of plasma departing a magnetic nozzle; the first is that plasma crosses the applied field becoming essentially demagnetized while the second involves no demagnetization and the plasma carries the applied field out to infinity. This second approach is the basis for magnetohydrodynamic ‘detachment’ theory for separating plasma from the magnetic nozzle. The plasma may carry the field with the ion momentum in a variety of ways. Two of the more supported theories involve either a super-Alfvénic flow stretching the applied field out to infinity or by small scale reconnection where magnetic islands propagate along with the plasma. Both of these ideas will be compared with experimental measurements below and assessed for validity.

Section 6.2.1: Super-Alfvénic field line stretching

It is claimed that when the plasma flow velocity, behaving as a single component fluid, exceeds the Alfvén velocity the flow is then energetically capable of pulling the magnetic field along as perturbations are unable to flow back upstream[70, 78, 89]. The dimensionless variable typically used to describe this transition is known as dynamic or kinetic beta, which is a measure of the plasma kinetic energy over the magnetic energy[70, 78]:

$$\beta_k = \frac{\mathrm{n}_i m_i \mathrm{v}_i^2}{\left(B^2/\mu_0\right)} \tag{6-19}$$

Shown in chapter 2 this value is identical to the square of the ratio of the plasma flow velocity to the Alfvén velocity.

The measured values of plasma density, ion flow velocity, and magnetic field were used to compute kinetic beta over the range of the plume. These results are shown in figure 6.7 for both low (Helicon) and high (ICH) ion energies. The flow exceeds the Alfvén velocity ($\beta_k > 1$) for both ion energies although at different locations. The transition occurs from about Z ~ 4.2 m (r = 0) to 4.4 m (r = 0.7 m) for low ion energy and from Z ~ 3.4 m (r = 0 m) to 3.9 m (r = 0.7 m) when the ion velocity is doubled. The value of β_k ranges from 0.03 – 10.6 during Helicon data window and 0.09 – 54.6 when the ions are energized during the ICH data window. It is interesting to note that the contour pattern also changes from slightly off-vertical to more slanted with the addition of ion energy via ICH. This slanted super-Alfvénic transition corresponds well across the inflection points where ion trajectories are become linearized as highlighted in figure 6.8. It is inconclusive if this is true for the lower energy ions produced during the Helicon discharge alone (figure 6.8a). There is not enough range in the translation stage to capture the full spread of the low energy plume beyond $\beta_k = 1$ to observe this effect, but with limited overlapping data it would appear that is not the case.

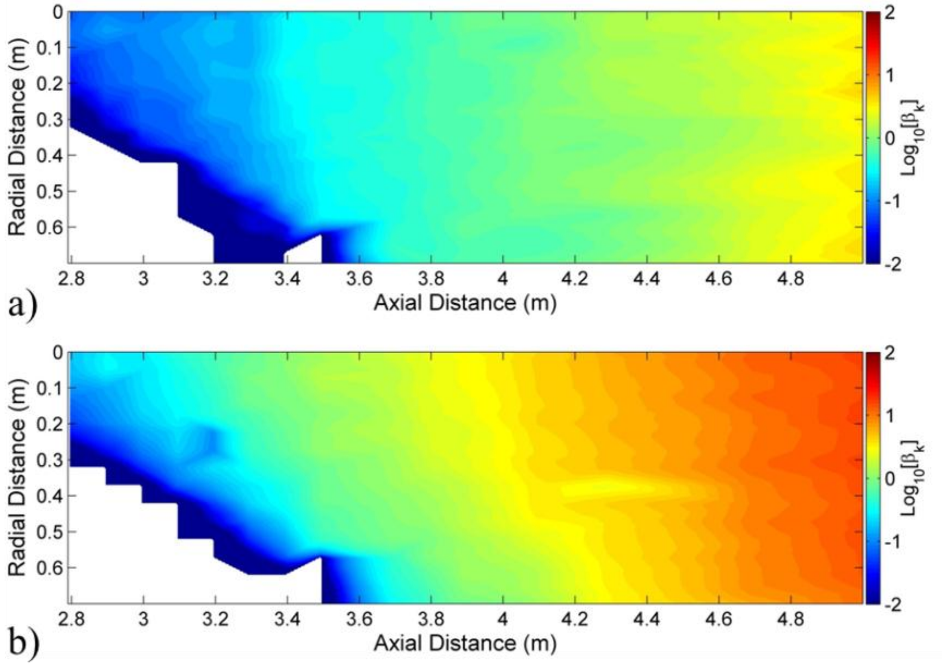

Figure 6.7: Contour maps of plasma kinetic beta during Helicon (a) and ICH (b) time windows.

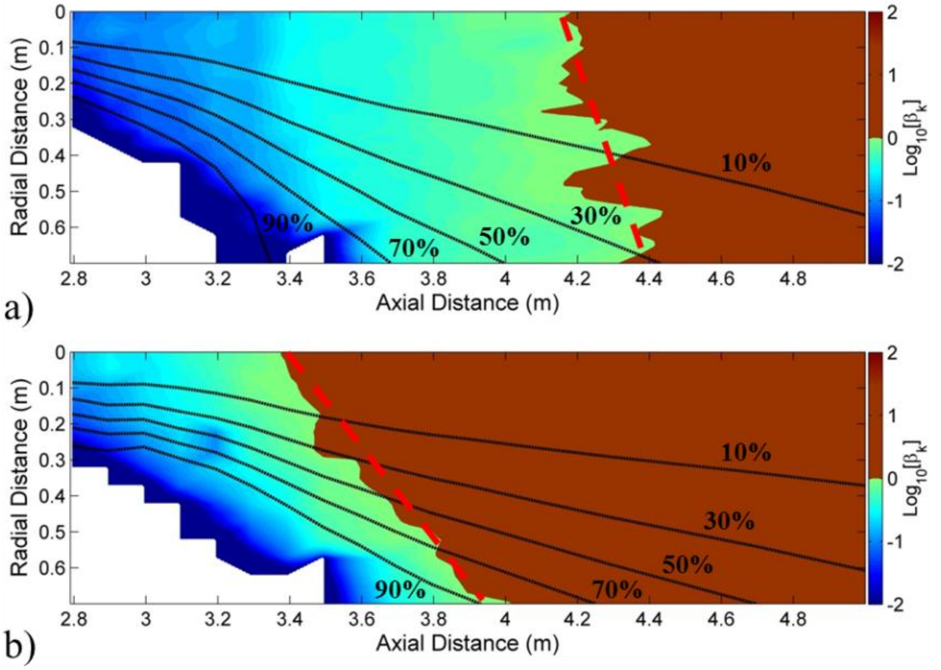

Figure 6.8: The same data as figure 6.7 except all values exceeding unity are darkened, a red dashed line highlights the transition, and lines of constant integrated ion flux are also displayed (black lines).

Despite the correlation between the super-Alfvénic transition to the linear ion trajectory inflection points, for higher energies, the ions were observed in section 5.3 to begin expanding at a different rate than the magnetic flux much closer to the nozzle throat. This difference would imply that kinetic beta approaching unity is more of an indicator for the location where the entire plume effectively detaches rather than the ions or electrons alone. Ions and electrons separating at different locations rather than all at once is a departure from the MHD assumption that the plasma behaves as a single fluid. Even if the plasma does not behave as a single fluid, a remaining anchor to this theory is if the super-Alfvénic flow is able to stretch the magnetic field lines out to infinity.

Winglee et. al.[89] has stated that the plasma has the ability to stretch the field lines so long as kinetic beta exceeds unity ($\beta_k > 1$), thermal beta is less than unity ($\beta_{th} < 1$), and the ion gyroradius is smaller than magnet scale length. Thermal beta, β_{th}, is defined as the ratio of plasma thermal energy to magnetic energy:

$$\beta_{th} = \frac{\mathrm{n} k_B T_i}{\left(B^2 / 2\mu_0 \right)} \tag{6-20}$$

The requirement for thermal beta to be less than unity is because the plasma thermal energy would remain unable to cause beam expansion while the plasma flow energy is able to stretches the field lines. It is essentially a balance of plume compression and tension forces. It is claimed that this effect can lead to self-collimation of the plasma beam[89]. Figure 6.9 displays thermal beta using gridded measurements of density (assuming quasineutrality), ion temperature, and magnetic field strength. Ion temperature is used instead of electron temperature to present limiting values since $T_i \sim T_e$ during the Helicon time window and $T_i > T_e$ when the ions are energized. Thermal beta exceeds unity during both modes of operation; at about Z ~ 4.9 m during Helicon and Z ~ 4.4 m during ICH. These transitions mark the boundaries to a region $\Delta Z = 0.5$ m wide where $\beta_k > 1$ and $\beta_{th} < 1$ and field line stretching, without thermal beam expansion, is possible between 4.4 m < Z < 4.9 m during Helicon and 3.9 m < Z < 4.4 m during ICH.

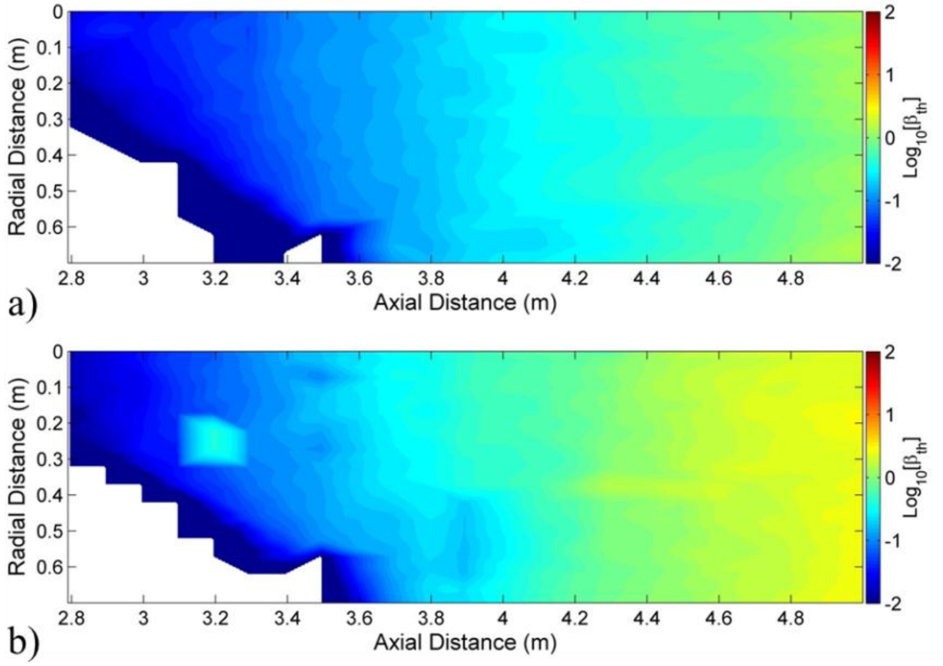

Figure 6.9: Contour maps of plasma thermal beta during Helicon (a) and ICH (b) time windows.

The theoretical model of Breizman[78] may be used to simulate the expected stretched magnetic field structure in this nozzle for super-Alfvénic flows using measured values of density, ion velocity, and magnetic field. This model is more applicable to the current experiment in that it assumes anisotropic heated ions and cold electrons operating at steady state, whereas the previous model assumed cold ions[70]. Both theories predict magnetic field line stretching divided into three regions: Straight field lines in the bulk plume, a rarefaction wave along the edge, and the vacuum region where the magnetic field is zero. The predicting equations for the cold ion case, listed in chapter 2 equations 2-17 through 2-19, are modified for the hot ion case to[78]:

$$\mathrm{B}(\mathrm{r},\mathrm{z}) = \mathrm{B}_0 \frac{z_0^2}{z^2} \begin{cases} 1, & \mathrm{r} \le \mathrm{r}_{rw} \\ \frac{1}{9}\left[M_A(\mathrm{z}\tan\theta_0 - r) + 2(z - z_0)\right]^2 (z - z_0)^{-2}, & \mathrm{r}_{rw} < \mathrm{r} < r_{pv} \\ 0, & r_{pv} \le r \end{cases} \qquad \text{6-21}$$

$$r_{rw} = z\tan\theta_0 \left[1 - \frac{1}{M_A \tan\theta_0}\left(1 - \frac{z_0}{z}\right)\right] \qquad \text{6-22}$$

$$\mathrm{r}_{pv} = z\tan\theta_0 \left[1 + \frac{2}{M_A \tan\theta_0}\left(1 - \frac{z_0}{z}\right)\right] \qquad \text{6-23}$$

where tan θ_0 is used instead of θ_0 since the small angle approximation cannot be assumed for the VX-200 plume. Using approximate divergence values, estimated in section 5.1, of 22° for the Helicon window and 20° during ICH, the expected stretched magnetic field during each time frame may be computed. These simulations are displayed in figure 6.10 for both ion energy settings.

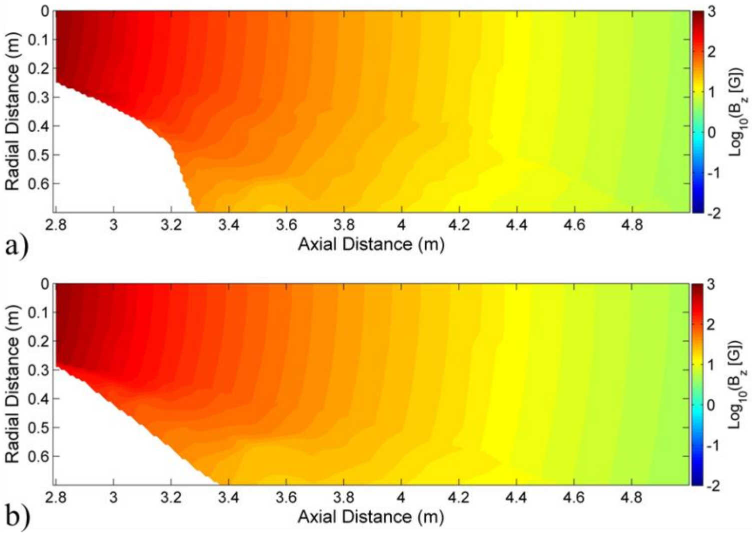

Figure 6.10: Simulation of magnetic field line stretching according to the hot anisotropic ion model[78] for plasma during the Helicon (a) and ICH (b) data windows. The areas in white represent field strengths of zero and are outside of the plasma-vacuum interface. Divergence angles of 22° and 20° were used respectively. The width of the rarefaction wave appears to narrow with increasing ion energy.

Each of the three regions is seen in both figure 6.10 a) and b). The largest determinant to these models aside from the nozzle divergence angle is the mapping of the Alfvén Mach number. The rarefaction wave appears much wider at lower energies (i.e. M_A) and narrows as the ions are energized. The regions colored in white represent the magnetic field at radii greater than the plasma-vacuum interface, which are zero according to the idealized conditions of this model. The plume edge in the ICH case has been pulled farther downstream, the bulk straight line region has widened, and the rarefaction wave has narrowed. It is curious is that the simulations do not necessarily demonstrate the more slanted kinetic beta transitions seen in figures 6.7 and 6.8. These simulated models show one expected possibility of magnetic field line stretching.

How well does this simulation compare with the observed magnetic field from the experiment data? Figures 5.7 & 5.8 plotted the measured magnetic field components, for the vacuum field and while plasma was flowing. The magnetic field did not change any noticeable amount from the applied vacuum field. There is certainly not any region of zero magnetic flux, let alone outside of the plasma-vacuum interface, as predicted by both theories presented by Arefiev[70] and Breizman[78]. The magnetic field from these previously presented figures bears no resemblance to the simulated stretched magnetic fields. The simulations were also run for other divergence angles (*not shown*: 30°, 45°, and 10°) to which none of them compared well with the measured data. This result is not surprising considering the Alfvén Mach number has a stronger dependence in the model than the divergence angle.

The assertion that the magnetic field lines are not stretching is strengthened by looking more closely at the magnitude of the magnetic field generated by the flowing

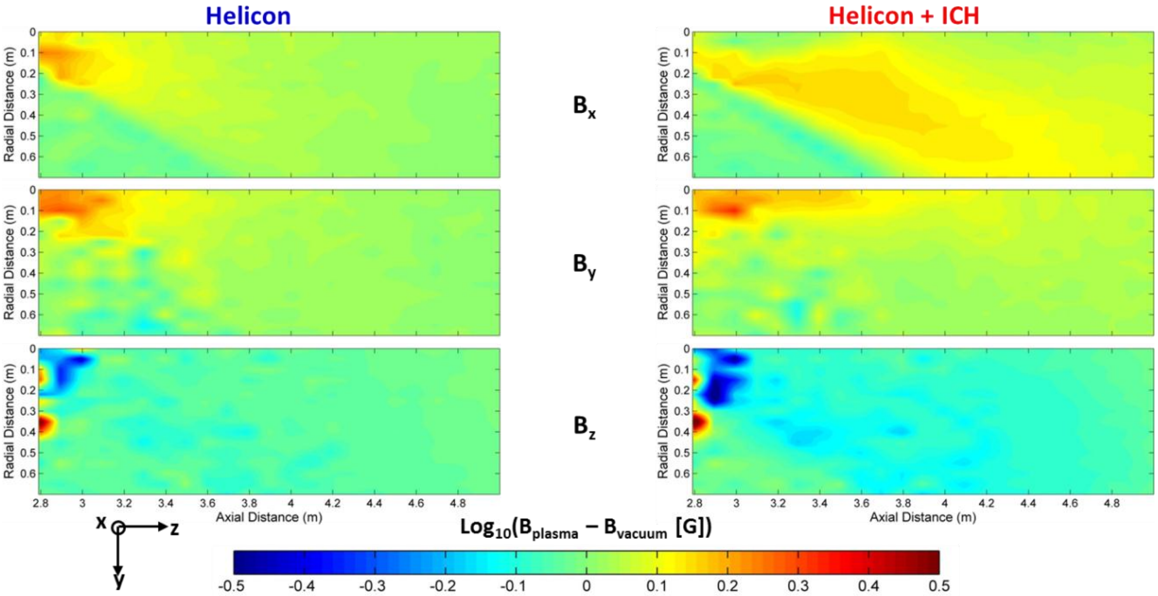

Figure 6.11: Contour maps of the magnetometer signal during plasma flow subtracting off the vacuum signal measurements for flows during the Helicon (*left*) and ICH (*right*) data windows. Although the values are small, the responses to a flowing plasma plume are seen in the data.

plasma. Contour maps of the measured magnetic field in each Cartesian direction, while subtracting off the vacuum field, are presented in figure 6.11 for both ion energy modes. The rows represent signals from the B_x, B_y, and B_z sensors mounted orthogonally in the magnetometer probe head, while the columns are organized by the RF power/ion energy. The right-hand rule was used to orient the sensors so that positive B_x is out of the page, positive B_y is along the radius towards the bottom of the plot, and B_z is positive along the nozzle axis. The responses to the flowing plasma are noticeable and the plasma magnetic field extends further downstream with greater ion energy. For the most part the trends involve an increase or positive magnetic field along x and y and a decrease in the z component. This trend indicates the effects of the flowing plasma are diamagnetic, opposing the applied field. This result directly contradicts the MHD field line stretching theories which predict a paramagnetic effect bringing the field lines closer to the axis. The plasma magnetic field is also quite small, measuring no larger than 0.6 G (B_z) during the Helicon window and 0.78 G (B_z) when for ICH. The average magnetic field for the Bx, By, and Bz directions is 0.02 G, 0.03 G, and -0.04 G respectively during Helicon (0.02 G, 0.065 G, and -0.067 G during ICH).

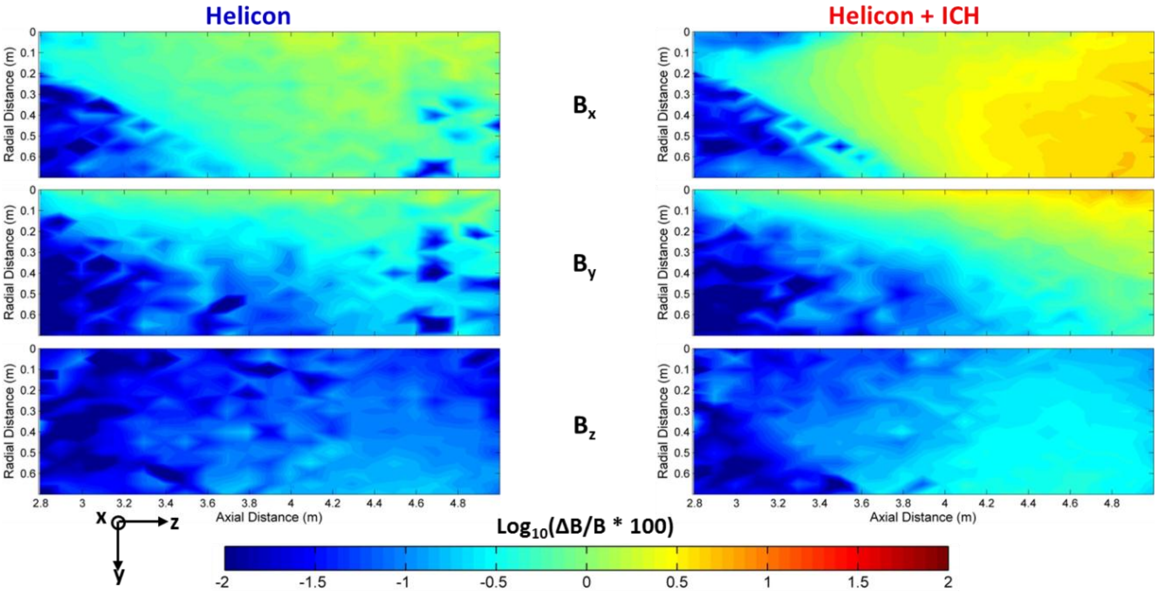

Figure 6.12: Contour plots showing the magnitude of the change in magnetic field with flowing plasma as a percentage of the local magnetic field strength during the Helicon (*left*) and ICH (*right*) data windows.

An argument could be made that the field lines may be stretched in regions where the applied magnetic field is weak; much like the case of plasma streaming out of the sun along the Parker spirals[127]. To test this possibility the magnetic field strengths from figure 6.11 are plotted as a percentage of each components magnitude in figure 6.12. The effects of the flowing plasma become more pronounced than in figure 6.11, but the percentage of change in the field does not become large unless the field direction reverses (as in B_y) or is close to a plane of symmetry (as with B_x). Outside of these extremes the magnetic field change is less than 1%. The magnitude of the measured field in the z-direction, within the measurement range of this experiment, does not exceed 0.2%.

For field line stretching theory to apply one would expect much larger percentages along the edges of the plume, especially in the super-Alfvénic regions. This effect, simply stated, is not occurring despite correlation with the linearization of ion trajectories along the kinetic beta transition. Since line stretching is a steady state prediction and is not seen in this setup with DC magnetic field measurements, preservation of the frozen-in field condition may still be plausible on faster time scales which will be explored in the following section.

Section 6.2.2: Magnetic islands/reconnection

The frozen-in condition may be preserved through the processes of magnetic field reconnection driven by AC perturbations. In this scenario the flowing plasma may alter the applied nozzle field to the extent that the field lines pinch off preserving a small ‘island’ of plasma confined to its own field that is then carried away with the plasma momentum. The ‘X’ line reconnection, necessary to the process, is thought to be brought about by plasma instabilities[129-131, 133]. In order to achieve detached flow at the measured ion velocities one should expect the formation of these magnetic ‘islands’ to occur at about the same rate as it may take an ion to traverse a small portion of the plume. Since the islands must travel at the same velocity as the ions one should expect to measure full, small amplitude, reversals of the magnetic field along both B_z and B_y

directions. In the frequency domain these reversals should resemble the ion velocity distribution of the outbound particles with peaks near ~ 15 kHz and ~ 30 kHz during the Helicon and ICH time windows, respectively. For low-frequency reconnection the fluctuations would necessarily be limited by the ion cyclotron frequency (~ 0.4 - 30 kHz) as the magnetic perturbation should not propagate faster than it takes an ion to complete a single orbit. A final expectation is that the magnetic islands would form a plume structure consistent with the other data, i.e. integrated ion trajectories.

The approach to measuring these magnetic islands is to Fourier transform the magnetometer time-domain signal (similar to figure 4.14) into the frequency domain. The output signal from the magnetometer conditioning electronics was digitized at 100 kHz permitting analysis in the frequency domain up to 50 kHz according to the Nyquist-Shannon sampling theorem. This maximum limit is large enough to capture frequencies beyond those corresponding to ICH level ion velocities in the high velocity ‘tail’ of the distribution; but saturation at 50 kHz would also indicate the presence of higher frequency (50 kHz – 100 kHz) magnetic fluctuations.

Transforming the finite-length time series data into the frequency-domain, a process known as discrete Fourier transform (DFT), is commonly performed using the fast Fourier transform (FFT) which is an algorithm for implementing the DFT. Because the purpose of Fourier spectral analysis is to approximate the continuous Fourier transform (CFT), formed from an infinite time series, with discrete time samples, some preconditioning of the signal prior to applying any transforming algorithm is necessary. Applying an FFT algorithm (such as Cooley-Tukey[225]) to any restricted time-series signal will produce the frequency representation involving the main frequencies and sidelobes[226]. These sidelobes, often referred to as spectral leakage, are not ‘pure’ frequencies in the signal and can overlap or otherwise hide the real frequencies. Signal offsets and applying window functions can reduce the amplitude of these sidelobes. Another effect that may cause erroneous results in the frequency domain is aliasing, where higher frequencies can masquerade as lower-frequency signals[226]. Aliasing, in this experiment, is treated prior to digitizing the magnetometer signal as the conditioning electronics are bandwidth limited beyond 100 kHz effectively filtering out much higher frequencies.

To reduce the effect of decaying sidelobes, the signal was pre-conditioned prior to using the FFT by offsetting the amplitude and applying the Hamming window function. Sharp edges in the time-domain, such as a direct transition from zero amplitude to full signal, are a large contributor to spectral leakage. An amplitude offset can be used to reduce the sharp edges by subtracting the signal average during each time window (Helicon and ICH) from the raw signal forcing the data to oscillate about the axis. In using this technique the only sharp transitions will be due to the oscillations in the signal itself. To further reduce the amplitude of the spectral leakage a window function may be used. A window function is a smooth symmetric function that ranges from zero at the extremes to one at the maximum and is multiplied to the time-domain data. Many different window functions are used across the discipline of digital filter design, but some of the more common or frequently used are rectangular, Hamming, Hann, and Blackman[226]. The Hamming, Hann, and Blackman windows are similarly based on a cosine function with varying coefficients. The Hamming window was selected because the sidelobes are more reduced about the peak than the other two[226]:

$$hamw_i = 0.54 - 0.46\cos\left(\frac{2\pi i}{N}\right) \qquad 6\text{-}24$$

where i is the time-domain sample number and N is the total number of samples within the data window.

After applying the amplitude offset and Hamming window, the data was then zero-padded on either side of the time-domain data. Zero-padding is a common technique where arrays of zeros are appended to the signal and is used to improve interpolation in the frequency-domain[226]. This practice is analogous to interpolating between values in time-domain data, effectively increasing the number of points and bringing the DFT approximation closer to the CFT. For the plume data an array length of 2N was appended on both ends of the signal making the signal both symmetric and five times longer. The native FFT function in matlab® was then applied to three time-domain windows: pre-plasma signal (100 ms), Helicon time window, and ICH time window. The pre-plasma frequencies serve to remove background-level noise and are subtracted from both the Helicon and ICH spectra. It is known that non-averaged or non-filtered frequency spectra can have normalized standard error as high as 100%[227]. Frequency smoothing was used to reduce this error because experiment time constraints prohibited ensemble smoothing. A boxcar averaging filter, 76.3 Hz wide (for ℓ = 50 contiguous spectral components), was used to smooth each spectrum reducing this uncertainty to under 15%. As a final treatment to reduce all outside influences in the signal, such as RF pickup in the magnetometer signal cables, a reference spectrum was subtracted from both filtered spectra. This reference spectrum was analyzed by the same process and taken during the same time windows but the probe was out of the plasma during a firing similar to the method used in the HF electric probe analysis.

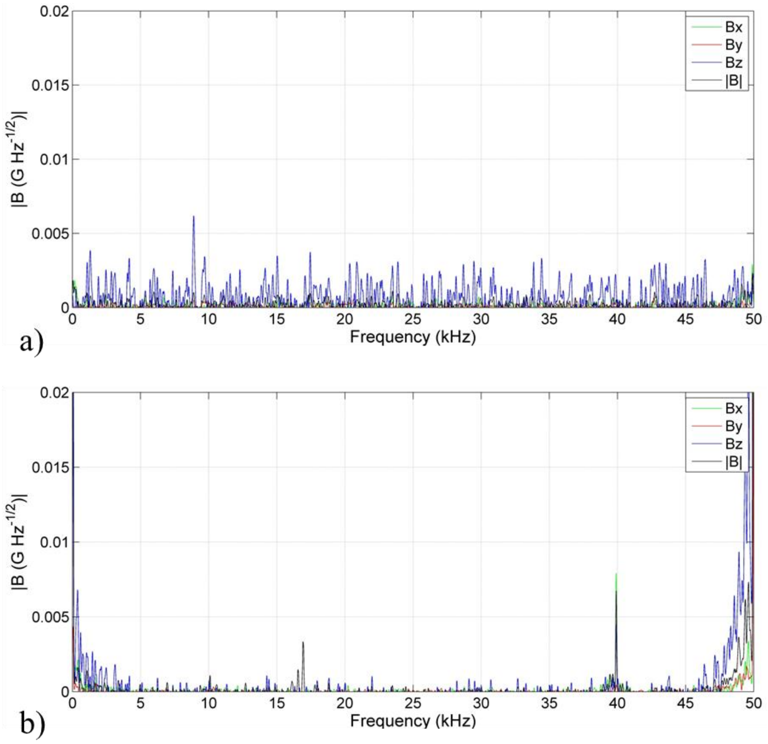

Figure 6.13: Single-sided amplitude spectra of the magnetic field during Helicon (a) and ICH (b) time windows. Data were taken along the nozzle axis at R = 0 m and Z = 2.79 m.

Shown in each sample spectrum of figure 6.13 are the resultant spectra from the B_x, B_y, B_z signals, and vector summation (|B|) for a single shot taken along the nozzle axis at the closest measurement location (Z = 2.79 m). During the Helicon time window (figure 6.13a), most of the spectra appear as random noise with only a single peak emerging above the rest (B_z @ 9 kHz). When ions are energized the previous spectrum disappears and a few prominent peaks appear at low frequency (< 2 kHz), ~ 17 kHz, 40 kHz, and at higher frequencies (50 – 100 kHz). Although the 17 kHz peak is near 15 kHz corresponding to Helicon ion velocities, the 40 kHz peak is above the 30 kHz expected to correlate with ICH level ion velocities. The amplitudes of the peaks are less than 20 mG and much larger field strengths would be needed to maintain magnetization of the particles. The peaks are also narrow whereas a broader distribution similar to the velocity distribution was expected. These two observations alone would be sufficient to conclude that magnetic islands, said to be moving along with the flow, are not playing a role in the plume dynamic but the question remains if these spectra are representative of the magnetic field fluctuations throughout the entire plume.

Collages of contour maps are presented in figures 6.14 and 6.15 to illustrate the extent of the B_z and B_y, respectively, magnetic fluctuations as a function of the radial position for each frequency spectrum at several discrete axial locations. The columns correspond to magnetic fluctuations during the Helicon and ICH time windows. No interpolation was used between the radial positions of each spectrum. It is seen that the scope of the B_z fluctuations (figure 6.14) differs little between low and high ion energy except at the frequency extremes. The radial distributions are fairly symmetric about the axis and dissipate with increasing axial distance. The amplitudes drop off to less than 1 mG except along a few sparse patches for distances greater than 30 cm downstream. There are no significant increases in amplitude above the sample spectrum (figure 6.13) and is no discernible plume structure that could align with any of the previous analyses (i.e. chapter 5). Even if the higher frequencies (50 – 100 kHz) were playing a role, those amplitudes also fall off to the level of the noise in the far plume.

Contour maps only up to an axial location of 3.59 m are displayed, but maps from 3.69 m to 5.49 m were virtually no different than those located at 3.59 m. A similar conclusion may be drawn from the B_y spectra shown in figure 6.15 where the amplitudes are overall much lower. No trending plume structure forms and the amplitudes at the higher frequencies spread out and reduce to noise levels in the far plume.

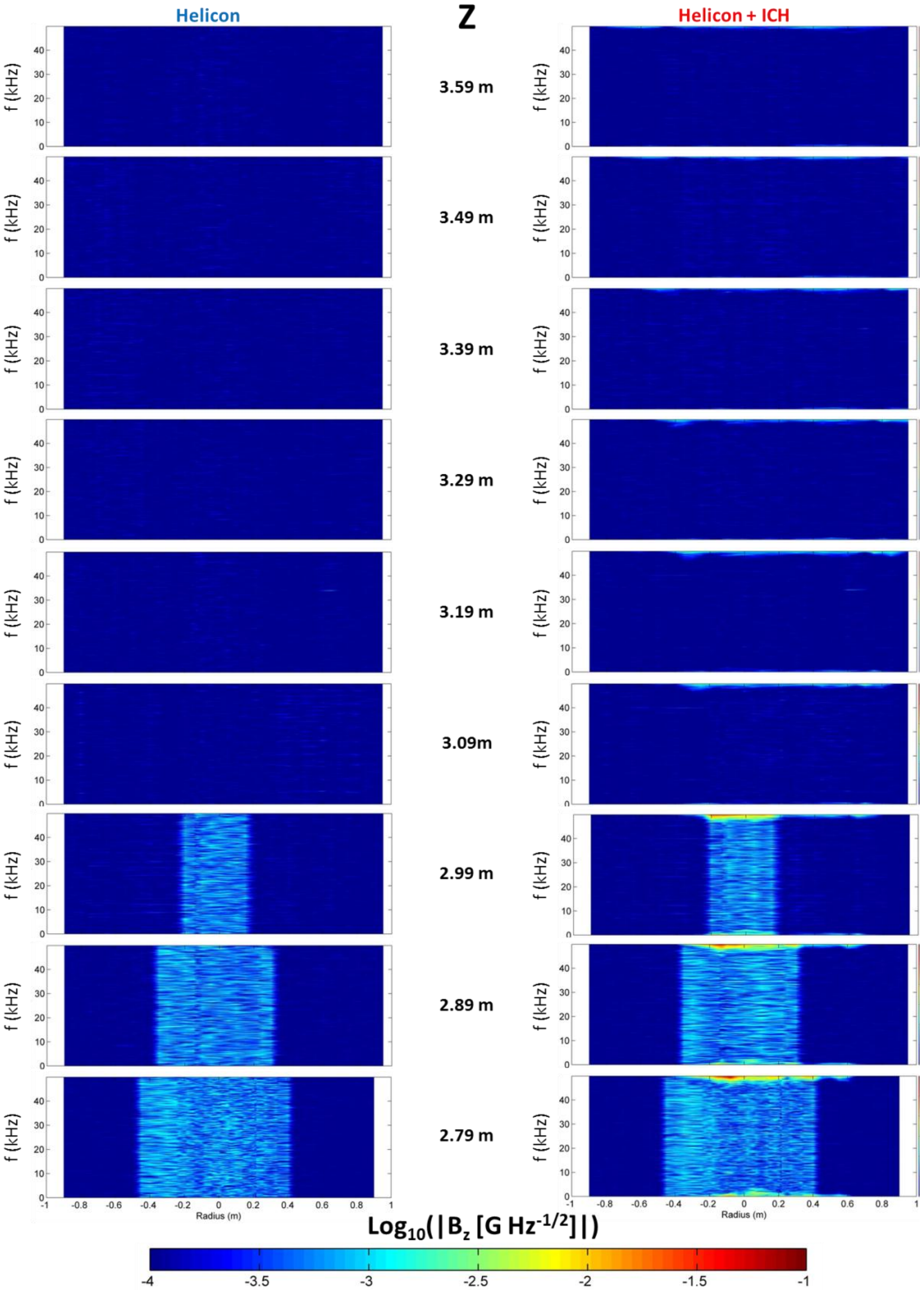

Figure 6.14: Collage of contour maps of single-sided B_z amplitude spectra as a function of radial position. Columns represent the time window/ion energy level (Helicon/low *left*, ICH/high *right*) while the rows correspond to discrete axial positions for the spectra. The region where spectral response is greatest narrows with increasing distance. The peak amplitudes fall off to background levels in the far plume.

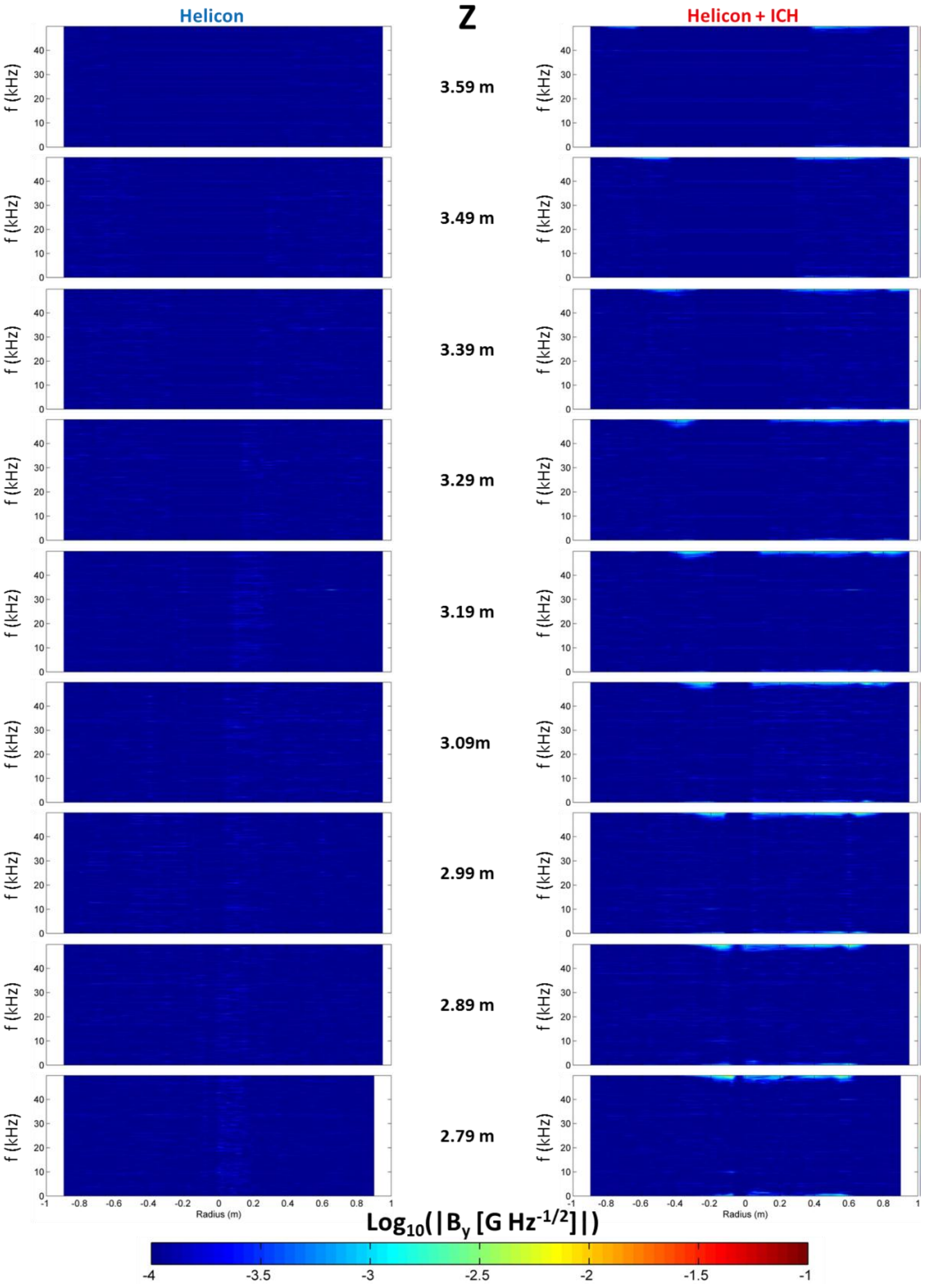

Figure 6.15: Collage of contour maps of single-sided B_y amplitude spectra as a function of radial position. Columns represent the time window/ion energy level (Helicon/low *left*, ICH/high *right*) while the rows correspond to discrete axial positions for the spectra. The peak amplitudes fall off to background levels in the far plume.

To summarize these observations, it was observed that the magnetic field amplitude spectra feature low amplitude peaks across the frequency spectrum. There are noticeable changes to the spectrum when ion energy is increased, but not to magnitudes that are consistent with magnetized flow. The widths of the peaks that did emerge were too narrow to correspond to magnetic fluctuations moving across the plume expected to match the ion velocity distribution. Maps of these fluctuating fields did not reveal any organized plume structure similar to what other plasma diagnostics had shown previously. These reasons are sufficient to conclude that magnetic islands frozen-into the flow are not playing a role in the detachment process from this magnetic nozzle.

Theories involving the preservation of the frozen-in condition such as magnetic field line stretching and magnetic islands are both shown not to be a part of the magnetic separation of this plume from the applied field. It is sufficient to say that treating the plasma as a single component fluid, as traditional MHD assumes, is not a realistic approach given the parameters of this experiment. Two-fluid or hybrid fluid treatments may be more applicable.

Section 6.3: Electron inertia

The scenario of non-magnetized ions but magnetized electrons detaching from a magnetic nozzle may be brought about by a mechanism known as electron inertia[60]. This theory involves an ion/electron pair electrostatically tied together forming a hybrid particle and is presented as a fundamental lower limit for detachment in the absence of many other common plasma effects. This hybrid particle, depending upon the value of a dimensionless parameter, G, would be energetically able to drift across the magnetic flux surfaces and separate from the field lines. Recalling from equation 2-29, this scaling parameter is defined as[60]:

$$G = \frac{1}{4}\Omega_e\Omega_i\left(\frac{r_0}{u_0}\right)^2 \qquad \text{6-25}$$

where $\Omega_{e/i}$ are the cyclotron frequencies, r_0 is the plasma radius at the nozzle throat, and u_0 is the ion velocity at the nozzle throat. It is said that smaller values of G are more favorable for detached flows[60]. The values of G in this experiment are calculated to be 4.3 x 10^6 and 1.1 x 10^6 during the Helicon and ICH time windows, respectively, and are much larger than the example values reported by Hooper.

To compare the likelihood of this drift being a suitable detachment mechanism for this experiment, a similar approach to the method used by Hooper[60] is followed. This approach involves integrating the equations for the flow of hybrid particle in a region of magnetic flux (equations 2-30 & 2-31), taking the limiting case of v = 0 where the particles become slowed to a halt, and using an applied field generated by a current loop. Rearranging and solving for z^2 gives:

$$z^2 = \frac{(1+a)^2 r^{4/3}}{\left[1 \pm \left(\frac{r}{G^{1/2}}\right)\right]^{2/3}} - (r+a)^2 \qquad \text{6-26}$$

where z is the axial distance away from the throat and *a* is the radius of the current loop creating the magnetic field.

Using the values determined in this experiment and normalizing distances to r_0, the positive and negative cases of equation 6-26 are plotted in figure 6.16 for both Helicon and ICH plasma operation. The large values of G are the reason for such high values of z^2 before the functions roll over. This roll-over indicates that plasma flow during both Helicon and ICH time windows are energetically unable to detach as the flux surfaces cause particles would slow down before forcing them to return. Plotted as a subset is a zoomed view of the same graph that features lines of constant integrated ion flux, out to 10% and 90%, which are also normalized to r_0. These lines were shown in chapter 5 to have separated from the magnetic flux but were still subject to ambipolar forces. For higher energy ions the trajectories inflected and became linear suggesting complete detachment of the plume including the electrons. It may also be argued that the trajectories of the lower energy ions, formed during the Helicon discharge, lying closer to the nozzle axis are also on a more linear trajectory and are able to detach completely.

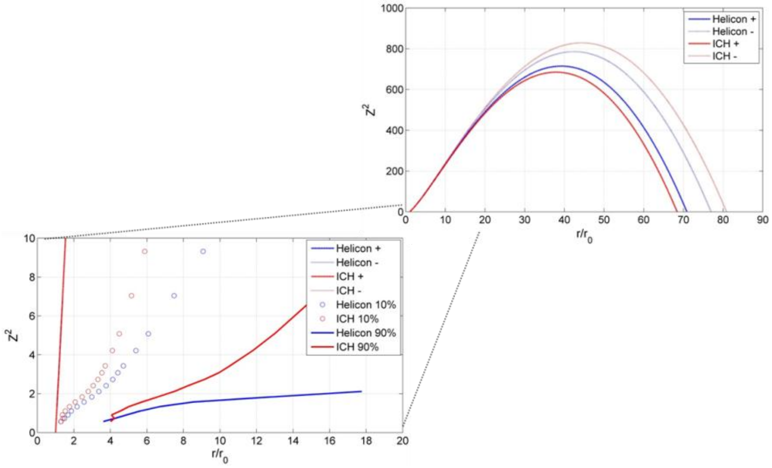

Figure 6.16: Electron inertia solution to plasma flow in a current loop, z^2 vs r. Distances are normalized to r_0. A subset figure featuring zoomed limits is shown displaying also the integrated ion flux lines out to 10% and 90%.

The ion trajectory data appears to be inconsistent with the electron inertia theory proposed by Hooper where the flow would be constrained between the positive and negative solutions to the equations of flow through a potential. Even trajectories very close to the nozzle axis would remain captured according to this model, being destined to return back around the closed field lines. The ion trajectory data lie firmly outside of these predicted flow surfaces and by most indications have detached. It is unclear what modifications would cause this theory to better align with the observed data. Hooper suggested that factors such as dissipation and turbulence could significantly alter this limiting approximation[60].

One author claimed, mostly as a mathematical exercise, that the addition of an azimuthal velocity component to the hybrid particle would be sufficient to enable complete detachment of the plume[85]. In this case the flux surfaces solved in the form of equation 6-26 from the Hooper model, when adding in an azimuthal velocity profile would then be modified to[85]:

$$Z^2 = \frac{\rho^{4/3}}{\left[\Delta \pm \left(\Delta - \frac{\rho^2}{[(\rho+1)^2 + Z^2]}\right)\right]^{2/3}} - (\rho+1)^2 \qquad \text{6-27}$$

$$\Delta = \frac{4\pi}{\mu_0 I a}\Psi_m \qquad \text{6-28}$$

where Z and ρ are normalized to the current coil aperture radius and the variable Δ includes the equilibrium flux surface, Ψ_m, affected by the rotation given by equation 2-33. A transcendental equation forms and the plus and minus signs depict solutions lying inside and outside of the equilibrium flux surface respectively. It is possible that an azimuthal velocity profile could be introduced into this system during the ICH process, but it is a difficult parameter to measure/estimate and was not done in this experiment. Schmit gives a model scenario including rotation, reducing Ψ_m by 85%, with an aperture ratio of 0.29 and divergence angle of 20°[85]. This angle is similar to what was estimated in section 5.1, but would require an azimuthal rotation frequency of ~ 325 kHz, which exceeds the local ion cyclotron frequency in the plume. This rotation is unlikely to happen without a number of other constraints breaking down, such as adiabaticity and the formation of other instabilities that may have adverse effects on the rotation. Even assuming that the ICH process introduces sufficient azimuthal velocity to detach, the low energy Helicon ions would remain rotation-less and would still be unable to separate. The non-rotation scenarios fall back to the Hooper model which was found to be inadequate. Since azimuthal rotation was not able to be measured, this theory shall be labeled inconclusive although improbable.

The other presented variant to the electron inertia theory presented in chapter 2 was from Ahedo[81, 84]. This theory involves two azimuthal currents, *swirl* and *hall*, contributing to an overall diamagnetic effect on the plume. These currents reshape the field lines to enable counter-streaming electrons, along the fringe of the plume, to follow the departing ions closer to the axis. This theory assumes a number of conditions must exist in the nozzle throat; such as the debye length and electron gyroradius must be smaller than the plasma radius, and thermal beta is much less than one. One condition which is not met in this experiment is that the electron-ion collision mean-free-path must be larger than the plasma radius; the plasma radius in the throat is of order cm while the electron→ion mean-free-path is less than 1 mm. Without a complete overhaul to the model it is unclear what role these collisions may play in the flux surfaces detaching from the applied field. It is stated that this model focuses on cold ions and induced magnetic fields and is not directly comparable to the ions accelerated by ICH[81]. Despite these upfront disclaimers, one similarity between observation and the model prediction is a diamagnetic response to the plasma (figure 6.11). Outside of this correlation the model predicts the closure of magnetic surfaces to enable counter-streaming electrons[84]. These upstream flowing electrons should have produced a noticeable current and would have been observed in the magnetometer data. The induced diamagnetic field during the cold ion scenario is too small to account for the effects of counter-streaming electrons. Therefore this model is not applicable but may show more promise once modified to allow for the effects due to collisions.

In summary the electron inertia models for electron detachment proposed by Hooper[60] have been found to be inconsistent with the observed data not following the expanding magnetic field. The Hooper model predicts that in all instances of this particular VASIMR® setup that virtually none of the plasma should detach from the nozzle field. The possibility remains that other influences to the model may permit some enhancement allowing a wider range of plasma flow to detach. Other theories for plasma detachment using electron inertia as a foundation have been found either inconclusive or not directly applicable. These include the addition of azimuthal ion rotation[85] and azimuthal currents enabling counter-streaming electrons from the edge of the plume to leave near the axis. It may be worth studying whether the Ahedo model[81, 84], reconfigured for hot ions and collisions, could permit electrons to cross the field lines without large diamagnetic effects similar to what is observed in this experiment.

Section 6.4: Loss of adiabaticity

Rather than detaching from the nozzle field by diffusion, drifting across the field due to electron inertia, or carrying the field with the plasma, a probable separation mechanism may be where the ions and electrons become demagnetized. This loss of magnetization can be brought about by a breakdown of the first adiabatic invariant where the magnetic conditions change on a scale that is too fast for either ions or electrons to respond. The guiding center trajectories are no longer strictly followed and the particles become effectively demagnetized. A commonly used analogy would be vehicles travelling along a highway moving too fast and missing a sudden exit ramp.

This principle is better described using the particles gyromotion about a field line in a divergent field. A particle orbiting about a magnetic line of force in a divergent field will experience a weaker field over part of the orbit and a stronger field over the other. This variable field strength will cause the orbit to become more elongated as the gyroradius increases. As described in chapter 2, if the orbit becomes too eccentric over the course of a single gyroperiod, the magnetic moment μ will break down as the electromotive force used in its derivation and defined by the line integral from Faraday's law becomes irrelevant[136]:

$$EMF = \oint E \cdot ds \neq -\int \frac{dB}{dt} \cdot dS \qquad \text{6-29}$$

where ds is the line element around a circular path and dS is a surface element enclosed by the path. The change in gyroradius over a single gyroperiod can be expressed in terms of the distance the particle travels in this time using equations 2-22 through 2-24:

$$\frac{\Delta r_c}{r_c} \approx \frac{\Delta\Omega_c}{\Omega_c} = \frac{\mathrm{v}}{\mathrm{f}_c L_B} \qquad \text{6-30}$$

where L_B is the scale length of the magnetic field defined as B/|∇B|. The components of the right hand side of equation 6-30, can be measured to get an estimate of where the adiabatic invariant is expected to hold up. For values greater than order unity, adiabaticity is not maintained and the particles may be considered demagnetized.

Contour maps of the right hand side of equation 6-30, here referred as the adiabaticity parameter, are plotted for ion and electron velocities throughout the plume in figures 6.17 and 6.18 for plasma conditions during the Helicon (a) and ICH (b) time windows. The velocities used were the most probable ion velocity measured by the RPA, and the electron thermal velocity computed from the electron temperature measured by the guard-ring probe. An effective plume edge is plotted for reference (black line) taken from the 90% integrated ion flux. For the ions, the adiabaticity parameter exceeds 1 for the majority of the measurable plume during both time windows. Increasing the ion energy during the ICH process shifts the larger values further upstream. In a narrow region along the axial exit plane during Helicon time window, the ions may still be considered somewhat magnetized (up to Z ~ 2.9 m). Further downstream adiabaticity is lost at both ion energies. During the ICH window, a sharp drop-off line crosses the 90% plume edge (also at Z ~ 2.9 m) indicating that, between Z = 2.7 m – 2.9 m, the magnetic moment for a portion (f_i ~ 70% – 90%) of the plume was still conserved. The center plume (up to f_i ~ 70%) during ICH must have lost adiabaticity further upstream beyond the measurement range of these plasma diagnostics. This location is consistent with the observed location of the ion flux diverging from the magnetic flux presented in figure 5.17. In that figure the range of ion flux separation from the enclosed magnetic flux

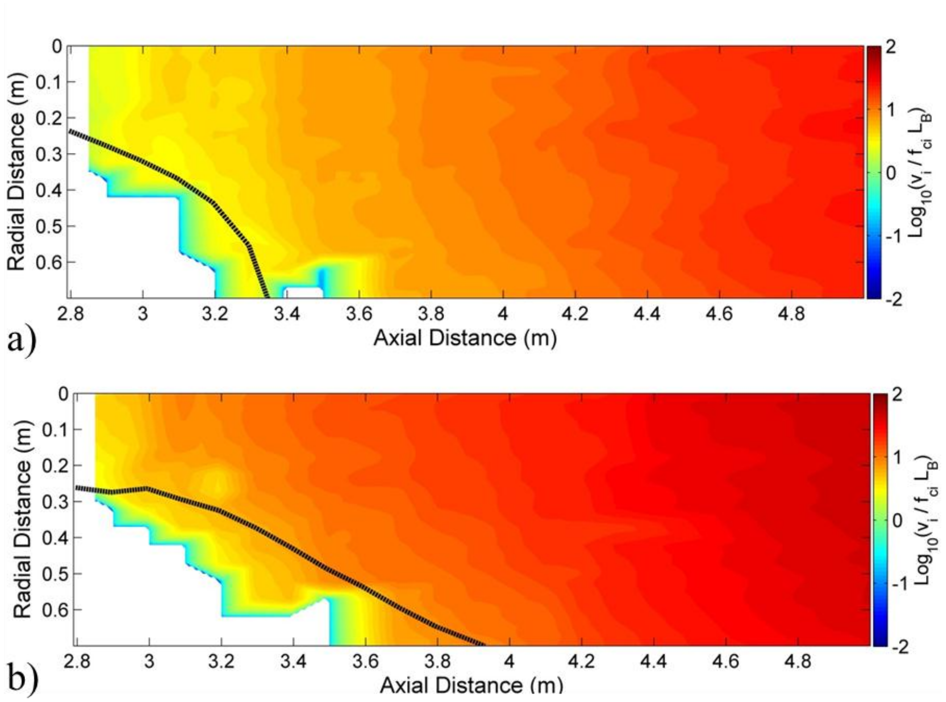

Figure 6.17: Contour maps of the ion adiabaticity parameter, $|v_i/f_{ci}L_B|$, for plasma during the Helicon (a) and ICH (b) time windows.

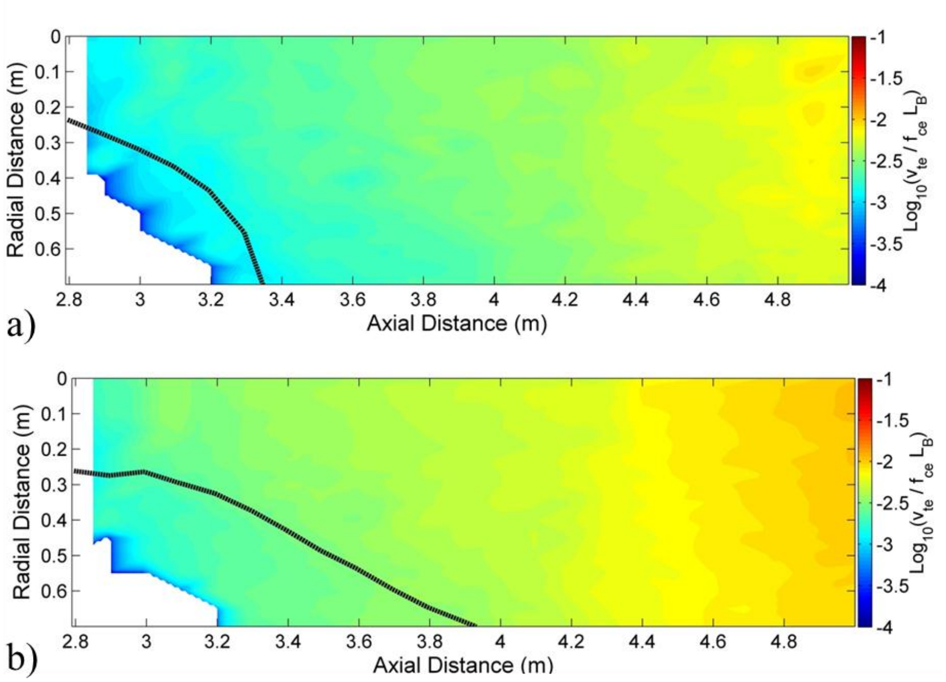

Figure 6.18: Contour maps of the electron adiabaticity parameter, $|v_{te}/f_{ce}L_B|$, for plasma during the Helicon (a) and ICH (b) time windows.

flux (dashed lines) during Helicon spans from 2.9 m < Z < 3.2 m and from 2.8 m < Z < 2.9 m during ICH. These ranges correspond to adiabaticity parameter values of 1.6 – 4.3 and 2.2 – 4.9, respectively which are above unity. The overlapping regions of ion flux divergence and adiabaticity parameters of order unity suggest the ions are becoming demagnetized by loss of magnetic moment conservation ($d\mu/dt \neq 0$).

The value of the electron adiabaticity parameter does not become of order unity over the measurable range of the diagnostics. It ranges from 0.0006 – 0.009 and 0.0014 – 0.013 during Helicon and ICH time windows, respectively. The magnetic field is not changing substantially over the course of an electron orbit and the conditions indicate they remain magnetized. Further downstream (Z > 5.0 m), where the electron gyroradius becomes large, the breakdown of the magnetic moment may be possible. There are no indications in this data, ion or electron, that correspond to either the location where the ion flux trajectories trend linear or where the collisional transport and electric fields appear to dissipate. The ions appear to have detached upstream by this mechanism while these other observations must be correlated to effects on the electrons by other actions.

Section 6.5: Plasma turbulence

With the conclusion that the ions have separated from the applied field through breakdown of the first adiabatic invariant while the electrons remain magnetized, to preserve space-charge the particles must respond with either electrons trapping the ions in the field or being towed along by more energetic ions. If the condition for preserving space-charge limits and large scale quasineutrality were to be violated, large amplitude

DC electric fields would form in the plume. Such a scenario would be unstable as nature tends to rearrange itself to the minimum energy configuration. These theoretical large amplitude DC electric fields were not observed indicating that one of the two above outcomes must be occurring.

For the electrons to trap the ions, the more mobile electrons diverge out in the flaring nozzle causing radial ambipolar forces on the slower ions. If the ions do not have sufficient momentum to escape they will spread in a manner to follow the magnetized electrons along the curved field lines. More energetic ions will have enough momentum to drive transport of the electrons across the field lines effectively towing them along. Recalling from section 6.1 the cross-field velocities from classical Coulomb collisions are insufficient to keep up with the ions. An additional mechanism is necessary to enhance electron transport above that due to electron→ion collisions to match the ion velocities. Anomalous resistivity may account for the enhanced collision rates to produce transport velocities capable to keep pace with escaping ions.

These anomalous collision rates are said to be brought on by electric field fluctuations, i.e. turbulence, caused by the lower hybrid drift instability (LHDI)[122, 126]. The LHDI is a T_e/T_i dependent form of the modified two stream instability (MTSI), with characteristic frequency in the lower hybrid range. This instability forms when two particle beams have flow velocities in different directions and the dispersion relation for the MTSI can take the form of[122, 135]:

$$1+\frac{k_z^2}{k^2}\frac{\omega_{pe}^2}{\Omega_{ce}^2}-\frac{\omega_{pi}^2}{(\omega-k_z\mathrm{v}_{de})^2}-\frac{k_y^2}{k^2}\frac{\omega_{pe}^2}{\omega^2}=0 \qquad \text{6-31}$$

where the drift velocity of the electron beam relative to the ion beam is v_{de}. When $k_z v_{de}$ is comparable to the lower hybrid frequency, ω_{LH}, the instability will grow causing fluctuations in the electric field and plasma density.

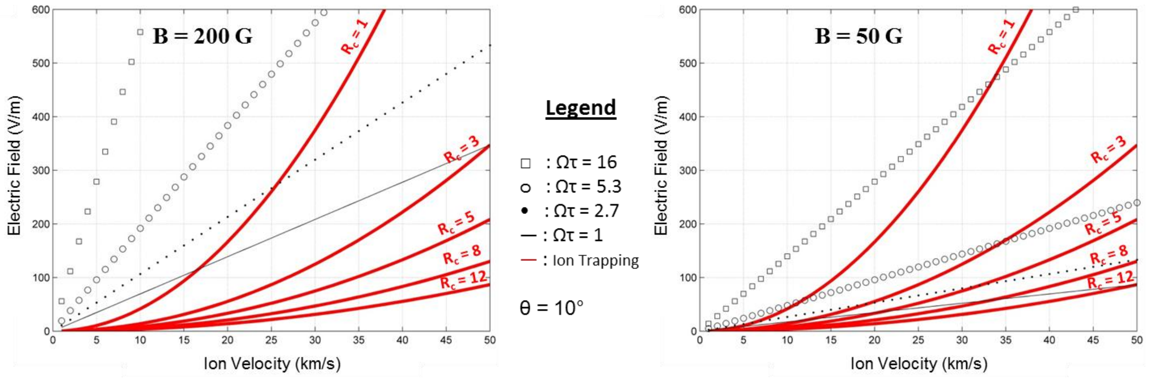

Figure 6.19: Theoretical electric field magnitudes as a function of ion velocity based on the ion/electron response to either ion trapping or anomalous diffusion in 200 G (*left*) and 50 G (*right*) magnetic fields. Each of the anomalous diffusion calculations (black markers) assumes a constant separation angle of 10°. The electric field required to trap ions is largely dependent upon the radius of curvature of the magnetic lines of force (R_c (m), red lines).

The dominant process, between ion trapping and anomalous diffusion, will be determined by an electrostatic force balance depending upon the electric/magnetic field strength, curvature of the magnetic field, angle of flow separation, and effective momentum transfer time according to equations 2-45 through 2-47. Theoretical values for the electric fields that arise from each process are plotted in figure 6.19 for two regions of different magnetic field strength in the plume. The electric fields required to drive anomalous diffusion are marked in black while those required to maintain centripetal motion of the ions are shown in red for varying radii of curvature. These plots assume regions of constant magnetic field and electron/ion divergence angle. The values of the magnetic field (200 G *left*, 50 G *right*) are based on the approximate axial field magnitude (between Z = 3.2 m – 3.9 m) corresponding to the regions where frequency dependent electric fields were observed (figure 5.33). A divergence angle of 10° was used as an estimate for the maximum divergence case, and hence largest electric field based on equation 2-46. The series involving different values of $\Omega\tau$ correspond to parameters of the mobility term with 16 being the Bohm-diffusion equivalent value, 5.3 is a factor of three greater than the Bohm value, 2.7 is a reference to a measured value known as 'Super-Bohm'[120], and 1 is the theoretical minimum. The process with the lowest electric field is expected to dominate as either ion trapping or anomalous diffusion will saturate the perpendicular electric field never reaching the other.

Figure 6.19 shows that for different regions of the VX-200 plume, conditions are permissible for anomalous diffusion to be a candidate for electron detachment in this magnetic nozzle. Higher velocities and weaker magnetic fields are more favorable as the anomalous transport undercuts the ion trapping curves even along the outer edges of the plume where the radius of curvature is low. One deceiving aspect of figure 6.19 is that ion trapping would appear to dominate for large radii of curvature but this is not necessarily the case as these regions are much closer to the nozzle axis where the divergence angle is expected to be much lower. A lower divergence angle results in reduced electric fields necessary for anomalous transport to levels comparable to ion trapping. This effect is confirmed by the absence of any significant oscillating electric fields near the nozzle axis in figure 5.33. Considering these trends the conditions for anomalous transport are more favorable along the outer half of the plume and in weaker magnetic fields, for the range of ion velocities seen during the ICH (27 – 32 km/s) window than for those seen during Helicon alone (13 – 17 km/s).

Calculations of the electric field were plotted in figure 6.19 for only two locations in the plume. Contour maps contrasting these same effects are displayed in figure 6.20 using the measured ion velocity and magnetic field for both Helicon (*left*) and ICH (*right*) time windows. The rows correspond to the ion trapping and anomalous transport scenarios (except $\Omega\tau = 1$) while assuming a constant divergence angle of 2°. Although the divergence angle is certainly variable along $\hat{\mathbf{r}}$**,** this angle was chosen to represent a smaller angle limiting case. Figure 6.20, under these assumptions, confirm the claim that there are regions in the plume where electric fields driving anomalous transport are lower than those that are said to preserve centripetal motion (ion trapping). Anomalous transport may be a plausible electron detachment mechanism and warrants further study.

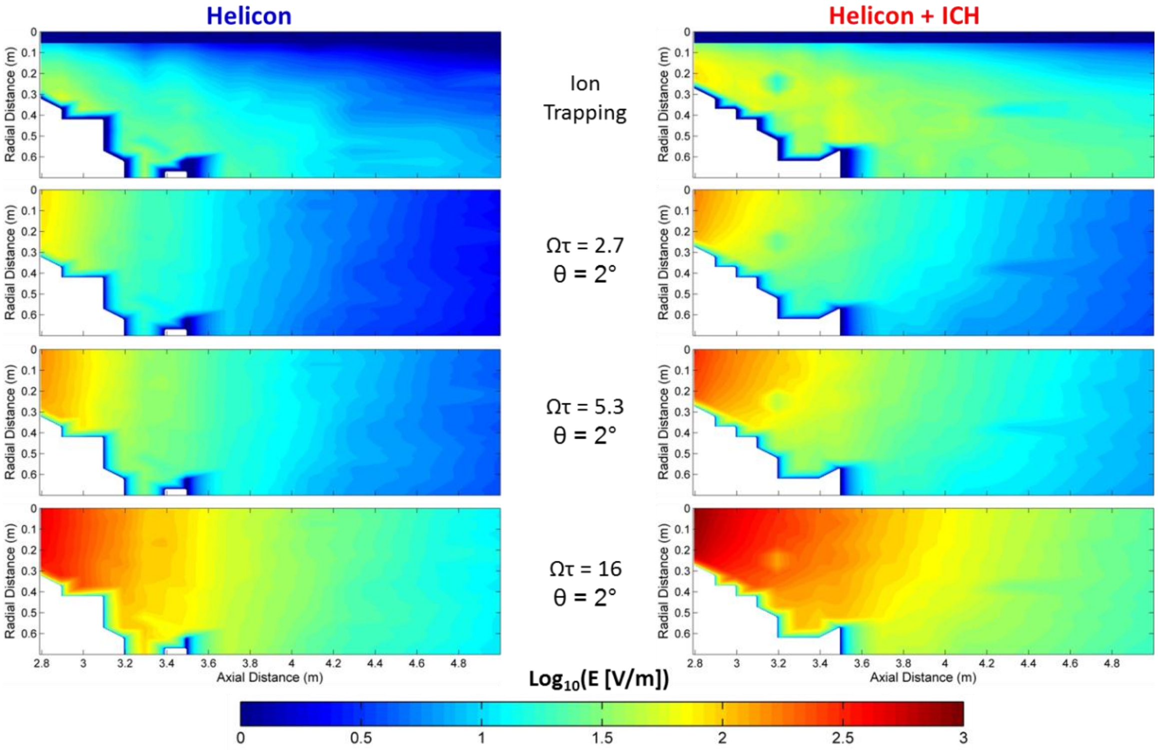

Figure 6.20: Contour maps of the estimated electric field for the contrasting processes of ion trapping and anomalous transport during the Helicon (*left*) and ICH (*right*) time windows. Values of $\Omega\tau$ range from 'Super-Bohm'[120] to Bohm equivalent mobility and assume a constant divergence angle of 2°.

From these calculations it is expected that, assuming low divergence angles and larger mobility ($\Omega\tau < 6$), anomalous transport would be effective for an axial range of Z > 3.5 m. Further upstream (Z < 3.4 m) the electric fields required for circular motion are lower and ion trapping is more dominant causing the non-magnetized ions to spread out. The region of Z = 3.4 m – 3.5 m appears to be a region transitioning from ion trapping processes to anomalous transport. These regions are reflected in the slope ratio and detachment angle data trends of section 5.3.3-4 (figures 5.20 & 5.22). Both sets of data show a distinct change in ion trajectory at an inflection point located at Z ~ 3.4 m suggesting the transition to anomalous cross field transport has occurred. The upstream spreading of the non-magnetized ions are also seen in the integrated ion flux trajectories (figure 5.17b) between Z ~ 3.0 m – 3.4 m where the paths spread out following a more quadratic fit. The paths then transition to a linear (ballistic) trajectory from Z ~ 3.4 m – 3.8 m depending upon the radial origin of each ion plume fraction. The effects are much stronger for higher ion velocities (ICH) but are still noticeable at lower ion velocities (Helicon) as the transition shifts further downstream (Z ~ 3.4 m – 3.7 m) and radially outward. Accordingly the ion trajectories during Helicon operation may take on similar ballistic trajectories to those observed during ICH but are more subtle and/or occur at radial locations beyond the movable limits of the translation stage.

Recognizing that regional conditions for anomalous transport should be found in the plume and trends from the ion flux trajectories, slope ratio, and detachment angle reflect these assertions, the question becomes one of where the fluctuating electric fields are located and of what magnitudes. An oscillating radial electric field was detected, detailed in section 5.5.2, and had frequencies spanning up to an order of magnitude above

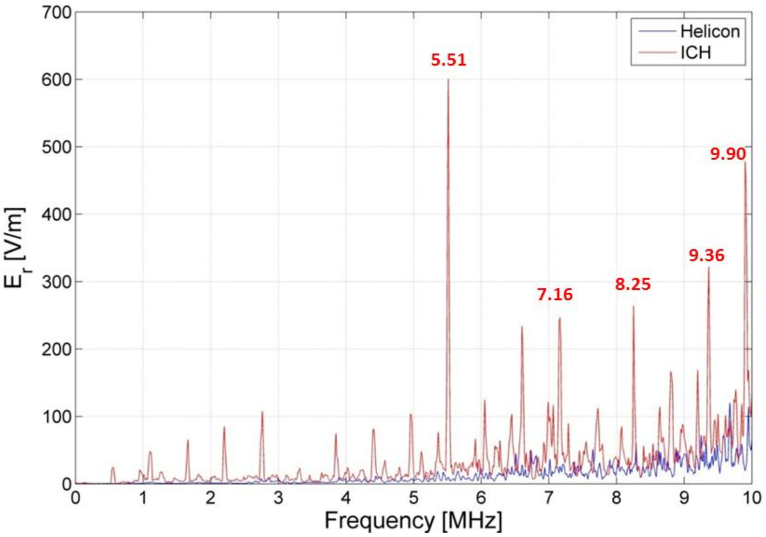

Figure 6.21: Electric field spectrum during both time windows, taken at (r, z) = (0.2 m, 3.23 m). The frequencies related to the five most prominent peaks during ICH are labeled for reference.

the lower hybrid frequency. One instance of this electric field spectrum, measured with the high frequency electric field probe using the spectrum analyzer, is displayed in figure 6.21 taken at an (r, z) or (0.2 m, 3.23 m). The fluctuating electric field during the ICH window stands out compared to that of the Helicon which exceeds 100 V/m only at the higher frequencies. The spatial structure of these electric fields is revealed by taking the amplitudes these peaks during each window (the ICH peaks are labeled for reference) and plotting over the measurement range. Maps of the radial electric field produced for discrete frequencies, corresponding to the five largest peaks from figure 6.21, and are arranged in figure 6.22. An effective plume edge, taken from the 90% ion flux integration during both time frames, is plotted as a solid black line.

Figure 6.22 shows that for lower ion energies (Helicon) no consistent electric field structure is found within the measurable limits of the translation stage. Only a few

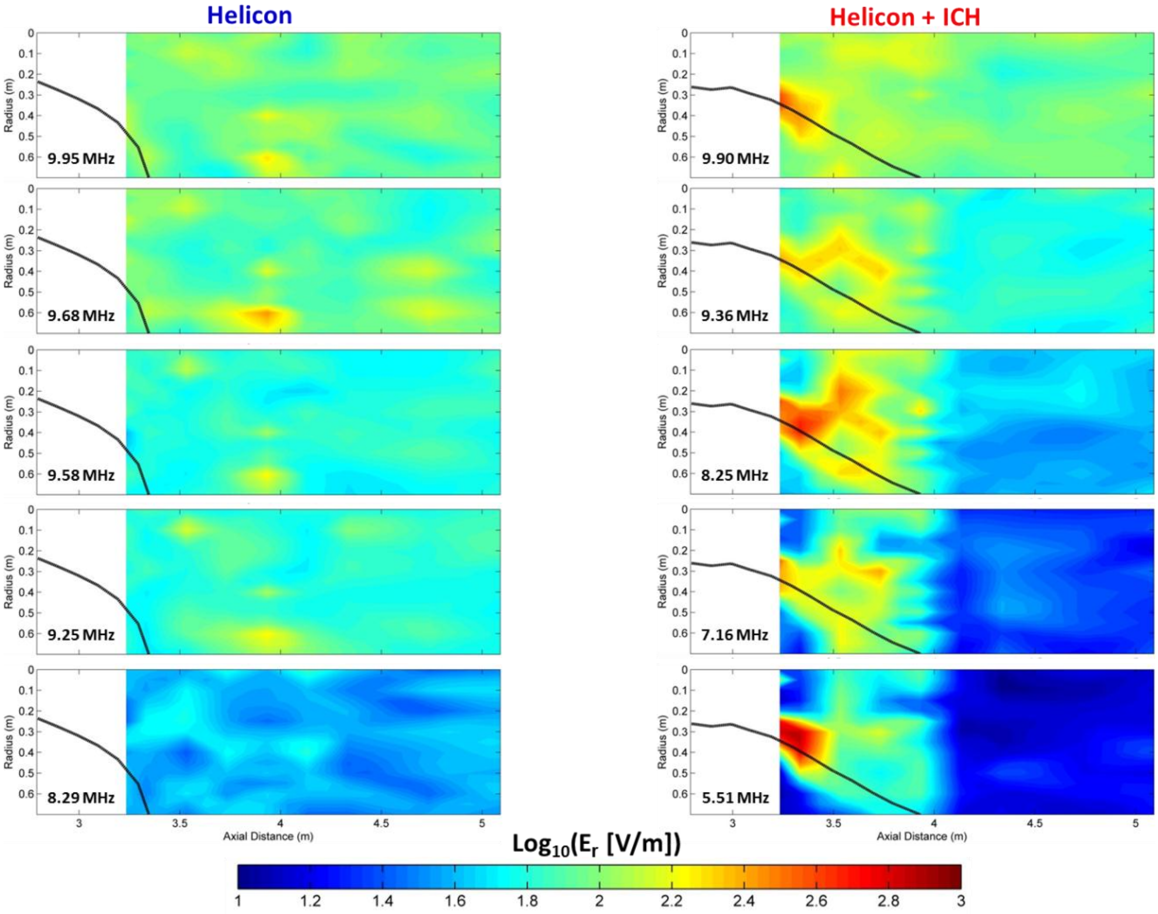

Figure 6.22: Contour maps of the frequency dependent radial electric field during the Helicon (*left*) and ICH (*right*) data windows at specific frequencies corresponding to the five largest peaks found in each spectrum. The frequencies are labeled within each map and an effective plume edge is plotted (black line) for reference taken from the 90% integrated ion flux. No interpolation between data points was performed and the white space represents areas without data.

isolated ‘hot spots’ are seen. The plume was observed to broaden more at these lower energies, so it may be possible that a more organized electric field exists further out where the magnetic field begins to curve back. For higher ion energies measured during the ICH window, the radial electric field has a distinct structure and is greatest along the edges of the plume. The greatest amplitude E_r measured was 740 V/m at a frequency of 5.51 MHz which is approximately ~ $3f_{LH}$. With increasing axial distance the well-defined field structure can be separated into three regions of a strong edge field ($Z < 3.4$ m), a medium strength electric field ($Z \sim 3.4$ m – 4.0 m), and a very weak field ($Z > 4.0$ m). The locations of these regions align well with the estimated transition from the region of ion trapping forces (strong field) to the anomalous transport region (medium field) described above. The weak electric field aligns with the location where the ion trajectories become completely linear (figure 5.17b). As the frequency increases the electric field along the edge persists but the far plume structure becomes more uniform. This uniformity indicates that the frequencies best aligning with this model are 5.51 MHz, 7.16 MHz, and 8.25 MHz corresponding to $\sim 3f_{LH}$, $\sim 4f_{LH}$, and $\sim 4.5f_{LH}$ respectively.

This organization about frequencies at multiples of the lower hybrid frequency, normalized to ω_{LH} according to one theory[126] (Eqn. 2-48) and implied to have the maximum instability growth rate near ω_{LH}[122], make it worthwhile to map out the electric fields in the plume at these frequency multiples. The data from these spectra were then frequency normalized to f_{LH} (opposed to ω_{LH} to keep units correct) and presented in a similar manner in figure 6.23. The amplitude of the radial electric field at frequencies from 1 – 5 f/f_{LH} are mapped out for both data time windows. At lower energies the organization of the electric field is virtually absent below $f = 4f_{LH}$. For higher ion energies the radial electric field, much like before, lies mostly along the edge of the plume and falls off beyond $Z > 4.0$ m. The largest electric fields occur at $f = 3f_{LH}$ but do fill up more of the central plume at the higher multiples. The three transition zones of this model are not as evident as before, especially along the edge of the plume. The fields dissipate for $Z > 4.0$ m corresponding to the detached plume and are strong up until $Z \sim 3.4$ m for the ion trapping zone, but outside of $f = 4f_{LH}$ the electric fields relating to anomalous

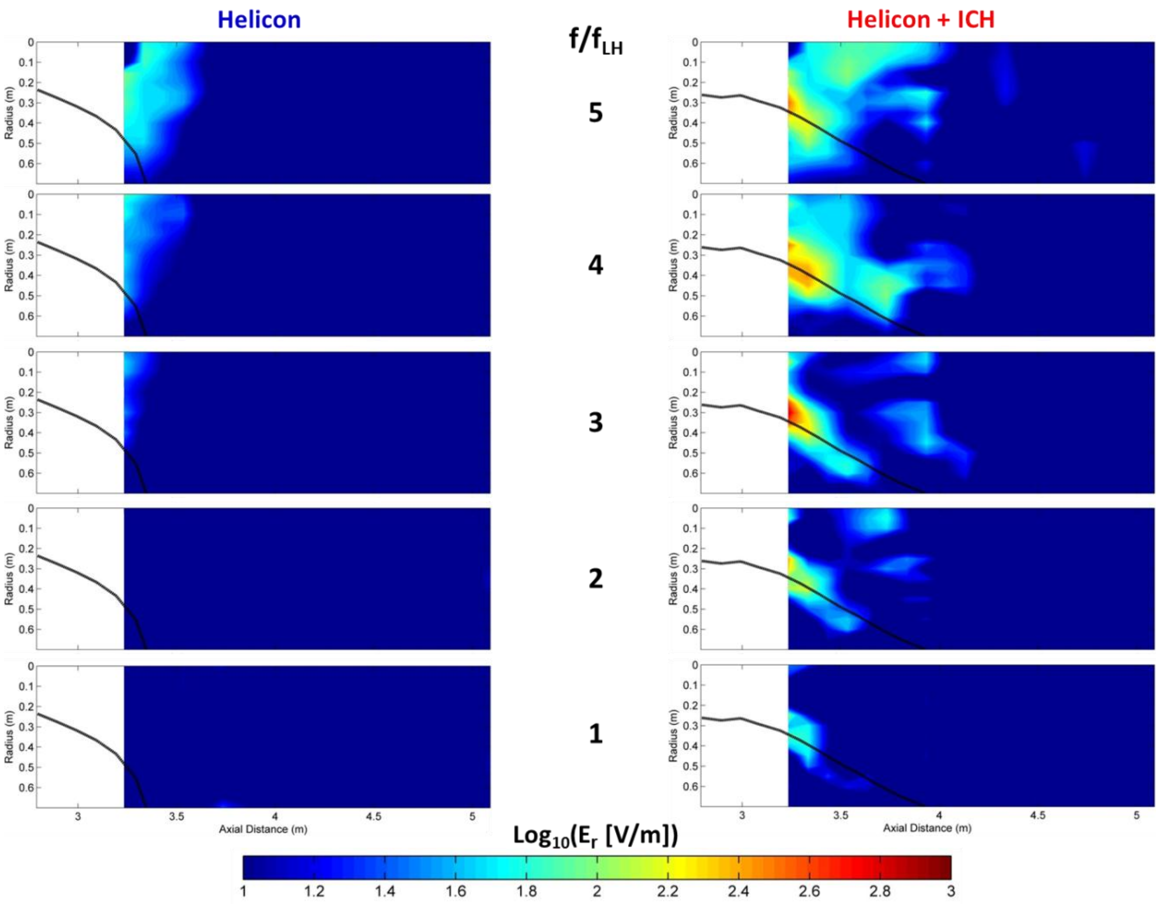

Figure 6.23: Contour maps of the frequency dependent radial electric field during the Helicon (*left*) and ICH (*right*) time windows plotted at frequency ratios normalized to the lower hybrid frequency. The electric field amplitude for integer frequency ratios from 1 – 5 were mapped out and an effective plume edge is plotted (black line) for reference taken from the 90% integrated ion flux. No interpolation between data points was performed and the white space represents areas without data.

transport are noticeably absent. A few possibilities may be that the anomalous transport dominant region may be more apparent at even larger multiples of f_{LH}, the data spatial resolution may need improvement, or integer multiples of the lower hybrid frequency are merely coincidental. Regardless, an electric field structure does appear at frequencies in the lower hybrid range suggesting the possibility that the LHDI may be playing some role in the ion and electron dynamics in the plume.

It is possible to estimate the value of Ωτ along the anomalous transport dominant region (3.5 m < Z < 4.0 m) according to the measured radial electric field, magnetic field, and ion velocity. Assuming a frequency of 5.51 MHz (during ICH) and a divergence angle of 10°, corresponding to separation angles along the plume edge, the transport coefficient is approximately $\Omega\tau \sim 4.0$. This value is closer to the 'Super-Bohm' equivalent mobility[120] than traditional Bohm transport. This equates to an effective momentum transfer rate of ~ 3.5×10^{8} s^{-1} which is a factor of 4±1 above the estimated electron collision frequency. The new field induced 'collision' frequency will undoubtedly enhance the net electron transport across the magnetic field lines in this region. This anomalous transport is in addition to any enhancement that the oscillating electric field itself will have on the classical collisional mobility.

To observe these effects, the estimated net electron cross-field velocity is plotted in figure 6.24, looking only at the plume during the ICH window, and the amplitude of the oscillating electric field is applied to the mobility contribution to equation 6-11:

$$\mathrm{u}_{\perp} = \pm\mu_{\perp}\left(E_{DC} + E(\mathrm{f})\right)_{r} - D_{\perp}\left(\frac{\nabla n_{\perp}}{n}\right)_{r} \qquad \text{6-32}$$

where the subscript r refers to the radial component of the electric field and density gradient since the axial component of the fluctuating electric field was not measured. The mobility and diffusion terms are those defined in section 6.1.1 and equation 6-12 where only the classical collision frequency is used. Comparing the amplitudes in figure 6.24 to the net electron cross field drift velocity from figure 6.4 it is apparent that the frequency dependent electric field increases the transport by about an order of magnitude for electron→ion collisions. The effects of this oscillating electric field on the

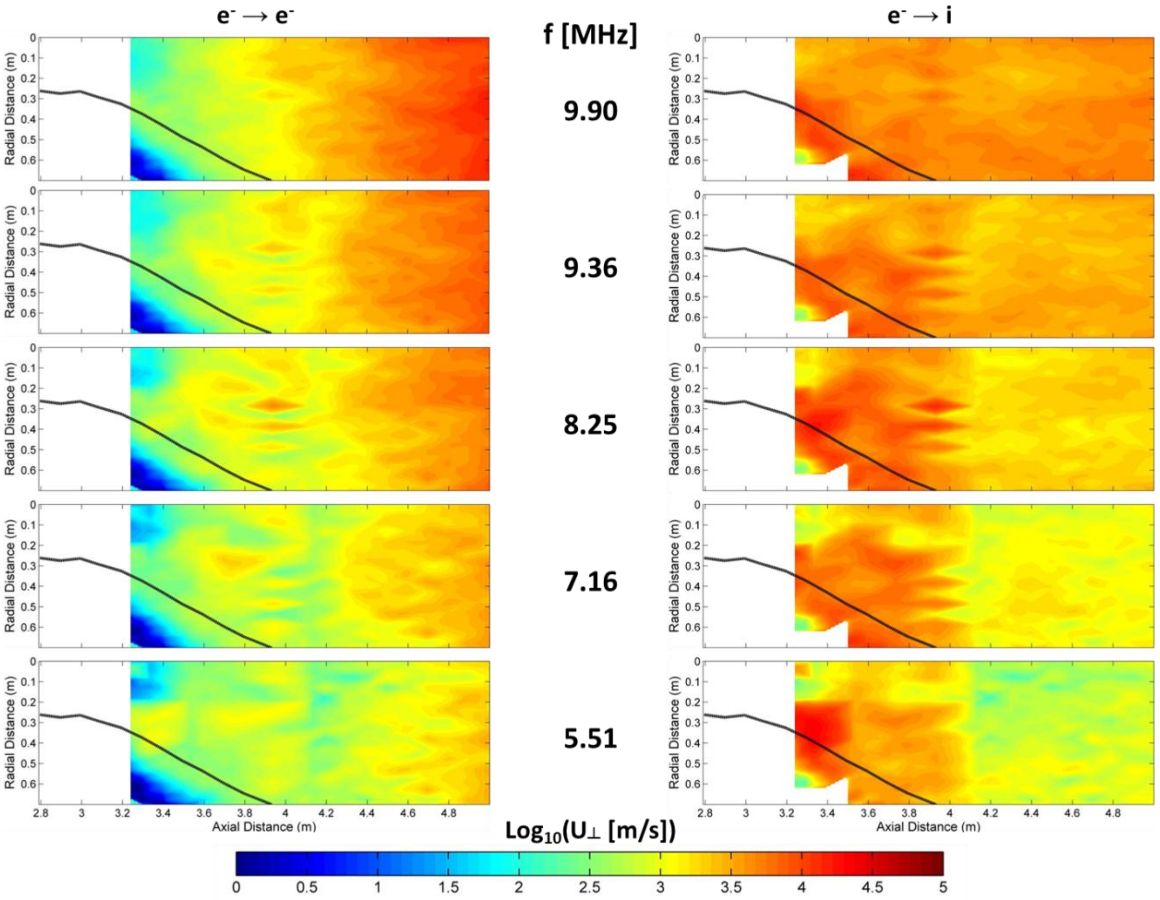

Figure 6.24: Color contour maps of the net electron cross field velocity (radial component) including the effects of the frequency dependent electric field on the classical collisional mobility during the ICH timeframe. Each row uses the radial electric field at the labeled frequency to compute the enhanced cross-field velocity from electron→electron (*left*) and electron→ion (*right*) coulomb collisions. An effective plume edge (black line) is plotted for reference based on the 90% integration of the ion flux. White regions represent locations without data.

electron→electron collisions are minimal except at much higher frequencies where the magnitude of the electric field extends further downstream. It is then confirmed that net transport due to electron→electron collisions in inadequate to explain electron detachment or other plume dynamics in the regions of interest (Z < 4.0 m). The velocity would still be lacking if the enhanced anomalous collision frequency were included. Electron→ion collisions, with the addition of the oscillating electric field, are able to account for the electron transport required for detachment as the cross-field velocities approach the expected values to match that of the departing ions. These values are present for each of the five frequencies mapped, but the lower three best explain the transition from an ion trapping region to an anomalous transport region to detached flow. It is expected that the effective collision frequency due to anomalous resistivity would further enhance this transport by a factor of 4±1 bringing the cross field velocities in the 25 – 30 km/s range between Z = 3.5 m – 4.0 m.

The above analysis explored the effects of the oscillating electric field at frequencies corresponding to the five largest spectral peaks. To see if comparable cross-field velocities are present at multiples of the lower hybrid frequency, considering the spatial structure observed in figure 6.23, a similar analysis was performed by normalizing the field to the local lower hybrid frequency and is presented in figure 6.25. The rows correspond to the mapped radial component of the cross-field velocity due to the fluctuating electric field at integer multiples of f/f_{LH} from 1 – 5 during the ICH timeframe. Like figure 6.24 the columns are assigned to electron→electron and electron→ion collisions. The amplitude of the cross-field velocity in this case is noticeably lower than at the individual frequencies and appears to be more localized along the edge of the plume. Previously the mapped velocities were spread out over a greater portion of the plume, especially along the axial region of Z = 3.5 m – 4.0 m where anomalous transport seems most probable. Electron→electron collisions appear to be unaffected by oscillating fields of this amplitude. These collisions are unable to match the ion flow even if the effective collision frequency be increased by up to a factor of 4 to allow for anomalous transport. The electron→ion collisions have a similar structure as in

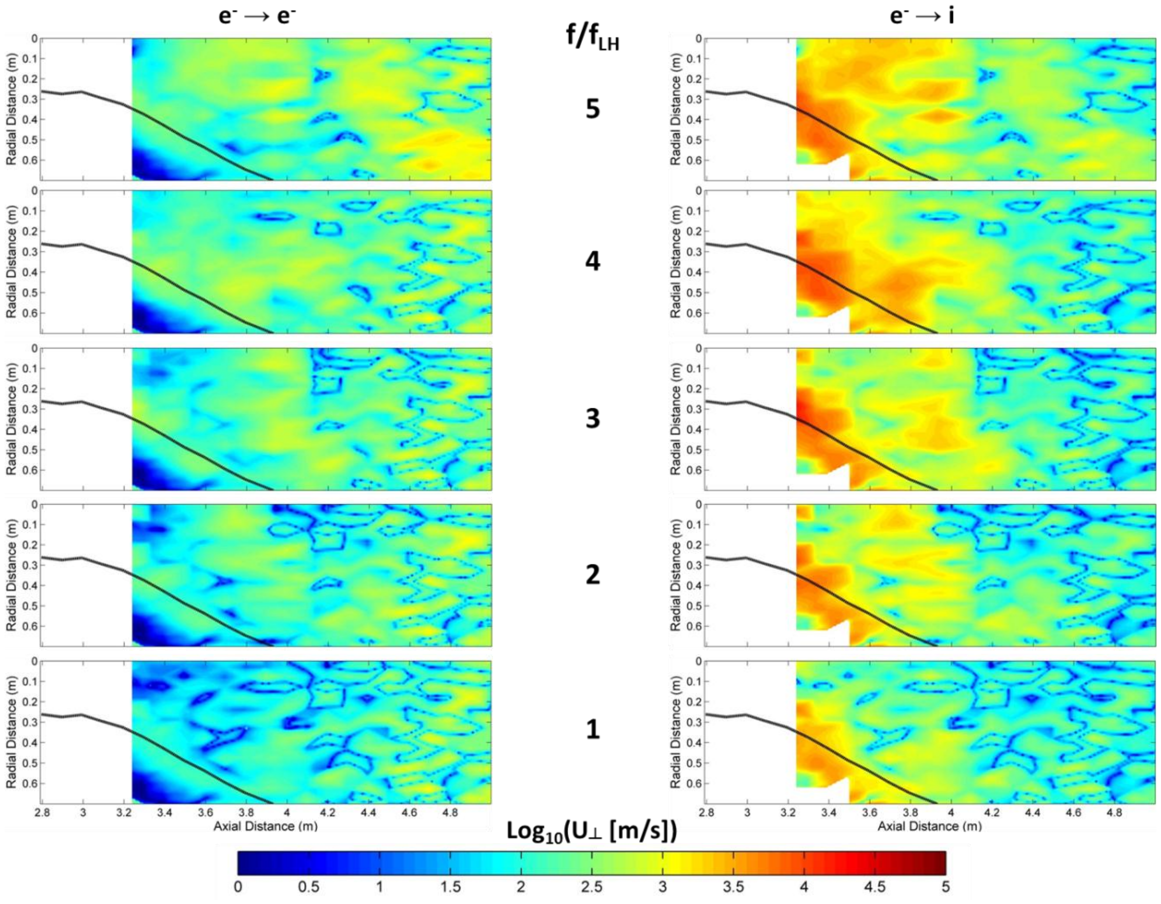

Figure 6.25: Color contour maps of the net electron cross-field velocity (radial component) including the effects of the frequency dependent electric field on the classical collisional mobility during the ICH timeframe. Each row uses the radial electric field at frequencies normalized to the lower hybrid frequency to compute the enhanced cross-field velocity from electron→electron (*left*) and electron→ion (*right*) coulomb collisions. An effective plume edge (black line) is plotted for reference based on the 90% integration of the ion flux. White regions represent locations without data.

figure 6.23 indicating that the mobility contribution from this oscillating electric field dominates the transport. The ion trapping region (Z < 3.5 m) is present in all of these maps as well as the detachment region (Z > 4.0 m). Only $f = 3 – 5f_{LH}$ appear capable of the cross-field velocities required to follow the ions in the anomalous transport region, but only if anomalous resistivity were included, otherwise the amplitudes are too low. Therefore exact integer multiples of the lower hybrid frequency do not fit this electron detachment model as well as individual frequencies from the turbulent electric field. That does not exclude the LHDI from driving this turbulence since the individual peaks are still within 1 – $10f_{LH}$, just not precisely at integer multiples.

The above analyses dealt entirely with the radial component of the measured turbulent electric field. Without having a measurement of $E_z(\omega)$ it is difficult to pinpoint exactly the correct dispersion relation; whether the MTSI or LHDI is most appropriate. Both remain likely candidates especially considering the LHDI is a limiting case of the MTSI. Future experiments may include new HF probes oriented to measure the axial component and better characterize this instability.

Section 6.6: Summary of analyzed detachment mechanisms

In this chapter the detachment theories and associated physical mechanisms discussed in chapter 2 were tested against the measured data and the results of each will be summarized here. In section 1 it was shown that although the ions are collisionless the electrons are not. Classical collision theory within the boundaries of this experiment revealed that resistive or diffusive mechanisms will play a role in this plume. To investigate how much of a role electron collisions play, each of the components of the cross-field velocity equation were tested and found to be within a factor of 5 of the Bohm equivalent diffusion velocity which is acceptable for an experiment of this type. The diffusion was locally organized, mostly along the plume edge, and matched suspected detachment regions noted in chapter 5. Despite this correlation the velocities resulting from both electron→electron and electron→ion collisions were not large enough to match the measured ion velocities needed to prevent localized space-charge build-up. Another mechanism must enable detachment of both ions and electrons or at minimum enhance the collisional diffusion velocity. Also studied in this section were various particle drifts that form in this setup, all of which were azimuthal. They may not play a large part in detachment but certainly in the momentum exchange processes of the nozzle.

In section 2 the two theories involving the preservation of frozen-in flow were explored. The first of these involved the MHD requirement that the plasma flow be super-Alfvénic. This was found to be the case during both the Helicon and ICH modes of operation. For the latter mode the Alfvénic Mach transition boundary lined up with the linearization inflection points of the ion flux trajectories, indicating detachment. This super-Alfvénic flow, predicted to be energetically capable to stretch the magnetic field lines, was simulated by using measured values for density, velocity, and magnetic field. These predictions, involving significant field line stretching and areas devoid of magnetic flux were compared to the plasma magnetic field and found to be completely inconsistent with the theory. The changes in the magnetic field were minimal and more consistent with the field created by an axial current flow of the approximate magnitude of this plume.

The second frozen-in theory involved the formation of magnetic islands that move at the same velocity as the detached flow. The magnetometer signal was capable of measuring changes in the field up to 50 kHz and frequency domain spectra for all axes were taken throughout the plume. These spectra showed some frequency dependent regions of the magnetic field but the amplitudes were small (< 0.2 G), dissipated 0.2 m downstream of the exit plane, and the structure did not align with any of the other observations in the plume. The region where the small amplitude, frequency dependent, magnetic structure formed was more consistent with the area where the ions were still magnetized, but may only be coincidental. It may be concluded that magnetic island formation is not occurring and that theories involving the preservation of frozen-in magnetic flux are not playing a role in the detachment process for this magnetic nozzle setup.

The detachment theory involving electron inertia was tested in section 3 which uses a dimensionless scaling parameter to compute the plasma flux surfaces were the flow is capable of separating. This same process was followed to compute the predicted flux surfaces for this setup to compare them with the measured flux lines. The predicted flux surfaces from this oft referred to theory, taken as a fundamental lower limit, were found to be inconsistent with all of the measured flux surfaces of this experiment. Referencing data implying the plasma has detached, as presented in chapter 5, it is concluded that without significant modification, such as including transport effects, electron inertia is not able to cause electron detachment in this nozzle. Other variants to this theory were estimated to either be 1) inconclusive yet improbable or 2) not directly applicable due to the base boundary conditions of the model, but with modification may be worth exploring.

The fourth section investigated the demagnetization of each particle by means of the breakdown of the first adiabatic invariant, or magnetic moment. If the gyroradius were to change significantly over the span of a single orbit the particle would lose adiabaticity and become unmagnetized. This change in gyroradius is tied to the particle velocity, cyclotron frequency, and magnetic field scale length and when $|v/f_c L_B| \sim 1$ the particles are no longer magnetized. It was found by mapping this adiabaticity parameter over the entire plume that the parameter explained the early behavior of the ions well. This ion detachment occurs within the first 0.1 – 0.2 m downstream of the closest measurement plane and align well with the divergence location of the integrated ion flux line with the magnetic flux. The adiabaticity parameter for the electrons was too low to explain detachment, but is likely to occur downstream where the magnetic field weakens. It is then concluded that the ions in this experiment detach by losing adiabaticity while the electrons remain tied to the magnetic field lines over the regions of measurement.

The last theory tested, in section 5, involved cross-field transport enhanced by turbulent electric and/or magnetic fields. This turbulence is created by plasma instabilities that likely arise due to the divergence of the fringe electrons from the ion central ion plume. Recalling in chapter 5 that oscillating electric fields were observed to have discernible structure, the particles response to these fields would determine the overall plume dynamics. The ion response to this field is a centrifugal force intent on preserving ion circular motion by following the magnetized electrons on the curved field lines and is known as ion trapping. The electron response is anomalous resistive transport across the field lines to follow departing ions. A theoretical calculation revealed that both ion trapping and anomalous transport were possible in this nozzle depending upon the magnitude of the magnetic field, curvature, particle velocity, and collision frequency. To test these responses the electric field structure at five discrete frequencies and integer multiples of the lower hybrid frequency were mapped out. The electric fields at frequencies corresponding to the five largest spectral peaks were organized stronger than those normalized to f_{LH}. These mappings revealed plume structure consistent with three separate regions: an ion trapping region ($Z < 3.5$ m), an anomalous transport region ($3.5 \text{ m} < Z < 4.0$ m), and a detached region ($Z > 4.0$ m). The locations of these regions are consistent with observed trends in the ion flux expansion data, especially for the frequencies of 5.51, 7.16, and 8.25 MHz.

It was estimated that the transport would be enhanced in the anomalous region approximately 4 times above that due to the classical collision frequencies. Despite this enhancement these oscillating fields play a role in the collisional transport. The turbulent electric fields were included in the collisional transport models and it was found that electron→ion collisions produced electron cross-field velocities that approximated the ion velocities; especially considering the approximate (4±1)x enhancement due to anomalous resistivity. Plasma turbulence and anomalous transport are then concluded to play a significant role in the electron detachment process. More data would be needed to figure out which instability is responsible, but the MTSI and LHDI remain as probable candidates.

Chapter 7: Conclusions

The goal of this concluding chapter is to summarize several of the primary conclusions that were made during the course of this research. Individual chapter summaries have already been presented for chapters 5 and 6 regarding observations made from the data that indicate detached plasma flow and the physical mechanisms playing a role in the detachment process. This final summary will link the main ideas from both of those analyses. The second section will discuss a few suggestions for future studies on this topic or ways clarify the various phenomena observed during this experiment. The final section will go over some of the implications for this physics on larger scales such as in astrophysical plasmas, as well as any other applications well suited for this research.

Section 7.1: Summary of conclusions

In the first chapter the fundamental problem was formed for understanding the physics involved in the separation of plasma flowing along a dipole magnetic nozzle. The plasma must either remain tied to the magnetic field, likely bouncing between mirror points and negating the effect of the nozzle, or separate from the field while imparting momentum. There are observed examples of plasma escaping from naturally diverging magnetic field systems such as astrophysical jets[21-25] and the solar atmosphere[1, 18-20, 40, 49, 50, 53-55]. Understanding the physics of detachment will shed new light on particle and thermal transport processes for these systems. Considering this experimental nozzle system is many orders of magnitude less in scale, making any valid comparisons to such natural plasmas requires the setup be capable to scale accordingly. Working through the Euler equations/assumptions posed by Ryutov[33] and using a similar approach to Hartigan[25], the plasma flow conditions in this experiment were found able to be scaled up to certain astrophysical systems. It was found that the solar chromosphere is a suitable comparison candidate as its parameter space aligns well ranging from density and electron temperature, to magnetic field strength and the range of kinetic beta. It may be concluded by extension that plasma ejected from these systems may occur through similar processes as those observed in the exhaust of the VASMIR® VX-200 magnetic nozzle.

The second chapter presented a background literary review of theories treating plasma detachment from magnetic nozzles dating as far back as the 1940s. These theories may be generalized into two categories of collisional and collisionless detachment. One of the two proposed collisional mechanisms, recombination detachment, was immediately ruled out as the rates for this process were found to be too low. All of the electron/ion pairs are unable to detach by this method within the observed time scales. Resistive diffusion detachment, the other collisional mechanism, was tested against the data in chapter 6. The collisionless detachment theories included electron inertia, particle demagnetization, plasma turbulence, and frozen-in flow methods such as MHD field line stretching and magnetic reconnection all of which were compared to the observed data in chapter 6.

None of this data would be of much use without a thorough explanation of the plasma source, nozzle conditions, and experiment setup which were presented in chapter 3. The plasma was created during two stages or phases of operation: Helicon alone and

Ion Cyclotron Heating (ICH) in addition to the Helicon plasma often referred as simply ICH. The ion flow during each stage was measured to range 13 – 17 km/s during Helicon and 27 – 32 km/s during ICH for an approximate factor of two increase in velocity and four in ion energy. The applied nozzle field was created and held constant using a superconducting electromagnet providing a measurable range of ~ 740 G at the exit plane to 10 G in the far plume region. The experiment was conducted within a 150 m^3 vacuum facility permitting a large unimpeded measurement area (~ 10 m^2) and pumping speed (~ 185,000 l/s) capable of minimizing the charge-exchange losses. These charge-exchange effects were also reduced by the ability to create fully energized plasma in 0.4 s, and keeping the neutral pressure low, allowing for mean free paths greater than 10 m during Helicon and 1 – 3 m during ICH. In addition to fast start-up, the plasma was found to be highly repeatable (< 1.2% variance in RF power) over mappings consisting of more than 2000 firings.

The fourth chapter provided a detailed description each of the plume diagnostics including their respective location on the translation stage. This detail included probe fundamentals, sample data, and a look into the data reduction process to create meaningful values. These diagnostics included Langmuir probes (swept and fixed bias), strain-gauge force targets (PMFS), a magnetometer, an RPA, and a high-frequency electric field probe. Combined together and measured over a common spatial range, the plasma parameters from these data were then used to visualize and compare trends throughout the nozzle.

The fifth and sixth chapters together provided detail discussing, both qualitatively and quantitatively, the plume data indicating evidence of detached plasma flow in this nozzle system and which of the theories are most consistent with all of these measurements. It was found that plasma detachment from this system is a two part process, at least in the scenario of ions accelerated during ICH, with ions separating ahead of the electrons. It is useful to summarize the detachment process one axial region at a time beginning with the plasma flow at the closest measurement location (Z ~ 2.8 m) and moving downstream. The high velocity ion flow (ICH) is magnetized for the first 0.1 m (2.8 m < Z < 2.9 m) before the magnetic flux diverges from the ion flux. The location of this separation is confirmed by the integrated ion flux, momentum flux, slope ratio data, and detachment angle data. The ion adiabaticity parameter at this point (Z = 2.9 m), roughly ΔZ ~ 0.9 m downstream of the nozzle throat, is ~ 2.5 which may be considered of order unity. This value is indicative of a breakdown in the magnetic moment of the ions. The ions have effectively become demagnetized, which is the first part of the detachment process.

The second part stems from the detached ions flowing in a different direction than the still magnetized electrons. This divergence of the ions and electrons cause an instability to form where the modified two-stream instability (MTSI) is a candidate. This instability can drive plasma density and electric field fluctuations, capably causing Coulomb field based ‘collisional’ transport. During ICH, the MTSI possibly takes a limiting form closer to the lower hybrid drift instability (LHDI), which has T_e/T_i dependence and characteristic frequency near the lower hybrid frequency. Differing ion/electron temperatures (T_i ~ 30, T_e ~ 6) and electric field oscillations on the order of f_{LH} have all been observed when ICH is applied. Net particle transport is determined by the particle responses to these oscillating electric fields. The ion response is to preserve centrifugal motion by the Lorentz force and is referred to as ‘ion trapping’. The electron response is anomalous cross-field transport radially inward towards the ions. The inter-particle force balance is determined by the oscillating electric field strength, magnetic field strength, field line radius of curvature, divergence angle, velocity, and effective field-momentum transfer time.

For higher ion velocities these oscillating electric fields are seen between 3.23 m < Z < 4.0 m and largely organized along the edge of the plume. It is certain these fields would be present further upstream, likely up to Z = 2.9 m if the HF electric field probe were capable of translating into those regions. The ion trapping region exists between 2.9 m < Z < 3.5 m, assuming electric field penetration upstream, where the larger magnetic field strengths are more prohibitive to anomalous transport. The frequency dependent electric fields peak in this region, reaching 740 V/m at 5.51 MHz before leveling off to an intermediate value beyond Z = 3.5 m. In this region the separated ions undergo a radial expansion approximating the magnetic field lines. This expansion is confirmed in the integrated ion flux data, slope ratio data, and detachment angle data from 2.9 m < Z < 3.5 m. Here the ion flux trajectories follow a more quadratic fit and the slope ratio/detachment angle data are bounded by inflection points trending towards unity (following the magnetic field) and a reduced angle of separation. This axial range also coincides with the span of the largest DC electric field located just outside the edge of the plume.

Along the span of 3.4 m < Z < 4.0 m, the anomalous transport of electrons begins to dominate. An overlapping transition region lies between the two zones from 3.4 m < Z < 3.5 m. This transition region contains the final inflection point in the slope ratio and detachment angle data showing where different parts of the plume favor one response over the other. By this point the magnetic field has decreased enough that the electric field strength necessary to drive anomalous transport is less than the required electric field for ion trapping. This region is reflected by integrated ion flux lines transitioning to a linear/ballistic trajectory, slope ratios dropping below unity, and detachment angles turning positive and increasing. The Alfvénic Mach number, in the form of kinetic beta, also transitions beyond unity throughout this zone. The $\beta_k = 1$ demarcation appears to align well with the inflection points marking the linearization of the ion flux trajectories. It is unclear whether this correlation is coincidental since the changes in the magnetic field thereafter, from an MHD standpoint, are negligible.

The enhancement of cross-field electron transport in the anomalous transport region is estimated to be 4±1 times that of the classical transport rates from to electron→ion collisions alone. Taking the classical electron→ion collisional mobility as a lower limit, including the effects of both the DC and oscillating electric fields (at frequencies ~ 5.51, 7.16, and 8.25 MHz) bring the estimated cross-field velocities to 5 – 10 km/s over this region. The enhancement factor of 4±1 to these values makes the electron velocity comparable to the ion velocity, during ICH, satisfying space-charge requirements. The momentum of the ions essentially tows the electrons across the magnetic field lines and the electric field structure and values predicted by anomalous resistivity are consistent with this claim.

The detached plasma region spans distances of Z > 4.0 m, approximately 2 m downstream of the nozzle throat. It is along this plane that the instabilities/oscillating electric fields dissipate, the edge DC electric field falls to zero, all of the integrated ion flux lines follow a linear trajectory, the slope ratios flatten out below a value of 1, and calculated detachment angles are steady with a slight positive trend as the magnetic field lines begin to curve away. Furthermore the articulating RPA data display a highly collimated flow across a radial section located at Z = 3.9 m with no indication of organization about the local magnetic field vectors. These are all indicative of an *effectively* detached flow of particles from the applied magnetic field; even though the electrons remain magnetized after crossing the field lines in the anomalous transport region. The electric fields (AC and DC) dropping off to zero are suggestive of electron/ion parallel flow. It is reasonable to assume that complete detachment of the electrons will occur as they follow the ions on field lines closer to the nozzle axis into regions of weaker magnetic field, where the gyroradii will subsequently grow and become demagnetized through magnetic moment breakdown. This loss of adiabaticity for the electrons would occur beyond the measureable range of the translation stage and would not be expected to alter the plume trajectory much further. The value of thermal beta, β_{th}, grows larger than 1 in this detachment region but does not appear to have much effect on the flow.

These main points and the delineation of each region are displayed in figure 7.1 for plasma flow during ICH operation. The two part detachment process, simply stated, involves ions losing adiabaticity followed by instability driven turbulence that at first curves the ion trajectories before enhancing electron cross-field transport. The plume is effectively detached after the instability dissipates and the electrons follow the outbound ions detaching once the magnetic field weakens sufficiently. Only one of these detachment processes, loss of adiabaticity, are directly observed for lower velocity ions

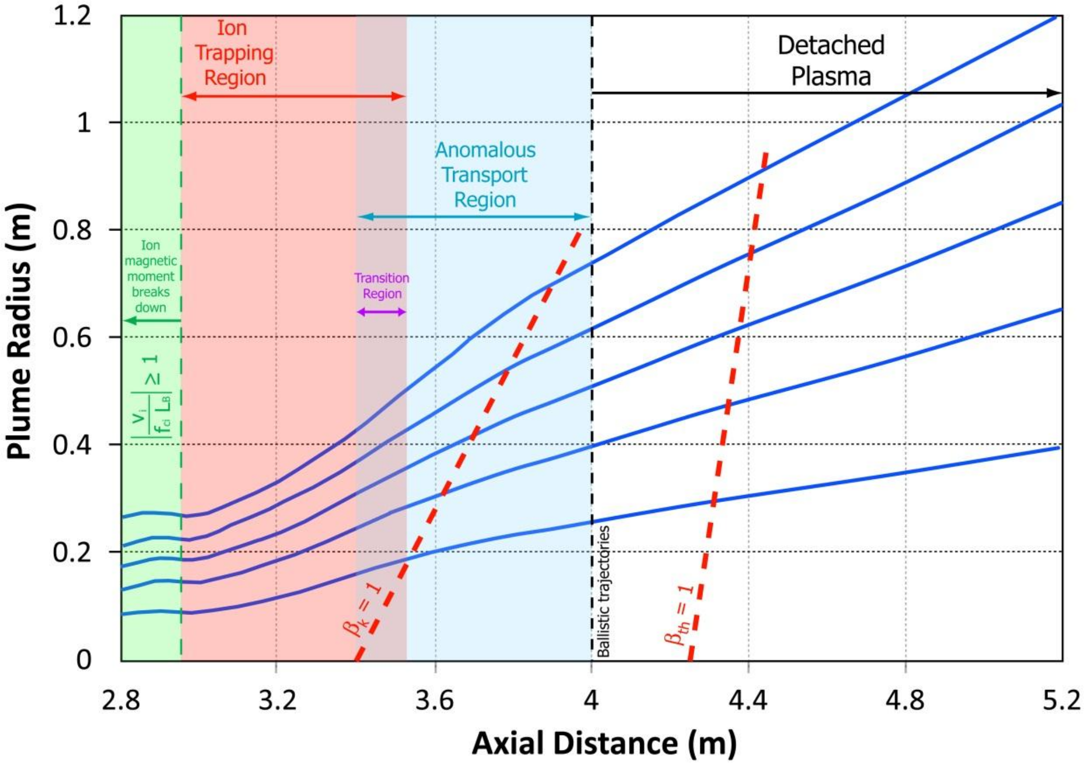

Figure 7.1: Image summarizing the various regions associated with the detachment process during the ICH timeframe. The flow lines (blue) are based on the integrated ion flux and extended out along the linear region.

created during the Helicon time window. In this scenario the magnetic moment of the ions is preserved and remain magnetized for the first 0.3 m (2.8 m < Z < 3.1 m) which is extended beyond the location observed during ICH. The ion adiabaticity parameter at this point (Z = 3.1 m) ranges from 2.5 – 4 which is of order unity and approximately the same value as the ICH flow upon ion separation. This ion detachment is confirmed by similar methods as reported for the ICH flow as the integrated ion flux diverges from the enclosed magnetic flux, the slope ratio data departs from a value of 1, and features non-zero detachment angles.

This difference between the Helicon and ICH plasma flows is that the low velocity ions are observed to diverge beyond the magnetic flux whereas the ICH ion flow was convergent. This may be due to a number of different causes, one of which may be the radial ambipolar forces having a greater effect on lower momentum ions. The oscillating electric field is essentially absent during the Helicon window except at the highest measured frequencies. It may be that the instability driving the turbulence during ICH occurs at higher frequencies or that the same instability is present at radial positions beyond the measurements taken in this experiment. The ion flux trajectories appear to become more linear by Z = 4.0 m which is supported by slope ratio and detachment angle data, but is spread out to a greater degree than ICH. The $\beta_k = 1$ transition does not appear to correlate with these inflection points occurring further downstream between $4.2 \text{ m} < Z < 4.4 \text{ m}$. Based on these differences it is unclear how the low velocity plume proceeds to the second part of the detachment process to cause electrons to cross the field lines. The low energy plume may behave similarly to the high energy plume at greater radial distances where the curvature is much smaller, the magnetic fields are weaker, and where lower magnitude oscillating electric fields take greater effect. Otherwise there must be a limiting ion velocity/energy for these processes rather than a trend focusing the plume towards the nozzle axis as ion energy increases.

Section 7.2: Proposed future research

Although much has been concluded on the detachment processes of charged particles flowing through a dipole magnetic nozzle, this research can be continued in more focused areas. The argon plasma created in this experiment was found to behave and detach by specific mechanisms. The ion cyclotron frequency used during the breakdown of the magnetic moment is dependent upon the ion mass. Also dependent upon ion mass is the electric field seen in the ion trapping region. It would be useful to study these phenomena using a variety of other plasmas and observe the shift in axial location from the regions found in this study. Hydrogen would be an ideal candidate, especially considering the direct comparison one could make with astrophysical magnetic nozzles, but is currently unfeasible in this VASIMR® VX-200 system due to the limitations in the magnetic field and RF electronics. Krypton as a source plasma would work in the current system with minimal modification and offers a factor of 2 increase in ion mass. The applied RF power may be adjusted so that a velocity increase of 2x could be realized from Helicon to ICH operation. The increased ion mass would reduce the cyclotron frequency, shifting the axial plane for ions magnetic moment breakdown further upstream. The effects on the fluctuating electric field in the ion trapping region would be brought in closer to the nozzle axis. Otherwise the fields would be required to grow by a factor of 2 for the same field line radii of curvature. It would be expected that the ion trapping and anomalous transport regions would shift further upstream as well as the kinetic beta transition. These effects could be measured in a new experiment campaign.

Aside from varying the ion mass one could vary the magnetic field. This nozzle geometry would not necessarily be directly comparable to those found in astrophysical systems. Other nozzle topologies may follow similar detachment processes as determined in this study or may be better suited for engineering applications. Compressing the nozzle would likely have the same effect as decreasing the ion mass but with the added effect of shifting the anomalous transport region further downstream. Flaring out the nozzle field would have the opposite effect. A uniform change in the magnetic field topology for this system would require a separate magnet coil located just downstream and coaxial to the VX-200 superconductor. This hardware upgrade would require significant modification and engineering which are currently not feasible with the resources available. Perhaps a less expensive technique would be to use a large mass of iron, in the form of a disk, along the exit plane into the plume region. This pole piece would cause the magnetic flux to flare out to a greater degree and has been implemented previously in electric propulsion research[228].

The ideas listed above possibly involve large system changes to alter the experiment setup or hardware. There are a few research ideas that can be approached without changing the plasma source or magnetic nozzle configuration. These ideas involve modified or new plasma diagnostics to measure or extend the range of a particular parameter. For example, future tests should attempt to make simultaneous measurements of the oscillating electric field in both the radial and axial directions. These measurements would involve a second set of calibrated electrodes, a dedicated voltage pre-amp circuit for each channel, and an updated spectrum analyzer capable of digitizing multiple spectra simultaneously. If within the capabilities of the electronics, it would also be useful to scan to higher frequencies, perhaps as high as 20 MHz or even 50 MHz since both sets of spectra appeared to be trending in that direction and other plasma instabilities may be present. Another useful diagnostic would be to implement a set of orthogonal B dot probes to measure any magnetic oscillations at frequencies comparable to those seen for the AC electric field. These new probes would equally require current-sensitive pre-amp circuits along with a spectrum analyzer. This measurement would answer the question of wave mode identification as the oscillating fields are currently presumed to be electrostatic and any magnetic modes could be then used to estimate an effective anomalous frequency as in equation 2-40. Other new probes that would be useful or provide more accurate measurements are a double Langmuir probe for electron temperature, a triple Langmuir probe to measure plasma density on faster timescales, and an emissive Langmuir probe to give a better estimate of plasma potential.

Lastly some of the measurements were limited by the radial range of the translation stage and would be particularly useful in during the Helicon window where the plume has expanded beyond complete measurement. Modifications to the translation stage could extend the radial range to ± 1.5 m with minimal engineering effort and reasonable funding. To extend the measurement of specific plasma diagnostics it is possible to increase the probe offsets (table 4.1) at the expense of symmetrically overlapping measurements, with minimal structural modification.

All of these proposed future research ideas would complement this work providing additional verification of the methods and processes. It would be at the discretion of any funding agencies and the Ad Astra Rocket Company for additional plume time, hardware modifications or acquisitions, and data reduction time but it is the opinion of this author such additional research would be extremely beneficial.

Section 7.3: Applications and Implications for Astrophysical Plasmas

At the end of a particular research effort it is worthwhile to reflect on how the work may find its way into engineering applications and/or to engage in a discussion of its implications to natural systems. In the frame of this research there are items to discuss on both fronts. First and foremost this research directly applies to the development efforts on extending the plume science of the VASIMR® engine. The VASIMR® fits in a particular category of electric propulsion whose thrust is directly related to the axial ion momentum and azimuthal drifts mentioned in section 6.1.2. Clarification of these detachment processes, especially for a variety of propellant species, would allow for the optimization of the nozzle efficiency which is part of the total system efficiency. Design decisions regarding the nozzle magnet topology, detachment location of the ions, losses due to collisions or other radial forces, etc. will be much easier in a cost-to-benefit estimate for a flight-ready system where launch mass comes at a premium.

Future experiments measuring the nozzle efficiency directly, testing the detachment properties of propellants such as Krypton, Hydrogen, Deuterium, and possibly Neon, and optimizing for thrust to RF input power are all on the development timeline. The current VASIMR® setup is a dipole configuration and testing detachment processes involving magnetic clustering to quadrupole, hexapole, or octopole configurations may be required where physics of the ‘x line’ reconnection could be an issue. These advanced tests are better suited for the Low Earth Orbit environment (LEO), possibly mounted to the International Space Station (ISS) which is being discussed[229, 230]. There are also other electric propulsion technologies such as the HDLT[90, 100, 102, 231] and MPD[72, 113, 126, 232-234] thruster where this research may prove useful in design considerations.

Other terrestrial applications of plasma flow through a magnetic nozzle, where argon is predominant, is plasma processing in the microchip industry[119]. Directionality and the spread of the argon plume are highly important to the sputtering rates in the etching process. Manufacturers prefer that the silicon wafers experience as uniform an ion energy plume as possible so as to limit variations in the etch depth. Knowledge of the detachment location and spread of the argon plume may help these factories calibrate, tune, or reposition their plasma sources for optimum productivity. In a trillion dollar industry such as this, small enhancements to efficiency can have great economic benefits. Another area possibly influenced by this study may be the fusion research where cross-field transport and confinement are widely discussed issues and the instabilities driving anomalous diffusion could be of interest.

Regarding the implications of this research to astrophysical plasmas, the physics of magnetic nozzles may have relevance in understanding the physics of particle, heat, and energy transport between different regions of the solar atmosphere. Over the past few decades a wealth of remote solar data has come in from several orbiting observatories such as RHESSI, SOHO, TRACE, ULYSSES, and WIND[1]. The data has provided insight on solar processes, the make-up of each layer of the heliosphere, particle distribution functions, and the solar wind to say the least. The upcoming IRIS mission with higher resolution instrumentation will advance this knowledge even further. Despite this influx of data many questions remain regarding magnetic reconnection, chromosphere\transition region\corona heating mechanisms, and the basic chain of physics involved in the heating and acceleration of the solar wind[237]. One issue is that information from remote sensing is inherently limited to methods of observing the electromagnetic spectrum and in-situ particle/field interactions with the spacecraft typically located at a distance of ~ 1 AU. Appropriate and scalable laboratory analogs to these systems may help measure and understand the natural physics of the larger systems and serve to narrow the focus of the observational study.

It was concluded at the end of chapter 1 that the most applicable analog environment for the scaling of these nozzle parameters is the upper solar chromosphere. Aside from the plasma species and scale size, the general range of parameters important to the Euler equations (Eqns. 1-4 to 1-8) are a close match to those found in the upper chromosphere and into the transition region. The transition of kinetic beta above unity in the solar atmosphere occurs within the chromosphere. Plasma flow along spicules, plasma jets, and plages, located within the chromosphere, may exhibit magnetic nozzle conditions where ions lose adiabaticity and drive a turbulent electric field affecting electrons. The detachment scenario studied in this research may help explain part of the process involved in the formation of the fast/slow solar wind, material transport from the chromosphere to replenish the corona, heat transport across the transition region, or general particle dynamics within the chromosphere. As seen in this experiment, preferential heating of the ions leads to turbulence that facilitates the detachment process and similar heating mechanisms in the solar atmosphere could drive these dynamics. Cranmer et. al.[237-244] argue that preferential ion heating occurs in the chromosphere and out into the corona as MHD turbulence drives Alfvén wave dissipation at ion cyclotron resonance. Other proposed ion heating mechanisms may include the formation of electric double layers[7], Alfvén/whistler turbulence[245-247], small scale reconnection and microflares[248-249], shocks[250-252], and stochastic heating processes[253-255].

Presuming that one of the above heating processes acts upon the Hydrogen ions, Helium ions, or other low-abundance ion species, the ions will lose adiabaticity in the expanding magnetic field across the chromosphere effectively becoming demagnetized. The flow separation of these ions from the electrons would form plasma instabilities driving anomalous electron transport. Assuming the LHDI is a factor, it would be expected that frequencies up to an order of magnitude above the lower hybrid frequency could be observed spectroscopically, perhaps by the Autler-Townes effect[256]. These frequencies would range from ~ 0.07 - 65 MHz for Hydrogen and 0.03 - 33 MHz for Helium based on the parameters listed in Appendix A. Whether the ions achieve escape velocity (~ 617 km/s) and contribute to the fast solar wind, remain gravitationally bound and fall back to the photosphere, or somewhere in between, the electric field magnitude for ion trapping and anomalous transport appear to be on the order of those seen in this experiment. Taking a conservative flow velocity of 200 km/s flowing through the corona[13], the electric fields required for ion trapping along the edge of the nozzle could range from 100 - 500 V/m for Hydrogen and 300 - 1600 V/m for Helium. Anomalous transport consistent with the levels found in this study ($\Omega\tau \sim 4\pm1$) would require electric field magnitudes 100 - 3600 V/m at these higher frequencies. Ion trapping should dominate in the lower-to-middle chromosphere before transitioning to an anomalous transport dominated upper chromosphere and corona.

While these mechanisms have not yet been directly observed in the solar atmosphere, it is reasonable to believe that loss of ion adiabaticity and instability driven electron transport may play a role, however minor, in the particle dynamics of the sun and should merit a more focused investigation.

References:

1. R. R. Fisher, *Heliophysics, The New Science of the Sun-Solar System Connection: Recommended Roadmap for Science and Technology 2005-2035,* in *Heliophysics*, NASA, Editor. 2006, NASA. p. 1-182.

2. L. J. Lanzerotti, *The Sun to the Earth - and Beyond: A Decadal Research Strategy in Solar and Space Physics,* N.A. Press, Editor. 2003, National Research Council. p. 1-197.

3. L. Biermann, *The plasma tails of comets and the interplanetary plasma*, in *Space Science Reviews*. 1963, Springer Netherlands. p. 553.

4. C. Eyles, et al., *The Heliospheric Imagers Onboard the STEREO Mission*, in *Solar Physics*. 2009, Springer Netherlands. p. 387-445.

5. C. M. Lisse, et al., *Discovery of X-ray and Extreme Ultraviolet Emission from Comet C/Hyakutake.* Science, 1996. **274**(5285): p. 205-209.

6. C. M. Lisse, et al., *Charge Exchange-Induced X-Ray Emission from Comet C/1999 S4.* Science, 2001. **292**(5520): p. 1343-1348.

7. R. W. Boswell, E. Marsch, and C. Charles, *The Current-Free Electric Double Layer in a Coronal Magnetic Funnel.* The Astrophysical Journal Letters, 2006. **640**(2): p. L199.

8. E. N. Parker, *Sweet's Mechanism For Merging Magnetic Fields in Conducting Fluids.* J. Geophys. Res., 1957. **62**(4): p. 509-520.

9. R. M. Kulsrud, *Important plasma problems in astrophysics.* Physics of Plasmas, 1995. **2**(5): p. 1735-1745.

10. J. F. Drake, *Magnetic Explosions in Space*, in *Nature*. 2001. p. 525-526.

11. H. E. Petchek. *The Physics of Solar Flares*. in *AAS-NASA Symposium on the Physics of Solar Flares*. 1964. Washington, DC: NASA.

12. P. Sweet, *The production of high energy particles in solar flares*, in *Il Nuovo Cimento (1955-1965)*. 1958, Italian Physical Society. p. 188-196.

13. B. W. Carroll and D. A. Ostlie, *An introduction to modern astrophysics*. 2007, San Francisco: Pearson Addison-Wesley.

14. A. S. Krieger, A. F. Timothy, and E. C. Roelof, *A coronal hole and its identification as the source of a high velocity solar wind stream*, in *Solar Physics*. 1973, Springer Netherlands. p. 505-525.

15. C. Y. Tu, et al., *Ion Temperatures in a Solar Polar Coronal Hole Observed by Sumer on SOHO.* The Astrophysical Journal, 1998. **503**(1): p. 475.

16. C. David, et al., *Measurement of the electron temperature gradient in a solar coronal hole.* Astronomy & Astrophysics, 1998. **336**: p. L90-L94.

17. J. B. Zirker, *Coronal holes and high-speed wind streams.* Rev. Geophys., 1977. **15**(3): p. 257-269.

18. F. P. Zuccarello, et al., *Initiation of Coronal Mass Ejections by Magnetic Flux Emergence in the Framework of the Breakout Model.* The Astrophysical Journal Letters, 2008. **689**(2): p. L157.

19. G. Dubey, B. van der Holst, and S. Poedts, *Initiation of cmes by magnetic flux emergence*, in *Journal of Astrophysics and Astronomy*. 2006, Springer India, in co-publication with Indian Academy of Sciences. p. 159-166.

20. B. van der Holst, C. Jacobs, and S. Poedts, *Simulation of a Breakout Coronal Mass Ejection in the Solar Wind.* The Astrophysical Journal Letters, 2007. **671**(1): p. L77.

21. P. Hartigan, et al., *Magnetic Fields in Stellar Jets.* The Astrophysical Journal, 2007. **661**(2): p. 910.

22. P. Hartigan, J. A. Morse, and J. Raymond, *Mass-Loss Rates, Ionization Fractions, Shock Velocities, and Magnetic Fields of Stellar Jets.* The Astrophysical Journal, 1994. **436**: p. 125-143.

23. J. D. Hurka, J. Schmid-Burgk, and P. E. Hardee, *Deflection of Stellar Jets by Ambient Magnetic Fields.* Astronomy & Astrophysics, 1999. **343**: p. 558-570.

24. R. Lopez, et al., *3-D Kinematics of the HH 110 Jet.* Astronomy & Astrophysics, 2008: p. 1-9.

25. P. Hartigan, et al., *Laboratory Experiments, Numerical Simulations, and Astronomical Observations of Deflected Supersonic Jets: Application to HH 110.* The Astrophysical Journal, 2009. **705**(1): p. 1073.

26. X. H. Deng and H. Matsumoto, *Rapid magnetic reconnection in the Earth/'s magnetosphere mediated by whistler waves*, in *Nature*. 2001, Macmillian Magazines Ltd. p. 557-560.

27. E. Ahedo, *Plasmas for space propulsion.* Plasma Physics and Controlled Fusion, 2011. **53**(12): p. 124037.

28. K. F. Schoenberg, et al., *Magnetohydrodynamic flow physics of magnetically nozzled plasma accelerators with applications to advanced manufacturing.* Physics of Plasmas, 1998. **5**(5): p. 2090-2104.

29. E. M. Hollmann, et al., *Particle balance measurements during detachment in a gas-target divertor simulator.* Physics of Plasmas, 2002. **9**(4): p. 1226-1232.

30. T. J. Dolan, *Fusion Research*. 1st ed. Vol. 1. 1982, New York: Pergamon Press. 272.

31. R. D. Hazeltine and J. D. Meiss, *Plasma Confinement*. 1st ed. The Advanced Book Program, ed. B. Holland. 1992, Redwood City: Addison-Wesley Publishing Company. 412.

32. L. D. Landau and E. M. Lifshitz, *Fluid Mechanics*. 2nd ed. Course of Theoretical Physics. Vol. 6. 1987: Butterworth-Heinemann. 552.

33. D. D. Ryutov, et al., *Similarity Criteria for the Laboratory Simulation of Supernova Hydrodynamics.* The Astrophysical Journal, 1999. **518**(2): p. 821.

34. D. D. Ryutov and B. A. Remington. *Optimizing Laboratory Experiments for Dynamic Astrophysical Phenomena*. in *6th Internation Conference on Superstrong Fields in Plasmas*. 2005. Varenna, Italy.

35. D. D. Ryutov, R. P. Drake, and B. A. Remington, *Criteria for Scaled Laboratory Simulations of Astrophysical MHD Phenomena.* The Astrophysical Journal Supplement Series, 2000. **127**(2): p. 465.

36. D. D. Ryutov and B. A. Remington, *Scaling astrophysical phenomena to high-energy-density laboratory experiments.* Plasma Physics and Controlled Fusion, 2002. **44**(12B): p. B407.

37. J. D. Huba, *NRL Plasma Formulary,* ed. N.R. Laboratory. 2012, Washington DC: The Office of Naval Research.

38. J. M. Fonenla, *Chromospheric plasma and the Farley-Buneman instability in solar magnetic regions.* Astronomy & Astrophysics, 2005. **442**: p. 1099-1103.

39. J. E. Vernazza, E. H. Avrett, and R. Loeser, *Structure of the Solar Chromosphere: Basic Computations and Summary of the Results.* The Astrophysical Journal, 1973. **184**: p. 605-631.

40. S. K. Solanki, *Structure of the solar chromosphere.* Proceedings of the International Astronomical Union, 2004. **2004**(IAUS223): p. 195-202.

41. H. Zanstra, *The Value of Observations of Continuous Spectra in the Chromosphere and Prominences.* Astronomy, 1950(1): p. 1289-1299.

42. M. J. Aschwanden, R. W. Nightingale, and D. Alexander, *Evidence for Nonuniform Heating of Coronal Loops Inferred from Multithread Modeling of TRACE Data.* The Astrophysical Journal, 2000. **541**(2): p. 1059.

43. B. C. Boland, et al., *The Heating of the Solar Corona.* Astronomy & Astrophysics, 1973. **22**: p. 161-169.

44. E. Landi, *Ion Temperatures in the Quiet Solar Corona.* The Astrophysical Journal, 2007. **663**(2): p. 1363.

45. V. I. Abramenko, A. Pevtsov, and P. Romano, *Coronal Heating and Photospheric Turbulence Parameters: Observational Aspects.* The Astrophysical Journal Letters, 2006. **646**(1): p. L81.

46. M. J. Aschwanden, et al., *Coronal Loop Oscillations Observed with the Transition Region and Coronal Explorer.* The Astrophysical Journal, 1999. **520**(2): p. 880.

47. D. F. Gray, *The Observation and Analysis of Stellar Photospheres*. 2nd ed. Cambridge Astrophysics Series, ed. C.U. Press. 1992, New York: Cambridge University Press. 452.

48. J. Vranjes, et al. *Flux of Alfven Waves in the Solar Photosphere*. in *12th European Solar Physics Meeting*. 2008. Freiburg, Germany.

49. H. Alfven and P. Carlqvist, *Currents in the solar atmosphere and a theory of solar flares,* in *Solar Physics*. 1967, Springer Netherlands. p. 220-228.

50. M. J. Aschwanden, J. Brown, and E. Kontar, *Chromospheric Height and Density Measurements in a Solar Flare Observed with RHESSI - II. Data Analysis,* in *Solar Physics*. 2002, Springer Netherlands. p. 383-405.

51. P. Carlqvist, *Current limitation and solar flares,* in *Solar Physics*. 1969, Springer Netherlands. p. 377-392.

52. D. Fujimura and S. Tsuneta, *Properties of Magnetohydrodynamic Waves in the Solar Photosphere Obtained with Hinode.* The Astrophysical Journal, 2009. **702**(2): p. 1443.

53. G. G. Allen, *Plasma Beta above a Solar Active Region: Rethinking the Paradigm*, in *Solar Physics*. 2001, Springer Netherlands. p. 71-86.

54. E. Marsch and C. Y. Tu, *Solar Wind and Chromospheric Network*, in *Solar Physics*. 1997, Springer Netherlands. p. 87-106.

55. C. Y. Tu and E. Marsch, *Two-Fuid Model For Heating of the Solar Corona and Acceleration of the Solar Wind by High-Frequency Alfven Waves*, in *Solar Physics*. 1997, Springer Netherlands. p. 363-391.

56. R. A. Gerwin, et al., *Characterization of Plasma Flow through Magnetic Nozzles*. 1990, Los Alamos National Laboratory. p. 173.

57. G. Schmidt, *Plasma Motion Across Magnetic Fields.* Physics of Fluids, 1960. **3**(6): p. 961-965.

58. J. M. Dawson, H. Okuda, and R. N. Carlile, *Numerical Simulation of Plasma Diffusion Across a Magnetic Field in Two Dimensions.* Physical Review Letters, 1971. **27**(8): p. 491-494.

59. T. M. York, *Plasma Flow Processes Within Magnetic Nozzle Configurations.* Journal of Propulsion and Power, 1992. **8**(5): p. 1023-1030.

60. E. B. Hooper, *Plasma detachment from a magnetic nozzle.* Journal of Propulsion and Power, 1993. **9**(5): p. 757-763.

61. H. Okuda and J. M. Dawson, *Theory and numerical simulation on plasma diffusion across a magnetic field.* Physics of Fluids, 1973. **16**(3): p. 408-426.

62. H. G. Kosmahl, *Three-Dimensional Plasma Acceleration Through Axisymmetric Diverging Magnetic Fields Based on Dipole Moment Approximation*, NASA, Editor. 1967, Lewis Research Center: Cleveland. p. 29.

63. D. L. Chubb, *Fully Ionized Quasi-One Dimensional Magnetic Nozzle Flow*, in *NASA TECHNICAL MEMORANDUM*. 1971, Lewis Research Center: Cleveland. p. 14.

64. J. Denavit, *Collisionless plasma expansion into a vacuum.* Physics of Fluids, 1979. **22**(7): p. 1384-1392.

65. I. G. Mikellides, et al., *Design of a fusion propulsion system-Part 2: Numerical simulation of magnetic-nozzle flows.* Journal of Propulsion and Power, 2002. **18**(1): p. 152-158.

66. P. G. Mikellides, P. J. Turchi, and I. G. Mikellides, *Design of a fusion propulsion system-Part 1: Gigawatt-level magnetoplasmadynamic source.* Journal of Propulsion and Power, 2002. **18**(1): p. 146-151.

67. A. V. Ilin, et al. *Simulations of Plasma Detachment in VASIMR*. in *40th AIAA Aerospace Sciences Meeting and Exhibit*. 2002. Reno, Nevada: AIAA.

68. G. J. M. Hagelaar, et al., *Role of anomalous electron transport in a stationary plasma thruster simulation.* Journal of Applied Physics, 2003. **93**(1): p. 67-75.

69. A. V. Arefiev and B. N. Breizman, *Theoretical components of the VASIMR plasma propulsion concept.* Physics of Plasmas, 2004. **11**(5): p. 2942-2949.

70. A. V. Arefiev and B. N. Breizman, *Magnetohydrodynamic scenario of plasma detachment in a magnetic nozzle.* Physics of Plasmas, 2005. **12**(4): p. 043504-10.

71. K. Sankaran, E. Y. Choueiri, and S. C. Jardin, *Comparison of Simulated Magnetohydrodynamic Thruster Flowfields to Experimental Measurements.* Journal of Propulsion and Power, 2005. **21**(1): p. 129-138.

72. J. T. Cassibry. *Theoretical Performance of an MPD Nozzle Using Super-Alfvenic Detachment*. in *42nd AIAA/ASME/SAE/ASEE Joint Propulsion Conference and Exhibit*. 2006. Sacramento, California: AIAA.

73. M. Colleti. *Simple thrust formula for an MPD thruster with applied-magnetic field from magnetic stress tensor*. in *43rd AIAA/ASME/SAE/ASEE Joint Propulsion Conference & Exhibit*. 2007. Cincinnati, Ohio: AIAA.

74. K. Sankaran and K. A. Polzin. *Development of Numerical Tools for the Investigation of Plasma Detachment from Magnetic Nozzles*. in *38th AIAA Plasma Dynamics and Lasers Conference*. 2007. Miami, Florida.

75. V. Lancellotti, et al. *Radiofrequency Plasma Thrusters: Modelling of Ion Cyclotron Resonance Heating and System Performance*. in *43rd AIAA/ASME/SAE/ASEE Joint Propulsion Conference and Exhibit*. 2007. Cincinnati, Ohio: AIAA.

76. C. A. Deline, *Characterization of the magnetic nozzle region of high powered electric propulsion thrusters using numerical simulation, RF interferometry, and electrostatic probes*, in *Electrical Engineering*. 2008, University of Michigan: Ann Arbor. p. 304.

77. A. V. Arefiev and B. N. Breizman, *Ambipolar acceleration of ions in a magnetic nozzle.* Physics of Plasmas, 2008. **15**(4): p. 042109-8.

78. B. N. Breizman, M. R. Tushentsov, and A. V. Arefiev, *Magnetic nozzle and plasma detachment model for a steady-state flow*. Physics of Plasmas, 2008. **15**(5): p. 057103-10.

79. A. V. Arefiev and B. N. Breizman, *Collisionless plasma expansion into vacuum: Two new twists on an old problem.* Physics of Plasmas, 2009. **16**(5): p. 055707-11.

80. K. Sankaran and K. A. Polzin. *Numerical Investigation of Near-Field Plasma Flows in Magnetic Nozzles*. in *45th AIAA/ASME/SAE/ASEE Joint Propulsion Conference & Exhibit*. 2009. Denver, Colorado: AIAA.

81. E. Ahedo and M. Merino, *On plasma detachment in propulsive magnetic nozzles.* Physics of Plasmas, 2011. **18**(5): p. 053504-8.

82. J. M. Little and E. Y. Choueiri. *The Inuence of Induced Currents on Magnetic Nozzle Acceleration and Plasma Detachment*. in *46th AIAA/ASME/SAE/ASEE Joint Propulsion Conference & Exhibit*. 2010. Nashville, Tennessee: AIAA.

83. E. Ahedo and M. Merino. *Preliminary assessment of detachment in a plasma thruster magnetic nozzle*. in *46th AIAA/ASME/SAE/ASEE Joint Propulsion Conference & Exhibit*. 2010. Nashville, Tennessee: AIAA.

84. E. Ahedo and M. Merino. *Two-dimensional plasma acceleration in a divergent magnetic nozzle*. in *45th AIAA/ASME/SAE/ASEE Joint Propulsion Conference & Exhibit*. 2009. Denver, Colorado: AIAA.

85. P. F. Schmit and N. J. Fisch, *Magnetic detachment and plume control in escaping magnetized plasma.* Journal of Plasma Physics, 2009. **75**(03): p. 359-371.

86. E. Ahedo and M. Merino. *Two-dimensional plasma acceleration in a divergent magnetic nozzle*. in *45th AIAA/ASME/SAE/ASEE Joint Propulsion Conference & Exhibit*. 2009. Denver, Colorado: AIAA.

87. E. Ahedo and M. Merino. *Acceleration of a focused plasma jet in a divergent magnetic nozzle*. in *31st International Electric Propulsion Conference*. 2009. University of Michigan, Ann Arbor, Michigan: IEPC.

88. R. Kawabuchi, et al., *Numerical simulation of plasma detachment from a magnetic nozzle by using fully Particle-In-Cell code.* Journal of Physics: Conference Series, 2008. **112**(4): p. 4.

89. R. Winglee, et al., *Simulation and laboratory validation of magnetic nozzle effects for the high power helicon thruster.* Physics of Plasmas, 2007. **14**(6): p. 063501-14.

90. F. N. Gesto, et al., *Ion Detachment in the Helicon Double-Layer Thruster Exhaust Beam.* Journal of Propulsion and Power, 2006. **22**(1): p. 24-30.

91. A. Meige, et al., *One-dimensional particle-in-cell simulation of a current-free double layer in an expanding plasma.* Physics of Plasmas, 2005. **12**(5): p. 052317-10.

92. J. Shebalin, et al. *VASIMR Theory and Computation Overview*. in *2005 VASIMR Workshop*. 2005. Houston, Texas.

93. A. G. Tarditi and J. V. Shebalin. *Magnetic Nozzle Plasma Exhaust Simulation for the VASIMR Advanced Propulsion Concept*. in *28th International Electric Propulsion Conference*. 2003. Toulouse, France: IEPC.

94. A. G. Tarditi and A. V. Ilin. *Simulation of Plasma Exhaust in the VASIMR Magnetic Nozzle*. in *53rd International Astronautical Congress, 2002 World Space Congress*. 2002. Houston, Texas: IAC.

95. A. G. Tarditi. *NIMROD Application to the VASIMR Plasma Thruster*. in *NIMROD Team Meeting 2001*. 2001. Madison, Wisconsin.

96. J. C. Sercel. *Simple Model of Plasma Acceleration in a Magnetic Nozzle*. in *21st International Electric Propulsion Conference*. 1990. Orlando, Florida: IEPC.

97. K. Kuriki and O. Okada, *Experimental Study of a Plasma Flow in a Magnetic Nozzle.* Physics of Fluids, 1970. **13**(9): p. 2262-2269.

98. C. A. Deline, et al., *Plume detachment from a magnetic nozzle.* Physics of Plasmas, 2009. **16**(3): p. 033502-9.

99. M. Inutake, et al., *Characteristics of a Supersonic Plasma Flow in a Magnetic Nozzle.* Journal of Plasma and Fusion Research, 2002. **78**(12): p. 1352-1360.

100. M. D. West, C. Charles, and R. W. Boswell, *Testing a Helicon Double Layer Thruster Immersed in a Space-Simulation Chamber.* Journal of Propulsion and Power, 2008. **24**(1): p. 134-141.

101. I. A. Biloiu, E. E. Scime, and C. Biloiu, *Ion beam acceleration in a divergent magnetic field.* Applied Physics Letters, 2008. **92**(19): p. 191502-3.

102. K. Takahashi, et al., *Electron Diamagnetic Effect on Axial Force in an Expanding Plasma: Experiments and Theory.* Physical Review Letters, 2011. **107**(23): p. 4.

103. D. B. Miller and E. F. Gibbons, *Experiments with an Electron Cyclotron Resonance Plasma Accelerator.* AIAA Journal, 1964. **2**: p. 35-41.

104. D. B. Miller, G. W. Bethke, and G. F. Crimi, *Investigation of Plasma Accelerator (Cyclotron Resonance Propulsion System)*. 1965, General Electric Co. p. GE 215-252.

105. W. D. Kilpatrick, J. H. Mullins, and J. M. Teem, *Propulsion Application of the Modified Penning Arc Plasma Ejector.* AIAA Journal, 1963. **1**: p. 806-13.

106. S. A. Andersen, et al., *Continuous supersonic plasma wind tunnel.* Physics of Fluids, 1969. **12**(3): p. 557-560.

107. R. W. Moses Jr., R. A. Gerwin, and K. F. Schoenberg, *Resistive plasma detachment in nozzle based coaxial thrusters.* AIP Conference Proceedings, 1992. **246**(1): p. 1293-1303.

108. M. D. Carter, et al. *Radio Frequency Plasma Applications for Space Propulsion*. in *International Conference on Electromagnetics in Advanced Applications*. 1999. Torino, Italy.

109. B. N. Breizman. *Physics Requirements for Detachment Experiments*. in *2005 VASIMR Workshop*. 2005. Houston, Texas.

110. B. N. Breizman and A. V. Arefiev, *Ion kinetics in a magnetized plasma source.* Physics of Plasmas, 2002. **9**(3): p. 1015-1024.

111. B. N. Breizman and A. V. Arefiev, *Single-pass ion cyclotron resonance absorption.* Physics of Plasmas, 2001. **8**(3): p. 907-915.

112. W. H. Bostick, *Experimental Study of Ionized Matter Projected across a Magnetic Field.* Physical Review, 1956. **104**(2): p. 292-299.

113. Y. Kagaya, H. Tahara, and T. Yoshikawa. *Effect of Applied Magnetic Nozzle in a Quasi-Steady MPD Thruster*. in *28th International Electric Propulsion Conference*. 2003. Toulouse, France: IEPC.

114. S. Robertson, et al., *Propagation of an Intense Ion Beam Transverse to a Magnetic Field.* Physical Review Letters, 1981. **47**(7): p. 508-511.

115. K. Terasaka, et al., *Observation of Ion Streamline Detachment and Onset of Azimuthal Rotation in a Diverging Magnetic Field.* IEEE Transactions on Plasma Science, 2011. **39**(11): p. 2470-2471.

116. K. Terasaka, et al., *Experimental studies on ion acceleration and stream line detachment in a diverging magnetic field.* Physics of Plasmas, 2010. **17**(7): p. 072106-6.

117. S. W. Simpson, *Ionisation and recombination rates in argon plasmas.* Journal of Physics D: Applied Physics, 1990. **23**(9): p. 1161.

118. F. F. Chen, *Introduction to Plasma Physics and Controlled Fusion*. 2nd ed. Vol. 1: Plasma Physics. 1984, New York: Plenum Press. 421.

119. M. A. Lieberman and A. J. Lichtenberg, *Principles of Plasma Discharges and Materials Processing*. 2nd ed, ed. I. John C. Wiley and Sons. 2005, Hoboken: John C. Wiley and Sons, Inc. 757.

120. N. Brenning, et al., *Faster-than-Bohm Cross-B Electron Transport in Strongly Pulsed Plasmas.* Physical Review Letters, 2009. **103**(22): p. 225003.

121. J. B. Taylor and B. McNamara, *Plasma Diffusion in Two Dimensions.* Physics of Fluids, 1971. **14**(7): p. 1492-1499.

122. T. Hurtig, N. Brenning, and M. A. Raadu, *The role of high frequency oscillations in the penetration of plasma clouds across magnetic boundaries.* Physics of Plasmas, 2005. **12**(1): p. 012308-13.

123. T. Hurtig, N. Brenning, and M. A. Raadu, *The penetration of plasma clouds across magnetic boundaries: The role of high frequency oscillations.* Physics of Plasmas, 2004. **11**(7): p. L33-L36.

124. N. Brenning, *Electron Detachment in Magnetic Nozzles (Unpublished)*, Personal Communication/Compiled Report of Ideas, 2008.

125. N. Brenning, T. Hurtig, and M. A. Raadu, *Conditions for plasmoid penetration across abrupt magnetic barriers.* Physics of Plasmas, 2005. **12**(1): p. 012309-10.

126. E. Y. Choueiri, *Anomalous resistivity and heating in current-driven plasma thrusters.* Physics of Plasmas, 1999. **6**(5): p. 2290-2306.

127. E. N. Parker, *Dynamics of the Interplanetary Gas and Magnetic Fields.* The Astrophysical Journal, 1958. **128**: p. 664-676.

128. A. Vaivads, A. Retino, and M. Andre, *Magnetic reconnection in space plasma.* Plasma Physics and Controlled Fusion, 2009. **51**(12): p. 8.

129. D. Tsiklauri, *A new fast reconnection model in a collisionless regime.* Physics of Plasmas, 2008: p. 1-7.

130. S. Servidio, et al., *Magnetic Reconnection in Two-Dimensional Magnetohydrodynamic Turbulence.* Physical Review Letters, 2009. **102**(11): p. 115003.

131. M. Scholer, et al., *Onset of collisionless magnetic reconnection in thin current sheets: Three-dimensional particle simulations.* Physics of Plasmas, 2003. **10**(9): p. 3521-3527.

132. J. F. Drake, et al., *Electron acceleration from contracting magnetic islands during reconnection.* 2006. **443**(7111): p. 553-556.

133. J. Egedal and M. Porkolab, *Magnetic Reconnection Experiments on VTF*, in *Introduction*, PSFC, Editor. 2012, MIT: Cambridge. p. Introduction to VTF.

134. J. B. Hsia, et al., *Generalized Lower Hybrid Drift Instability.* Physics of Fluids, 1979. **22**(9): p. 1737-1746.

135. J. B. McBride, et al., *Theory and Simulation of Turbulent Heating by the Modified Two-Stream Instability*. Physics of Fluids, 1972. **15**(12): p. 2367-2383.

136. L. Spitzer Jr., *Physics of Fully Ionized Gases*. 1st ed. Interscience Tracts on Physics and Astronomy, ed. R.E. Marshak. Vol. 3. 1956, New York: Interscience Publishers, Inc. 105.

137. T. Hurtig and J. Wistedt, *Probes for high-frequency measurements in a plasma gun.* Review of Scientific Instruments, 2003. **74**(2): p. 1153-1155.

138. D. Lundin, et al., *Anomalous electron transport in high power impulse magnetron sputtering.* Plasma Sources Science and Technology, 2008. **17**(2): p. 025007.

139. E. A. Bering, et al. *Ion Acceleration By Single Pass Ion Cyclotron Heating in the VASIMR Engine*. in *29th International Electric Propulsion Conference*. 2005. Princeton, New Jersey: IEPC.

140. C. S. Olsen, *Ion Flux Maps and Helicon Source Efficiency in the VASIMR VX-100 Experiment Using a Moving Langmuir Probe Array*, in *Physics and Astronomy*. 2009, Rice University: Houston. p. 155.

141. F. R. Chang-Diaz, *The VASIMR Rocket*, in *Scientific American*. 2000. p. 9.

142. F. R. Chang-Diaz. *An overview of the VASIMR engine: High power space propulsion with RF plasma generation and heating*. in *AIP Conference Proceedings*. 2001. Oxnard, California: AIP.

143. F. R. Chang-Diaz. *Fast, Power-Rich Space Transportation, Key to Human Space Exploration and Survival*. in *53rd International Astronautical Congress, The World Space Congress*. 2002. Houston, Texas.

144. F. R. Chang-Diaz. *Progress on the VASIMR Engine*. in *39th AIAA/ASME/SAE/ASEE Joint Propulsion Conference*. 2003. Huntsville, Alabama: AIAA.

145. F. R. Chang-Diaz, et al. *The Development of the VASIMR Engine*. in *International Conference on Electromagnetics in Advanced Applications*. 1999. Torino, Italy.

146. E. A. Bering, et al. *Progress Toward the Development of a 50 kW VASIMR Engine*. in *43rd AIAA Aerospace Sciences Meeting and Exhibit*. 2005. Reno, Nevada: AIAA.

147. J. P. Squire, et al., *Investigation of a Light Gas Helicon Plasma Source for the VASIMR Space Propulsion System.* AIP Conference Proceedings, 2003. **694**(1): p. 423-426.

148. T. W. Glover, et al. *Principal VASIMR Results and Present Objectives*. in *Space Technology and Applications International Forum*. 2005. Albuquerque, New Mexico.

149. T. W. Glover, et al. *Projected Lunar Cargo Capabilities of High-Power VASIMR(TM) Propulsion*. in *30th International Electric Propulsion Conference*. 2007. Florence, Italy: IEPC.

150. E. A. Bering, et al. *High Power Electric Propulsion Using VASIMR(TM): Results from Flight Prototypes*. in *47th AIAA Aerospace Sciences Meeting and Exhibit*. 2009. Orlando, Florida: AIAA.

151. J. P. Squire, et al. *VASIMR Performance Measurements at Powers Exceeding 50 kW and Lunar Robotic Mission Applications*. in *International Interdisciplinary Symposium on Gaseous and Liquid Plasmas*. 2008. Sendai, Japan.

152. L. D. Cassady, et al. *VASIMR(R) Technological Advances and First Stage Performance Results*. in *45th AIAA/ASME/SAE/ASEE Joint Propulsion Conference and Exhibit*. 2009. Denver, Colorado: AIAA.

153. B. W. Longmier, et al., *Ambipolar ion acceleration in an expanding magnetic nozzle.* Plasma Sources Science and Technology, 2011. **20**(1): p. 015007.

154. C. S. Olsen, et al. *Experimental determination of plasma detachment from the diverging magnetic nozzle of the VASIMR VX-200 electric thruster*. in *53rd APS Division of Plasma Physics*. 2011. Salt Lake City, Utah: APS.

155. E. A. Bering, et al., *Observations of single-pass ion cyclotron heating in a trans-sonic flowing plasma.* Physics of Plasmas, 2010. **17**(4): p. 043509-19.

156. F. F. Chen, *Plasma ionization by helicon waves.* Plasma Physics and Controlled Fusion, 1991. **33**(4): p. 339.

157. R. W. Boswell, *Very efficient plasma generation by whistler waves near the lower hybrid frequency.* Plasma Physics and Controlled Fusion, 1984. **26**(10): p. 1147.

158. R. W. Boswell and F. F. Chen, *Helicons-the early years.* Plasma Science, IEEE Transactions on, 1997. **25**(6): p. 1229-1244.

159. F. F. Chen and R. W. Boswell, *Helicons-the past decade.* Plasma Science, IEEE Transactions on, 1997. **25**(6): p. 1245-1257.

160. O. A. Popov, *High Density Plasma Sources*. First ed, ed. O.A. Popov. Vol. 1. 1995, Woburn, Massachusetts: Noyes Publications. 463.

161. M. D. Carter, et al., *Comparing experiments with modeling for light ion helicon plasma sources.* Physics of Plasmas, 2002. **9**(12): p. 5097-5110.

162. S. M. Yun, J. H. Kim, and H. Y. Chang, *Electrical characteristics of helicon wave plasmas.* Plasma Science, IEEE Transactions on, 1998. **26**(2): p. 159-166.

163. E. Ahedo. *Cylindrical model of a helicon-generated plasma*. in *31st International Electric Propulsion Conference*. 2009. University of Michigan, Ann Arbor, Michigan: IEPC.

164. M. D. Carter, et al., *Combined rf and transport effects in magnetized capacitive discharges.* Journal of Applied Physics, 2006. **100**(7): p. 073305-13.

165. T. H. Stix, *Ion cyclotron heating of a plasma.* Journal of Nuclear Energy. Part C, Plasma Physics, Accelerators, Thermonuclear Research, 1961. **2**(1): p. 84.

166. A. V. Ilin, et al. *Particle Simulations of Plasma Heating in VASIMR*. in *36th AIAA/AMSE/SAE/ASEE Joint Propulsion Conference*. 2000. Huntsville, Alabama: AIAA.

167. A. V. Ilin, et al. *Plasma Heating Simulation in the VASIMR System*. in *43rd AIAA Aerospace Sciences Meeting and Exhibit*. 2005. Reno, Nevada: AIAA.

168. E. A. Bering, et al., *Electromagnetic ion cyclotron resonance heating in the VASIMR.* Advances in Space Research, 2008. **42**(1): p. 192-205.

169. E. A. Bering, et al. *High Power Ion Cyclotron Heating in the VASIMR Engine*. in *45th AIAA Aerospace Sciences Meeting and Exhibit*. 2007. Reno, Nevada: AIAA.

170. A. V. Ilin, et al. *Improved simulation of the ICRF waves in the VASIMR plasma*. in *Computer Physics Communications Proceedings of the 18th International Conferene on the Numerical Simulation of Plasmas*. 2004.

171. T. W. Glover, et al. *Ion Cyclotron Heating Results in the VASIMR VX-10*. in *40th AIAA/AMSE/SAE/ASEE Joint Propulsion Conference and Exhibit*. 2004. Fort Lauderdale, Florida.

172. T. W. Glover, *Measurement of Plasma Parameters in the Exhaust of a Magnetoplasma Rocket by Gridden Energy Analyzer and Emissive Langmuir Probe*, in *Physics and Astronomy*. 2002, Rice University: Houston. p. 112.

173. J. F. O'Hanlon, *A User's Guide to Vacuum Technology*. 3rd ed, ed. I. John C. Wiley and Sons. 2003, Hoboken: John C. Wiley and Sons, Inc. 516.

174. D. Rapp and W. E. Francis, *Charge Exchange between Gaseous Ions and Atoms.* The Journal of Chemical Physics, 1962. **37**(11): p. 2631-2645.

175. B. J. Nichols and F. C. Witteborn, *Measurements of Resonant Charge Exchange Cross Sections in Nitrogen and Argon between 0.5 and 17 eV*, NASA, Editor. 1966, Ames Research Center: Moffett Field, California. p. 31.

176. A. V. Phelps, *Cross Sections and Swarm Coefficients for Nitrogen Ions and Neutrals in N2 and Argon Ions and Neutrals in Ar for Energies from 0.1 eV to 10 keV*. Journal of Physical and Chemical Reference Data, 1991. **20**(3): p. 557-573.

177. L. S. Frost and A. V. Phelps, *Momentum-Transfer Cross Sections for Slow Electrons in He, Ar, Kr, and Xe from Transport Coefficients.* Physical Review, 1964. **136**(6A): p. A1538-A1545.

178. P. S. Krstic and D. R. Schultz, *Consistent definitions for, and relationships among, cross sections for elastic scattering of hydrogen ions, atoms, and molecules.* Physical Review A, 1999. **60**(3): p. 2118-2130.

179. B. M. Smirnov, *Tables for Cross Sections of the Resonant Charge Exchange Process.* Physica Scripta, 2000. **61**(5): p. 595.

180. P. M. Stier and C. F. Barnett, *Charge Exchange Cross Sections of Hydrogen Ions in Gases.* Physical Review, 1956. **103**(4): p. 896-907.

181. H. M. Mott-Smith and I. Langmuir, *The Theory of Collectors in Gaseous Discharges.* Physical Review, 1926. **28**(4): p. 727-763.

182. J. M. Anderson, *History and reflections on the way things were,* in *IEEE Power Engineering Review*. 2002.

183. I. H. Hutchinson, *Principles of Plasma Diagnostics*. 2nd ed, ed. C.U. Press. 2002, Cambridge: Cambridge Univserity Press. 440.

184. N. Hershkowitz and O. Auciello, *How Langmuir Probes Work*. Plasma Diagnostics: Discharge Parameters and Chemistry, ed. D.L. Flamm. 1989: Academic Press Inc. 113-183.

185. J. D. Swift and M. J. R. Schwar, *Electrical Probes For Plasma Diagnostics*. 1970. 341.

186. N. Hershkowitz, *How does the potential get from A to B in a plasma?* Plasma Science, IEEE Transactions on, 1994. **22**(1): p. 11-21.

187. N. A. Krall and A. W. Trivelpiece, *Principles of Plasma Physics*. 1st ed. International Series in Pure and Applied Physics, ed. J. L. Farnsworth and M.E. Margolies. 1973, New York: McGraw-Hill.

188. T. J. M. Boyd and J. J. Sanderson, *The Physics of Plasmas*. 1st ed, ed. C.U. Press. 2003, Cambridge: Cambridge University Press. 532.

189. M. Tuszewski and J. A. Tobin, *The accuracy of Langmuir probe ion density measurements in low-frequency RF discharges.* Plasma Sources Science and Technology, 1996. **5**(4): p. 640.

190. S. J. Jeon, et al., *Multichannel rf-compensated Langmuir probe array driven by a single bias supply.* Review of Scientific Instruments, 2002. **73**(2): p. 277-282.

191. P. C. Zalm, *Some Useful Yield Estimates for Ion Beam Sputtering and Ion Plating at Low Bombarding Energies.* Journal of Vacuum Science and Technology, 1984. **2**(2): p. 161-162.

192. J. Bohdansky, J. Roth, and H. L. Bay, *An analytical formula and important parameters for low-energy ion sputtering.* Journal of Applied Physics, 1980. **51**(5): p. 2861-2865.

193. B. W. Longmier, *Plasma Sheath Behavior in a Total Nonambipolar Radio Frequency Generated Plasma Electron Source*, in *Nuclear Engineering and Engineering Physics*. 2007, Univeristy of Wisconsin: Madison, WI. p. 179.

194. W. Lochte-Holtgreven, *Plasma Diagnostics*. 2nd ed. American Vacuum Society Classics, ed. A. Press. 1995, New York: AIP Press. 928.

195. D. G. Chavers, et al. *Momentum and Heat Flux Measurements in the Exhaust of VASIMR Using Helium Propellant*. in *28th International Electric Propulsion Conference*. 2003. Toulouse, France: IEPC.

196. D. G. Chavers and F. R. Chang-Diaz, *Momentum flux measuring instrument for neutral and charged particle flows.* Review of Scientific Instruments, 2002. **73**(10): p. 3500-3507.

197. B. W. Longmier, et al., *Validating a Plasma Momentum Flux Sensor to an Inverted Pendulum Thrust Stand.* Journal of Propulsion and Power, 2009. **25**(3): p. 7.

198. X. Chen, *The impact force acting on a flat plate exposed normally to a rarefied plasma plume issuing from an annular or circular nozzle.* Journal of Physics D: Applied Physics, 2010. **43**(31): p. 315205.

199. K. L. Bell, N. S. Scott, and M. A. Lennon, *The scattering of low-energy electrons by argon atoms.* Journal of Physics B: Atomic and Molecular Physics, 1999. **17**(23): p. 4757.

200. A. W. Molvik, *Large acceptance angle retarding-potential analyzers.* Review of Scientific Instruments, 1981. **52**(5): p. 704-711.

201. T. S. Green, *Space charge effects in plasma particle analyzers.* Plasma Physics, 1970. **12**(11): p. 877.

202. E. A. Bering, K. G. Weber, and U. V. Fahleson, *An upper limit on the aperture separation of ion drift meters*, in *Astrophysics and Space Science*. 1982, Springer Netherlands. p. 37-49.

203. L. W. Parker and E. C. Whipple, *Theory of a satellite electrostatic probe.* Annals of Physics, 1967. **44**(1): p. 126-161.

204. U. Fahleson, *Theory of Electric Field Measurements Conducted in the Magnetosphere with Electric Probes.* Space Science Reviews, 1967. **7**: p. 25.

205. Agilent, *Agilent 4395A Spectrum Analyzer Awareness Brochure*. 2000: www.agilent.com. p. 6.

206. Agilent, *Agilent 4395A Network/Spectrum/Impedance Analyzer Technical Overview*. 2008, Agilent Technologies: www.agilent.com. p. 16.

207. Agilent, *Agilent 4395A Network/Spectrum/Impedance Analyzer Data Sheet*. 2008, Agilent Technologies: www.agilent.com. p. 20.

208. Agilent, *Agilent 4395A Network/Spectrum/Impedance Analyzer Operation Manual*. 2008, Agilent Technologies: www.agilent.com. p. 575.

209. Agilent, *Agilent Spectrum Analysis Basics*. 2006, Agilent Technologies: www.agilent.com. p. 120.

210. G. D. Reed, W. A. Hargus Jr., and M. A. Cappelli. *Microwave Interferometry (90 GHz) for Hall Thruster Plume Density Characterization*. in *AIAA/ASME/SAE/ASEE Joint Propulsion Conference*. 2005. Tuscon, Arizona: AIAA.

211. D. T. Sandwell, *Biharmonic Spline Interpolation of GEOS-3 and SEASAT Altimeter Data.* Geophysical Research Letters, 1987. **14**(2): p. 139-142.

212. A. V. Ilin, et al., *Accuracy Improvement in Magnetic Field Modeling for an Axisymmetric Electromagnet*. 2000, NASA. p. 50.

213. H. H. Madden, *Comments on the Savitzky-Golay convolution method for least-squares-fit smoothing and differentiation of digital data.* Analytical Chemistry, 1978. **50**(9): p. 1383-1386.

214. A. Savitzky and M. J. E. Golay, *Smoothing and Differentiation of Data by Simplified Least Squares Procedures.* Analytical Chemistry, 1964. **36**(8): p. 1627-1639.

215. J. Steinier, T. Y, and J. Deltour, *Smoothing and differentiation of data by simplified least square procedure.* Analytical Chemistry, 1972. **44**(11): p. 1906-1909.

216. P. R. Bevington and D. K. Robinson, *Data Reduction and Error Analysis for the Physical Sciences*. 2nd ed, ed. W. McGraw-Hill. 1992, Boston: WCB McGraw-Hill. 328.

217. W. Horton and R. D. Estes, *Anomalous drift-wave transport analysis of tokamak discharges.* Nuclear Fusion, 1979. **19**(2): p. 203.

218. A. Hasegawa and M. Wakatani, *Plasma Edge Turbulence.* Physical Review Letters, 1983. **50**(9): p. 682-686.

219. S. C. Cowley, et al., *Plasma Science: Advancing Knowledge in the National Interest*, ed. N.R. Council. 2007, Washington DC: National Academies Press. 280.

220. S. J. Zweben and R. W. Gould, *Structure of edge-plasma turbulence in the Caltech tokamak.* Nuclear Fusion, 1985. **25**(2): p. 171.

221. B. A. Trubnikov, *Particle Interactions in a Fully Ionized Plasma*. Reviews of Plasma Physics. Vol. 1. 1965, New York: Consultants Bureau. 105.

222. D. E. Golden, *Comparison of low-energy total and momentum-transfer scattering cross sections for electrons on helium and argon.* Physical Review, 1966. **151**(1): p. 48.

223. K. L. Bell, N. S. Scott, and M. A. Lennon, *The scattering of low-energy electrons by argon atoms.* Journal of Physics B: Atomic and Molecular Physics, 1999. **17**(23): p. 4757.

224. D. M. Goebel and I. Katz, *Basic Plasma Physics*, in *Fundamentals of Electric Propulsion*. 2008, John Wiley & Sons, Inc. p. 37-90.

225. J. W. Cooley and J. W. Tukey, *An algorithm for the machine calculation of complex Fourier series.* Mathematics of computation, 1965: p. 297-301.

226. D. Donnelly and B. Rust, *The fast Fourier transform for experimentalists.* Computing in Science & Engineering, 2005. **7**(3): p. 71.

227. J. S. Bendat and A. G. Piersol, *Random Data Analysis and Measurement Procedures.* Measurement Science and Technology, 2000. **11**(12): p. 1825.

228. A. Shebshelowitz and A. Gallimore, *Performance and Probe Measurements of a Radiofrequency Plasma Thruster.* Journal of Propulsion and Power (submitted), 2012.

229. *Ad Astra Rocket Company and NASA Johnson Space Center sign agreement on VASIMR payload safety and reliability report*. 2012: www.adastrarocket.com. p. 2.

230. *NASA and Ad Astra Rocket Company sign Agreement for flight test of the VASIMR rocket engine aboard the International Space Station*. 2008: www.adastrarocket.com. p. 2.

231. C. Charles, *Plasmas for spacecraft propulsion.* Journal of Physics D: Applied Physics, 2009. **42**(16): p. 163001.

232. D. W. Marriott, et al. *Design, Construction, and Initial Performance Results of a Multi-Megawatt MPD Thruster for Magnetic Nozzle Testing*. in *38th AIAA/ASME/SAE/ASEE Joint Propulsion Conference and Exhibit*. 2002. Indianapolis, Indianna: AIAA.

233. U. Spadavecchia, et al. *Numerical Study on Magnetic Nozzle for Efficient MHD Application*. in *50th AIAA Aerospace Sciences Meeting*. 2012. Nashville, Tennessee: AIAA.

234. K. F. Schoenberg, et al., *Preliminary investigation of power flow and performance phenomena in a multimegawatt coaxial plasma thruster.* Plasma Science, IEEE Transactions on, 1993. **21**(6): p. 625-644.

235. D. W. Koopman, *Measurement of Charge-Exchange Cross Sections for H+, H2+, and He+ Ions.* Physical Review, 1967. **154**(1): p. 79-85.

236. H. Tawara, *Cross sections for charge transfer of hydrogen beams in gases and vapors in the energy range 10 eV -10 keV.* Atomic Data and Nuclear Data Tables, 1978. **22**(6): p. 491-525.

237. S. R. Cranmer, A. V. Panasyuk, and J. L. Kohl, "Improved Constraints on the Preferential Heating and Acceleration of Oxygen Ions in the Extended Solar Corona," The Astrophysical Journal, 2008. **678** (2), p. 1480.

238. S. R. Cranmer and A. A. van Ballegooijen, "Alfvenic Turbulence in the Extended Solar Corona: Kinetic Effects and Proton Heating," The Astrophysical Journal, 2003. **594** (1), p. 573.

239. S. R. Cranmer, "Coronal holes and the high-speed solar wind," Space Science Reviews, 2002. **101** (3), p. 229-294.

240. S. R. Cranmer, "Ion cyclotron diffusion of velocity distributions in the extended solar corona," Journal of Geophysical Research. A. Space Physics, 2001. **106**, p. 24.

241. S. R. Cranmer, "Ion Cyclotron Wave Dissipation in the Solar Corona: The Summed Effect of More than 2000 Ion Species," The Astrophysical Journal, 2000. **532** (2), p. 1197.

242. S. R. Cranmer and A. A. van Ballegooijen, "On the Generation, Propagation, and Reflection of AlfvÃ©n Waves from the Solar Photosphere to the Distant Heliosphere," The Astrophysical Journal Supplement Series, 2005. **156** (2), p. 265.

243. S. R. Cranmer, A. A. van Ballegooijen, and R. J. Edgar, "Self-consistent Coronal Heating and Solar Wind Acceleration from Anisotropic Magnetohydrodynamic Turbulence," The Astrophysical Journal Supplement Series, 2007. **171** (2), p. 520.

244. S. R. Cranmer, G. B. Field, and J. L. Kohl, "Spectroscopic Constraints on Models of Ion Cyclotron Resonance Heating in the Polar Solar Corona and High-Speed Solar Wind," The Astrophysical Journal, 1999. **518** (2), p. 937.

245. J.A. Miller and R. Ramaty, "Ion and relativistic electron acceleration by Alfven and whistler turbulence in solar flares," Solar Physics, 1982. **113** (1), p. 195-201.

246. H. Peter, "On the nature of the transition region from the chromosphere to the corona of the Sun," Astronomy and Astrophysics, 2001. **374** (3), p. 1108-1120.

247. W. H. Matthaeus, G. P. Zank, S. Oughton et al., "Coronal Heating by Magnetohydrodynamic Turbulence Driven by Reflected Low-Frequency Waves," The Astrophysical Journal Letters, 1999. **523** (1), p. L93.

248. U. Narain and P. Ulmschneider, "Chromospheric and coronal heating mechanisms," Space Science Reviews, 1990. **54** (3), p. 377-445.

249. U. Narain and P. Ulmschneider, "Chromospheric and coronal heating mechanisms II," Space Science Reviews, 1996. **75** (3), p. 453-509.

250. E. Schatzman, presented at the Annales d'Astrophysique, 1949 (unpublished).

251. R. Ramaty and RJ Murphy, "Nuclear processes and accelerated particles in solar flares," Space science reviews, 1987. **45** (3), p. 213-268.

252. D. C. Ellison and R. Ramaty, "Shock acceleration of electrons and ions in solar flares," The Astrophysical Journal, 1985. **298**, p. 400-408.

253. V. Petrosian and S. Liu, "Stochastic Acceleration of Electrons and Protons. I. Acceleration by Parallel-Propagating Waves," The Astrophysical Journal, 2004. **610** (1), p. 550.

254. R. J. Hamilton and V. Petrosian, "Stochastic acceleration of electrons. I-Effects of collisions in solar flares," The Astrophysical Journal, 1992. **398**, p. 350-358.

255. J. M. Pryadko and V. Petrosian, "Stochastic acceleration of low-energy electrons in cold plasmas," The Astrophysical Journal, 2009. **482** (2), p. 774.

256. S. H. Autler and C. H. Townes, "Stark Effect in Rapidly Varying Fields," Phys. Rev. J1 - PR, 1955. **100** (2), p. 703-722.

Appendix A: Comparison of laboratory and space plasma magnetic nozzle systems

The following tabulated plasma parameters (tables A.1 and A.2) were computed directed by the NRL Plasma Formulary[37] using estimates/values taken from published literature and experimental results.

Category (Units)	Laboratory Plasma		Space Plasma				
	VASIMR Magnetic Nozzle		Solar Plasma Properties				Stellar Jet
Basic Plasma Properties	**30 kW Helicon**	**100 kW (Helicon + ICH)**	**Photosphere**	**Chromosphere**	**Corona**	**Coronal Hole**	**HH110**
Scale Length (cm)	200	200	8x10^{7}	2x10^{8}	1x10^{10}	3x10^{9}	1x10^{15}
Plasma Density (cm^{-3})	4.4x10^{11} - 1.16x10^{13}	5.3x10^{11} - 8.4x10^{12}	1x10^{14}	2x10^{10} - 1x10^{14}	1x10^{9}	3x10^{9}	1.12x10^{4}
Electron Temperature (eV)	1.25 - 2.18	2.05 - 6.17	0.5	0.5 - 2	1x10^{2}	1x10^{2}	0.6
Ion Temperature (eV)	6.6 - 10.2	27.6 - 37.1	0.5	0.5 - 2	1x10^{2}	1x10^{1}	2x10^{2}
Ion Species	Ar	Ar	H	H	H	H	H
Magnetic Field Strength (G)	10 - 740	10 - 740	1000	1 - 1000	10	10	3x10^{-3}
Electron Cyclotron Frequency (rad/s)	1.8x10^{8} - 1.3x10^{10}	1.8x10^{8} - 1.3x10^{10}	1.8x10^{10}	1.8x10^{7} - 1.8x10^{10}	1.8x10^{8}	1.9x10^{8}	5.3x10^{4}
Ion Cyclotron Frequency (rad/s)	2.4x10^{3} - 1.8x10^{5}	2.4x10^{3} - 1.8x10^{5}	9.5x10^{6}	9.5x10^{3} - 9.5x10^{6}	9.5x10^{4}	1.0x10^{5}	2.9x10^{1}
Electron Plasma Frequency (rad/s)	3.7x10^{10} - 1.9x10^{11}	4.1x10^{10} - 1.6x10^{11}	5.6x10^{11}	8.0x10^{9} - 5.6x10^{11}	1.8x10^{9}	3.1x10^{9}	6.0x10^{6}
Ion Plasma Frequency (rad/s)	1.4x10^{8} - 7.1x10^{8}	1.5x10^{8} - 6.1x10^{8}	1.3x10^{10}	1.9x10^{8} - 1.3x10^{10}	4.2x10^{7}	7.2x10^{7}	1.4x10^{5}
Electron Gyroradius (cm)	0.005 - 0.27	0.008 - 0.34	0.0017	0.0017 - 3.4	2.4	2.3	610
Ion Gyroradius (cm)	2.2 - 206	4.6 - 393	0.072	0.072 - 145	100	38.2	450000
Debye Length (cm)	0.00032 - 0.0013	0.00064 - 0.0015	0.000053	0.000053 - 0.007	0.24	0.14	5.4
Ion Velocity (cm/s)	1.4x10^{6} - 1.7x10^{6}	2.7x10^{6} - 3.5x10^{6}	9.7x10^{5}	9.7x10^{5} - 2x10^{6}	1.4x10^{7}	6.3x10^{6}	1.8x10^{7}
Electron Thermal Velocity (cm/s)	4.7x10^{7} - 6.2x10^{7}	6x10^{7} - 1x10^{8}	3.0x10^{7}	3.0x10^{7} - 5.9x10^{7}	4.2x10^{8}	4.4x10^{8}	3.3x10^{7}
Ion Thermal Velocity (cm/s)	4.0x10^{5} - 4.9x10^{5}	8.1x10^{5} - 9.4x10^{5}	6.9x10^{5}	6.9x10^{5} - 1.4x10^{6}	9.8x10^{6}	4.0x10^{6}	1.3x10^{7}
Ion Sound Speed (cm/s)	2.2x10^{5} - 3.0x10^{5}	2.9x10^{5} - 5.0x10^{5}	8.2x10^{5}	8.2x10^{5} - 1.6x10^{6}	1.2x10^{7}	1.2x10^{7}	9.0x10^{5}
Alfven Velocity (cm/s)	5.2x10^{5} - 7.5x10^{6}	4.7x10^{5} - 8.8x10^{6}	2.2x10^{7}	1.5x10^{6} - 2.2x10^{7}	6.9x10^{7}	4.3x10^{7}	6.2x10^{6}
Collisional Properties							
electron→electron Collision Frequency (s^{-1})	1.0x10^{8} - 5.5x10^{8}	4.7x10^{7} - 1.2x10^{8}	1.9x10^{10}	1.0x10^{6} - 1.9x10^{10}	2.1x10^{2}	5.2x10^{2}	5.0x10^{0}
electron→ion Collision Frequency (s^{-1})	1.9x10^{8} - 1.0x10^{9}	8.7x10^{7} - 2.2x10^{8}	3.6x10^{10}	1.9x10^{6} - 3.6x10^{10}	4.3x10^{2}	1.1x10^{3}	9.3x10^{0}
electron→neutral Collision Frequency (s^{-1})	9.4x10^{1} - 8.8x10^{2}	1.5x10^{3} - 3.4x10^{4}	2.5x10^{12}	5.3x10^{6} - 2.5x10^{12}	1.4x10^{1}	2.1x10^{1}	1.1x10^{-1}
ion→ion Collision Frequency (s^{-1})	6.1x10^{2} - 4.4x10^{4}	8.9x10^{1} - 1.7x10^{3}	2.8x10^{8}	1.5x10^{4} - 2.8x10^{8}	2.7x10^{0}	8.9x10^{1}	1.8x10^{-5}
ion→electron Collision Frequency (s^{-1})	3.5x10^{2} - 1.9x10^{3}	1.6x10^{2} - 4.1x10^{2}	5.2x10^{6}	2.7x10^{2} - 5.2x10^{6}	6.2x10^{-2}	8.2x10^{-1}	6.7x10^{-4}
ion→neutral Collision Frequency (s^{-1})	1.1x10^{2} - 1.3x10^{2}	1.5x10^{3} - 1.6x10^{3}	5.8x10^{10}	1.2x10^{5} - 5.8x10^{10}	3.3x10^{-1}	1.9x10^{-1}	4.4x10^{-2}
electron→electron Collision Time (s)	1.8x10^{-9} - 1x10^{-8}	8.3x10^{-9} - 2.1x10^{-8}	5.3x10^{-11}	5.3x10^{-11} - 1.0x10^{-6}	4.8x10^{-3}	1.9x10^{-3}	2.0x10^{-1}
electron→ion Collision Time (s)	1x10^{-9} - 5.3x10^{-9}	4.5x10^{-9} - 1.1x10^{-8}	2.8x10^{-11}	2.8x10^{-11} - 5.3x10^{-7}	2.3x10^{-3}	9.1x10^{-4}	1.1x10^{-1}
ion→ion Collision Time (s)	2.3x10^{-5} - 1.6x10^{-3}	5.9x10^{-4} - 1.1x10^{-2}	3.6x10^{-9}	3.6x10^{-9} - 6.7x10^{-5}	7.1x10^{-2}	4.8x10^{-2}	9.1x10^{0}
ion→electron Collision Time (s)	5.3x10^{-4} - 2.9x10^{-3}	2.4x10^{-3} - 6.3x10^{-3}	1.9x10^{-7}	1.9x10^{-7} - 3.7x10^{-3}	1.6x10^{1}	1.2x10^{0}	1.5x10^{3}
electron→electron Mean Free Path (cm)	0.05 - 0.3	0.5 - 1.7	1.5x10^{-3}	1.5x10^{-3} - 5.9x10^{1}	2x10^{6}	8.5x10^{5}	6.6x10^{6}
electron→ion Mean Free Path (cm)	0.03 - 0.18	0.29 - 0.89	8.2x10^{-4}	8.2x10^{-4} - 3.2x10^{1}	9.8x10^{5}	4.2x10^{5}	3.5x10^{6}
electron→neutral Mean Free Path (cm)	7.1x10^{4} - 3.5x10^{5}	2.9x10^{3} - 2.9x10^{4}	1.2x10^{-5}	1.2x10^{-5} - 1.1x10^{1}	3.0x10^{7}	2.1x10^{7}	2.9x10^{8}
ion→ion Mean Free Path (cm)	43 - 1010	650 - 12900	0.0025	0.0025 - 91.9	3.6x10^{6}	44000	7.4x10^{11}
ion→electron Mean Free Path (cm)	320 - 1740	2760 - 7230	0.13	0.13 - 5000	1.6x10^{8}	4.8x10^{6}	1.9x10^{10}
ion→neutral Mean Free Path (cm)	4810 - 5130	730 - 750	1.2x10^{-5}	1.2x10^{-5} - 1.1x10^{1}	3.0x10^{7}	2.1x10^{7}	2.9x10^{8}
Charge-Exchange Mean Free Path (cm)	1200 - 7700	125 - 310	4.8x10^{-5}	4.8x10^{-5} - 4.4x10^{1}	9.5x10^{7}	7.4x10^{7}	8.5x10^{8}

Table A.1: Detailed comparison of laboratory and space plasma parameters (part 1)[14-17, 21-25, 37, 43, 49, 51, 61, 175-178, 180, 235, 236].

Category (Units)	Laboratory Plasma		Space Plasma				
	VASIMR Magnetic Nozzle		Solar Plasma Properties				Stellar Jet
Conductivity/Resistivity Properties	**30 kW Helicon**	**100 kW (Helicon + ICH)**	**Photosphere**	**Chromosphere**	**Corona**	**Coronal Hole**	**HH110**
electron→electron Parallel Conductivity (s^{-1})	$3.1x10^{12}$ - $7.7x10^{12}$	$6.0x10^{12}$ - $3.1x10^{13}$	$1.3x10^{12}$	$1.3x10^{12}$ - $5.1x10^{12}$	$1.2x10^{15}$	$1.5x10^{15}$	$5.8x10^{11}$
electron→electron Pedersen Conductivity (s^{-1})	$6.6x10^{9}$ - $1.3x10^{11}$	$8.7x10^{8}$ - $9.5x10^{10}$	$7.2x10^{11}$	$1.6x10^{10}$ - $7.2x10^{11}$	$1.7x10^{3}$	$1.1x10^{4}$	$5.0x10^{3}$
electron→electron Hall Conductivity (s^{-1})	$2.3x10^{11}$ - $6.1x10^{11}$	$1.6x10^{11}$ - $7.5x10^{11}$	$6.6x10^{11}$	$2.9x10^{11}$ - $6.6x10^{11}$	$1.4x10^{9}$	$4.0x10^{9}$	$5.4x10^{7}$
electrion→ion Parallel Conductivity (s^{-1})	$1.6x10^{12}$ - $4.1x10^{12}$	$3.2x10^{12}$ - $1.6x10^{13}$	$7.0x10^{11}$	$7.0x10^{11}$ - $2.7x10^{12}$	$5.9x10^{14}$	$7.2x10^{14}$	$3.1x10^{11}$
electron→ion Pedersen Conductivity (s^{-1})	$1.2x10^{10}$ - $2.1x10^{11}$	$1.6x10^{9}$ - $1.7x10^{11}$	$5.7x10^{11}$	$3.1x10^{10}$ - $5.7x10^{11}$	$3.5x10^{3}$	$2.2x10^{4}$	$9.4x10^{3}$
electron→ion Hall Conductivity (s^{-1})	$2.2x10^{11}$ - $5.5x10^{11}$	$1.6x10^{11}$ - $7.2x10^{11}$	$2.8x10^{11}$	$2.9x10^{11}$ - $2.8x10^{11}$	$1.4x10^{9}$	$4.0x10^{9}$	$5.4x10^{7}$
ion→ion Parallel Conductivity (s^{-1})	$2.4x10^{12}$ - $5.1x10^{12}$	$1.6x10^{13}$ - $3.8x10^{13}$	$4.9x10^{10}$	$4.9x10^{10}$ - $1.8x10^{11}$	$5.1x10^{13}$	$4.6x10^{12}$	$8.8x10^{13}$
ion→ion Pedersen Conductivity (s^{-1})	$9.9x10^{9}$ - $1.6x10^{11}$	$7.1x10^{8}$ - $3.6x10^{10}$	$4.9x10^{10}$	$4.9x10^{10}$ - $1.3x10^{11}$	$4.1x10^{4}$	$3.4x10^{6}$	$3.3x10^{1}$
ion→ion Hall Conductivity (s^{-1})	$2.2x10^{11}$ - $6.2x10^{11}$	$1.6x10^{11}$ - $7.6x10^{11}$	$1.7x10^{9}$	$1.7x10^{9}$ - $8.2x10^{10}$	$1.4x10^{9}$	$4.0x10^{9}$	$5.4x10^{7}$
ion→electron Parallel Conductivity (s^{-1})	$1.2x10^{13}$ - $3.0x10^{13}$	$2.4x10^{13}$ - $1.2x10^{14}$	$2.6x10^{12}$	$2.6x10^{12}$ - $1.0x10^{13}$	$2.2x10^{15}$	$5.0x10^{14}$	$2.3x10^{12}$
ion→electron Pedersen Conductivity (s^{-1})	$1.7x10^{9}$ - $3.3x10^{10}$	$2.2x10^{8}$ - $2.4x10^{10}$	$6.1x10^{11}$	$8.3x10^{9}$ - $6.1x10^{11}$	$9.4x10^{2}$	$3.1x10^{4}$	$1.3x10^{3}$
ion→electron Hall Conductivity (s^{-1})	$2.3x10^{11}$ - $6.3x10^{11}$	$1.6x10^{11}$ - $7.6x10^{11}$	$1.1x10^{12}$	$2.9x10^{11}$ - $1.1x10^{12}$	$1.4x10^{9}$	$4.0x10^{9}$	$5.4x10^{7}$
Transverse Spitzer Resistivity (s)	$3.3x10^{-14}$ - $8.2x10^{-14}$	$8.1x10^{-15}$ - $4.1x10^{-14}$	$1.9x10^{-13}$	$5.0x10^{-14}$ - $1.9x10^{-13}$	$2.1x10^{-16}$	$1.7x10^{-16}$	$4.3x10^{-13}$
Diffusion Properties							
Electron Bohm Diffusion Coefficient ($cm^2\ s^{-1}$)	$1.8x10^{4}$ - $7.8x10^{5}$	$5.2x10^{4}$ - $1.3x10^{6}$	3100	3100 - $1.3x10^{7}$	$6.3x10^{7}$	$6.4x10^{7}$	$1.3x10^{9}$
Ion Bohm Diffusion Coefficient ($cm^2\ s^{-1}$)	$5.6x10^{4}$ - $6.4x10^{6}$	$2.3x10^{5}$ - $2.3x10^{7}$	3100	3100 - $1.3x10^{7}$	$6.3x10^{7}$	$9.5x10^{6}$	$3.6x10^{11}$
Electron Radial Diffusion Coefficient ($cm^2\ s^{-1}$)	1.4 - 1450	1.2 - 1600	2.2	2.2 - 31000	69	100	$2.6x10^{6}$
Ion Radial Diffusion Coefficient ($cm^2\ s^{-1}$)	370 - 397000	320 - 436000	95	95 - $1.4x10^{6}$	3000	4400	$1.1x10^{8}$
Electron Diffusion Coefficient ($cm^2\ s^{-1}$)	$5.3x10^{6}$ - $3.2x10^{7}$	$8.3x10^{7}$ - $8.6x10^{7}$	$2.4x10^{4}$	$2.4x10^{4}$ - $1.9x10^{9}$	$4.8x10^{14}$	$1.9x10^{14}$	$1.1x10^{14}$
Ion Diffusion Coefficient ($cm^2\ s^{-1}$)	$2.9x10^{6}$ - $1.9x10^{8}$	$1.6x10^{8}$ - $2.5x10^{9}$	1700	1700 - $1.3x10^{8}$	$7.6x10^{13}$	$1.8x10^{11}$	$2.5x10^{17}$
Ambipolar Diffusion Coefficient ($cm^2\ s^{-1}$)	$3.3x10^{6}$ - $1.2x10^{8}$	$1.4x10^{8}$ - $8.6x10^{8}$	3200	3200 - $2.4x10^{8}$	$1.1x10^{14}$	$1.4x10^{12}$	$2.9x10^{16}$
Dimensionless Properties							
Kinetic Beta	0.03 - 10.7	0.09 - 54.6	0.002	0.002 - 1.6	0.4	0.021	8.8
Ion Mach Number	4.6 - 7.6	5.4 - 12.2	1.2	1.2	1.2	0.5	20.0
Alfven (Karman) Number	0.3 - 5.5	0.1 - 3.3	22.0	0.79 - 22.0	5.0	6.8	0.3
Magnetic Mach Number	0.2 - 3.3	0.3 - 7.4	0.05	0.05 - 1.3	0.2	0.15	3.0
Magnetic Reynolds Number	90 - 290	360 - 2360	$1.1x10^{7}$	$2.8x10^{7}$ - $2.2x10^{8}$	$1.8x10^{13}$	$3.0x10^{12}$	$1.1x10^{15}$
Lorentz Number	$4.5x10^{-5}$ - $5.7x10^{-5}$	$9.0x10^{-5}$ - $1.2x10^{-4}$	$3.2x10^{-5}$	$6.5x10^{-5}$ - $3.2x10^{-5}$	$4.6x10^{-4}$	$2.1x10^{-4}$	$6.1x10^{-4}$
Lundquist Number	35 - 1260	63 - 5930	$2.5x10^{8}$	$1.7x10^{8}$ - $6.3x10^{8}$	$9.0x10^{13}$	$2.1x10^{13}$	$3.9x10^{14}$
Ion Peclet Number	$7.6x10^{-13}$ - $1.9x10^{-12}$	$7.3x10^{-14}$ - $1.2x10^{-13}$	$1.0x10^{-6}$	$2.5x10^{-6}$ - $1.1x10^{-5}$	$1.6x10^{-7}$	$3.5x10^{-6}$	0.01
Electron Peclet Number	$1.2x10^{-11}$ - $3.9x10^{-11}$	$1.7x10^{-12}$ - $1.5x10^{-11}$	$5.7x10^{-5}$	$1.9x10^{-5}$ - $1.4x10^{-4}$	$5.2x10^{-7}$	$1.3x10^{-7}$	$1.5x10^{3}$
$\lambda_{charge-exchange} / L$	6.1 - 38.7	0.62 - 1.6	$6.0x10^{-13}$	$6.0x10^{-13}$ - $2.2x10^{-7}$	0.01	0.025	$8.5x10^{-7}$
$\lambda_{charge-exchange} / \Omega_i$	6.3 - 3300	0.34 - 63.3	0.00067	0.00066 - 0.31	$9.3x10^{5}$	$1.9x10^{6}$	1900
ω_{pi} / Ω_i	4000 - 58000	3400 - 63000	1400	1400 - $2.0x10^{4}$	440	700	4900
ω_{pe} / Ω_e	15 - 210	13 - 230	32	32 - 450	10	16	110
$\lambda_{electron-electron} / \lambda_{Debye}$	500 - 1030	1850 - 2370	29	29 - 8000	$8.4x10^{6}$	$5.9x10^{6}$	$1.2x10^{6}$
$\lambda_{electron-ion} / \lambda_{Debye}$	270 - 550	980 - 1260	16	16 - 4240	$4.2x10^{6}$	$2.9x10^{6}$	$6.5x10^{5}$
$\lambda_{ion-ion} / \lambda_{Debye}$	$8.4x10^{4}$ - $1.2x10^{6}$	$7.9x10^{5}$ - $1.2x10^{7}$	47	47 - 12000	$1.6x10^{7}$	$3.1x10^{5}$	$1.4x10^{11}$
$\lambda_{ion-electron} / \lambda_{Debye}$	$9.4x10^{5}$ - $3.2x10^{6}$	$5.4x10^{6}$ - $8.4x10^{6}$	2500	2500 - $6.8x10^{5}$	$6.7x10^{8}$	$3.4x10^{7}$	$3.5x10^{9}$
$\nu_{electron-electron} / \omega_{pe}$	0.013 - 0.054	0.003 - 0.009	0.034	$1.3x10^{-4}$ - 0.034	$1.2x10^{-7}$	$1.7x10^{-7}$	$8.2x10^{-7}$
$\nu_{electron-ion} / \omega_{pe}$	0.025 - 0.1	0.005 - 0.017	0.064	$2.4x10^{-4}$ - 0.064	$2.4x10^{-7}$	$3.4x10^{-7}$	$1.5x10^{-6}$
$\nu_{electron-neutral} / \omega_{pe}$	$8.4x10^{-9}$ - $2.6x10^{-8}$	$2.2x10^{-7}$ - $1.5x10^{-6}$	4.4	$6.6x10^{-4}$ - 4.4	$7.8x10^{-9}$	$6.9x10^{-9}$	$1.9x10^{-8}$
$\nu_{ion-ion} / \omega_{pi}$	$2.6x10^{-5}$ - $1.2x10^{-4}$	$4.0x10^{-6}$ - $1.8x10^{-5}$	0.021	$8.1x10^{-5}$ - 0.021	$6.4x10^{-8}$	$1.2x10^{-6}$	$1.2x10^{-10}$
$\nu_{ion-electron} / \omega_{pi}$	$1.2x10^{-5}$ - $5.0x10^{-5}$	$2.6x10^{-6}$ - $8.2x10^{-6}$	0.0004	$1.5x10^{-6}$ - 0.0004	$1.5x10^{-9}$	$1.1x10^{-8}$	$4.8x10^{-9}$
$\nu_{ion-neutral} / \omega_{pi}$	$9.8x10^{-7}$ - $5.2x10^{-6}$	$1.6x10^{-5}$ - $7.1x10^{-5}$	4.4	$6.6x10^{-4}$ - 4.4	$7.7x10^{-9}$	$2.6x10^{-9}$	$3.2x10^{-7}$
$\nu_{electron-electron} / \Omega_e$	0.22 - 8.9	0.04 - 1.6	1.1	0.057 - 1.1	$1.2x10^{-6}$	$2.7x10^{-6}$	$9.3x10^{-5}$
$\nu_{electron-ion} / \Omega_e$	0.41 - 1.7	0.08 - 3.1	2.05	0.11 - 2.05	$2.4x10^{-6}$	$5.5x10^{-6}$	0.00017
$\nu_{electron-neutral} / \Omega_e$	$2.9x10^{-7}$ - $3.6x10^{-6}$	$1.2x10^{-5}$ - $5.6x10^{-5}$	140	0.3 - 140	$7.9x10^{-8}$	$1.1x10^{-7}$	$2.1x10^{-6}$
$\nu_{ion-ion} / \Omega_i$	0.5 - 1.8	0.06 - 0.23	29	1.6 - 29	$2.8x10^{-5}$	0.00086	$6.1x10^{-7}$
$\nu_{ion-electron} / \Omega_i$	0.06 - 2.3	0.011 - 0.42	0.55	0.029 - 0.55	$6.5x10^{-7}$	$7.9x10^{-6}$	$2.4x10^{-5}$
$\nu_{ion-neutral} / \Omega_i$	0.0043 - 0.31	0.06 - 4.0	6100	12.9 - 6100	$3.4x10^{-6}$	$1.8x10^{-6}$	0.0016

Table A.2: Detailed comparison of laboratory and space plasma parameters (part 2)[14-17, 21-25, 37, 43, 49, 51, 61, 175-178, 180, 235, 236].

Appendix B: Langmuir probe and RPA electronic circuitry

Some of the electrostatic probes used in this experiment needed to measure current from plasma neutralizing onto a metal collector. As a side requirement to prevent damage to the sensitive data acquisition system from possible current spikes, each collector must also have proper voltage isolation. These measurements and circuit isolation is accomplished with two forms of current-to-voltage measurement techniques. The first is the fairly common passive conversion method involving the measurement of current as a voltage drop across a known precision resistor. The second method uses active I-to-V conversion where an Op Amp to output a voltage signal proportional to the input signal where the feedback resistor is a known value. Each of these circuits was used to measure the signals from Langmuir probes (both fixed and swept voltage bias) and the Retarding Potential Analyzer (RPA).

This first circuit is a fairly typical isolation amplifier circuit used for Langmuir probe measurements where the voltage drop across the sense resistor is often negligible. The schematic below (figure B.1) displays a two channel isolation circuit with each channel consisting of four main components: An isolation amplifier (U1 & U2), a solid state switching DC power supply (U3 & U4), a line driver (U5 & U6), and a unity gain op-amp (U7 & U8). The solid state isolation amplifier helps reduce noise in the signal from a number of sources, such as ground loops, feedback from RF and other electronics, power supplies, etc. It must be powered by two sources, ±15 V on both sides of the isolator; one must be measured with respect to the biasing power supply and the other with respect to the instrument ground reference. A solid state switching power supply provides power to the probe side of the isolator, but is inherently noisy due to an internal 500 kHz oscillator. A capacitor bank is placed on the board to filter this high frequency noise to ground. Appropriate impedance matching for the output of the ISO124P to the input of a differential line driver is done using a unity gain op-amp. At this point signals can either be directly input into the analog to digital converter or fed into a line driver in the case of weak signals which may need extra current to be properly fed into the DAQ system. This circuit provides a very clean signal from the probe to the DAQ system.

Given that the first circuit is a passive current-to-voltage conversion method, this second circuit uses an active current-to-voltage conversion where a voltage drop across a resistor is unacceptable, as in the case of very small currents measured by an RPA. This Op Amp based transimpedance amplifier circuit is displayed in figure B.2. The signal enters from the left on a coaxial cable passing by a transient voltage suppressor diode, serving as a hardware protection from voltage spikes, and into the AD547KH metal can Op Amp. A small LEMO coaxial test port is also included for troubleshooting purposes. A trimpot (R1), a firm offset gain resistor (R2), and noise reducing capacitor (C1) are included in the signal side and are calibrated to the specific probe setup. The Op Amp is powered by ±15V and the gain is controlled by a 10 turn, 10k, circular potentiometer. The output voltage is then the product of the measured current with the gain resistor. This signal is fed into an AD215AY isolation amplifier whose 120 kHz bandwidth, 1500 V_{rms} isolation rating, 6 V/μs slew rate, and low noise characteristics were selected specifically for this application. Other various resistors and capacitors are selected for noise isolation as the device is used in an RF EMI environment. The RPA sweep is passed into both the positive input of the Op Amp and input common of the isolation amplifier. The isolated signal is then passed out of the board via coax terminal and into the analog-to-digital converters.

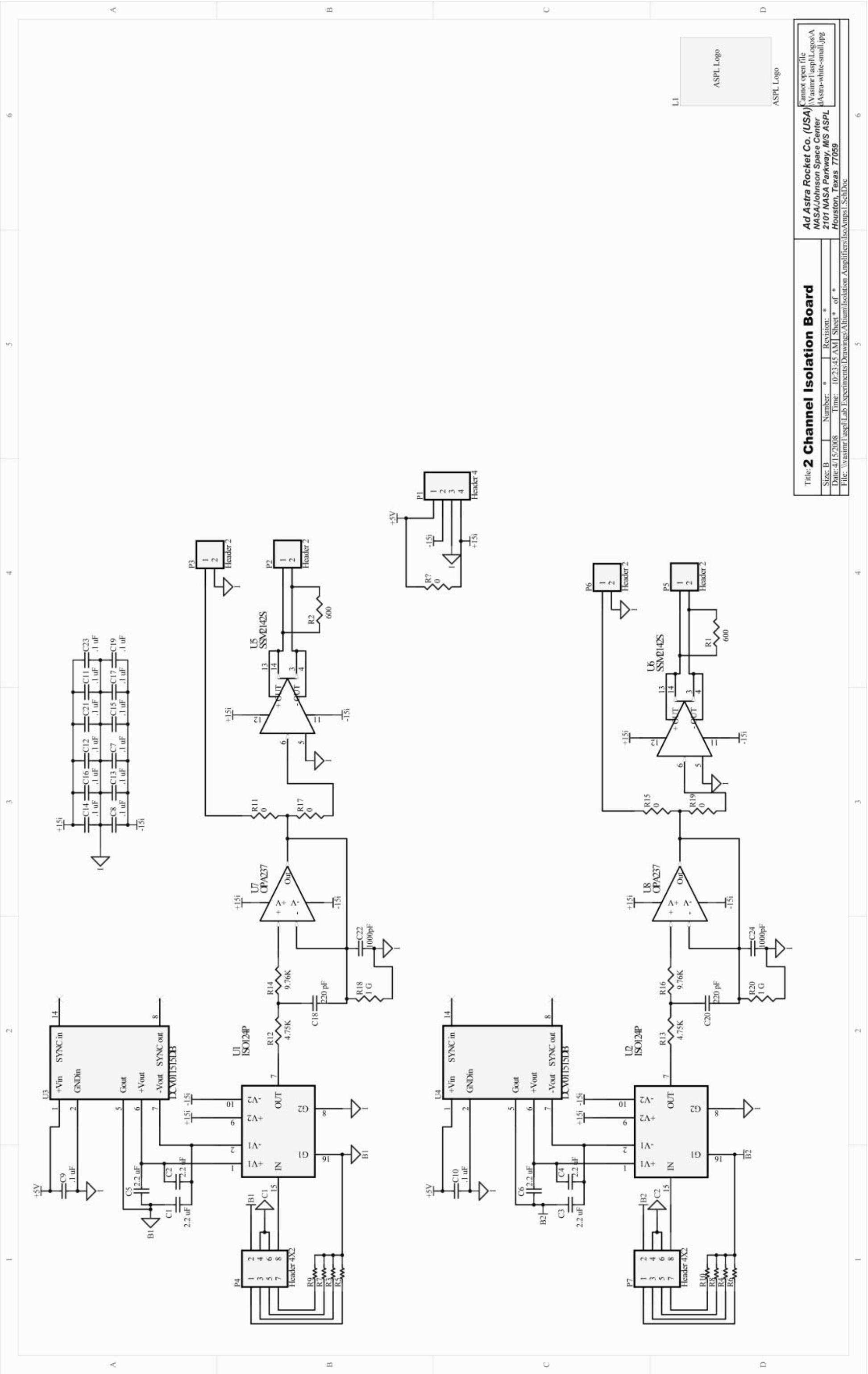

Figure B.1: Two channel isolation amplifier circuit used for Langmuir probe measurements. The line driver path may be used for weak signals or for DAQ systems requiring differential measurements.

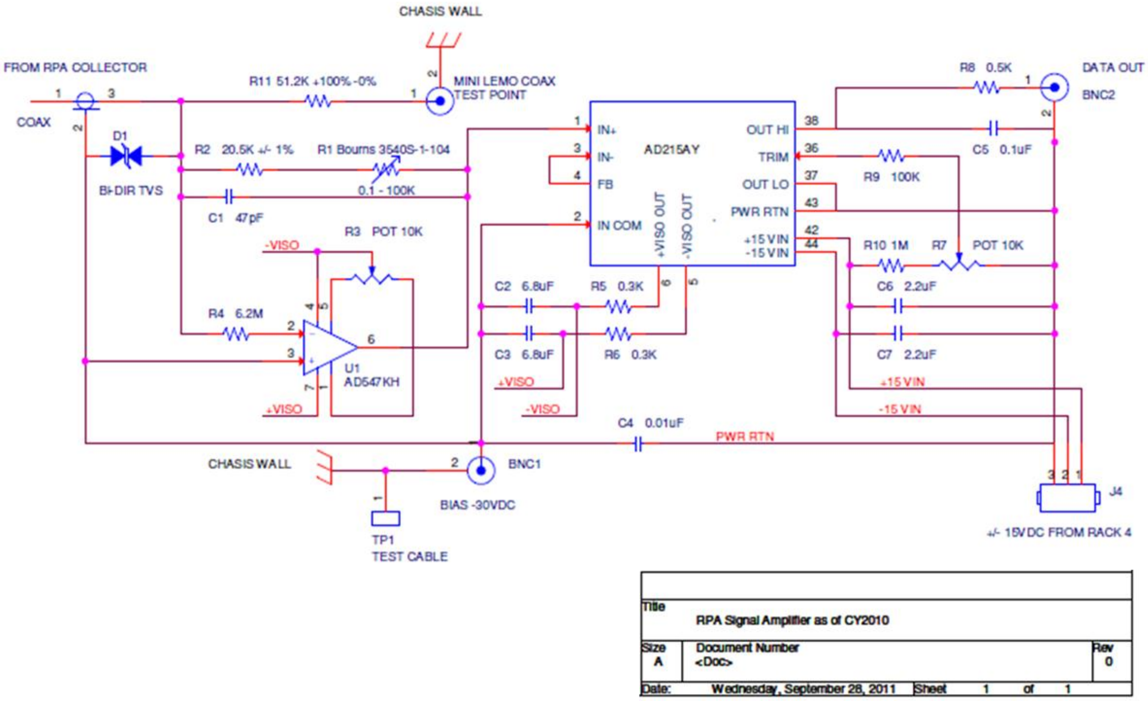

Figure B2: Transimpedance amplifier circuit used to measure current signals from the RPA as low as 1 µA without the effects of a resistor voltage drop.